ISTANBUL TECHNICAL UNIVERSITY ★ GRADUATE SCHOOL OF SCIENCE ENGINEERING AND TECHNOLOGY

MONITORING TROPOSPHERIC WATER VAPOR VARIATIONS WITH PPP DURING SEVERE WEATHER

Ph.D. THESIS

Engin TUNALI

Department of Geomatics Engineering

Geomatics Engineering Programme

JANUARY 2018

ISTANBUL TECHNICAL UNIVERSITY ★ GRADUATE SCHOOL OF SCIENCE ENGINEERING AND TECHNOLOGY

MONITORING TROPOSPHERIC WATER VAPOR VARIATIONS WITH PPP DURING SEVERE WEATHER

Ph.D. THESIS

Engin TUNALI
(501102608)

Department of Geomatics Engineering

Geomatics Engineering Programme

Thesis Advisor: Assoc. Prof. Dr. M. Tevfik ÖZLÜDEMİR

JANUARY 2018

İSTANBUL TEKNİK ÜNİVERSİTESİ ★ FEN BİLİMLERİ ENSTİTÜSÜ

TROPOSFERİK SU BUHARI DEĞİŞİMLERİNİN PPP İLE KÖTÜ HAVA KOŞULLARINDA İZLENMESİ

DOKTORA TEZİ

Engin TUNALI
(501102608)

Geomatik Mühendisliği Anabilim Dalı

Geomatik Mühendisliği Programı

Tez Danışmanı: Doç. Dr. M. Tevfik ÖZLÜDEMİR

OCAK 2018

Engin Tunalı, a Ph.D. student of ITU Graduate School of Science Engineering and Technology student ID 501102608, successfully defended the thesis entitled "MONITORING TROPOSPHERIC WATER VAPOR VARIATIONS WITH PPP DURING SEVERE WEATHER" which he prepared after fulfilling the requirements specified in the associated legislations, before the jury whose signatures are below.

Thesis Advisor :	**Assoc. Prof. Dr. M. Tevfik ÖZLÜDEMİR** Istanbul Technical University	.....
Jury Members :	**Prof. Dr. R. Nurhan ÇELİK** Istanbul Technical University	.....
	Prof. Dr. Ş. Hakan KUTOĞLU Bülent Ecevit University	.....
	Prof. Dr. Orhan AKYILMAZ Istanbul Technical University	.....
	Assoc. Prof. Dr. M. Selim ÇEPNİ Kocaeli University	.....

Date of Submission : 13 December 2017
Date of Defense : 4 January 2018

To my wife and parents,

FOREWORD

First of all, I want to express my special thanks to my supervisor, Assoc. Prof. Dr. Mustafa Tevfik ÖZLÜDEMİR, for his academic guidance and encouragement during the period of my PhD studies. In addition, I wish to express my thanks to my supervisory committee members: Prof. Dr. Rahmi Nurhan ÇELİK and Prof. Dr. Şenol Hakan KUTOĞLU for their time, discussions they made to improve my study and recommendations. Moreover, I would like to express my gratitude to jury members: Prof. Dr.Orhan AKYILMAZ and Assoc. Prof. Dr. Murat Selim ÇEPNİ for their contributions before my thesis defense.

I would like to express my sincere gratitude to head of Hacettepe University Geomatics Engineering Dpt., Prof. Dr. Mustafa TÜRKER for his support and understanding during my PhD studies. Many thanks to all my colleagues at Hacettepe Geomatics. Thank you for your help when I needed, either by an advice or just by stress reducing chats.

Financial supports from The Scientific and Technological Research Council of Turkey (TÜBİTAK) is appreciated to sponsor my study in Helmholtz-Centre Potsdam - GFZ German Research Centre for Geosciences for 12 months. A special thanks to Prof. Dr. Harald Schuh for inviting me to be a part of wonderful GNSS Group Section-1 in GFZ.

I want to thank my mother, father and sister for their encouragement and financial support from the first day of my graduate life.

Finally, I would like to express my gratitude to my wife. My Yasmin…my treasure, beloved one. Nothing would be worth without you. I love you endlessly…

January 2018

Engin TUNALI
(Geomatics Engineer)

TABLE OF CONTENTS

Page

FOREWORD ..... **ix**
TABLE OF CONTENTS ..... **xi**
ABBREVIATIONS ..... **xiii**
SYMBOLS ..... **xvii**
LIST OF TABLES ..... **xxi**
LIST OF FIGURES ..... **xxiii**
SUMMARY ..... **xxvii**
ÖZET ..... **xxxi**
1. INTRODUCTION **1**
1.1 Background 1
1.2 Research Objectives 6
1.3 Thesis Outline 7
2. GNSS AND PPP **9**
2.1 GNSS System Architecture 10
2.1.1 GPS 10
2.1.2 GLONASS 14
2.1.3 GALILEO 15
2.1.4 BEIDUO 16
2.2 GNSS Modernization 17
2.3 Precise Point Positioning 18
2.3.1 Mathematical model of PPP 21
2.3.2 Parameter estimation 24
2.3.2.1 Constraints 28
2.3.2.2 Parameterization 29
2.3.2.3 Parameter (NEQs) stacking 30
2.3.3 Kalman filter 32
2.4 PPP Services 34
2.4.1 PPP software 38
3. ERROR SOURCES AND MITIGATION METHODS IN PPP **41**
3.1 Introduction 41
3.2 Site Displacement Effetcs 41
3.2.1 Solid earth tides 42
3.2.2 Ocean tidal loading 43
3.2.3 Atmospheric tidal loading 45
3.2.4 Non-tidal loading 46
3.2.5 Polar tides 46
3.3 Carrier Phase Wind-up 47
3.4 Relativistic Clock Correction 48
3.5 Multipath 50
3.6 Antenna Phase Center Offsets and Variations 51
3.7 Instrumental Biases 54

3.8 Atmospheric Effects on Signal Propagation 57
3.8.1 Fundamentals of wave propagation: phase and group velocity 58
3.8.2 Ionospheric refraction 60
3.8.3 Ionosphere modeling 63
4. TROPOSPHERIC PATH DELAY 69
4.1 Introduction 69
4.2 Tropospheric Refraction for Microwave Signals 70
4.3 Troposphere Modeling for GNSS Measurements 74
4.3.1 Zenith hydrostatic delay 75
4.3.2 Extraction of meteorological parameters 77
4.3.3 Zenith wet delay 82
4.4 Slant Delay Models 83
4.4.1 Mapping functions 84
4.4.2 Azimuthal Asymmetry and Horizontal Gradients 89
4.5 GNSS METEOROLOGY 91
4.5.1 The role of water vapor 91
4.5.2 Measurement techniques of water vapor 92
4.5.2.1 Radiosondes 92
4.5.2.2 Water vapor radiometer 94
4.5.2.3 Very long baseline interferometry (VLBI) 96
4.5.2.4 GNSS 97
5. CENTRAL EUROPEAN FLOODING 101
5.1 Methodology and PPP Processing 105
5.2 Zenith Wet Delays 110
5.2.1 Validation of PPP results with differential GNSS 119
5.2.2 Orbits and clocks comparison 122
5.2.3 Analysis center comparison 124
5.2.4 Clock Comparison 125
5.2.5 Cut-off elevation angles and parameter spacing 126
5.2.6 Baseline length comparison 128
5.2.7 Epoch-wise kinematic coordinates 129
5.3 Monitoring PWV with GNSS PPP 130
5.3.1 Real-time water vapor monitoring with IGS URP products 138
6. REAL-TIME SERVICES FOR PPP 141
6.1 RTCM DATA and Products 144
6.1.1 Broadcast ephemeris and observations 144
6.2 Real Time Satellite and Clock Correction Calculations 145
6.3 Real Time Ambiguity Resolution 147
6.4 IGS RTS versus CODE final ephemeris 148
6.5 PPP Solutions using Real Time Platforms and Products 151
6.6 Real-Time Water Vapor Monitoring with IGS RTS 156
6.7 Validation of RT PPP Derived PWV with MODIS derived PWV 164
7. CONCLUSIONS AND RECOMMENDATIONS 167
7.1 Conclusions 167
7.2 Recommendations 171
REFERENCES 173
APPENDICES 183
APPENDIX A 184
APPENDIX B 191
CURRICULUM VITAE 195

ABBREVIATIONS

AC : Analysis Center
AIUB : Astronomical Institute of the University of Bern
ANTEX : Antenna Exchange Format
APC : Antenna Phase Center
APL : Atmospheric Pressure Loading
AR : Ambiguity Resolved
ARP : Antenna Reference Point
A-S : Anti-Spoofing
BDS : Beidou Navigation Satellite System
BKG : Bundesamt für Kartographie und Geodäsie
BNC : BKG NTRIP Client
BPE : Bernese Processing Engine
C/A : Coarse / Acquisition
CBIS : Central Bureau Information System
CDDIS : Crustal Dynamics Data Information System
CDMA : Code Division Multiple Access
CGCS2000 : China Geodetic Coordinate System 2000
CLK : Clock RINEX
CMC : Center of mass correction
CNES : Le Site Du Centre National D'études Spatiales
CODE : Center for Orbit Determination in Europe
CoM : Center of Mass
CS : Commercial Services
DAAC : Distributed Active Archive Center
DCB : Differential Code Bias
DD : Double-Difference
DGNSS : Differential GNSS
DoD : Department of Defense
DOP : Dilution of Precision
DoY : Day of Year
ECEF : Earth Centered Earth Fixed
ECMWF : European Centre for Medium-range Weather Forecasts
ECI : Earth Centered Inertial
EOP : Earth Orientation Parameters
EPN : EUREF Permanent GNSS Network
ERP : Earth Rotation Parameters
ESA : European Space Agency
ESOC : European Space Operations Centre
FDMA : Frequency Division Multiple Access
FIN : Final Orbits
FOC : Full operational capability
FTP : File Transfer Protocol
GAPS : GPS Analysis and Positioning Software
GDOP : Geometry Dilution of Precision

GFZ : GeoForschungZentrum
GIM : Global ionosphere models
GIS : Geographic Information Systems
GNSS : Global Navigation Satellite Systems
GPL : GNU General Public License
GPS : Global Positioning System
GPT : Global Pressure and Temperature
GPT2 : Global Pressure and Temperature 2
GRGS : Groupe de Recherche de Géodésie Spatiale
HTTP : Hyper-Text Transfer Protocol
IAG : International Association of Geodesy
ICD : Interface Control Document
IERS : International Earth Rotation and Reference System Service
IF : Ionosphere-Free
IFB : Inter-frequency biases
IGG : Institute of Geodesy and Geophysics
IGEX : International GLONASS Experiment
IGLOS PP : International GLONASS Service Pilot Project
IGRA : Integrated Global Radiosonde Archive
IGS : International GNSS Service
IMF : Isobaric Mapping Function
IONEX : Ionosphere model Exchange format
IOV : In Orbit Validation
IR : Infrared
ISB : Inter-system biases
ISLR : Satellite Laser Ranging Service
ITRF : International Terrestrial Reference Frame
ITRS : International Terrestrial Reference System
ITU : International Telecommunications Union
IWV : Integrated Water Vapor
JPL : Jet Propulsion Laboratory
KF : Kalman Filter
LAADS : Atmosphere Archive & Distribution System
LC : Linear Combination
LSA : Least Squares Adjustment
MGEX : Multi-GNSS Experiment and Pilot Project
MIT : Massachusetts Institute of Technology
MODIS : Moderate Resolution Imaging Spectroradiometer
MW : Melbourne – Wubbena
NAD83 : North American Datum of 1983
NASA : National Aeronautics and Space Administration
NAVSTAR : NAVigation Satellite Timing and Ranging
NCEP : National Centers for Environmental Prediction
NEQ : Normal Equation
NGS : National Geodetic Survey
NIR : Near-Infrared
NL : Narrow Lane
NMF : Niell Mapping Function
NAPEOS : Navigation Package for Earth Observation Satellites
NOAA : National Oceanic and Atmospheric Administration

NRCan : Natural Resources Canada
NTRIP : Networked transport of RTCM via Internet protocol
NWM : Numerical Weather Model
NWP : Numerical Weather Prediction
OS : Open Services
PCO : Phase Center Offsets
PCV : Phase Center Variations
PDOP : Position Dilution of Precision
PP : Post Process
PPP : Precise Point Positioning
PPS : Precise positioning service
PRN : Pseudo Random Noise
PRS : Public Regulated Services
PW : Precipitable Water
PWV : Precipitable Water Vapor
PZ-90 : Parametry Zemli 1990
QZSS : Quasi-Zenith Satellite System
RCP : Right-hand circularly polarized
RF : Radio frequency
RINEX : Receiver INdependent EXchange format
RPD : Rapid Orbits
RS : Radiosonde
RT : Real Time
RTAC : Real-Time Analyses Centers
RTCM : Radio Technical Commission for Maritime Services
RTS : Real-Time Service
SA : Selective Availability
SAR : Search and Rescue
SBAS : Space Based Augmentation Systems
SINEX : Software independent exchange formats
SIP : Stochastic ionosphere parameters
SISRE : Signal in Space Range Error
SLM : Single-layer model
SLR : Satellite Laser Ranging
SoL : Safety of Life
SIO : Scripps Institution of Oceanography
SP3 : Standard Product v.3
SSR : State-space representation
St.Dev : Standard Deviation
STEC : Slant Total Electron Content
SVN : Satellite vehicle number
TDOP : Time Dilution of Precision
TEC : Total Electron Content
TECU : Total Electron Content Unit
TUM : Technical University of Munich
UNB : University of New Brunswick Troposphere Model
UNB3m : University of New Brunswick Troposphere Model 3m
UPC : Universitat Politecnica de Catalunya
UPD : Un-calibrated satellite Phase Delays
URP : Ultra-Rapid Orbits

US : United States
USNO : United States Naval Observatory
UofC : University of Calgary
UTC : Universal Time, Coordinated
VDOP : Vertical Dilution of Precision
VLBI : Very Long Baseline Interferometry
VMF : Vienna Mapping Function
VMF1 : Vienna Mapping Function 1
VMFG : Vienna Mapping Function Grids
VTEC : Vertical Total Electron Content
WAAS : Wide Area Augmentation System
WL : Wide Lane
WLS : Weighted Least Squares Solution
WVR : Water Vapor Radiometer
ZHD : Zenith Hydrostatic Delay
ZPD : IGS Zenith Path Delay
ZTD : Zenith Total Delay
ZWD : Zenith Wet Delay

SYMBOLS

A	**:** Design matrix coefficients
a_c, a_p and b_p	**:** Amplitudes of code signals C / A and P
$a_{h,w}$, $b_{h,w}$, $c_{h,w}$	**:** The coefficients used for calculation of dry and wet mapping functions
Amp_0	**:** GPT spherical harmonic derived amplitude of the requested meteorological parameter
Amp_φ	**:** UNB look-up table derived amplitude of the requested meteorological parameter
a_{nm}, b_{nm}	**:** The coefficients of the harmonic series for phase centre variation function
B1, B2, B3	**:** Frequencies of Beidou satellites
B_3	**:** Ambiguity plus satellite / receiver hardware delays in ionosphere-free solution
B_1^s, B_2^s	**:** Satellite related biases
B_{C1}, B_{P1}, B_{P2}	**:** Biases observed at code observations
b_{Li}^r	**:** Receiver hardware phase delays
b_{Li}^s	**:** Satellite hardware phase delays
b_{Pi}^r	**:** Receiver hardware code delays
b_{Pi}^s	**:** Satellite hardware code delays
c	**:** Speed of light in a vacuum
C(t)	**:** C / A code sequence with state ± 1
C/A	**:** Coarse / Acquisition
c_0, c_1, c_2	**:** Polynomial coefficients derived with broadcast message to calculate clock offset
D(.)	**:** Dispersion Matrix
D(t)	**:** Data stream with state ± 1
DCB_{P1-C1}	**:** Differential interfrequency code biases
DCB_{P1-P2}	
dt_r	**:** Receiver clock error
dt^s	**:** Satellite clock error
dt_{SSR}^S	**:** Corrected real time clocks via IGS RTS corrections
e	**:** Water vapor pressure
E(.)	**:** Statistical expectation
e_0	**:** Partial pressure of water vapor
E1, E6, E5	**:** GALILEO satellites frequency bands (PRN codes)
E5a, E5b	
e_{across}	**:** Space State Representative orbit correction in across-track
e_{along}	**:** Space State Representative orbit correction in along-track
e_{radial}	**:** Space State Representative orbit correction in radial
f_0	**:** Fundamental GNSS frequency
F1(k)/F2(k)	**:** Constant frequency ratio for GLONASS satellites
F(z)	**:** Ionospheric mapping function

f_1, f_2 : Frequencies of two carriers
G : Straight geometrical path
g(z) : Gravity along the vertical coordinate of the site
G3 : New generation GLONASS satellites
G_e : East – West direction tropospheric gradient
g_{eff} : The effectivity (mean) gravity acceleration
g_m : Gravity acceleration
GM_E : Gravitational constant parameter of the Earth
GM_J : Gravitational constant parameter of the Moon
G_n : North – South direction tropospheric gradient
H : Jacobian Matrix for observations
h : Observed minus computed vector for constraints
H_k : Design matrix
h_{nm} : Love numbers
I_i : First order Ionospheric delay
k : GLONASS frequency channel number
K : Kelvin
κ : Unitless conversion factor between ZWD and PWV
k_1 : Dry coefficient determined empirically to compute refractivity of troposphere
k_2, k_3 : Wet coefficients determined empirically to compute refractivity of troposphere
K_k : Gain matrix
L1, L2 : GPS signal carrier waves
L1C, L2C : Modernized GPS signals for civil users
L_3, P_3 : Ionosphere-free phase and code observation
L_4, P_4 : Geometry-free linear combination of phase and code observations
L5C : GNSS civil signal
l_{mn} : Shida numbers
M_d, M_w : Molar mass densities for dry air and water vapor
$Mean_0$: GPT spherical harmonic derived annual average of meteorological parameter for determined latitude
$Mean_\varphi$: UNB look-up table derived annual average of meteorological parameter for determined latitude
mf_{dry} : Dry mapping function
mf_{wet} : Wet mapping function
$mf_h(e)$: Elevation dependent hydrostatic mapping function
$mf_w(e)$: Elevation dependent wet mapping function
n – u : Degree of freedom
N : Normal Equation matrix
n : Number of observations
N_0 : Refractivity of real part of the non-dispersive medium troposphere
N_f : Refractivity imaginary part with frequency dependency
N_i : Integer ambiguity
n_{ph}, n_{gr} : Phase and group refractive index in the neutral atmosphere layers
N^{trop} : Refractivity of troposphere layer
N_w, N_d : Wet and hydrostatic refractivity
O - C : Observed minus computed parameters
p : Vector of unknown parameters for constrained equations
P : Weight matrix of the observations

$\mathbf{P(.)}$: Statistical probability
$\mathbf{P(t)}$: P code sequence with state ± 1
$\mathbf{P_0}$: Surface pressure
$\mathbf{P_{1,2}}$: Precise code
$\mathbf{p_d}$: Partial pressure of dry air
$\mathbf{P_h^{-1}}$: Weight matrix of the constraining equations
$\mathbf{P_k^{-1}}$, $\mathbf{P_k}$: Predicted and corrected covariance matrix of the state
$\mathbf{P_{NM}}$: Legendre's function
$\mathbf{P_i}$, $\mathbf{L_i}$: Code and phase measurements
$\mathbf{Q_{ll}}$: Cofactor matrix (inverse of the weight matrix)
$\mathbf{R}$: Transformation matrix between ECEF and CEL systems
$\mathbf{r(t)}$: Satellite orbit coordinate vector
$\mathbf{r(t)_{corrected}}$: Corrected coordinate vector of IGS RTS orbits
$\mathbf{R_d}$, $\mathbf{R_w}$: Specific gas constant of dry air and water vapor
$\mathbf{R_E}$: Equatorial radius of the Earth
$\mathbf{R_H}$: Relative Humidity
$\hat{\mathbf{R}}_\mathbf{j}$, $\mathbf{R_j}$: Unit vector from the Geo-center to the Moon or the Sun and its magnitude
$\hat{\mathbf{r}}^{\mathbf{sat}}$, $\hat{\mathbf{v}}^{\mathbf{sat}}$: Satellite radius vector and the velocity vector
$\dot{\mathbf{r}}$: Velocity vector of satellite
$\hat{\mathbf{r}}$, $\mathbf{r}$: Unit vector from the geo-center to the station and its magnitude
$\mathbf{S_1}$, $\mathbf{S_2}$: Tidal signals representing atmospheric tidal loading
$\mathbf{sz}$: Sample size
$\mathbf{S - G}$: Signal geometric bending effect
$\mathbf{T}$: Temperature
$\mathbf{T_{(z)}}$: BNC's total zenith troposphere delay
$\mathbf{T_{apr(z)}}$: BNC's a priori zenith troposphere delay
$\mathbf{T_{bf}}$: Brightness temperature
$\mathbf{T_{bf1}}$, $\mathbf{T_{bf2}}$: Linearized brightness temperature
$\mathbf{T_{bg}}$: Cosmic background temperature
$\mathbf{T_m}$: Mean temperature
$\mathbf{Tr_{zwd}}$: Estimated ZWD as a correction to the a priori troposphere ZHD
$\mathbf{trop^n_{apr}}$: A priori troposphere path delay
$\mathbf{u}$: Number of unknowns
$\mathbf{v}$: Residual vector of observations
$\mathbf{v_h}$: Residual vector over the constraints
$\mathbf{v_{ph}}$, $\mathbf{v_{gr}}$: Phase and group velocity of electromagnetic wave
$\mathbf{v^T P v}$: Weighted sum of the squares of the residuals
$\mathbf{w(z)}$: Weighting function of observation
$\mathbf{w_k}$, $\mathbf{v_k}$: Independent variables representing state and measurement noise
$\mathbf{x}$: Vector of unknowns (corrections)
$\mathbf{X_{\varphi,\,doy}}$: Calculated meteorological parameter for specific latitude and day of year
$\hat{\mathbf{x}}_\mathbf{k}$: Estimate of the state vector at the epoch k
$\hat{\mathbf{x}}_\mathbf{k}^-$, $\hat{\mathbf{x}}_\mathbf{k}^+$: Predicted and corrected state vectors
$\mathbf{X_p}$-$\hat{\mathbf{X}}_\mathbf{p}$, $\mathbf{Y_p}$-$\hat{\mathbf{Y}}_\mathbf{p}$: Pole displacements
$\mathbf{y}$: Vector of observed minus computed observations (residual vector)
$\mathbf{z}$: Zenith angle of satellite
$\mathbf{Z_d}$, $\mathbf{Z_w}$: Compressibility factors for dry air and water vapor

$\mathbf{z_k}$: Measurement vector
$\hat{\sigma}_0^2$: A posteriori variance of unit weight
σ_i^2 : Variance of the observations
ε_{Li} : Phase multipath and noise
ε_{Pi} : Code multipath and noise
Δ_{across} : Across-track orbit corrections
Δ_{along} : Along-track orbit corrections
Δ_{radial} : Radial orbit corrections
$\dot{\Delta}_{across}$: Across-track orbit correction rates
$\dot{\Delta}_{along}$: Along-track orbit correction rates
$\dot{\Delta}_{radial}$: Radial orbit correction rates
$\Delta\bar{r}$: Site displacement vector in ECEF Cartesian coordinates
ΔR_{OCN} : Ocean loading site displacement vector
ΔT_{wet}^{z} : Zenith wet delay
$\Delta t_{constant}$: Constant relativistic correction
Δt_{ecc} : Eccentricity correction of each satellite
$\Delta t_{periodic}$: Periodic relativistic correction
Δt_{rel} : Relativistic correction
ΔU : Gravitational potential difference of the satellite's orbit and the Geoid
ΔX : Correction of coordinate X
ΔY : Correction of coordinate Y
ΔZ : Correction of coordinate Z
$\Delta\rho$: Signal propagation delay in the neutral atmosphere
$\Delta\rho^{trop}$: Tropospheric delay
$\Delta\rho_h^z$: Zenith hydrostatic delay
$\Delta\rho_w^z$: Zenith hydrostatic delay
$\Delta\phi(\alpha, z)$: Antenna phase centre correction function
$\Delta\phi'(\alpha,z)$: Azimuth and elevation angle dependent phase center variation
ρ : Receiver – Satellite geometric range involving loads and relativistic effects
ρ_d, ρ_w : Mass density of dry air and water vapor
ρ_v : Water vapor density
ρ_w : Density of liquid water
Σ_{ll} : Variance-covariance matrix of the observation
Φ_k : Transition matrix moving the state at the previous epoch k to the current epoch k-1
δ_{12} : Correlation coefficients
δt^s : Satellite clock corrections
δt_r : Receiver clock corrections
$\delta\phi$: Wind-up error
γ_{orb} : Space State Representative orbit correction vector in radial, along-track and across-track
λ_i : Wavelength
$\tau(f, h)$: Opacity

LIST OF TABLES

Page

Table 2.1 : Legacy GPS signal structure (Seeber, 1993). **13**
Table 2.2 : Galileo Navigation Signals (Wellenhof et al., 2008). **16**
Table 2.3 : The IGS satellite ephemerides and satellite/station clocks with different accuracy and latency rates. **37**
Table 2.4 : The GLONASS satellite ephemerides. **37**
Table 2.5 : The IGS atmospheric products. **37**
Table 2.6 : The IGS Earth Rotation Parameters. **38**
Table 3.1 : The ionospheric layers with different densities with respect to height (Seeber, 2003). **61**
Table 4.1 : Experimental values of coefficients used to calculate the refractivity from different publications. **74**
Table 4.2 : Look up table of UNB model (Leandro et al., 2006). **78**
Table 4.3 : Some properties and availability of meteorological data from different sources (Böhm et al. 2009). **82**
Table 4.4 : Coefficients of the Niell hydrostatic and wet mapping functions (Niell, 1996). **87**
Table 5.1 : IGS sites selected for monitoring the atmosphere during severe weather. **103**
Table 5.2 : Statistical information for the ZWD differences from different PPP solutions and IGS products. **115**
Table 5.3 : Mean positioning residuals (mm) of the PPP solutions differing in used troposphere model. **116**
Table 5.4 : Mean convergence (minutes) of the daily PPP solutions that using GPT/GMF troposphere model. **118**
Table 5.5 : The RMS of the positioning repeatability for the static PPP solution with respect to the atmosphere models of both GPT and VMF1 ..... **118**
Table 5.6 : Mean (mm), Max (mm) and RMS (mm) of the differences between the PPP and the DD solutions. **121**
Table 5.7 : A-posteriori sigma of PPP and DD solution for each day (a-priori sigma of unit weight = 1.0 mm). **122**
Table 5.8 : Mean wet delay differences at POTS, GANP and GRAZ sites due to processing GNSS products from different AC **124**
Table 5.9 : The statistics derived from the network solutions with different baseline lengths. **129**
Table 5.10 : The mean positioning residuals and standard deviations of the residuals of the kinematic coordinates with respect to the three troposphere models. **130**
Table 5.11 : The IGS and the radiosonde sites used in the analyses. **132**
Table 5.12 : Data statistics of the PPP and Network GNSS (DD) derived PWVs with respect to the radisonde data (RS). **135**
Table 5.13 : PWV cross-comparison between the IGS, PPP and Network solutions. **137**

Table 5.14 : Mean differences, RMS values and maximum detected differences of GNSS solutions (PPP and Network) and radiosonde readings for all relevant sites. **140**
Table 6.1 : Broadcast Ephemeris Streams. **144**
Table 6.2 : NTRIP Broadcasters which provide real-time observation (Weber et al., 2016). **144**
Table 6.3 : RTCM v3 streams of ephemeris corrections to support RT PPP (Weber et al., 2016). **145**
Table 6.4 : Orbits and Clocks comparison between IGS RTS (CLK 91) and CODE Final ephemeris products for 21 consequtive days in 2013 **150**
Table 6.5 : RMS values and convergence times of RT PPP positioning with ambiguity float (IGS03), ambiguity fixed (CLK91) and post-process float PPP solutions (CODE) that all are validated through CODE's weekly coordinates. **153**
Table 6.6 : Statistical comparison of average differences and RMS of the differences between RT PPP troposphere and post process PPP troposphere **156**
Table 6.7 : The statistics of the PW differences between the PPP solutions and the Radiosonde data for each GNSS site co-located with the radiosonde sensor. **162**
Table 6.8 : Positions and widths of five MODIS near-IR channels used in the water vapor extraction. **165**
Table 6.9 : Statistical comparison between the MODIS PWV and GNSS PPP (post-process and real-time). **166**
Table A.1 : Input RINEX Measurements. **185**
Table A.2 : Prefit Resdiuals obtained from the solution. **187**
Table A.3 : Prefit Resdiuals and design matrix components for the unknowns. **188**
Table A.4 : Estimated unknowns for each observed epoch. **189**
Table A.5 : Estimated unknowns for each epoch by using Kalman filter. **190**
Table B.1: WEB addresses for GNSS RINEX Observation data. **191**
Table B.2: WEB addresses of GNSS Precise Ephemeris Products: Orbits, Clocks and Earth Rotation Parameters. **192**
Table B.3: Differential Code Biases. **194**
Table B.4: Troposphere and Ionosphere. **194**
Table B.5: ANTEX files. **194**
Table B.6: VMF1 GRID data. **194**
Table B.7: ITRF Coordinates and velocities. **194**
Table B.8: IERS Ocean Loading File. **194**
Table B.9: Phase Center Variations file. **194**

LIST OF FIGURES

Page

Figure 2.1 : Horizontal and Vertical Errors before and after S.A. switch off on May 2, 2000 (GPS: The Global Positioning System, 2002). **9**
Figure 2.2 : Statistics on the satellite types in the GPS constellation in September 2015. ..... **11**
Figure 2.3 : The GPS satellite constellation status, showing each satellite's position in its orbital plane. Dated the 6th of July, 2006 (Navigation Center of Excellence, 2006). **11**
Figure 2.4 : Generation of GNSS signal (Seeber, 1993). **12**
Figure 2.5 : PPP convergence time needed for an accurate positioning in north, east and up directions for "ANKR" IGS site. **20**
Figure 2.6 : Some error sources affecting GNSS positioning accuracy (Sanz et al, 2013). **21**
Figure 2.7 : Kalman Filter diagram used in the traditional PPP solution. **33**
Figure 2.8 : IGS Tracking Network Map (More than 505 stations – green dots) retrieved from IGS web page (Url-1). **35**
Figure 3.1 : Signal range change due to Solid Earth Tides' effect. **43**
Figure 3.2 : Ocean tidal loading file derived from FES2004.BLQ. **44**
Figure 3.3 : Spatial variations of pressure anomaly and vertical displacements at 00 UTC on January 1, 2010 (Wijaya et al, 2013, p.139). **45**
Figure 3.4 : Carrier phase wind-up effect on the total range for the GANP IGS site and PRN: 20. ..... **47**
Figure 3.5 : Variation in the range due to the relativistic clock correction. **49**
Figure 3.6 : Ionosphere free code (L_3) – phase (L_3) (left) and geometry-free (L_4) linear combinations (right). **50**
Figure 3.7 : Antenna phase center offset variations and phase patterns for the receiver (Wellenhof et al, 2008). **51**
Figure 3.8 : Satellite antenna phase center corrections at the GANP station: Horizontal positioning error with and without satellite APC correction (top); Vertical positioning error with and without satellite APC correction (bottom). **53**
Figure 3.9 : CODE's differential P1-P2 (left) and P1-C1 (right) code monthly average biases and their accuracy for GPS satellites. **56**
Figure 3.10 : The daily and monthly average sunspot counts from 2004 to 2017 with two different interpolation techniques in order to predict the future solar activities (SC: Standard Curves Interpolation; CM: Combining regression with Geomagnetic Index) (SIDC - Solar Influences Data Analysis Center, N.d). **60**
Figure 3.11 : Geometry of the Single Layer Model (SLM). **64**
Figure 3.12 : The IONEX file with 3D Ionosphere TEC maps. **67**

Figure 4.1 : The refractivity variation of microwave domain with respect to height for Ionosphere and Troposphere (Seeber, 2003). ……..**70**
Figure 4.2 : The contribution of induced and permanent dipole moment of water vapor to the total wet refractivity (Thayer, 1974). ……**72**
Figure 4.3 : The geometric bending effect due to the refractivity. The signal will take the S path during propagation, and since the signal propagates with a low velocity with respect to vacuum, it covers large distance than actual geometrical path G. ……**75**
Figure 4.4 : The hydrostatic and wet mapping functions comparison among the VMF1 and GMF for DOY: 136, 2013 at 5º elevation angle at mean sea level. ……..**89**
Figure 4.5 : Tilting of the tropospheric zenith (MacMillan, 1995). ……..**90**
Figure 4.6 : IGRA file sample collected from Lindenberg radiosonde station located in Germany. ……..**93**
Figure 4.7 : Intra / inter-technique comparison of tropospheric zenith path delay during the IVS-CONT08 campaign for co-located site HartRAO – Hartebeesthoek / South Africa (Teke, 2011). ……**97**
Figure 5.1 : Flooding effect on Passau near the Danube River – Geromany (left), Dresden near the Elbe River - Germany (right) on June 2, 2013 (European Reanalyses and Observations for Monitoring – EURO4M, 2013). ……..**101**
Figure 5.2 : Daily precipitation amounts in the period 30 May – 2 June (From upper left to lower right). Gridded precipitation maps derived from E-OBS dataset (ASCII) by Global Mapper..... **102**
Figure 5.3 : Time series of 1-, 4- and 10-day accumulated precipitation amounts for the river basins of the Elbe (left) and the Danube west of 20° E (right) (European Reanalyses and Observations for Monitoring – EURO4M, 2013)..... **103**
Figure 5.4 : Observed IGS sites for performing the GNSS Meteorology experiment during severe weather conditions. **104**
Figure 5.5 : The scheme presenting the data processing steps in order to estimate ZWDs. **109**
Figure 5.6 : The estimated ZWDs and RMS values of the solution; The IGS ZPDs used for validation. **110**
Figure 5.7 : ZHD derived from the GPT (red), the UNB (green) and the ECMWF (blue)..... **113**
Figure 5.8 : Scatter plot of the PPP ZWDs (GPT2 and VMF1 grid) data with respect to the IGS ZWD data. **114**
Figure 5.9 : GRAZ station positioning results and convergence periods under different atmosphere models; the coordinate set of CODE's weekly SINEX solutions were used as reference data. **117**
Figure 5.10 : Comparison of ZWD estimates derived from PPP and Network solution for stations: FFMJ, GANP, GOPE, GRAZ, WROC, POTS, WTZR, ZIMM, PTBB, LEIJ. **119**
Figure 5.11 : PPP ZWD solutions for station GANP using IGS Final, Rapid and URP (up) and their solution accuracy (mm) (bottom)..... **123**
Figure 5.12 : ZWD estimates (up) and RMSs of the solutions at the site GRAZ where the PPP was performed with different clocks. **125**
Figure 5.13 : RMS values for the wet delay estimates at different cut-off elevation angles: 3°, 10°, 20°. **127**

Figure 5.14 : The ZWDs estimated with different time resolution; IGS site GANP on June 2, 2013. ..... **127**
Figure 5.15 : RMS values of the ZWD estimates at the IGS site POTS processed by the network solutions with different baseline lengths. **128**
Figure 5.16 : POTS inematic receiver North, East and Up residuals to nominal a priori position (ITRF2008 – epoch: June 2, 2013). **130**
Figure 5.17 : IGS and RS sites used in the PWV monitoring during the 3-week period (20 May – 10 June 2013). **131**
Figure 5.18 : PWV differences between the radiosonde data, the PPP solutions and the relative solutions with respect to different troposphere models at six IGS sites: GANP, GOPE, GRAZ, POTS, WROC and ZIMM. ... **133**
Figure 5.19 : Discrepancies between the PPP PWVs (gpt: red and ecmwf: blue), Network PWVs (gpt: green and ecmwf: brown) and the PWV derived from the IGS USNO AC (solid black line) at the GANP station. **137**
Figure 5.20 : Scatter plot comparison between PWVs derived by PPP and Network sessions with the URP and PWVs generated from IGS Final troposphere products. **138**
Figure 5.21 : PWV comparison between the Radisonde data and the PPP session using the URP products at GANP. **139**
Figure 5.22 : PWV comparison between the Radisonde data and the Network session using the URP products at GANP..... **140**
Figure 6.1 : RTS stations distributed worldwide (green: operational, red: no data received for last 10 days) (Url-11, 14.10.2017)..…… **142**
Figure 6.2 : The flowchart of BNC using the real-time correction streams and broadcast ephemeris to produce precise epehmeris orbits (sp3) and clocks (rinex clock). …… **143**
Figure 6.3 : Diagram of RT PPP solution with fixed ambiguity as developed by CNES PPP-Wizard Project (Laurichesse et al, 2011). …… **148**
Figure 6.4 : Mean differences in radial, along-track and across-track directions between the IGS RTS (CLK91) and CODE Final ephemeris. …… **149**
Figure 6.5 : X,Y and Z residuals of the IGS RTS (CLK91) with respect to the CODE Final ephemeris product. …… **150**
Figure 6.6 : Clock differences between the IGS RTS and CODE Final. …… **151**
Figure 6.7 : Positioning and convergence performance of the real-time integer PPP solution (right) with respect to CODE's Final PPP results (left). …… **153**
Figure 6.8 : ZTD time seriescomparison between an ambiguity fixed RT PPP (CLK91), an ambiguity float RT PPP (IGS03) and ambiguity float PP PPP (CODE) solutions. …… **155**
Figure 6.9 : Convergence performance of the IGS RTS streams (CLK91 vs IGS03) in terms of estimated troposphere path delays. …… **156**
Figure 6.10 : The architecture of the real time PPP session performed within the BERNESE 5.2. ..…… **158**
Figure 6.11 : RT PPP derived PWV and radiosonde time series at the sites GANP, GOPE, GRAZ, POTS, WROC and accumulated daily precipitation recorded at the sites. ……..**159**
Figure 6.12 : The mean and RMS values of the PW differences between the real time and post-process PPP. …… **162**

MONITORING TROPOSPHERIC WATER VAPOR VARIATIONS WITH PPP DURING SEVERE WEATHER

SUMMARY

The Global Navigation Satellite Systems (GNSS) have been used for atmosphere monitoring since the early 1990's owing to its accurate, continuous, and high coverage in all-weather operable data. The approach has been known as "GNSS Meteorology" and it is based on the correlation between a GNSS signal delay in the receiver - satellite signal path and humidity (i.e., water vapor content) in the atmosphere. Atmospheric water vapor is an important greenhouse gas and a significant element for the energy exchange in the atmosphere and thus it must be monitored with a high accuracy. However, its spatiotemporal variability brings some limitations in terms of a correct interpretation of weather events. It has been revealed in many studies that zenith wet delays (ZWDs), estimated from a GNSS processing, are associated with the water vapor content, namely precipitable water vapor (PWV), a crucial parameter that has been extensively used in climate studies.

Until recently, most of the studies that have been performed on the GNSS Meteorology are based on GNSS solutions using network GNSS observations within a dense regional or global Continuously Operating Reference System (CORS) networks. The advantage of a network solution is the mitigation of potential error sources by differencing observations formed between stations tracking same satellites. However, a computational burden due to a high number of observations and the necessity of using a reference site to form a baseline between sites are the weak points of the solution. In contrast, Precise Point Positioning (PPP) stands out as an alternative GNSS measurement technique, which uses undifferenced code and phase observations of a dual frequency single receiver and highly accurate precise orbits and clocks distributed by the International GNSS Service (IGS). In order to achieve a similar accuracy to a network based GNSS solution, all error sources in PPP have to be modeled or eliminated from observations either by applying correct models or by using linear combinations of observations. Therefore, from one point of view, PPP is one of the best quality control tool for assessing the reliability of each parameter defined in observation equations.

Meteorological data are crucial part of the GNSS based atmosphere monitoring. The data may be obtained from in-situ measurements when available or may be derived from external sources such as analytical prediction models and numerical weather models (NWM). Analytical models, such as the Global Pressure and Temperature (GPT and GPT2) and the University of New Brunswick (UNB), are widely used models because of their ability to predict meteorological data at any time and for any site location. However, they are produced based on annual and semiannual data averages and amplitudes of meteorological data that makes these analytical models insufficient for observing sudden air changes. Contrary, NWM like the European Centre for Medium-Range Weather Forecasts (ECMWF) and the Vienna Mapping Function grids (VMFG) that provides the ECMWF data four times within a day, are

based on real weather analyses using frequently updated meteorological data, and represent spatio-temporal atmospheric variations better than the analytical models. But, the VMFG offers the ECMWF data with a latency of several hours that prevents users from performing real-time GNSS analyses. Similarly, several modern mapping functions have been developed as a result of analyzing of several years' meteorological data from different stations and elevation angles. Those functions have increased the performance of GNSS-based atmosphere monitoring by means of being susceptible to low elevation angle observations and by using advanced virtual models, i.e., analytical or numerical, that statistically strong in order to represent the dry and wet part of the troposphere. Global Mapping Function (GMF), Niell Mapping Function (NMF) and Vienna Mapping Function (VMF1) are few examples of these commonly used mapping functions that were all developed to be used collaboratively with the GPT, UNB and VMFG (i.e., ECMWF data), respectively. Using different analytical and NWMs and their associated mapping functions to model the troposphere affects estimates derived from GNSS observations and thus weather predictions utilized based on these estimates vary from each other. Furthermore, the performance of these mentioned models and corresponding mapping function for each one of them have never been tested during extreme weather conditions before.

In this dissertation, modern troposphere modeling approaches derived from both analytical prediction models and NWMs have been evaluated via GNSS PPP sessions during severe weather conditions. The sessions were processed in both post-process (PP) and real-time (RT) mode with dual frequency ionosphere-free observations. ZWDs, which are estimated through the Least Squares Parameter Adjustment (LSA), converted to the PWV estimates at each site in order to observe variations in the water vapor and to monitor the potential precipitation fronts. The Central European Flooding in summer 2013 was one of the extreme periods when some of the European regions experienced a monthly average rainfall within a day. The water vapor variations in May and June of 2013 were exceptionally high and thus this period was selected to reveal the relationship between the GNSS derived troposphere parameters and severe weather events. In order to accomplish the task, eleven IGS sites that are located within the affected regions were selected and daily observations of these sites were processed through static PPP sessions. IGS Final orbits and clocks for satellites were introduced to the analyses to enhance the accuracy of the zenith wet delay estimates and, therefore, weather forecasts. Besides IGS Final ephemerides, other published IGS ephemerides products such as IGS Rapid (IGR) and IGS Ultra-Rapid (URP) products were also processed in the PPP sessions to determine if any significant changes are occurring in the estimates due to employ different IGS product sets varying in accuracy and latency. The ZWD estimates derived from the PPP sessions that only differ in applied troposphere model and mapping function (i.e., GPT / GMF, UNB / Niell and ECMWF / VMF1) were compared to each other and the ZWDs derived from the network GNSS solutions. The results were also validated by the ZWD estimates derived from IGS Final troposphere products (i.e., IGS Zenith Path Delays (ZPD)) and by the radiosonde derived ZWDs that calculated from co-located (or close) sites. The ZWD estimates of each session were derived simultaneously using both LSA and Kalman filter (KF) algorithms and no significant differences arising from using different processing strategy was observed.

Based on the results of the PP data analyses, the PWV parameters, which are calculated from the ZWD estimates via a conversion factor, offer more consistent results with the IGS derived PWVs if an analytical function of the GPT/GMF is employed in the PPP

solution. The analyses result also confirmed that the PPP derived PWV values, which are processed with the ECMWF / VMF1, better agreed with the radiosonde derived PWV values while the biggest discrepancies were observed for the PPP sessions applied the UNB / Niell approach. In overall, the performance of the PPP sessions using the ECMWF and VMF1 exceeds the other solutions in terms of atmosphere monitoring during severe weather events.

In this thesis, the implementation procedure of real-time orbit and clock correction streams, which are disseminated by the IGS Real-Time Service (IGS RTS), has been investigated through real-time (RT) PPP analyses. Long convergence times due to un-calibrated receiver and satellite based phase biases were also assessed in order to accelerate real-time solutions. It was noticed that using real-time derived biases along with real-time orbits and clocks help to reduce long convergence periods to several minutes. In addition, regardless of the applied troposphere model, the accuracy level of PWV estimates derived from the RT PPP sessions, were found to be consistent with the results derived from the PP PPP analyses and the radiosonde readings. The reliability of the RT PPP in atmosphere monitoring was also validated by showing the strong correlation between the PWV variations and the daily accumulated precipitation rates recorded at the observed sites. As observed in the PP analyses, the best agreement with the radiosonde and precipitation data was obtained for the RT sessions using the ECMWF / VMF1.

This study also highlighted the use of the Moderate-Resolution Imaging Spectroradiometer (MODIS) to verify both the RT and the PP PPP PWV estimates. It is observed that the PP PPP estimates showed more consistent results with the MODIS data that the real-time solutions.

The thesis provides a comprehensive guide for GNSS based troposphere monitoring, in particular with PPP solutions and during extreme weather conditions. The impact of using different troposphere models, IGS product sets and processing strategies on the estimates were investigated for both PP and RT GNSS solutions.

TROPOSFERİK SU BUHARI DEĞİŞİMLERİNİN PPP İLE KÖTÜ HAVA KOŞULLARINDA İZLENMESİ

ÖZET

Küresel Konum Belirleme Sistemleri (GNSS – Global Navigation Satellite System) sinyali uydu anteni ve yeryüzündeki alıcı arasındaki mesafeyi yol alırken atmosferde iyonosfer ve troposfer tabakalarından geçmekte ve sinyal yolu boyunca gecikmelere uğramaktadır. Frekans bağımlı iyonosfer tabakasından kaynaklanan gecikmeler, GNSS kod ve taşıyıcı faz gözlemlerinin çift frekanslı iyonosfer bağımsız lineer kombinasyonları ile büyük oranda giderilebilmektedir. Frekans bağımsız troposfer tabakası nedeniyle oluşan gecikmeler ise gözlem denklemlerinin lineer kombinasyonları ile giderilemez ve bu gecikmelerin uygun modeller ile modellenmesi ve etkilerinin gözlem denklemlerinden giderilmesi gerekmektedir. Troposfer kaynaklı gecikmeyi oluşturan iki bileşenden biri olan zenit hidrostatik gecikme (ZHD – Zenith Hydrostatic Delay), atmosferdeki kuru gazların etkilerini içermekte olup bölgede gerçekleştirilmiş hassas basınç ölçmeleri yardımıyla ve Saastamoinen troposfer modelini kullanarak yüksek bir doğruluk ile hesaplanabilmektedir. İkinci bileşen olan zenit ıslak troposfer gecikmesi (ZWD – Zenith Wet Delay) ise atmosferdeki nem oranı ile olan yüksek korelasyonundan dolayı zamansal ve mekânsal değişim gösteren, modellenmesi zor ve atmosferik olayların oluşum ve gelişim süreçlerinin yorumlanması için çok önemli bir parametredir. Bu parametreyi doğrudan ölçebilen teknolojiler (radyosonda, su buharı radyometresi, uzaktan algılama uyduları) mevcut olduğu gibi deneysel (analitik) modeller kullanılarak da yaklaşık tahmin değerleri elde edilebilmektedir. GNSS oturumlarında, ZWD etkisi; gözlem denklemlerinde bir bilinmeyen olarak tanımlanmakta ve parametre kestirimi sonucunda değeri stokastik süreçler ile bulunmaktadır.

GNSS, sahip olduğu yüksek doğruluk, süreklilik, geniş kapsama alanı ve tüm hava koşullarında çalışabilme özelliğinden dolayı atmosfer hareketlerini izlemek için 1990'lı yılların başından beri kullanılmaktadır. Bu gözlemler "GNSS Meteorolojisi" olarak adlandırılmakta ve temeli; troposferdeki alıcı – uydu sinyal yolu gecikmesi ile atmosferdeki nem (su buharı) arasındaki ilişkiye dayanmaktadır. Bir sera gazı olan atmosferik su buharı atmosferdeki enerji değişim süreçlerinde etkili, lokal ve küresel hava olaylarının oluşumunda önemli bir parametredir fakat sahip olduğu hızlı mekânsal ve zamansal değişkenlik bu parametrenin doğrudan radyosonda ve su buharı radyometresi gibi geleneksel yöntemleri ile belirlenmesine ve dolayısıyla hava koşullarının istenilen doğrulukta tahmin edilebilmesine engel oluşturmaktadır. Geleneksel yöntemler ile veri üretilirken yaşanan zamansal gecikmeler, örnekleme gerçekleştirilen istasyonların konumsal dağılımının yetersizliği ve ekonomik etkenler bu yöntemlere alternatif yeni yaklaşımların ortaya çıkmasına neden olmuştur. GNSS gözlemleri ile kestirilen ZWD ve yağmur oluşum sürecindeki temel değişken olan yoğuşabilir su buharı (PWV – Precipitable Water Vapor) arasındaki yüksek korelasyon kullanılarak gerçek zamanlı (RT – real time) ve art-işlem (PP – post process) hava tahmin ve iklim çalışmaları yürütülebilmektedir. GNSS gözlemleri sonucunda kestirilmiş su buharı değerlerinin klasik yöntemler ile elde edilmiş

değerlere yakın sonuçlar vermesi; GNSS gözlemlerinden türetilen verilerin, sayısal hava modelleri tarafından etkin bir şekilde kullanılmasının önünü açmıştır.

Günümüze kadar yürütülen GNSS Meteorolojisi çalışmalarının büyük bir çoğunluğu, GNSS ağ çözümü yaklaşımlarını temel alan, Sürekli Çalışan Referans Sistemi (CORS – Continuosly Operating Reference System) uygulamalarıdır. GNSS gözlemlerinde karşılaştığımız uydu yörünge, uydu ve alıcı saat hataları, uydu ve alıcıda donanım kaynaklı sapmalar ve tamsayı faz belirsizliği gibi kestirim hassasiyetini bozan hata kaynaklarının, aynı uydulara gözlem yapan istasyonların gözlem farklarından kısa süreler içinde giderilebilmesi, konum doğruluğunu santimetre mertebelerine düşürürken kestirilen troposfer parametrelerinin de hassasiyetini arttırmaktadır. Fakat, çözümlerde kullanılan istasyon sayısı arttıkça, gözlemlerin sayısı, hesap yükü ve istasyonlar arasındaki korelasyon da artmaktadır. Bu sebeple, ağ çözümüne alternatif, ekonomik, hesap yükü daha az olan ve kestirim doğruluğu ağ çözümüne yakın yeni yöntemler üzerinde durulmaktadır. Hassas Konum Belirleme (PPP – Precise Point Positioning) bu ihtiyaca cevap vermek için geliştirilmiş, tek bir alıcıdan ve fark alma teknikleri kullanılmaksızın okunan faz ve kod gözlemlerini işleyen bir GNSS ölçme tekniğidir. PPP, Uluslararası GNSS Servisi (IGS – International GNSS Service) tarafından sağlanan hassas uydu yörünge ve saat efemeris bilgisi ürünlerini işleyerek yüksek doğrulukta parametre kestirimi yapabilmektedir. Ağ GNSS çözümleri ile etkisi giderilen her bir hata kaynağı, PPP'de dikkatle ele alınmalı, doğru model yaklaşımları ve gözlemlerin lineer kombinasyonları kullanılarak etkileri modellenmeli ve giderilmelidir. Bu özelliğinden dolayı PPP, GNSS gözlemlerindeki her bir parametre için kalite kontrol aracı olarak da kullanılmaktadır.

GNSS gözlemleri kullanılarak troposfer hareketleri modellenirken gerekli olan anlık meteorolojik veriler; geleneksel yöntemlerin yanı sıra, istasyon bölgesinde yapılan yersel ölçmeler, yeryüzü ölçmelerinin bulunmadığı durumlarda ise analitik tahmin fonksiyonları ve gerçek verilere dayanan sayısal hava modelleri (NWM – Numerical Weather Model) kullanılarak ilgili konum ve zaman dilimi için türetilebilmektedir. Benzer şekilde, uzun yıllara ait meteorolojik verilerin analizlerine dayalı olarak ve farklı uydu eğim açılarına göre geliştirilmiş izdüşüm fonksiyonları da GNSS gözlemlerinin atmosferi daha gerçekçi yansıtmasının ve kullanıcıların daha gerçekçi hava tahmin çalışmaları yürütmesinin önünü açmıştır. Günümüzde, hem ZHD hem de ZWD hesabında kullanılmak üzere sayısal hava modelleri verilerine dayanan birçok analitik atmosfer modeli geliştirilmiştir. Avrupa Orta Menzilli Hava Tahminleri Merkezi'nin (ECMWF - European Centre for MediumRange Weather Forecasts) uzun yıllara dayanan Re-Analysis (ERA-40, 1999 – 2002), ve ERA-Interim (2001-2011) analizleri kapsamında, ihtiyaç duyulan meteorolojik parametrelerin yıllık ortalama değerleri ve yıllık değişim oranları (genlik katsayıları) hesaplanmıştır. Grid formatında saklanan bu değerler küresel harmoniklere açılarak herhangi bir konum ve zaman dilimi için sürekli veri sağlayabilmekte, gerçek zamanlı çözümleri desteklemektedir. Küresel Basınç ve Sıcaklık (GPT - Global Pressure and Temperature), 9. derece ve 9. mertebeden deniz seviyesinde küresel harmonik bir fonksiyondur ve ölçme yapılan bölgede meteorolojik veriye ulaşma imkânı bulunmayan durumlarda sıklıkla tercih edilmektedir. GPT, konumu ve gözlem tarihi bilinen bir istasyon için ihtiyaç duyulan sıcaklık, basınç, nem, su buharı basıncı ve izdüşüm fonksiyonu katsayılarını kullanıcılara sağlamaktadır. GPT2, GPT'nin kaba olan yatay grid çözünürlüğünü arttırmış (GPT:15°; GPT2: 5°), çok yağışlı dönemler ile çok kuru dönemlerin hakim olduğu bölgelerin daha iyi yansıtılması için meteorolojik verilerin yarıyıllık ortalama değerlerini ve genliklerini hesaplamıştır. Küresel İzdüşüm Fonksiyonu (GMF – Global

Mapping Function), GPT (~GPT2) ile birlikte çalışmak için geliştirilmiş bir izdüşüm fonksiyonu olup ECMWF analiz verilerinin küresel harmoniklere açılması ile ilgili konum ve gün için kuru ve ıslak izdüşüm fonksiyon katsayılarını hesaplamaktadır. Diğer bir analitik fonksiyon olan New Brunswick Üniversitesi (UNB – University of New Brunswick) 5°'lik enlem bant aralıklarında tanımlanmış ve meteorolojik parametrelerin yıllık ortalama ve genliklerini içeren tablo değerlerinin küresel harmoniklere açılması sonucu istenilen konum ve gün için tahmini değerler üretmektedir. Bu değerler daha sonra Saastamoinen troposfer modelinde kullanılmakta ve Niell izdüşüm fonksiyonu (NMF – Niell Mapping Function) ile gecikme hesaplanmaktadır. Ani hava değişimlerine duyarlı olmayan bu analitik modeller; istenilen konum ve zaman için anlık veri sağlamakta, GNSS gözlem denklemlerine kolayca entegre edilebilmektedir. ECMWF analizleri sonucunda hesaplanan ve 2.5° (boylam) x 2.0° (enlem) grid formatında günde 4 kez yayınlanan (00:00, 06:00, 12:00, 18:00 UTC) VMF1; içeriğinde kuru ve ıslak izdüşüm fonksiyonlarının parametreleri ile verilen grid noktaları için hesaplanmış ZHD ve ZWD değerlerini bulundurmaktadır. VMF1, ilgili konum ve yükseklik için ara değer hesabıyla gerçeğe en yakın troposfer tahminlerini sağlayan yaklaşımdır. 6 saatlik ECMWF verilerini girdi olarak kullanmasından dolayı ani hava değişimlerine duyarlı ve aynı sebepten dolayı GNSS yazılımlarına uygulanması zordur. Belli bir gecikme ile PPP çözümünde kullanabilen VMF1, daha çok yakın gerçek zaman uygulamalarına katkı vermektedir. PPP çözümlerinde, denklemlerde tercih edilen hava tahmin modeli ve izdüşüm fonksiyonuna bağlı olarak kestirilen ZWD ve bu kestirimlerden türetilen PWV parametreleri farklılık göstermekte, art işlem, yakın gerçek ve gerçek zamanlı hava tahmin sonuçları da bu farklılıklardan etkilenmektedir. Bahsi geçen analitik modelleri, NWM ve bunlarla birlikte çalışabilen izdüşüm fonksiyonlarını çözümlerinde kullanan PPP oturumlarının performansı daha önce olağan dışı hava koşulları altında test edilmemiş, PPP ile atmosfer hareketlerini izlemede, hangi model yaklaşımının diğerine göre nerede üstünlük kurduğu karşılaştırmalı olarak bir çalışma altında sunulmamıştır.

Bu tez çalışmasında, güncel hava tahmin ve sayısal hava modellerine dayanarak üretilmiş öncül troposfer modellerini çözümlerinde kullanan PP ve RT PPP oturumları olağandışı hava koşulları altında test edilmiştir. Çözümler hem PP hem de RT uygulamalar için çift frekanslı iyonosfer bağımsız gözlemlerin işlenmesiyle gerçekleştirilmiştir. En küçük kareler (EKK) yöntemine göre kestirilen ZWD değerleri, zenit doğrultusunda her istasyon için ortalama su buharı sıcaklığı ve ilgili istasyon konumunun bir fonksiyonu olarak hesaplanan dönüşüm faktörünü kullanarak PWV'ye dönüştürülmüştür. Böylece atmosfer hareketleri ve gözlemlenen yağış olayları ile kestirilen atmosferik su buharı değerleri arasındaki ilişkinin ortaya konması hedeflenmiştir. Bu amaçla, 2013 yazında Avrupa'da son yüzyılın en büyük sel felaketine neden olan yağmur geçişleri ele alınmıştır. 20 Mayıs – 10 Haziran tarihleri arasında 3 haftalık süre için 11 IGS istasyonuna ait günlük GNSS gözlemleri işlenerek bölgedeki su buharı değişimleri kestirilmiş ve sonuçların birden çok yöntemle geçerliliği kıyaslamalı olarak test edilmiştir. PP oturumlarda kestirim doğruluğunu arttırmak için gözlem anından yaklaşık 13 gün sonra yayınlanan IGS Final yörünge ve saat verileri kullanılmıştır. IGS tarafından yayınlanan ve farklı gecikme ve doğruluk değerlerine sahip Rapid (IGR) ve Ultra-rapid (URP) ürünleri de aynı PPP oturumlarında kullanılmış, böylece PPP kestirimlerinde farklı efemeris ürün setlerini kullanmaktan kaynaklanan değişimler incelenmiştir. Gözlemlerinde farklı atmosfer model yaklaşımlarını (GPT, UNB, ECMWF – VMF1 grid) ve bu modeller ile birlikte çalışabilen izdüşüm fonksiyonlarını (GMF, Niell ve VMF1) kullanan PP PPP

oturumları sonucunda kestirilen ZWD değerleri incelenmiştir. Bu kestirimler, sırasıyla, aynı istasyonlarda gerçekleştirilen ağ GNSS çözümü sonucunda kestirilen ZWD değerleriyle, IGS tarafından her istasyon için ve günlük olarak yayınlanan toplam zenit troposfer gecikme (ZPD – Zenith Path Delay) değerlerinden türetilmiş değerler ile ve GNSS istasyonu ile aynı ya da yakın konumlu radyosonda okumalarından türetilen değerler ile kıyaslanmıştır. Aynı PPP çözümleri, hem en EKK hem de Kalman Filtresi (KF) için ayrı ayrı gerçekleştirilmiş, çözüm yönteminin farklılığından kaynaklanan ve troposfer kestirimlerinde kendini gösteren önemli bir sapma gözlemlenmemiştir.

PP PPP analizlerinin sonuçları incelendiğinde: IGS referans verisine en yakın sonuçların, çözümlerinde GPT / GMF troposfer modelini kullanan PPP çözümlerince sağlandığı, analitik fonksiyonların kullanıldığı çözümlerin genel olarak IGS referans verisi ile daha uyumlu olduğu gözlemlenmiştir. Referans verisi olarak radyosonda gözlemlerinin kullanıldığı durumlarda ise en tutarlı sonuçların ECMWF / VMF1 troposfer modelini kullanan PPP çözümleri ile sağlandığı; en büyük sapmaların UNB / Niell çiftini kullanan PPP oturumları için oluştuğu tespit edilmiştir. Genel olarak, troposferi modellemek için ECMWF verilerini ve VMF1 izdüşüm fonksiyonlarını kullanan PPP oturumlarının, diğer analitik modelleri kullanan PPP çözümlerine göre, ani hava değişimlerini daha iyi yansıttığı ve geleneksel yöntemler ile elde edilen su buharı değerleriyle daha uyumlu kestirimler sağladığı sonucuna varılmıştır.

Aynı istasyonlarda PPP ve ağ çözümleri arasındaki kestirim farkları incelendiğinde; PPP çözümlerinin ağ çözümlerine göre ortalama 20 dakika ile 30 dakika arasında daha geç yakınsadığı, yakınsadıktan sonra iki çözümün de benzer karakteristik gösterdiği gözlemlenmiştir. 11 istasyonda yapılan gözlemler sonucu: ECMWF / VMF1 troposfer modelini kullanan PPP ve ağ oturumlarının birbirine daha yakın troposfer kestirim değerleri verdiği, PPP ve ağ çözümleri arasındaki sapmaların UNB/ Niell kullanıldığında arttığı tespit edilmiştir.

RT PPP uygulamaları, IGS'nin yayın efemerisine düzeltme yayınlamaya başladığı Nisan 2013'den sonra hız kazanmıştır. IGS Gerçek Zaman Servisi (RTS) bünyesindeki analiz merkezleri, gerçek zamanlı çözümler için oluşturulmuş küresel istasyon ağlarını kullanarak, yayın efemerisine (broadcast) getirilecek uydu yörünge ve saat düzeltmelerini gerçek zamanlı hesaplayabilmektedir. Bu düzeltmeler, Radio Technical Commission for Maritime Services / State Space Representation (RTCM / SSR) formatında ve Networked Transport of RTCM via Internet Protocol (NTRIP) protokollerine uygun olarak kullanıcılara yayınlanmaktadır. Bu çalışmada, birden çok IGS analiz merkezi tarafından üretilen gerçek zamanlı düzeltmelerin ağırlıklı ortalaması alınarak PPP çözümlerinde kullanılabilecek hassas yörünge ve saat ürünleri oluşturulmuştur. Bu ürünler, daha sonra IGS Final yörünge ve saat ürünleri ile karşılaştırılmış ve gerçek zamanlı diğer bir ürün seti olan URP'ye göre daha hassas sonuçlar verdiği ortaya konmuştur. Bu uydu yörünge ve saatlerinin işlendiği RT PPP oturumları ile atmosferdeki su buharı hareketleri kestirilmiş, kullanılan troposfer model yaklaşımından bağımsız olarak tüm RT PPP oturumları sonucunda elde edilen su buharı değerleri, aynı istasyonlarda gerçekleştirilmiş PP PPP kestirimleri ve radyosonda okumaları ile iyi uyum göstermiştir. Gerçek zamanlı uydu yörünge ve saatlerinin kullanıldığı ağ çözümleri, beklendiği üzere, PPP çözümlerinden daha çabuk yakınsayarak daha hassas sonuçlar vermiştir.

Bu çalışma kapsamında ayrıca, faz belirsizliğinin tamsayı karakterini bozduğu kabul edilen, uydu ve alıcı kaynaklı donanımsal sapmaların, CORS ve benzeri ağ çözümleri

yardımıyla gerçek zamanlı modellenmesi, kestirilen düzeltmelerin RT PPP çözümlerinde kullanılması ve böylece yakınsama sürelerinin kısaltılması üzerine uygulamalar gerçekleştirilmiştir. Analiz sonuçlarına göre; RT PPP çözümleri eğer tamsayı belirsizliği çözümü uygulanmışsa 5 - 15 dakika aralığında istenilen hassasiyete ulaşmakta, belirsizlik çözümü uygulanmadıysa istenilen hassasiyete ulaşmak için 30 dakika ve üzerinde sürelere ihtiyaç duyulmaktadır.

Amerika Birleşik Devletleri merkezli federal bir kuruluş olan Ulusal Atmosferik Araştırmalar Merkezi (National Center Atmospheric Research - NCAR), Küresel Yağış İzleme ve Klimatoloji Projesi (GPCP - Global Precipitation Climatology Project) analizleri kapsamında, küresel ölçekte ve 1° x 1° mekânsal çözünürlükte günlük yağış birikimi değerlerini 1996 - 2015 yılları arasında hesaplamıştır. Proje kapsamında, uzaktan algılama uydularından ve yersel yağmur ölçüm aygıtlarından gelen verileri temel alarak hesaplanan grid değerlerinden ara-değer hesabı ile ilgili GNSS istasyonlarının bulunduğu bölgeye düşen yağış miktarı belirlenmiştir. 5 IGS istasyonunda yapılan RT PPP analizleri ile kestirilen atmosferik su buharı ile GCPC kapsamında aynı istasyonlar için hesaplanan yağmur geçişleri arasında büyük oranda bir korelasyon olduğu, fakat su buharı kestirimlerindeki her ani değişimin yağmur olayı ile sonuçlanmadığı tespit edilmiştir.

Amerikan Ulusal Uzay ve Havacılık Dairesi (NASA) uyduları olan Terra ve Aqua üzerinde bulunan Moderate-Resolution Imaging Spectroradiometer (MODIS) platformu aracılığıyla atmosferik su buharı değerleri elde edilebilmektedir. 1 kilometre mekânsal çözünürlüklü MODIS 2. seviye ürünlerinden (MOD5_L2) türetilen yoğuşabilir su buharı değerleri, gerçek zamanlı ve art-işlem PPP kestirim sonuçları ile kıyaslanmıştır. MODIS görüntülerinden türetilen su buharı hareketleri ile PPP çözümleri arasındaki ortalama farkların santimetre altında kaldığı, farkların ortalama hatalarının da 5 milimetrenin altında olduğu gözlemlenmiştir.

Bu tez çalışması, GNSS PPP ile atmosferin izlenmesine yönelik çalışmalar için kapsamlı bir kılavuz görevi görmektedir. Farklı troposfer model yaklaşımlarının, GNSS veri işleme tekniklerinin ve farklı IGS ürün setlerinin PP ve RT GNSS Meteorolojisi çalışmalarına olan etkileri karşılaştırmalı olarak değerlendirilmiş, PPP çözümlerinin diğer çözümlere göre üstün ve zayıf yönleri ortaya konulmuştur.

1. INTRODUCTION

1.1 Background

Electromagnetic signals of Global Navigation Satellite System (GNSS) are time delayed when passing through the atmosphere due to temporally and spatially non-uniform and unpredictable atmospheric properties. Frequency-dependent part of the atmosphere, namely the ionosphere is an error source in the GNSS and its effect can be fully (i.e., 99 %) eliminated by the use of linear combinations of two or more frequencies. The frequency independent part, called the neutral atmosphere, however, is a non-dispersive part and need to be corrected for by other techniques. The tropospheric delay is a consequence of temporally and spatially highly variable and difficult to predict atmospheric properties. It is a signal delay between a ground station and a signal transmitting satellite caused by the neutral atmosphere and integrated over the whole ray path. This delay consists of a dry component called the zenith hydrostatic delay (ZHD), which can be modeled with a high accuracy using in-situ surface pressure measurements or data derived from Numerical Weather Prediction (NWP) models. On the contrary, a non-hydrostatic part of the delay, i.e. the zenith wet delay (ZWD), which is mostly due to highly variable atmospheric humidity content with space and time, is difficult to model and thus it is estimated as a difference between the observed zenith total delay (ZTD) and the calculated ZHD. It is even more problematic if GNSS signals are received from different signal paths with different azimuth and elevation angles. Then, mapping functions (MFs) are usually applied to map neutral atmospheric delays from different directions to the zenith. Assuming azimuthal symmetric troposphere is a big fundamental error since the thickness of the atmosphere varies due to the passages of weather fronts. Although ZHDs and ZWDs are nuisance parameters for positioning, they are significant for atmosphere monitoring.

Water vapor is a dominant greenhouse gas in the atmosphere and plays a fundamental role in the hydrological cycle causing many global and regional meteorological

phenomena such as water transport, clouds, precipitation tropical storms, and floods. Currently, the water vapor is very poorly measured in real-time using conventional instruments and techniques. Radiosondes and Water Vapor Radiometers (WVR) are used to measure water vapor in the atmosphere directly, but they have severe limitations such as high cost, time delay, and poor spatial coverage. The radiosonde is still an important data provider as it reads meteorological parameters directly via its sensors on-board and calculates the water vapor amount in the atmospheric column above the site. Better weather predictions are accessible by measuring water vapor accurately both in time and space via GNSS observations. The use of GNSS for a weather forecasting and climate studies by measuring the atmospheric water vapor is currently referred to as "GNSS Meteorology". The relation found by Bevis et al. (1992) can express the strong correlation between GNSS ZWD estimates and water vapor content. Based on this relation the water vapor derived from the GNSS measurements are usually expressed as precipitable water vapor (PWV). It has already been shown that the GNSS solutions with hourly or higher resolution provide PWV estimates with 1 - 3 mm root mean square (RMS) accuracy with respect to traditional atmosphere measurements and sensing techniques (Bevis et al, 1992; Tregoning et al, 1998). Recently, several NWMs have been employed in the GNSS solutions that help users identifying characteristics of the lower neutral atmosphere. These models can be either regional or global, developed by weather services to produce outputs of temperature, pressure and humidity data along with calculated ZHD and ZWD values for a location of interest. These models are generally used to derive a priori ZHD values and mapping functions coefficients for a given location. Since almost all prediction models depend on non-linear partial differential equations, they can provide approximate values, but not exact ones. The European Centre for Medium-Range Weather Forecasts (ECMWF) and the National Centers for Environmental Prediction (NCEP) are two important models whose data are generally employed within GNSS Meteorology applications, particularly when in-situ measurements are unavailable.

GNSS derived ZWD estimates from network GNSS solutions are vital inputs for NWMs and weather forecasting operations. Regarding the ability to mitigate main error sources such as orbits, clocks, hardware delays, and biases within a network by differencing observations, network solutions can provide millimeter to centimeter-level positioning accuracy. However, the spatial correlation between stations due to

short baseline lengths, a computational burden that show up with an increased number of observations, and the hardware cost of using at least two receivers in the field become a major concern for users.

Precise Point Positioning (PPP) was proposed by Zumberge et al. (1997) as a positioning technique using only a dual frequency single receiver without any reference station and any correlation among stations. An accuracy of at least decimeter level can be achieved with PPP by employing IGS precise orbits and clocks. Contrary to network GNSS solutions, receiver and satellite-based biases, phase ambiguities and other error sources, which decrease the accuracy of the estimates and increase the convergence time of the solutions, remain in PPP observations. The traditional PPP model uses ionosphere-free code and phase observations, IGS products and geophysical models recommended by the International Earth Rotation and Reference Systems Service (IERS) (Petit and Luzum, 2010) to reach a high positioning accuracy. Monitoring ability of weather events and water vapor variations continuously with a single GNSS receiver, at a large number of stations, makes the PPP as one of the economic and the appropriate way to catch the real state of the atmosphere. The moisture content of the atmosphere and potential precipitation events can be monitored by observing PPP derived ZWD estimates that associated with the amount of integrated water vapor in the zenith direction. An integrated water vapor can also be expressed as precipitable water vapor (PWV) that is equivalent to the height of the signal path above the observed site. Thus, PPP derived ZWDs are among the potential source that can be assimilated by NWMs to operate global and regional studies.

Over the last three decades, several atmosphere models have been introduced to model a neutral atmosphere, hydrostatic and non-hydrostatic parts and to provide mapping functions coefficients. However, most of these models, particularly the older ones, use empirical standard atmosphere values instead of a real meteorological data, hence, troposphere analyses using these models may offer dissimilar results with respect to real atmospheric conditions, particularly during severe weathers. Similarly, the PPP sessions using these old models provide less accurate tropospheric estimates in comparison to in-situ measurements and to the PPP sessions using more modern models.

ZHD can be calculated through Saastamoinen (1972) formula with a high accuracy if surface pressure measurements are available. The agreement between the

Saastamoinen derived ZHDs and the ZHDs derived from ray tracing analyses of NWM, are in the range of sub-millimeters, whereas this agreement is at the millimeter level for other models such as Hopfield (1969), Baby et al. (1988) and Davis et al. (1985). However, neither surface meteorological parameters nor NWMs are sufficient to reflect the real characteristics of the wet part of the atmosphere due to highly variable water vapor density with an altitude and latitude. Thus, in practice, the ZHD parameters, calculated via Saastamoinen and in-situ pressure, are implemented to the GNSS observations as the a priori troposphere delays while the ZWD parameters are defined as unknowns (i.e., corrections) and estimated by an adjustment of GNSS observation equations. When a surface meteorological data and NWM derived data are not nearby, analytical models are generally employed as a source to derive a priori meteorological data. In addition to the Berg's (1948) height dependent and old empirical model that only uses standard atmospheric values to derive a meteorological data, there are more sophisticated models such as the University of New Brunswick (UNB) (Leandro et al, 2006), the Global Pressure and Temperature model (GPT - Boehm et al, 2007; GPT2 – Böhm et al, 2015). UNB3m is a look-up table based model with a standard atmosphere data at five latitude bands symmetric with respect to the equator. A priori meteorological data is interpolated by using the look-up table for a specific latitude, height and day of year (DoY). The GPT is based on spherical harmonic up to degree and order nine and developed from the analyses consist of 3 years of 15°×15° global grids including monthly means and amplitudes for temperature, pressure and humidity data that derived from the 40 years re-analyses data of the ECMWF. The GPT2 was developed in order to enhance some weakness of the GPT, in particular the spatial resolution and ability to represent sub-annual variations for extremely wet and dry areas. The GPT (≈ GPT2) uses latitude, longitude, height and day of year to produce a priori meteorological parameters and mapping function coefficients. Although the GPT (≈ GPT2) and UNB3m are available at any time and any location, they are empirical models with annual averages and coarse spatial resolution that insufficient in terms of catching short-period weather variations. Contrary, these variations can be reflected by processing NWM (i.e., ECMWF) derived functions such as the VMF1 global grids (ECMWF grids - VMFG) (Boehm et al. 2009). The Department of Geodesy and Geoinformation (GEO) at the Vienna University of Technology uses a daily ECMWF data to derive a priori ZHDs, ZWDs, and mapping function coefficients and meteorological data that all are published four

times a day on global grids (2.5° x 2.0°). Instead of standard atmosphere values, using the analysis results from NWM leads the VMF1 grids to reflect the real atmospheric conditions better than analytical models.

Present day mapping functions use a truncated form of a continued fraction as expressed by Marini (1972) and most of them are formed either based on analyses of ray tracing measurements or from analytical weather models. Vienna Mapping Function (VMF1 - Boehm et al. 2006a) and Isobaric Mapping Function (IMF – Niell (2000)) are mapping functions whose coefficients are in the continued fraction and derived from ray-tracing methods through the real-time meteorological data of the ECMWF. Unlike the VMF1 and the IMF, the Global Mapping Function (GMF) (Boehm et al. 2006b) and the Niell Mapping Function (NMF) (Niell, 1996) are analytical functions that do not need any external input as they use spherical harmonic expansion of yearly averages and amplitudes to derive required coefficients. Thus, the GNSS solutions using these empirical functions could only represent seasonal averages and thus it must be considered that using different mapping functions derived from different source could change the performance of the GNSS monitoring.

A large part of the GNSS Meteorology studies that has been carried out until recently, are post-process (PP) GNSS network applications. However, with the advent of the IGS Real-Time Service (RTS) and due to high demands coming from the weather forecasting (and now-casting) community, a number of the real-time (RT) GNSS applications have remarkably increased over the past three years. The IGS RTS generates orbit and clock corrections globally to be applied to the broadcast ephemeris products in real time. The corrections are distributed via subscription and over streams of Networked Transport of RTCM via Internet protocol - State Space Representation (NTRIP - SSR) format. The users, who receive the RTCM – SSR correction streams, are able to form precise orbits and clocks to carry out RT PPP applications. However, the major weakness of the conventional PPP: an estimation of unknowns with a float solution, which often takes at least 30 minutes to reach to a centimeter-level positioning accuracy, still restrict users to perform real-time analyses with PPP. Hardware based biases of receiver and satellites destroy the integer nature of unambiguous phase and increase time that required for reaching consistent results. Some IGS Analysis Centers (ACs) model these biases in real-time and distribute them via NTRIP casters to allow GNSS users reducing long convergence times in PPP

sessions and monitoring neutral atmosphere variations in real-time. Based on these latest developments, it is not hard to say that the PPP technique will be used as an alternative to the network GNSS in the near future.

1.2 Research Objectives

One of the objectives of this thesis is studying the benefits of GNSS PPP technique in neutral atmosphere monitoring, in particular, during extreme weather conditions. Besides, the GNSS processing results need to be quantified to reveal the effect of processing different atmosphere models and mapping functions in the analyses. Furthermore, it is intended to prove that PPP can offer comparable water vapor estimates to network GNSS solutions for both PP and RT processing modes. Each individual PPP campaign, which only differs in processed IGS orbits and clocks of different accuracy and latency, was also evaluated with this study in order to show their influence on the derived parameters.

The success of RT PPP sessions in atmosphere monitoring has been tested by processing real-time correction streams. It is another goal of the study to prove that the PPP solutions using real-time orbits and clocks derived from these corrections offer more accurate troposphere estimates than the PPP solutions using the IGS's real-time precise ephemeris; i.e. Ultra-rapid (URP) products.

Furthermore, an impact of the resolving phase ambiguity by correcting hardware origin biases of satellites and receivers were investigated regarding the performance of real-time PPP and reducing the convergence time.

To achieve these objectives, the following tasks are accomplished:

- Review and discussion of a GNSS PPP and its comparison with a network GNSS.
- Investigation of recent atmosphere models and mapping functions used in the Geodesy.
- Evaluation of the relationship between troposphere path delays and water vapor variations and precipitation regime during severe weathers.
- Comparison of the LSA and the KF processing strategies in terms of derived ZWDs and PWVs accuracy.

- Assessment of analytical atmosphere models and NWMs by evaluating their performance during humid periods.
- Validation of the PPP results with the IGS derived Final tropospheric products (i.e., Zenith Path Delays - ZPD) and co-located radiosonde readings.
- Building up an automatic approach for applying the IGS real-time correction streams into the PPP sessions in order to increase the consistency of RT GNSS in atmosphere monitoring.
- Assessment of the performance of the ambiguity fixed RT PPP solutions using real-time correction streams of hardware biases against to the ambiguity float and post-process PPP solutions regarding convergence periods and water vapor monitoring.
- Measure the correlation between the PPP derived atmosphere and recorded precipitation events at the same sites during a severe weather.
- Validation of the PPP analyses results with the water vapor data derived from Moderate Resolution Imaging Spectroradiometer (MODIS).

1.3 Thesis Outline

This thesis is organized as follows:

Chapter 2 introduces the fundamentals of GNSS with a detailed description of the PPP and associated mathematical and stochastic model are discussed in this chapter. The LSA and the KF procedures followed in the thesis are briefly reviewed. In addition, PPP services and a number of PPP software used by the GNSS community are also discussed here.

Chapter 3 introduces the PPP error sources and their mitigation methods. The effects of error sources on the unknown parameters are illustrated in this chapter. In addition, the ionosphere effects on GNSS signals are also reviewed.

Chapter 4 evaluates the theoretical aspects of the troposphere in detail and the techniques to account its effect on GNSS signals. Modern atmosphere delay models and mapping functions are defined with their mathematical background. A priori troposphere models derived from analytical models and numerical weather models are

described here. The importance of the water vapor in Meteorology and Geodetic applications are addressed along with the water vapor extraction methods.

Chapter 5 evaluates the troposphere monitoring performance of the PP PPP. The impacts of using different analytical models, NWMs, and mapping functions to model the troposphere are examined. In addition, IGS orbits and clocks with a dissimilar accuracy and latency and different configuration settings are investigated regarding their influence on the troposphere estimates.

Chapter 6 is dedicated to understand the skills of the RT PPP solution in regards of using real-time correction streams for troposphere modeling. The accuracies of real-time correction streams are tested within the PPP solutions and advantages of reducing hardware origin biases are examined by assessing the convergence behavior and the accuracy of the estimates. This chapter also reviews the relationship between the estimates and the recorded precipitation events. In addition, basics of water vapor extraction with the MODIS using infrared and near-infrared, including the comparison with the PPP results, are evaluated in this chapter.

2. GNSS AND PPP

GNSS is a worldwide satellite-based system designed to make sure that a user at any point on earth obtains an accurate position. Satellite-based navigation techniques started in the beginning of 1970's. The US Department of Defense (DoD) decided to build, improve and test a space-borne system called NAVigation Satellite Timing and Ranging Global Positioning System (NAVSTAR GPS). A detailed definition of GPS is given as below:

> The NAVSTAR Global Positioning System (GPS) is an all-weather, space-based navigation system under development by the U.S. Department of Defense to satisfy the requirements for the military forces to accurately determine their position, velocity, and time in a common reference system, anywhere on or near the earth on a continuous basis (Wooden, 1985, p.404).

The GPS was originally designed for military purposes and clock degrading signal effect, Selective Availability (S.A.) made the system unreliable for civilians when the high accuracy demanded. On May 2, 2000, U.S. Congress made a decision to eliminate the S.A. effect from the broadcasting signal and the high accuracy civilian applications have been developed enormously since then. The positioning improvement after removing SA is illustrated in Figure 2.1.

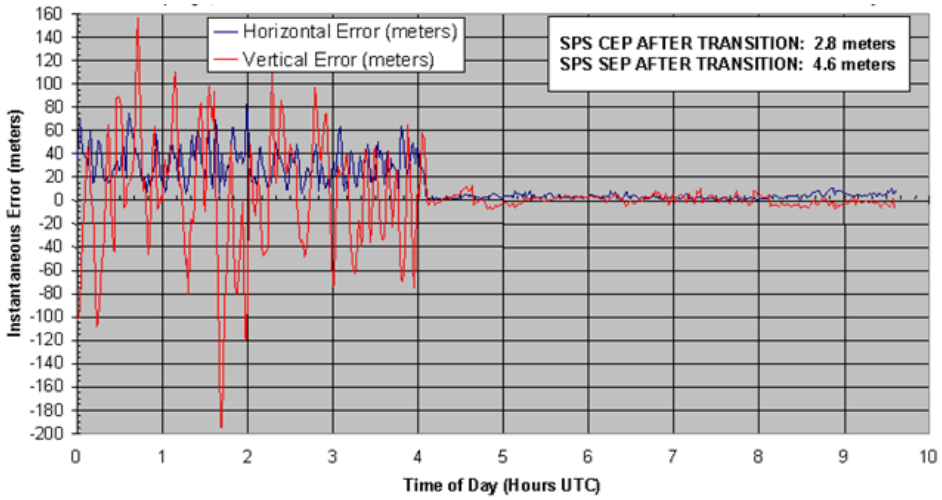

Figure 2.1 : Horizontal and Vertical Errors before and after S.A. switch off on May 2, 2000 (GPS: The Global Positioning System, 2002).

In addition to the GPS, Russia's operational Global Navigation Satellite System (GLONASS), new coming systems: European GNSS establishment GALILEO, Chinese BeiDou, Japanese Quasi-Zenith Satellite System (QZSS) and Indian GAGAN are other GNSS systems that provide continuous positioning over the earth.

2.1 GNSS System Architecture

The description of the GNSS system consists of three main segments: space, control and user segment. The purpose of these segments is to provide continuous positioning and timing services for GNSS users. The space segment consists of satellites that orbiting around the Earth; the control segment of GNSS includes a master and monitoring control stations and ground antennas, and the user segment is military and civil users with GNSS receivers to acquire accurate positioning and precise timing results.

2.1.1 GPS

The space segment of GPS comprises the satellites located in six orbital nearly circular orbits with an altitude of about 20200 km above the Earth, inclined by 55º relative to the equator and a revolution period of 11 hours, 58 minutes and 2 seconds (half a sidereal day). For many years more than 30 GPS satellites has been actively used and with a nominal constellation of 24 satellites allows for a global coverage of four to eight visible satellites above an elevation angle 20º.

The GPS satellites in the orbit are identified based on several ways: the serial number of the satellite, a satellite vehicle number (SVN) and pseudo-random noise number (PRN); a unique code transmitted by each satellite to identify itself in the constellation. Several types of satellites have been developed until today: Block I, Block II, Block IIA, Block IIR, Block IIR-M and Block IIF. Figure 2.2 depicts the latest satellite distribution in the GPS constellation.

The Block III satellites bring a remarkable improvement to the system with interoperability developments and the addition of new civil signals (L1C). All satellites are equipped with solar panels for recharging power using the sun, reaction wheels for changing altitude rapidly, and a propulsion system for orbit changes and adjustments.

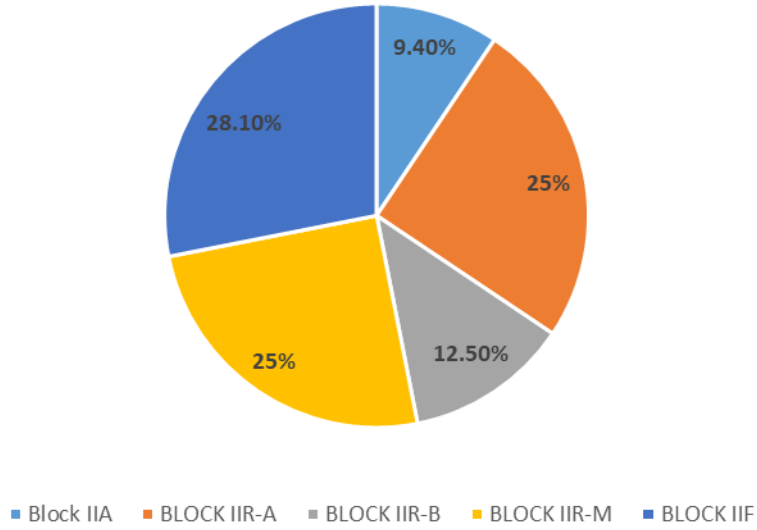

Figure 2.2 : Statistics on the satellite types in the GPS constellation in September 2015.

The nominal constellation of 24 satellites in six orbital planes provide global coverage of minimum 4 to 8 visible satellites above the elevation angle of 15°. The sample of the constellation architecture of the GPS is given in Figure 2.3.

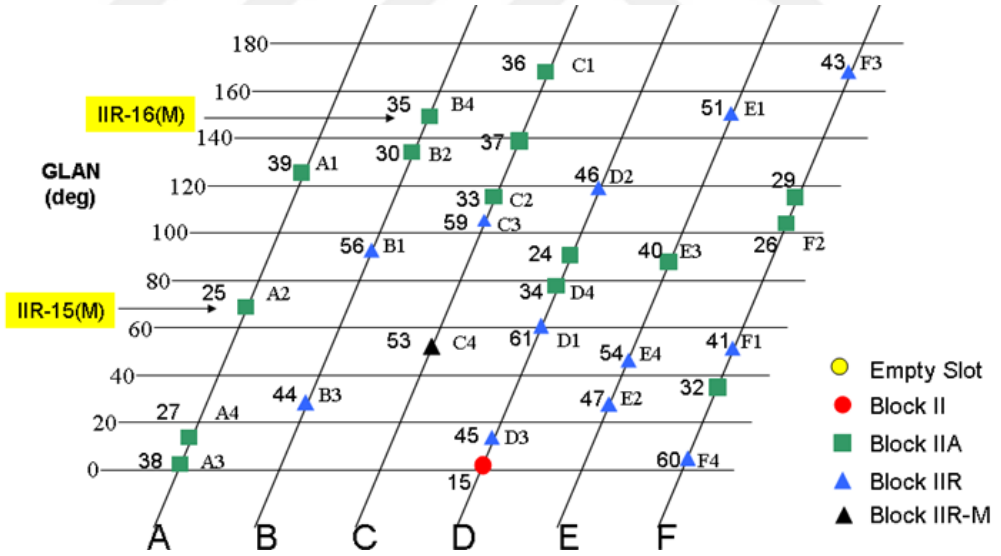

Figure 2.3 : The GPS satellite constellation status, showing each satellite's position in its orbital plane. Dated the 6th of July, 2006 (Navigation Center of Excellence, 2006).

The control segment of GPS consists of a master control station located in Colorado Spring, USA, globally distributed monitoring stations and ground antennas. Monitoring Stations are equipped with atomic clocks tracking all visible satellites and transmit the data to the Master Control Station to calculate the ephemerides and clock

errors of the satellites. Calculated orbits and clock corrections are forwarded to the ground antennas and uplinked to the satellites three times per day via S - band.

The GNSS receivers are the backbone of the user segment. The main purpose of the receivers is the determination of pseudorange and solve the navigation equations to compute the coordinates and provide a very accurate time. The GPS signals are transmitted on two radio frequencies in the L band and derived from the fundamental frequency $f_0 = 10.23\ Mhz$ of the satellite oscillator. The fundamental frequency is produced by highly accurate atomic clocks. The carrier waves L1 and L2 are generated by multiplying the fundamental frequency with 154 and 120, respectively. This gives the frequency of 154 x 10.23 MHz=1575.42 MHz and a wavelength of 19 cm for the carrier $L1$ and the frequency of 120 x 10.23 MHz $= 1227.42$ MHz and a wavelength of 24 cm for the carrier $L2$. These carrier frequencies are modulated with the ranging codes and the navigation message to transmit the data of satellite clocks and the orbital parameters. The GPS uses the Code Division Multiple Access (CDMA) principle that allows sending different code signals (PRN) emitted from each GPS satellite on the same radio frequency. As it is illustrated in Figure 2.4, all GPS satellites have three code signal modulated onto two carrier frequencies: A Coarse/Acquisition (C/A) code and Precise (P1) code on L1, and a Precise code (P2) on carrier L2.

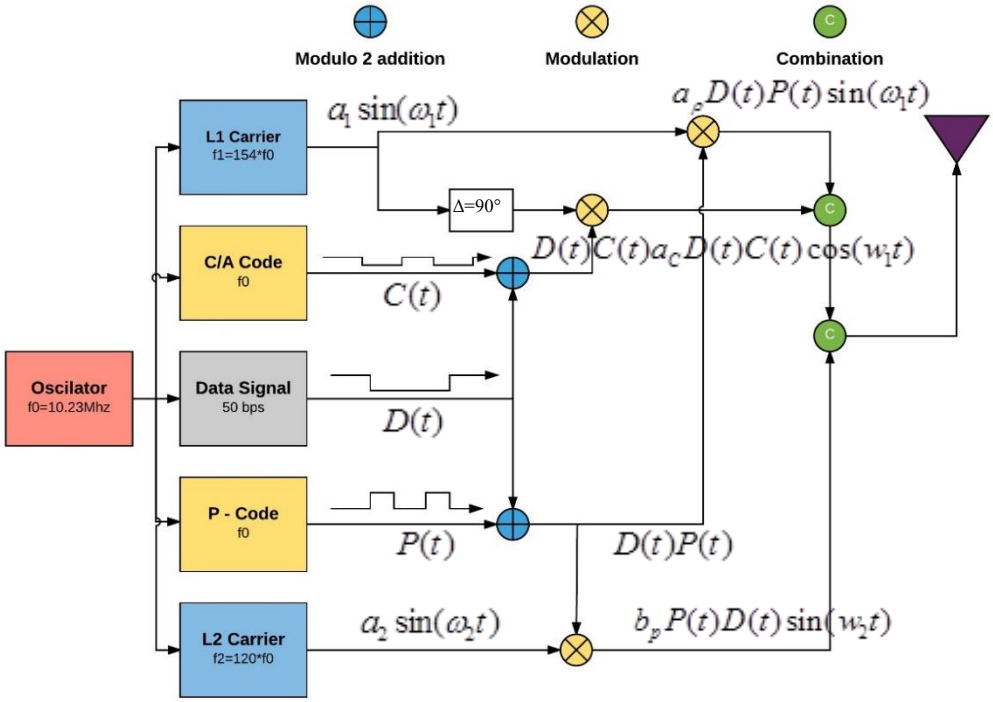

Figure 2.4 : Generation of GNSS signal (Seeber, 1993).

C/A code has a wavelength of approx. 300 m and is repeated every millisecond (i.e., a chipping rate of 1.023 MHz). This code is only defined for single frequency service; standard positioning service (SPS). On the other hand, the P–code has a frequency of 10.23 MHz and wavelength of 30 m defines the precise positioning service (PPS). The P-code sequence is long: repeats after 38 weeks. Each seven-day period from this 37-week period is selected as one-week PRN code and assigned to the various satellites. The third type of signal is the broadcast message which is sent at a rather slow rate of 50 bits per second from a GPS satellite and modulated over both carriers. The navigation message contains information about the satellite clock, the satellite orbit, health status and other quantities related to the satellite. Table 2.1 summarizes the signal structure of the GPS that has been used for the last twenty years. The U.S. government has been developing three new signals for civil purposes: namely L2C, L5 and L1C, which will improve the ionospheric correction and will enhance the positioning accuracy dramatically. The former signal, i.e. L1C will offer cooperative operations, including different navigation satellite systems that will enhance the range and robustness of the whole system.

Table 2.1 : Legacy GPS signal structure (Seeber, 1993).

Fundamental frequency (atomic clock)	10.23 MHz
L1 carrier	154 x 10.23 MHz
L1 frequency	1575.42 MHz
L1 wavelength	19.0 cm
L2 carrier	120 x 10.23 MHz
L2 frequency	1227.60 MHz
L2 wavelength	24.4 cm
P – code frequency	10.23 MHz
P – code wavelength	29.30 m
P – code period	266 days: 7 days/satellite
C/A code frequency	1.023 MHz
C/A code wavelength	293 m
C/A code period	1 millisecond
Broadcast message frequency	50 bps
Broadcast message cycle length	30 seconds

Modulated signals onto two carrier frequencies formulated as follows (i.e., equations 2.1 and 2.2):

$$L_1(t) = a_c C(t) D(t) \cos(w_1 t + \phi_{L1}) + a_p P(t) D(t) \cos(w_1 t + \phi_{L1}) \quad (2.1)$$

$$L_2(t) = b_p P(t) D(t) \sin(w_2 t + \phi_{L2}) \quad (2.2)$$

where a_c, a_p and b_p are the amplitudes of code signals C/A and P; $P(t)$ is the P-code sequence with state ± 1; $D(t)$ is the data stream with state ± 1; and $C(t)$ is the C/A code sequence with state ± 1. The L2 signal structure is much simpler because it does not include the C/A code.

2.1.2 GLONASS

The Russian satellite system GLONASS (GLObalnaya NAvigatsionnaya Sputnikovaya Sistema) is a counterpart of the GPS system and similarly developed as a military system. The Nominal constellation includes 24 satellites and 3 spares distributed equally in three orbital planes with an inclination of 64.8º and a revolution period of 11 hours 15 minutes 44 seconds at an altitude of 19130 km. The planned full operational capability (FOC) aims to achieve at least five observable satellites from every location on the Earth. Nowadays, three types of satellites are operational: GLONASS, GLONASS-M and a new generation satellite GLONASS-K. The most of the ground segment of GLONASS located in Russian territory. The only monitoring station outside the Russia was established in Antarctica in 2010 in order to improve the accuracy of the GLONASS ephemeris data.

IGS has been using the GLONASS constellation and related products since 1998 by the foundation of organization International GLONASS EXpirement (IGEX) service (Slater et al, 1999; Willis et al, 2000) as a complementary to the GPS. Later, this service was transferred into the International GLONASS Service Pilot Project (IGLOS-PP). CODE and most the ACs of the IGS provide GLONASS only and GPS/GLONASS combined solutions based on products obtained from two systems.

GLONASS signals are right-hand circularly polarized and like the GPS signals, they are defined on two carrier frequencies in the L band called G1 and G2. C/A code is modulated on G1 while high accuracy P–code and navigation messages are modulated on both G1 and G2. However, the new generation GLONASS-M satellites provide

C/A signal in the G2 band too. In addition, next generation GLONASS satellites will provide signals on a third frequency G3 (Povalyaev, 2013).

Contrary to CDMA technology used by GPS, each GLONASS satellite uses Frequency Division Multiple Access (FDMA) technology and thus all satellites transmit the same C/A and P-codes at a particular carrier frequency defined by equations 2.3 and 2.4;

$$G1 = F1(k) = 1602 + k \times 9/16 = (2848 + k) \times 9/16 MHz \quad (2.3)$$

$$G2 = F2(k) = 1246 + k \times 7/16 = (2848 + k) \times 7/16 MHz \quad (2.4)$$

where k is the frequency channel number. The frequency ratio of $\mathrm{F1(k)/F2(k)}$ is constant for all GLONASS satellites. After 2005, the GLONASS satellites had to use channels $k = -7, \ldots, +6$, in order to avoid interference with radio astronomy frequencies. The GLONASS navigation message includes information on the health status of all GLONASS satellites, satellites clock offsets with respect to GLONASS system time (UTC - SU) and the orbital parameters defined by positions and velocities in Parametry Zemli 1990 (i.e., PZ–90), Earth centered and Earth fixed reference frame with lunisolar acceleration perturbation parameters. On the contrary, the GPS broadcasts the ephemeris data via Keplerian orbital elements.

2.1.3 GALILEO

The European system Galileo is a joint attempt of the European Commission and the European Space Agency (ESA). It is a civil navigation satellite system and planned to have 27 operational and 3 spare satellites in three orbital planes which are 56º inclined with reference to the equatorial plane (i.e., 10 satellites per each plane). The satellites will be orbiting the Earth at an altitude of 29600 km, with a revolution period of 14h 4min 45sec and a ground track repeat cycle of approx. 10 days that corresponds to 17 revolutions. This constellation geometry will guarantee a minimum of six visible satellites from any point on the Earth with a minimum cut-off elevation angle of 10º. The Galileo program has two phases: In Orbit Validation phase (IOV) and Full Operational Capability (FOC) phase. The IOV phase of Galileo includes an extensive space segment and ground segment tests and operations conducted via two test satellites GIOVE-A and GIOVE-B and four complementary satellites to test and validate the space and the ground segments. The primary goal of IOV phase was to

secure the allocated frequency bands to Galileo by the International Telecommunications Union (ITU) and gathering vital data related to the Galileo orbit environment in order to design of the full constellation. The FOC phase is expected to be reached by 2020, with a constellation of 30 satellites and interoperable with other GNSS.

With FOC phase, each Galileo satellite will broadcast 10 different navigation signals modulated on five frequency bands: E1, E6, E5, E5a, and E5b. All these signals are configured to support Galileo's civil services such as Open Services (OS), Safety of Life (SoL), and Commercial Services (CS), Public Regulated Services (PRS) and Search and Rescue (SAR) services. Similar to the GPS, all Galileo satellites use the same frequencies and the CDMA technology to attribute a signal to a satellite. Binary offset carrier modulation, a split spectrum modulation scheme used by the Galileo, aims to reduce interference with GPS signals. Therefore, the Galileo signals can share same frequency bands with GPS and new generation GLONASS signals, i.e. G3, without any interference. The carrier frequencies and all timing processes are based on the fundamental frequency $f_0 = 10.23\ Mhz$. Table 2.2 illustrates the current signal structure of the system.

Table 2.2 : Galileo Navigation Signals (Wellenhof et al, 2008, p384).

Carrier	Frequency (MHz)	Wavelength (cm)	PRN codes	Navigation message
E1	154 x 10.23 = 1575.420	19.0	E1A E1B E1C	PRS OS, CS, SoL OS, CS, SoL
E6	125 x 10.23 = 1278.750	23.4	E6A E6B, E6C	PRS CS
E5	116.5 x 10.23 = 1191.795	25.2		
E5a	115 x 10.23 = 176.450	25.5	I, Q	OS
E5b	118 x 10.23 = 1207.140	24.8	I, Q	OS/CS/SoL

The two Galileo carrier frequencies, E5a and E1 coincide with the carrier frequencies L5 and L1 of the GPS system respectively in order to increase interoperability between two systems.

2.1.4 BEIDOU

The Beidou Navigation Satellite System (BDS) is a Chinese system formerly known as Compass. Beidou is already in operation (Phase II) for the Chinese and Asian Pacific Area and will provide global coverage planned by 2020 when all 35 satellites

will have been launched (Phase III). The nominal constellation will consist of 35 satellites which includes 5 geostationary orbits and 30 non-geostationary satellites; 27 Medium Orbit and 3 inclined Geosynchronous Orbit. At an altitude of 21528 km in three orbital planes with an inclination of 55º, the non-Geo satellites will orbit the Earth with a revolution period of 12 hours 53 minutes repeating the full track each seven sidereal days (BeiDou-SIS-ICD, 2016). The remaining 5 Geo satellites positioned at different longitudes (58º, 80º, 110º, 140º, 160º) will orbiting the Earth at an altitude of 35786 km. BDS will adopt the China Geodetic Coordinate System 2000 (CGCS2000) as a reference coordinate system identical to the International Terrestrial Reference System (ITRS) and Beidou navigation satellite system time (BDT) which is identical to UTC as a time reference.

The Phase II / III satellites will transmit right hand circularly polarized signals defined on three radio frequencies in the L band: B1=1561.098MHz, B2=1207.140MHz, and B3=1268.520MHz. Like GPS, Galileo and the generation GLONASS satellites, Beidou ranging signals differentiated by using the CDMA technique (BeiDou-SIS-ICD, 2016). The information of different navigation signals, signal characteristics, and supported services can be found in the latest version of BDS Interface Control Document i.e. BeiDou Navigation Satellite System Signal in Space Interface Control Document.

2.2 GNSS Modernization

The interoperability between different constellations (e.g., GPS, GLONASS, GALILEO, BEIDOU, Japan MSAS & QZSS and Indian Regional Navigation Satellite System - IRNSS) increases the global coverage and performance of applications related to the accuracy, availability, integrity, and reliability. The GPS signal modernization with several new GPS Block III type of satellites and new ranging codes and carriers (i.e., L1C, L2C, L5C) will allow more frequent and precise satellite commands that will improve accuracy for users. The modernization of the GLONASS with a new GLONASS – K satellites, by adding a new frequency G3 and, by using the CDMA principle will improve the interoperability of GLONASS with other GNSS and will bring solutions to ambiguity resolution.

In development systems, i.e. the European Galileo and Chinese Beidou navigation satellite systems will bring additional frequencies and public services that will upgrade

both architecture and hardware of the GNSS receivers and antennas. For civil users, the new signals will provide; robustness against interference, mitigation of ionospheric effect, resolution of integer ambiguities via linear combinations and a significant increase in total accuracy and in the quality of services. Radio frequency compatibility is the key point, ensuring that satellite navigation signals do not interfere with each other. It would be helpful if the system operators could agree upon methods to solve intersystem biases. In addition, GNSS data & product providers like CODE and IGS should adapt their solutions and software according to new signals and GNSS features.

2.3 Precise Point Positioning

PPP is a high accuracy; a single receiver point positioning technique based on zero-differenced code and carrier phase observations using precise satellite orbit and clock correction products. With the development and introduction of precise satellite orbit and clock corrections from IGS ACs such as Centre of Orbit Determination in Europe (CODE), German Research Institute Geo Forschungs Zentrum (GFZ) and etc., it is now possible to perform a high accuracy point positioning without differencing simultaneous observations from reference and rover receivers, as with the case of differential positioning.

The PPP technique using undifferenced code and carrier observations from dual frequency receivers was first proposed by Zumberge et al. (1997) who proved that PPP is able to achieve a centimeter-level positioning accuracy by using IGS precise orbits and clocks, and ionosphere-free code and phase observations.

The first study describing the details of the PPP technique with the traditional observation model was published by Kouba and Heroux (2001). They used un-differenced code and carrier phase observations from dual frequency receivers. Using 30 seconds sampling rate of GPS data and estimating unknown parameters at 15-minute intervals, they found almost similar results with Zumberge et al. (1997). Gao and Shen (2001) proposed the University of Calgary (UofC) PPP model that uses ionosphere-free code and carrier phase observations in order to estimate station coordinates, receiver clock, troposphere delay and float ambiguities.

Several PPP studies have been expanded applications from post – processing to real time processing as well as from static positioning to kinematic positioning. One of

them presented by Gao et al. (2003) achieved an accuracy at a sub – decimeter level in kinematic PPP and centimeter level accuracy in real time static PPP with accurate satellite clocks and orbits. Moreover, Chen and Gao (2005) reached to sub – decimeter level accuracy in the studies of single frequency PPP solutions.

Unlike the relative mode of the GNSS sessions where most errors and biases are essentially canceled, almost all errors and biases must be rigorously modeled and mitigated in the PPP. Despite the fact that the PPP approach has indicated remarkable advantages from the points of operational flexibility and cost-effectiveness, it requires a long initialization time before a solution reaches its optimal precision. Normally, it will take about 30 to 60 minutes for the position solution to converge to a decimeter level as it is illustrated in Figure 2.5. The centimeter level accuracy is achieved after several hours of process.

The long convergence time, which arises from un-resolved ambiguities, is also dependent on many factors such as the number and geometry of visible satellites, user environment, observation quality and sampling rate (Bisnath and Gao, 2008). Moreover, a large convergence time for fixing ambiguities prevent users from carrying out RT PPP applications. PPP requires accurate satellite orbits and satellite clocks (as provided, e.g. by the IGS), and undifferenced code and phase observations.

The unknown parameters to be estimated are station coordinates, receiver clock errors, troposphere path delays and phase ambiguities while upper atmospheric refraction, i.e. ionospheric refraction, can be mitigated 99 % by means of the linear combination of dual frequency of code and carrier phases. Due to unknown carrier phase biases of both satellites and receivers, ambiguities lose their integer nature because of absorbing most of the carrier phase biases. In a network solution, these biases can be removed from observations by differencing and thus bias-free ambiguity can be fixed to an integer value. However, it is not possible to model and eliminate these biases with a single receiver PPP solution alone. Ge et al. (2011) suggested using a global or regional receiver network to estimate the uncalibrated satellite phase delays (UPDs) which are highly associated with fractional part of ambiguities. The integer nature of ambiguities may be revealed by separating the fractional parts from the real-valued ambiguities. Laurichesse and Mercier (2007), Juan et al. (2010) and Banville et al. (2008) conducted researches focusing on undifferenced ambiguity fixing by reducing these biases and increase the convergence performance of PPP.

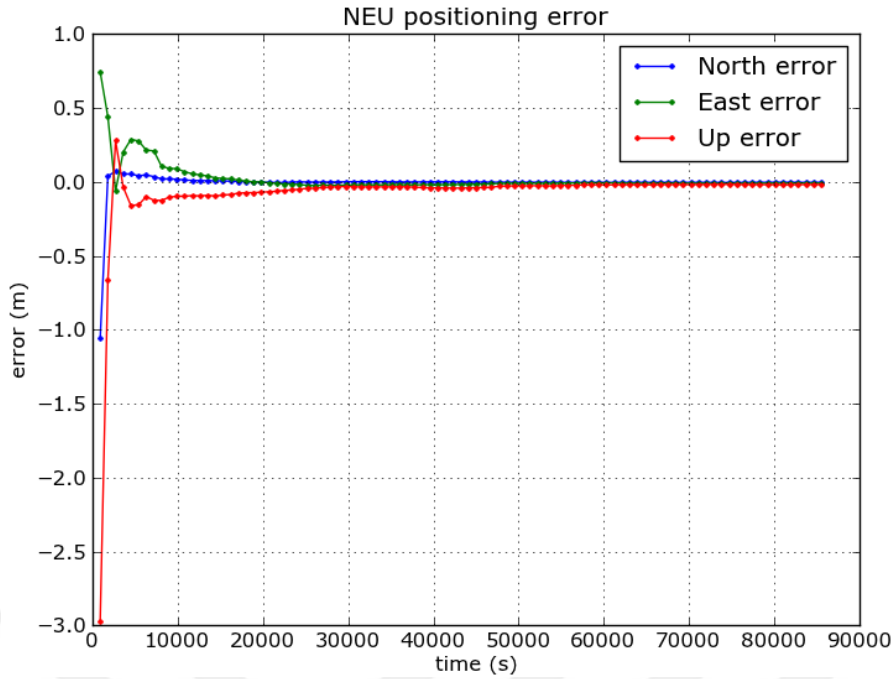

Figure 2.5 : PPP convergence time needed for an accurate positioning in north, east and up directions for "ANKR" IGS site.

A key issue for precise point positioning to achieve high-accuracy positioning is how to mitigate all potential errors involved in the space segment, signal propagation, ground environment and receiver segment. The potential error sources that need to be considered in solutions are satellite orbit and clock errors, ionospheric refraction, troposphere delay, receiver clock offset, multipath, measurement noise, satellite and receiver antenna phase center offsets, phase wind up, relativistic effects, Earth tides, ocean tide loading, atmospheric loading, and Sagnac effect.

Most of these errors can be mitigated to some extent through modeling. The receiver clock offsets and tropospheric delays may be estimated as unknown parameters in the observation equations 2.5a and 2.5b while the ionospheric refraction is usually canceled by adopting ionosphere-free linear combinations. The PPP error sources and their mitigation methods will be discussed in chapter 3.

Because of the clear environmental conditions around IGS sites, multipath effects are usually neglected, whereas the remaining error sources either are mitigated or eliminated based on recommendations of the IERS conventions (McCarthy and Petit, 2004) and the announcements of IGS. The potential error sources having an impact on signal propagation from satellite to receiver for pseudorange measurements are illustrated in Figure 2.6.

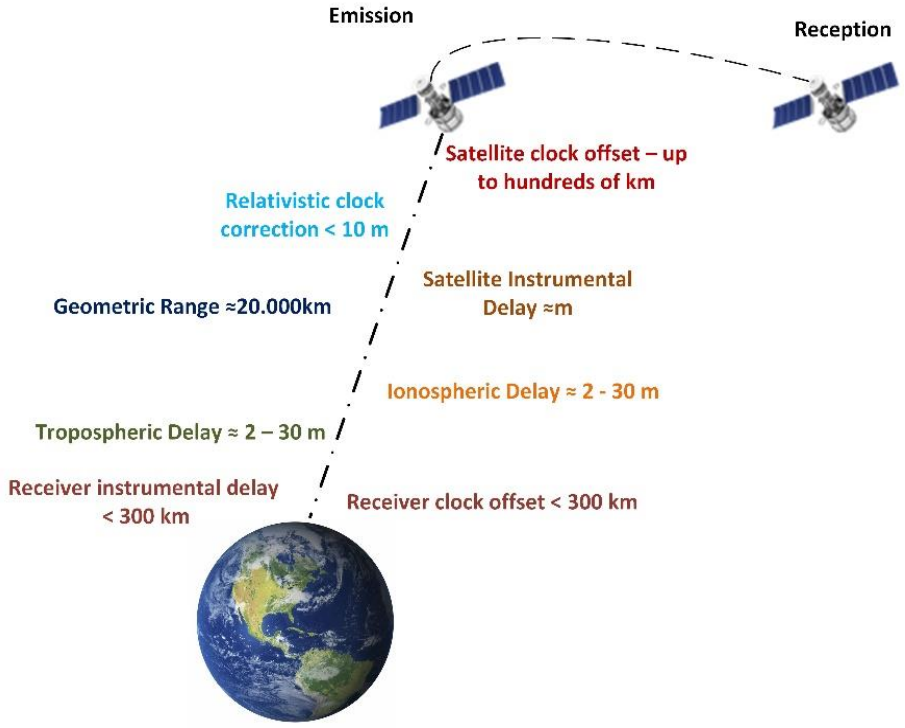

Figure 2.6 : Some error sources affecting GNSS positioning accuracy (Sanz et al, 2013, p.96).

2.3.1 Mathematical model of PPP

Current traditional PPP models are implemented only by assuming GPS based observations that is not appropriate anymore because of the availability of Multi-GNSS constellations and new signals. However, the standard model that most of PPP packages such as GIPSY – OASIS (Zumberge et al, 1997), BERNESE (Dach et al, 2015), CSRS-PPP and GAMIT-GLOBK (Herring et al, 2015), have been utilized, is the traditional model with an ionosphere-free combination of pseudorange and carrier phase observations. An observation model is a projection of the relation between observations and unknowns. By choosing a processing strategy (e.g., LSA or KF), GNSS measurements can be associated to unknown parameters.

The traditional PPP model including all potential error sources in the undifferenced observation equations for code and carrier phase expressed in metric units in equations 2.5a and 2.5b:

$$P_i = \rho + c\left(dt^r - dt^s\right) + \Delta\rho^{trop} + I_i + b^r_{Pi} - b^s_{Pi} + \varepsilon_{Pi} \tag{2.5a}$$

$$L_i = \rho + c\left(dt^r - dt^s\right) + \Delta\rho^{trop} - I_i - \lambda_i N_i + b^r_{Li} - b^s_{Li} + \varepsilon_{Li} \tag{2.5b}$$

where i = 1, 2 and

P_i : Code measurements (m),

L_i : Phase measurements (m),

ρ : Receiver – Satellite geometric range involves loads and relativistic effects,

c : Speed of light in a vacuum (m/s),

dt_r : Receiver clock error (s),

dt^s : Satellite clock error (s),

$\Delta\rho^{trop}$: Tropospheric delay (m),

I_i : First order ionospheric refraction (m),

λ_i : Wavelength (m),

N_i : Integer phase ambiguity (cycle),

b_{Pi}^r : Receiver hardware code delays (m),

b_{Pi}^s : Satellite hardware code delays (m),

b_{Li}^r : Receiver hardware phase delays (m),

b_{Li}^s : Satellite hardware phase delays (m),

ε_{Pi} : Code multipath and noise delays (m),

ε_{Li} : Phase multipath and noise delays (m).

The ionosphere-free code and carrier phase observations (L_3, P_3) mitigate the troublesome effect caused by the ionosphere and lead to centimeter level accuracy in a static mode and at least decimeter level for kinematic mode. Neglecting multipath and noise effect for both phase and code observations and embedding all corrections of relativistic effects, phase center variations, phase wind-up effects and site displacement effects into the range (ρ), the ionosphere-free code and phase observations can be illustrated as given in equations 2.6a and 2.6b. These equations are the linear combination formed by equation 2.7.

$$P_3 = \rho + c\left(dt^r - dt^s\right) + \Delta\rho^{trop} + b^r_{P3} - b^s_{P3} \tag{2.6a}$$

$$L_3 = \rho + c\left(dt^r - dt^s\right) + \Delta\rho^{trop} - \lambda_3 N_3 + b^r_{L3} - b^s_{L3} \tag{2.6b}$$

where

$$P_3 = \frac{f_1^{\,2}P_1 - f_2^{\,2}P_2}{f_1^2 - f_2^2}; \quad L_3 = \frac{f_1^{\,2}L_1 - f_2^{\,2}L_2}{f_1^2 - f_2^2} \tag{2.7}$$

In the equations above, f_1 and f_2 are the frequencies of any two carriers, b^r_{Pi}, b^s_{Pi} and b^r_{Li}, b^s_{Li} represent the remaining unmodelled biases of receiver and satellite for code and phase ionosphere-free observations, respectively. Measurement noise of L_3 is three times bigger relative to L_1 classic measurement noise. It is worth noting that the ambiguity term N_i in the equation 2.6b is a linear combination of L_1 and L_2 that the ambiguity loses its integer nature and thus estimated as a float value.

In order to get accurate estimates, a measurement model of PPP must be formed considering all model terms that defined in equations 2.5a and 2.5b. A modeling phase of a PPP solution contains some necessary instructions need to be followed to reach a centimeter-level positioning accuracy. These instructions are listed below as:

- Precise orbits and clocks products generated by IGS ACs such as GFZ, CODE and Jet Propulsion Laboratory (JPL) must be used instead of broadcast ephemeris products with a lower accuracy.
- The satellite clock corrections must be used with an original sampling rate as obtained from e.g. IGS AC and should not be interpolated to lower sampling rate.
- The gravitational path range correction due to the orbital eccentricity may be considered as a part of the satellite clock correction and need to be calculated before data processing.
- The first order ionospheric refraction and differential code biases (DCBs) are canceled by taking advantage of the fact that the ionosphere is a dispersive medium and combination of dual frequency measurements can be used to mitigate the ionospheric refraction.

- The hydrostatic part of the troposphere i.e. ZHD may be modelled by using prediction models or functions or directly calculated form ground meteorological measurements.
- The remaining part of the troposphere delay i.e. ZWD is usually estimated via LSA along with the coordinates, receiver clocks, and phase ambiguities.
- IGS Antenna files must be implemented to solutions for modeling phase center offsets (PCO) and variations (PCV) of antennas for both satellite and receiver.
- The carrier phase wind-up effect due to satellite motion must be considered while the satellites under eclipse must to be removed from the solution to prevent large orbital errors.
- According to the IERS conventions, the ITRF solution is based on a tide free reference system. Thus, site displacement effects caused by an elasticity of the Earth such as solid tides, ocean loading, and polar tides, and atmospheric loading must be considered based on methods recommended by the IERS up-to-date conventions.

2.3.2 Parameter estimation

Parameter estimation is a critical process identifies system characteristics through mathematical models just as statistical probability distribution functions. The mathematical model is often considered of as being composed of two parts: the functional model that defines the deterministic properties of the system or physical situation and the stochastic model defines the probabilistic properties of the system variables involved. The unknown parameters can be linked to the measurements through LSA.

The positioning principle in PPP is based on finding a solution to the geometric problem from the measured ranges to the known satellites. The estimation of seven unknown parameters for each satellite in view (i.e., receiver coordinates: X, Y, Z, zenith troposphere total path delay (ZTD), receiver clock corrections, and phase ambiguity) is based on linearization of the function of the geometric non-linear equation and applying the Gauss-Markoff Adjustment model.

Neglecting multipath and measurement noise and using the phase (2.6a) and the code (2.6b) measurements the following equation system (2.8a and 2.8b) can be expressed as:

$$P_3 - C \approx \sqrt{\left(X_0 - X\right)^2 + \left(Y_0 - Y\right)^2 + \left(Z_0 - Z\right)^2} + c\delta t + \Delta trop_{wet}^{z} + b_{P_3}^{r} - b_{P_3}^{s} \tag{2.8a}$$

$$L_3 - C \approx \sqrt{\left(X_0 - X\right)^2 + \left(Y_0 - Y\right)^2 + \left(Z_0 - Z\right)^2} + c\delta t + \Delta trop_{wet}^{z} + B_3 \tag{2.8b}$$

The left-hand side of the equations is the prefit residuals including observed measurements i.e. P_3, L_3 and the calculated modeled terms i.e. $C = -ct^{sat} + trop_{apriori}^{zhd} + tides + windup$. The right-hand side, on the other hand, contains the unknown parameters to be estimated. The equation 2.8b also includes the phase ambiguity factor i.e. B_3 which is not an integer anymore due to absorbed phase hardware biases from satellites and receivers as expressed in equation 2.9.

$$B_3 = \lambda_3 N_3 + b_{L3}^{r} - b_{L3}^{s} \tag{2.9}$$

Equations 2.8a and 2.8b are non-linear systems defined by functions (eq. 2.10) and must be linearized (eq. 2.11) around a priori receiver coordinates using the zero and first-order terms of Taylor series expansion:

$$y = f(X, Y, Z, trop_{wet}, N + biases) \tag{2.10}$$

$$y_i + v_i = f(\Phi_i)_{x_0} + \frac{\partial f(\Phi_i)}{\partial x_i} dx_i + .. \tag{2.11}$$

The estimation is performed to compute the values to correct the a priori values of the unknowns. The functional model between observations and unknowns in the matrix form of Gauss – Markov model is given as:

$$y = Ax + v \tag{2.12}$$

where

n, u : number of observations and number of unknowns respectively,

A : coefficients (design) matrix $[n \times u]$,

x : vector of unknowns (corrections) $[u \times 1]$,

y : vector of observed minus computed observations (O-C) $[n \times 1]$,

v : residual vector of observations

The vector y (i.e. prefit residuals) includes the differences between observed observations and predicted observations with a priori estimates, expressed as below:

$$y = \begin{bmatrix} P_3^1 - \rho_0^1 + c\delta t^1 - ZHD \\ L_3^1 - \rho_0^1 + c\delta t^1 - ZHD \\ . \\ . \\ . \\ P_3^n - \rho_0^n + c\delta t^n - ZHD \\ L_3^n - \rho_0^n + c\delta t^n - ZHD \end{bmatrix} \tag{2.13}$$

where n is the number of observations contributing to the PPP solution, δt^n is the satellite clock corrections which also include satellite relativistic clock corrections due to orbital eccentricity. In this vector, effects of the solid Earth tides, ocean and atmospheric loadings are implemented to the range ρ parameter. The term ZHD is the a priori troposphere that can be found with 99 % accuracy if high accuracy pressure readings available at the site. The mapping function mf_{wet} is a component of the design matrix, and ZWD is defined as an unknown parameter in the unknown's vector. Equation 2.14 illustrates the design matrix A as:

$$A = \begin{bmatrix} \frac{X_0 - X^1}{\rho_0^1} & \frac{Y_0 - Y^1}{\rho_0^1} & \frac{Z_0 - Z^1}{\rho_0^1} & 1 & mf_{(e)} & \frac{\partial mf}{\partial e}\cos(\alpha)^1 & \frac{\partial mf}{\partial e}\sin(\alpha)^1 & 0 & 0 & 0 \\ \frac{X_0 - X^2}{\rho_0^2} & \frac{Y_0 - Y^2}{\rho_0^2} & \frac{Z_0 - Z^2}{\rho_0^2} & 1 & mf_{(e)} & \frac{\partial mf}{\partial e}\cos(\alpha)^2 & \frac{\partial mf}{\partial e}\sin(\alpha)^2 & 1 & 0 & 0 \\ \vdots & & & & & & & & & \\ \vdots & & & & & & & & & \\ \frac{X_0 - X^{n-1}}{\rho_0^{n-1}} & \frac{Y_0 - Y^{n-1}}{\rho_0^{n-1}} & \frac{Z_0 - Z^{n-1}}{\rho_0^{n-1}} & 1 & mf_{(e)} & \frac{\partial mf}{\partial e}\cos(\alpha)^{n-1} & \frac{\partial mf}{\partial e}\sin(\alpha)^{n-1} & 0 & 0 & 0 \\ \frac{X_0 - X^n}{\rho_0^n} & \frac{Y_0 - Y^n}{\rho_0^n} & \frac{Z_0 - Z^n}{\rho_0^n} & 1 & mf_{(e)} & \frac{\partial mf}{\partial e}\cos(\alpha)^n & \frac{\partial mf}{\partial e}\sin(\alpha)^n & 0 & 0 & 1 \end{bmatrix} \tag{2.14}$$

The parameter vector of unknowns x (i.e. equation 2.15) for the traditional PPP contains X, Y, Z coordinate corrections, receiver clocks' corrections, ZWDs and tropospheric gradients in North (G_n) and East (G_e) direction, and float ambiguity for each observed satellite (N_{rec}^{sat}).

$$x = [\Delta X, \Delta Y, \Delta Z, c\delta t_{rec}, ZWD, G_n, G_e, N_{rec}^{sat1}, N_{rec}^{sat2}, ..., N_{rec}^{satn}]^T \tag{2.15}$$

The stochastic model of the functional model is represented by the variance-covariance (or dispersion) matrix (i.e. equation 2.16) of the observations Σ_{ll} .

$$D(l) = \sum_{ll} = \sigma_0^2 Q_{ll} \tag{2.16}$$

with σ_0^2 being the a priori variance of unit weight and Q_{ll} is the cofactor matrix which is an inverse of the weight matrix as defined in equation 2.17.

$$P = Q_{ll}^{-1} = \sigma_0^2 \Sigma_{ll}^{-1} \tag{2.17}$$

The elements of the variance - covariance matrix of the observations Σ_{ll} are formed by the variances of the observations σ_i^2 and correlation coefficients δ_{12} as given in equation 2.18 :

$$\Sigma_{ll} = \begin{bmatrix} \sigma_1^2 & \delta_{12}\sigma_1\sigma_2 & \cdots & \delta_{1n}\sigma_1\sigma_n \\ \delta_{21}\sigma_1\sigma_2 & \sigma_2^2 & \cdots & \delta_{2n}\sigma_2\sigma_n \\ \vdots & \vdots & \vdots & \vdots \\ \delta_{n1}\sigma_1\sigma_n & \delta_{n2}\sigma_2\sigma_n & \cdots & \sigma_n^2 \end{bmatrix} \tag{2.18}$$

The adjustment procedure is based on minimizing the sum of squares of residuals (equation 2.19):

$$v^T P v = (y - Ax)^T P (y - Ax) = \min \tag{2.19}$$

The estimated vector of unknowns denoted as equation 2.20:

$$x = \left(A^T P A\right)^{-1} A^T P y = N^{-1} n; \quad Nx = n \tag{2.20}$$

where N is the normal equation matrix and n is the measurement vector. These are the normal equations that satisfy the criterion of the LSA i.e. $v^T P v = \min$. Based on given equations above a posteriori variance of unit weight becomes (equation 2.21):

$$\hat{\sigma}_0^2 = \frac{\hat{v}^T P \hat{v}}{n - u} \tag{2.21}$$

where $n - u$ defining the degree of freedom.

The algorithm described above is based on the principal assumption of Gaussian normally distributed error and uncertainties, therefore, any previously detected outlier or bias must be removed before adjustment procedure.

Observations at low elevations tend to be influenced from refraction and multipath effects more than higher elevation observations. On the other hand, using low elevation observations improves the satellite geometry and accelerate the de-correlation process between estimated tropospheric path delays and vertical component of station position (Rothacher and Beutler, 1998; Meindl et al. 2004). An elevation angle dependent weighting is recommended while observing satellites with an elevation lower than $10°$. The weighting function of the observations i.e., $w(z)$ is expressed in equation 2.22, where z is the zenith angle of the satellite.

$$w(z) = \cos^2(z) \tag{2.22}$$

The root mean square (RMS) of unit weight (σ_0^2) is used to scale given constraints to the specific parameter and often specified as 0.001 m with elevation dependent weighting. Changing the RMS of unit weight will change the strength of the constraints specified to the parameters.

2.3.2.1 Constraints

In GNSS data analyses, observations must often satisfy specified relations or it is sometimes necessary to fix an observation to one value. In order to avoid singularity during formation of Normal Equation Systems (NEQs), an additional information might be needed before performing LSA. These conditions, specified into the parameters, are known as constraints and expressed by linear observation equation 2.23 as:

$$H_p = h + v_h \quad \text{and} \quad D(h) = \sigma^2 P_h^{-1} \tag{2.23}$$

where H_p is the Jacobian matrix with given coefficients, h is the vector of the known constants (i.e., O-C for constraints), p is the vector of unknown parameters, v_h is the residual vector and P_h^{-1} is the weight matrix of the introduced constraining equations.

Non – linear constraints must be linearized via first order Taylor series. The constraints may be interpreted as pseudo-observations and defined as following equation 2.24:

$$\begin{bmatrix} y \\ h \end{bmatrix} + \begin{bmatrix} v_y \\ v_h \end{bmatrix} = \begin{bmatrix} A \\ H \end{bmatrix} \hat{p} \quad \text{and} \quad D\left(\begin{bmatrix} y \\ h \end{bmatrix}\right) = \sigma^2 \begin{bmatrix} P^{-1} & 0 \\ 0 & P_h^{-1} \end{bmatrix} \tag{2.24}$$

or as the corresponding NEQ as given in equation 2.25

$$\left(A^T PA + H^T P_h H\right) \hat{p} = A^T Py + H^T P_h h. \tag{2.25}$$

As it can be seen from the equation 2.25, by adding the terms $H^T P_h H$ and $H^T P_h h$ to the original NEQ system, a priori constraints are introduced. Constraints can be introduced for parameter types such as static and kinematic coordinates, troposphere, ionosphere, global ionosphere parameters (i.e. stochastic ionosphere parameters - SIPs), orbits, EOPs, reference clocks, receiver and satellite antenna offsets. Constraining parameters to any a priori value and set the parameter improvement to zero, an absolute constraint is specified. A relative constraint, on the other hand, limits the improvement of parameters relative to each other and can be specified for parameters such as ZWDs, gradients, and SIPs. Parameters may also be fixed to a priori values, however, it is not recommended because it is not possible to change the datum information in NEQs after fixing parameters in LSA. Therefore, an optimal solution is constraining parameters tight but not fix them.

2.3.2.2 Parameterization

The parameterization of adjustable parameters as a function of time may have different forms. For example, station coordinates, dynamic orbital parameters, and bias parameters may be constant over time while troposphere and ionosphere parameters are parameterized in a continuous piece-wise linear function. The piece-wise linear parameters are modeled in each particular time interval specified by the user.

Epoch-wise parameterization is only valid for one single epoch solution as in case of receiver and satellite clocks and kinematic coordinates. Since their large number and long CPU process, it is not recommended to keep these epoch-wise parameters in the NEQs. Recently, some GNSS software support the epoch-wise pre-elimination and back-substitution steps which reduce the CPU memory and process time remarkably without losing any information from the NEQs. These steps only available for un-correlated epoch-wise parameters: kinematic coordinates, wet delays and horizontal tropospheric gradients.

2.3.2.3 Parameter (NEQs) stacking

The theory of combining sequential solutions has been used in GNSS studies for a long time. Using sequential adjustment techniques at the NEQ level is independent of observations, and thus, results from different techniques can be merged to perform one final solution. Based on this ability multi-session solutions can be combined and computed fast and flexible over NEQs. The LSA with all observations in one step is not different from dividing LSA into different parts and combining results at the end. The evidence of equivalence of both methods is based on the assumption that the observations are uncorrelated. Parameter stacking is a procedure for the unknown parameters that are common to more than one normal equation systems by gathering them as pseudo - observations into one combined parameter in the combined NEQs (Teke, 2011).

Parameter stacking is usually performed in a PPP, particularly when station coordinates, tropospheric path delays and dynamical orbit parameters from different NEQs are combined to a single parameter set.

The observation equations in the matrix form defined as in equation 2.26:

$$\begin{bmatrix} y_1 \\ y_2 \end{bmatrix} + \begin{bmatrix} v_1 \\ v_2 \end{bmatrix} = \begin{bmatrix} A_1 \\ A_2 \end{bmatrix} [p_c] \text{ with } D\left(\begin{bmatrix} y_1 \\ y_2 \end{bmatrix} \right) = \sigma_c^2 \begin{bmatrix} P_1^{-1} & \theta \\ \theta & P_2^{-1} \end{bmatrix} \tag{2.26}$$

or can be expressed by equation 2.27:

$$\left[A_1^T P_1 A_1 + A_2^T P_2 A_2 \right] [p_c] = \left[A_1^T P_1 y_1 + A_2^T P_2 y_2 \right] \tag{2.27}$$

where y_1 and y_2 are independent observations forming the whole observation i.e. y_c and the goal is to estimate the parameters i.e. p_c common to the both observations: y_1 and y_2.

The independence of observations can be deduced from the dispersion (variance-covariance) matrix. The corresponding NEQ system is

$$\left[A_1^T P_1 A_1 + A_2^T P_2 A_2 \right] [p_c] = \left[A_1^T P_1 y_1 + A_2^T P_2 y_2 \right] \tag{2.28}$$

In contrast to the one step adjustment solution, the sequential LSA assumes that each observation is independent and an estimation procedure follows only particular unknowns related with corresponding observation series. The observation equations can be written as given in equation 2.29:

$$\begin{aligned} y_1 + v_1 &= A_1 p_1 \qquad \text{with} \qquad D(y_1) = \sigma_1^2 P_1^{-1} \\ y_2 + v_2 &= A_2 p_2 \qquad \text{with} \qquad D(y_2) = \sigma_2^2 P_2^{-1} \end{aligned} \tag{2.29}$$

In more general representation (equation 2.30) for i=1, 2:

$$y_i + v_i = A_i p_i \qquad \text{with} \qquad D(y_i) = \sigma_i^2 P_i^{-1} \tag{2.30}$$

where p_i represents the unknowns to be estimated only responding to the observations of y_i.

The NEQs for observations in equation 2.30 can be given as in equation 2.31:

$$\left[A_i^T P_i A_i\right]\left[\hat{p}_i\right] = \left[A_i^T P_i y_i\right] \qquad \text{and} \qquad D(\hat{p}_i) = \hat{\sigma}_i^2 \left(A_i^T P_i A_i\right)^{-1} \tag{2.31}$$

Individual solutions given as in the equation 2.30 are used to reveal the common parameter, i.e. $\hat{p}_c$, which is satisfying all independent observations and they are represented by equations 2.32 and 2.33:

$$\begin{bmatrix} p_1 \\ p_2 \end{bmatrix} + \begin{bmatrix} v_{p1} \\ v_{p2} \end{bmatrix} = \begin{bmatrix} I \\ I \end{bmatrix} \hat{p}_c \qquad ; \qquad D\left(\begin{bmatrix} \hat{p}_1 \\ \hat{p}_2 \end{bmatrix}\right) = \sigma_c^2 P_p^{-1} = \sigma_c^2 \begin{bmatrix} \Sigma_1 & \theta \\ \theta & \Sigma_2 \end{bmatrix} \tag{2.32}$$

$$A_p^T P_p A_p \hat{p}_c = A_p^T P_p y_p \tag{2.33}$$

and, after substitution the equation 2.33, the final NEQ system is formulated as:

$$\left[A_1^T P_1 A_1 + A_2^T P_2 A_2\right] \hat{p}_c = \left[A_1^T P_1 y_1 + A_2^T P_2 y_2\right] \tag{2.34}$$

that is equal to the one step adjustment of NEQ system in the equation (2.28).

2.3.3 Kalman Filter

Kalman Filter (KF) is a processing strategy that gathers all available data and using a recursive approach by considering an initial information and measurements, thus the unknown parameters are estimated statistically with a minimum error. It is a recursive approach that it is not necessary to save previous epoch observations. Contrary, previous results are moved forward in the filter. KF is an optimal design that being consistent, unbiased estimator with minimum square error (Mikhail and Ackermann, 1976) as expressed by following equations (2.35, 2.36 and 2.37):

$$\lim_{sz\to\infty} P\left(\left|k\hat{x} - kx\right| < \varepsilon\right) = 1 \tag{2.35}$$

$$E\left(k\hat{x}\right) = kx \tag{2.36}$$

$$E\left\{\left(k\hat{x} \text{ - } E\left(k\hat{x}\right)\right)^T \left(k\hat{x} - E\left(k\hat{x}\right)\right)\right\} = \min \tag{2.37}$$

where

sz : sample size,

kx : state vector,

$k\hat{x}$: estimate of the state vector,

ε : very small values,

$P()$: statistical probability,

$E()$: statistical expectation.

KF includes state model (i.e. equation 2.38) and system model (i.e. equation 2.39) and their corresponding stochastic models.

$$x_k = \Phi_{k-1} x_{k-1} + w_{k-1} \tag{2.38}$$

$$z_k = H_k x_k + v_k \tag{2.39}$$

where x_k , x_{k-1} are the state vectors at epoch k and $k-1$, respectively; Φ_{k-1} is the transition matrix moving the state at the previous epoch k to the current epoch $k-1$; z_k is the measurement vector; H_k is the design matrix, w_k and v_k are independent variables representing state and measurement noise, respectively. Following a normal probability distribution for w_k and v_k (i.e. equation 2.40):

$$w_{k-1} \sim N\left(0, Q_{k-1}\right); \quad v_k \sim N(0, R_k) \tag{2.40}$$

where Q and R are the covariance matrix of system noise and measurement noise, respectively. The discrete Kalman filter consists of two important steps: the first one is prediction i.e. time update and the second one is measurement update i.e. correction. The prediction steps are shown by equations 2.41a and 2.41b while the prediction steps are given by equations 2.42a, 2.42b and 2.42c, respectively,

Prediction steps:

$$\hat{x}_k^- = \Phi_{k-1}\hat{x}_{k-1} \tag{2.41a}$$

$$P_k^- = \Phi_{k-1}P_{k-1}\Phi_{k-1}^T + Q_{k-1} \tag{2.41b}$$

Correction steps:

$$K_k = P_k H_k^T \left(H_k P_k^- H_k^T + R_k\right)^{-1} \tag{2.42a}$$

$$\hat{x}_k = \hat{x}_k^- + K_k\left(z_k - H_k\hat{x}_k^-\right) \tag{2.42b}$$

$$P_k = \left(I - K_k H_k\right)P_k^- \tag{2.42c}$$

where $\hat{x}_k^-$ and $\hat{x}_k$ are predicted and corrected stated vectors, respectively. P_k and P_k^- are predicted and corrected covariance matrix of the state and K_k is a gain matrix. The diagram of the working principle for the KF algorithm, used in the traditional PPP, is given in Figure 2.7.

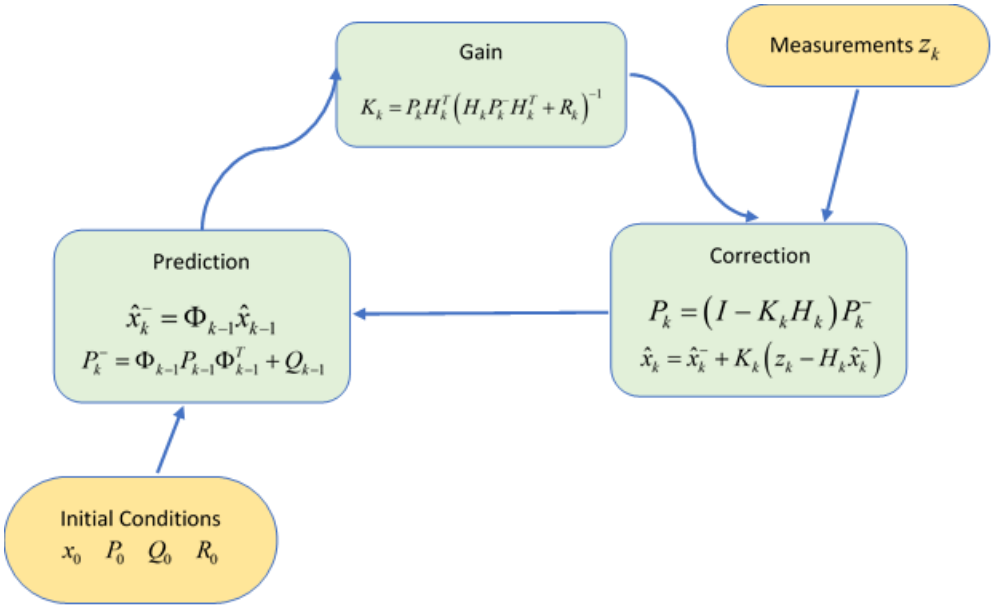

Figure 2.7 : Kalman Filter diagram used in the traditional PPP solution.

The principle of KF can be summarized as the weighted least squares (WLS) solution that improved with the prediction of the estimates. The first step must be identifying the problem and its related model, from which the physical model, state transmission matrix and the process noise matrix, are derived. For example, for a zenith tropospheric total delay, these matrices are derived from tropospheric delay equations of both ZHD and ZWD.

The linear observation model of PPP can be solved using a KF by specifying coordinates as constant parameters (i.e., fixed receiver), clock offset as white noise (i.e. no correlation between epochs) parameters with zero mean and ZWDs as random-walk estimates. Carrier phase biases, which remain constant along continuous arcs, are modeled as a white noise during cycle slips. Under these conditions, the initial state vector, transition and the process noise matrices can be determined. The procedure followed for the PPP is as an ambiguity float PPP solution where the ambiguity parameters are estimated as real values. An example showing the working principle of KF in PPP code based positioning is illustrated in Appendix A.

2.4 PPP Services

The International GNSS Service (IGS), formerly the International GPS Service was formally established by the International Association of Geodesy (IAG) in 1993 and has been sharing GNSS data and products since January 1994. The IGS consists of more than 200 worldwide agencies, universities and research institutes in more than 100 countries that gathering resources and permanent GNSS station data to generate precise products such as satellite orbits and clock solutions. The IGS offers highest quality data and products as the standard for GNSS to support Earth science research, applications and education. In addition, the IGS contributes to the maintenance and improvement of the International Terrestrial Reference Frame (ITRF) by monitoring tectonic movements, sea-level variations, and precise time transfer applications. The primary mission of the International GNSS Service, as stated in the organization's 2013-2016 Strategic Plan is:

> "Establish IGS as the world benchmark for GNSS products and services with leading-edge expertise and resources; and the development, integration, and evolution of services and performance to meet user needs. Ensure that the IGS plays an expert advisory role on GNSS matters through expertise and policy advocacy. Maintain the highest level of governance of the

IGS, and exercise funding development needed to maintain its infrastructure and operation" (Strategic Plan 2013-2016, 2012).

In order to achieve this goal, the IGS uses key components: an international network of over 505 continuously operating dual-frequency GNSS stations as illustrated in Figure 2.8, in addition to regional data centers, global data centers, analysis centers, and a number of associate or regional analysis centers.

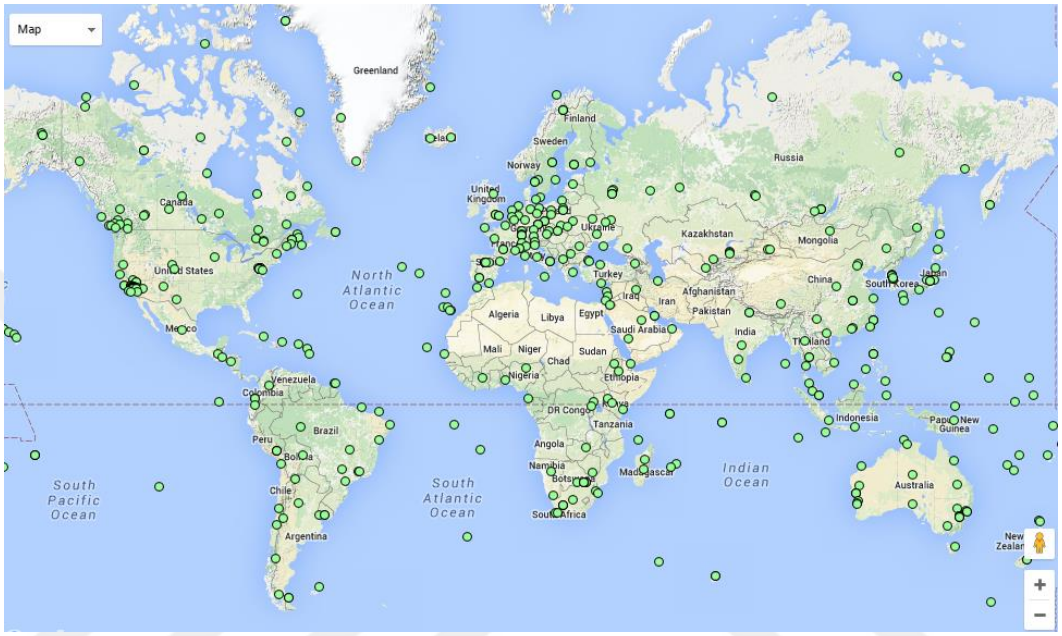

Figure 2.8 : IGS Tracking Network Map (More than 505 stations – green dots) retrieved from IGS web page (Url-1).

The Central Bureau for the service is located at the Jet Propulsion Laboratory, which maintains the Central Bureau Information System (CBIS) and ensures access to IGS products and information. The IGS data are available on the Internet free of charge and it supports of data sets of sufficient accuracy to carry out a wide range of geodetic and multidisciplinary research and applications. Some of the derived products from the IGS dataset are listed below (Strategic Plan 2013-2016, 2012):

- GNSS satellite ephemerides,
- Earth rotation parameters,
- Global tracking station coordinates and velocities,
- Satellite and IGS tracking station clock information,
- Zenith tropospheric path delay estimates,
- Global ionospheric maps.

In addition to the satellite ephemerides and clocks, the IGS also provides raw GNSS observation measurements in Receiver Independent EXchange (RINEX) format. Data from the permanent, continuously operating, dual frequency receivers are collected in a raw format and archived in RT, near RT, high rate, hourly or daily in receiver and software independent exchange formats (i.e., RINEX and SINEX, respectively) at four Global Data Centers, six Regional Data Centers and 17 Operational Data Centers. IGS ACs designate the fundamentals and standards of producing IGS data and products. Using a global IGS network tracking data the ACs produce and disseminate high-quality products such as precise satellite orbits, site and satellite clock information, Earth Rotation Parameters (EOP) and atmosphere related products for both PP and RT GNSS applications. There are currently 12 ACs developing the IGS combined products:

- Center for Orbit Determination in Europe, (Astronomical Institute of the University of Bern – AIUB), Switzerland (CODE),
- European Space Operations Center, ESA, Germany (ESOC),
- Groupe de Recherche de Géodésie Spatiale (GRGS), France,
- GFZ, Germany, NASA JPL, USA,
- National Oceanic and Atmospheric Administration (NOAA) / National Geodetic Survey (NGS),
- Natural Resources Canada, Canada (NRCan),
- Scripps Institution of Oceanography, USA (SIO),
- U.S. Naval Observatory, USA (USNO),
- Massachusetts Institute of Technology, USA (MIT),
- Geodetic Observatory Pecny, Czechia (GOP-RIGTC) and
- Wuhan University, China.

IGS components are produced by IGS Working Groups that working on several topics and meet basic requirements of IGS infrastructure. Today, the IGS provides daily URP, IGR and Final GNSS orbit and clock information. URP orbits with an accuracy of about 3 cm are available in RT whereas PP orbits both Rapid and Final have a delay of approximately one day and 13 days, respectively. The accuracy of the estimated PP orbits is better than 3 cm. The precise ephemerides in ASCII format (i.e., standard product - sp3) includes satellite positions and velocities at a sampling rate of 15 minutes. The positions and velocities between the sampling rates generally derived by

applying a low order polynomial interpolation. In addition to the satellite orbits and clocks, the IGS shares the raw tracking data, EOPs, GIMs and ZPDs through File Transfer Protocol (FTP) services of the IGS. Tables 2.3, 2.4, 2.5 and 2.6 present latest IGS products including broadcast orbits, precise orbits and clocks, GLONASS ephemeris data, final ZPDs, GIMs, and EOPs. All products are classified considering accuracy, latency and sampling intervals.

Table 2.3 : The IGS satellite ephemerides and satellite/station clocks with different accuracy and latency rates.

TYPE		Accuracy	Latency	Updates	Sample Interval
Broadcast	Orbits	~100 cm	Real Time	--	Daily
	Sat. clocks	~5 ns RMS ~2.5 ns S.Dev			
Ultra-Rapid (predicted)	Orbits	~5 cm	Real Time	at 03, 09, 15, 21 UTC	15 min
	Sat. clocks	~3 ns RMS ~1.5 ns S.Dev			
Ultra-Rapid (observed)	Orbits	~3 cm	3 – 9 hours	at 03, 09, 15, 21 UTC	15 min
	Sat. clocks	~150 ps RMS ~50 ps S.Dev			
Rapid	Orbits	~2.5 cm	17 – 41 hours	at 17 UTC daily	15 min
	Sat. & Stn. clk	~75 ps RMS ~25 ps S.Dev			5 min
Final	Orbits	~2.5 cm	12 - 18 days	Every Thursday	15 min
	Sat. & Stn. clk	~75 ps RMS ~20 ps S.Dev			Sat: 30s Stn: 5 min

Table 2.4 : The GLONASS satellite ephemerides.

Type	Accuracy	Latency	Updates	Sample Interval
Final	~3 cm	12 – 18 days	Every Thursday	15 min

Table 2.5 : The IGS atmospheric products.

Type	Accuracy	Latency	Updates	Sample Interval
Zenit Path Delay	4 mm	< 4 weeks	Daily	5 minutes
Final Ionospheric TEC Grid	2 – 8 TECU	~11 days	Weekly	2 hours 5° (lon) x 2.5° (lat)
Rapid Ionospheric TEC Grid	2 – 9 TECU	< 24 hours	Daily	2 hours 5 ° (lon) x 2.5 ° (lat)

Table 2.6 : The IGS Earth Rotation Parameters.

Type	Accuracy		Latency	Updates	Sample Interval
Ultra-Rapid (predicted)	PM	~200 µas	Real Time	at 03, 09, 15, 21 UTC	daily integrations at 00, 06 12, 18 UTC
	PM rate	~300 µas/day			
	LOD	~50 µs			
Ultra-Rapid (observed)	PM	~50 µas	3 – 9 hours	at 03, 09, 15, 21 UTC	daily integrations at 00, 06 12, 18 UTC
	PM rate	~250 µas/day			
	LOD	~10 µs			
Rapid	PM	~40 µas	17 – 41 hours	at 17 UTC daily	daily integrations at 12 UTC
	PM rate	~200 µas/day			
	LOD	~10 µs			
Final	PM	~30 µas	11 – 17 days	Every Wednesday	daily integrations at 12 UTC
	PM rate	~150 µas/day			
	LOD	~10 µs			

Since 1992, the AIUB operates the CODE (Dach et al, 2015) that is one of the global AC for IGS and European Permanent Network (EPN) and associated AC to the International Satellite Laser Ranging Service (ISLR). It is a consortium of AIUB, the Swiss Federal Office of Topography (swisstopo, Wabern, Switzerland), the BKG, and the Technische Universität München (TUM, Germany). CODE publishes precise satellite orbits, clocks and station coordinates, EOPs, GIMs and ZPDs, that all of them computed through daily processing of observation data and products by the Bernese Processing Engine (BPE). The Orbit products and other parameters are available via FTP address of the center (i.e., see Appendix B).

2.4.1 PPP software

There are several software products, having static and kinematic PPP processing ability, have been developed by universities, government agencies, and private industries. Some of these PPP software processing undifferenced code and phase observations are listed below:

- GIPSY-OASIS, or GIPSY (Zumberge et al, 1997), the GNSS-Inferred Positioning System and Orbit Analysis Simulation Software package, developed by the JPL, and maintained by Near Earth Tracking Applications and Systems groups.
- Bernese Software (Dach et al, 2015) which is a GPS/GLONASS PP package

developed by AIUB.

- ESA/ Universidad Politècnica de Catalunya - UPC GNSS-Lab Tool suite (Sanz et al. 2012) is an interactive software package for GNSS data processing and analysis, including Precise Positioning.
- Navigation Package for Earth Observation Satellites (NAPEOS) is another software system for GNSS data processing and Multi-satellite high precision orbit determination, developed and maintained by the European Space Operations Centre (ESOC) of the European Space Agency (ESA).

Furthermore, there are several PPP services sites available online for free. Based on a client – server architecture, when a client submits the RINEX observation files on these sites, the data will be processed by the server side and the results will be sent back to the user via mail or FTP services.

Some of the online processing software supporting PPP solution described below:

- GPS Analysis and Positioning Software (GAPS) (Url-2) developed by UNB is available as an online post-processing engine conducting static as well as kinematic processing. The RINEX 2.10 or 2.11 formats observation files are necessary for data analyzing and IGS orbits and clocks are extracted automatically from IGS global data centers.
- magicGNSS (Url-3) is a GNSS Orbit Determination and Precise Positioning software that processes static and kinematic GPS and GLONASS real-time data in the RINEX format and only dual-frequency PPP solutions are supported. Real-time orbits and clocks needed by the software generated internally. Rapid and Final orbits can be used too if they are available.
- Automatic Precise Positioning Service (APPS) uses GIPSY codes and solutions. APPS supports input in RINEX 2.10, RINEX 2.11 files and GIPSY TDP files to process static and kinematic GPS real-time data.
- NRCan PPP (Url-4) is a Global GPS post-processing service, developed by Natural Resources Canada. NRCan provides post-processed position estimates from GPS observation files submitted by the user in RINEX format. Precise position estimates are referred to the North American Datum of 1983 (NAD83) as well as the International Terrestrial Reference Frame (ITRF).

The main advantage of the PPP is being an independent solution that it does not need any reference stations with known coordinates as in relative solutions. On the other

hand, a convergence, i.e. a minimum time required for estimated parameters to reach a consistent solution, is typically between 30 minutes and a couple of hours that is impracticable for real-time PPP operations. Ambiguities and quality of satellite orbits and clocks are the main parameters having a strong influence on convergence. GNSS modernization with the development of new satellites (e.g. GALILEO, BEIDOU, QZSS etc.) and a growing number of signals will improve the whole system. The availability of new free signals on new frequencies enables new developments in ambiguity resolution studies.

PPP solution in real-time is possible if precise reference satellite orbits and clocks are available in real time. There are ongoing studies in development phase, both for real-time IGS products and for RT PPP. It should be noted that no standard for Real-Time PPP has been defined yet, but standardization efforts are being carried by the Radio Technical Commission for Maritime Services (RTCM) Special committee 104. Although the limiting factor in real-time operations is clearly the availability of precise orbits and clock products, IGS Real-time Service (RTS) extends the capability of GNSS studies by supporting applications demanding real-time access to precise orbits and clocks.

The Multi-GNSS Experiment and Pilot Project (MGEX) is established by the IGS to track and analyze all available GNSS signals coming from satellites including BeiDou, Galileo, QZSS, as well as new generation GPS and GLONASS satellites and Space Based Augmentation Systems (SBASs). Today, a global network of MGEX has grown to almost 170 IGS reference stations and the increase in the number of stations and additional satellites not only enhances navigation applications but also atmosphere monitoring applications (ionosphere and troposphere) that dense and homogeneous GNSS signals passing through the atmosphere can interpret the lower and upper atmospheric layers of both regional and global areas. MGEX raw RINEX observations, precise orbits and clock products, DCBs, and real time products are available through MGEX analysis centers (e.g., Centre National d'Etudes Spatiales - CNES, GFZ, CODE, TUM and Wuhan).

3. ERROR SOURCES AND MITIGATION METHODS IN PPP

3.1 Introduction

Unlike in differential solution, common errors do not cancel in PPP and thus, all errors caused by space segment, signal propagation, receiver and geophysical environment need to be mitigated. The mitigation process can be performed by modeling, estimation or through linear combinations. Most of the errors as geophysical errors, antenna phase centers offset and variations and relativistic effects can be mitigated to some extent through modeling. The tropospheric path delay and receiver clock error are usually estimated from data analysis, while the effects of the ionospheric delay and phase ambiguity are reduced by observations of linear combinations. This chapter introduces a brief description of these error sources as well as the mitigation strategies.

3.2 Site Displacement Effects

The receiver station coordinates are affected by geophysical influences such as tectonic motions, solid earth tides, ocean tides and atmospheric tidal and non-tidal effects and all must be accounted for when a high positioning accuracy is requested. Although in the ITRF frame these effects are often neglected (i.e., tide-free), the station displacement effects must be considered when conducting a PPP analysis.

3.2.1 Tectonic motions

Tectonic plate motions have been the topic of geodetic and geophysical research for many years. The displacement of tectonic plates, which causes station coordinates to change, can be monitored by different techniques such as Very Long Baseline Interferometry (VLBI), Satellite Laser Ranging (SLR), and GNSS. The movement can be compensated by propagating the reference epoch coordinates to the observation epoch if the vectors of plate tectonic displacements, namely site velocity vectors are available. The velocities of IGS reference stations may be obtained either from IGS database or can be calculated from a plate motion model, like NNR-NUVEL-1/A (DeMets et al, 1994) that is consistent with IERS conventions (Petit and Luzum, 2010).

Tectonic plate motions are generally detected by using regional or global tectonic networks, and tracking time series of long period site observations.

3.2.2 Solid earth tides

The solid Earth tides are induced by the gravitational attraction and temporal variations of the external bodies such as the Sun and the Moon. With gravitational effects of external bodies, the station shows permanent, periodic and episodic movements. The displacements at station coordinates can be modeled by a spherical harmonics expansion defined by the Love (h_{mn}) and Shida (l_{mn}) numbers (McCarthy and Petit, 2004). According to IERS Conventions the simplified two steps solution model (i.e., degree 2 and 3 tides) is capable of modeling the solid earth's tide with an accuracy of few mm. The displacement vector due to degree 2 tides in ECEF Cartesian coordinates given by the following expression:

$$\Delta\bar{r} = \sum_{j=2}^{3} \frac{GM_j R_E^4}{GM_E R_j^3} \left\{ h_2 \hat{r} \left(\frac{3}{2} (\hat{R}_j \bullet \hat{r})^2 - \frac{1}{2} \right) + 3l_2 \left(\hat{R}_j \bullet \hat{r} \right) \left[\hat{R}_j - \left(\hat{R}_j \bullet \hat{r} \right) \hat{r} \right] \right\} \qquad (3.1)$$

where

$\Delta\bar{r}$ is a site displacement vector in ECEF Cartesian coordinates,

GM_j is the gravitational parameter of the Moon,

GM_E is the gravitational parameter of the Earth,

$\hat{R}_j, R_j$ are unit vectors from the geo-center to the Moon or the Sun and magnitude of that vector,

R_E is the equatorial radius of the Earth (R_E=6378136.6 m),

$\hat{r}, r$ are unit vectors from the geo-center to the station and the magnitude of the vector,

h_2, l_2 are nominal degree 2 Love (0.6078) and Shida (0.0847) numbers respectively.

From the equation 3.1 the displacement is the sum of the displacement excited by the moon and displacement excited by the sun. The nominal values for Love and Shida numbers have to be corrected for the latitude dependency by using equations 3.2a and 3.2b:

$$h_2 = 0.6078 - 0.0006\left[\left(3\sin^2\phi - 1\right)/2\right] \tag{3.2a}$$

$$l_2 = 0.0847 - 0.0002\left[\left(3\sin^2\phi - 1\right)/2\right] \tag{3.2b}$$

The refinement due to the degree 3 tides is given by McCarthy and Petit, (2004);

$$\Delta\vec{r} = \sum_{j=2}^{3} \frac{GM_j R_E^5}{GM_E R_j^4} \left\{ \begin{array}{l} h_3\hat{r}\left(\frac{5}{2}(\hat{R}_j \bullet \hat{r})^3 - \frac{3}{2}\left(\hat{R}_j \bullet \hat{r}\right)\right) + \\ l_3\left(\frac{15}{2}\left(\hat{R}_j \bullet \hat{r}\right)^2 - \frac{3}{2}\right)\left[\hat{R}_j - \left(\hat{R}_j \bullet \hat{r}\right)\hat{r}\right] \end{array} \right\} \tag{3.3}$$

where h_3 = 0.292 and l_3 = 0.015. In the equation 3.3, only the Moon's contribution $(j = 2)$ is considered since the Sun's contribution (j = 3) is almost negligible. In practice, the Moon's contribution to the radial displacement is up to 1.7 mm, while it does not exceed 0.02 m in transversal components. The solid Earth tides must be taken into account in PPP solution because its effect can reach up to decimeter level in the total range as depicted in Figure. 3.1.

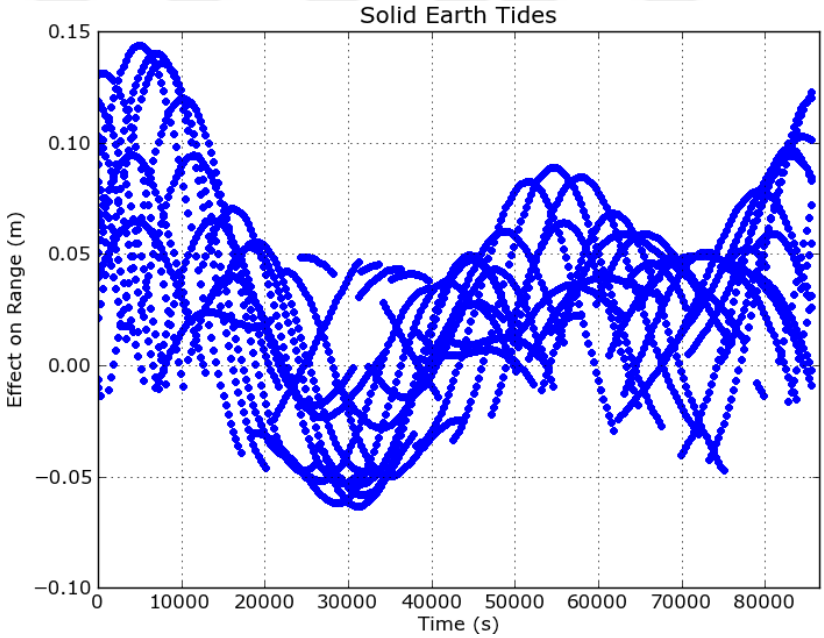

Figure 3.1 : Signal range change due to Solid Earth Tides' effect.

3.2.3 Ocean tidal loading

The ocean loading tides are the crustal deformations of the sea floor and coastal land that results from the redistribution of mass due to ocean tides. The ocean loading is induced by the temporal variations of the ocean mass distribution and it does not

include a permanent tide. In addition, it is more localized and almost an order of magnitude smaller than the solid earth tides. It is formulated in equation 3.4 as:

$$\Delta R_{OCN} = \sum f_j A_{cj} \cos\left(w_j t + x_j + u_j - \Phi_{cj}\right) \tag{3.4}$$

where:

ΔR_{OCN} is the site displacement vector in (radial, west, south) coordinates,

j represents 11 tidal waves: $M_2, S_2, N_2, K_2, K_1, O_1, P_1, Q_1, M_f, M_m, S_{sa}$,

f_j , u_j depend on the longitude of the lunar node,

w_j is the tidal angular velocity at time t = 0h,

x_j is an astronomical argument at time t = 0h,

A_{cj} is a station-specific amplitude,

Φ_{cj} is a station-specific phase.

For stations that are located far from ocean, static positioning over 24-hour period, the ocean loading effects can be safely ignored (Kouba and Heroux, 2001). For stations that located close to a coastline and for shorter observation campaign, i.e. < 24hour, this effect must be taken into account. The magnitude of the surface displacement caused by ocean tides can reach up to 5 cm in vertical and 2 cm in horizontal and if it not modeled correctly, the errors caused from displacements will be mapped into the tropospheric path delay and receiver clock corrections. Figure 3.2 shows a sample of ocean loading ASCII file for the IGS stations FFMJ and GANP that extracted from the Finite Element Solution 2004 (FES2004) file including all IGS core sites.

```
  FFMJ
$$ Complete FES2004
$$ OLCMC/ OLFG, H.-G. Scherneck, Onsala Space Observatory 2015-Oct- 3
$$ FFMJ,                     RADI TANG  lon/lat:    8.6650   50.0906  178.210
  .00602 .00214 .00141 .00051 .00125 .00162 .00042 .00038 .00032 .00022 .00024
  .00254 .00041 .00063 .00007 .00211 .00120 .00068 .00023 .00003 .00003 .00001
  .00182 .00032 .00040 .00013 .00358 .00241 .00119 .00043 .00041 .00026 .00021
   -87.8  -59.4 -106.8  -70.6  139.4  138.8  139.1  130.3   86.0   52.7    7.4
   119.0  154.3   96.7  162.1   74.3   40.5   74.2    4.6  -72.2  162.5   37.5
    80.9  119.9   72.2   79.2  -99.1 -113.5  -99.3 -129.3   67.6   31.3    7.0
$$
  GANP
$$ Complete FES2004
$$ OLCMC/ OLFG, H.-G. Scherneck, Onsala Space Observatory 2015-Oct- 3
$$ GANP,                     RADI TANG  lon/lat:   20.3229   49.0347  746.000
  .00435 .00159 .00107 .00038 .00182 .00173 .00060 .00038 .00029 .00017 .00018
  .00171 .00021 .00044 .00004 .00174 .00092 .00056 .00016 .00006 .00004 .00004
  .00120 .00022 .00025 .00009 .00383 .00247 .00127 .00042 .00038 .00024 .00019
   -94.3  -67.7 -110.7  -80.1  145.8  143.2  145.4  138.8  105.0   64.1    8.8
   125.3 -160.4  101.1 -130.9   86.8   52.8   87.4   12.1  117.5   97.4   14.7
    79.4  140.8   73.8   80.8  -97.9 -113.5  -98.1 -129.7   70.1   30.7    7.1
```

Figure 3.2 : Ocean tidal loading file derived from FES2004.BLQ.

The conventional IERS models to compute ocean loading displacements do not include the motion of the origin (center of mass correction: CMC) of the coordinate system. The CMC data is needed when transferring satellite positions from the Earth-fixed frame to the celestial frame to compute satellite positions with respect to the center of mass (CoM). Users looking for solutions with high accuracy can use the web service at http://holt.oso.chalmers.se/loading/ to get a table of the ocean loading coefficients for requested stations, for which the displacements are given positive in Up, South and West directions.

3.2.4 Atmospheric tidal loading

The atmospheric mass above the Earth's surface causes a load on the surface and additional site displacement due to differential heating between different latitudinal areas and variations of the low and high air pressures with respect to the reference pressure (surface pressure anomaly). Moreover, surface pressure variations may also change the Earth's rotational motion and gravity potential. The surface pressure anomalies show strong variations at mid-latitudes where atmospheric pressure loading (APL) is stronger than other regions and can reach up to more than 2 cm both vertically and horizontally as expressed in Figure 3.3.

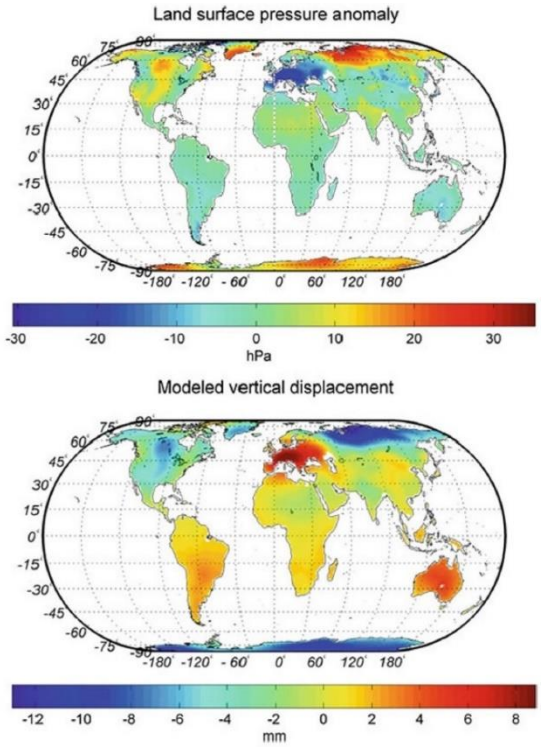

Figure 3.3 : Spatial variations of pressure anomaly and vertical displacements at 00 UTC on January 1, 2010 (Wijaya et al, 2013, p.139).

The atmospheric tidal loading expressed by the dominant and tidal signals for which amplitudes can reach up to 2.0 mm in equatorial regions. According to the IERS conventions 2010 (Petit and Luzum 2010), there are two different techniques to model the APL effect: The first approach is the geophysical model using spherical harmonics and Green's function computed from Load Love Numbers to represent the global convolution of the load effect. The second one is the empirical model using site-specific actual deformations obtained from geodetic measurements.

3.2.5 Non-tidal loading

The non-tidal effects such as atmospheric non-tidal, ocean non-tidal, and hydrostatic pressure loading can cause to several centimeters displacements in the site coordinates. The atmospheric non-tidal effect is more dominant for inland sites while ocean non-tidal effects occur in coastal areas. The total loading displacement of the atmosphere is equal to the sum of non-tidal displacement and the harmonic model of the tidal loading displacements. As recommended by the IERS conventions (Petit and Luzum 2010), the displacement corrections related to non-tidal loading shall not be applied to any product because of the non-existence of standard procedure for handling these effects.

3.2.6 Polar tides

Polar tides are periodical deformations caused by the changes of the Earth's spin axis with respect to the Earth's crust. The polar tide effects should be modeled for long observations more than 2-3 months. The station displacements due to the polar tides can reach about 7 mm in the horizontal direction and 25 mm in the height direction (Kouba, 2009). By employing the IERS 2010 (Petit and Luzum 2010) conventions and Love numbers (h=0.6027; l=0.0836), the approximate corrections of the latitudinal and the radial components can be given in equation 3.5 as:

$$\begin{aligned}
\Delta\phi &= -9\cos 2\phi\left[\left(X_P - \bar{X}_P\right)\cos\lambda - \left(Y_P - \bar{Y}_P\right)\sin\lambda\right] \\
\Delta\lambda &= 9\sin\phi\left[\left(X_P - \bar{X}_P\right)\sin\lambda - \left(Y_P - \bar{Y}_P\right)\cos\lambda\right] \\
\Delta h &= -32\sin 2\phi\left[\left(X_P - \bar{X}_P\right)\cos\lambda - \left(Y_P - \bar{Y}_P\right)\sin\lambda\right]
\end{aligned} \tag{3.5}$$

The pole displacements ($X_P - \bar{X}_P$, $Y_P - \bar{Y}_P$) can be found at FTP site of the Paris Observatory IERS Centers (Url-5).

3.3 Carrier Phase Wind-up

GNSS phase signals are right-hand circularly polarized (RCP) and therefore one small change in the relative orientation between the receiver antenna and the satellite antenna interpreted as a change in the line of sight distance. For observations with static receivers, the phase wind-up effect is due to the satellite's orbital motion. The satellite rotates slowly in order to adjust the solar panels towards the sun and when the antenna orientation changes, the direction of the electric field and measured phase at the receiver will change. Phase wind-up error can reach a phase cycle. In Figure 3.4, the effect of correcting the carrier wind-up for the PPP kinematic solution at the IGS site GANP is illustrated where the total range changes vary in the level of cm.

The phase wind up error can be mitigated through relative baseline solutions. However, this error is quite important for PPP solutions and it can be computed by using formulation by Wu et al. (1993) below:

$$\delta\phi = sign(\xi)\cos^{-1}\left(\vec{D}'\bullet\vec{D}/\left(\left|\vec{D}'\right|\left|\vec{D}\right|\right)\right) \tag{3.6}$$

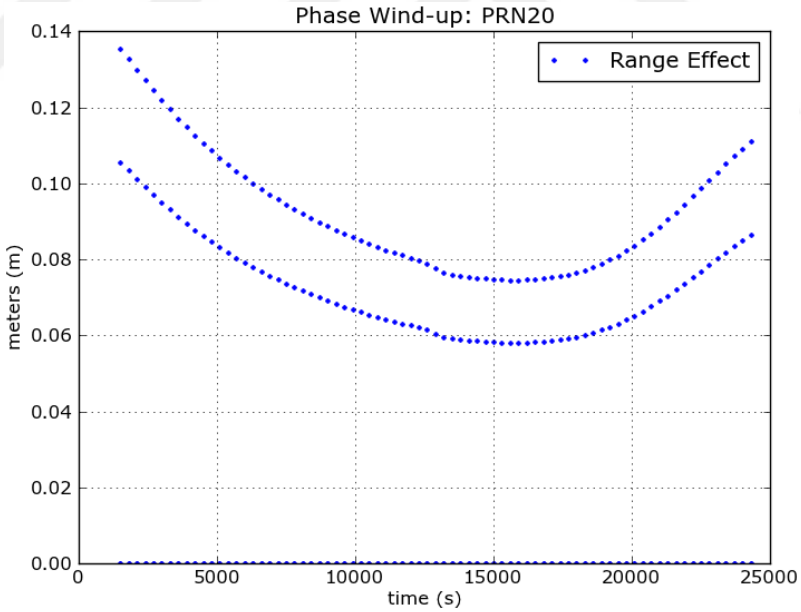

Figure 3.4 : Carrier phase wind-up effect on the total range for the GANP IGS site and PRN: 20.

Where $\xi = \vec{k}\bullet\left(\vec{D}'\bullet\vec{D}\right)$ and $\vec{k}$ is the unit vector from satellite to receiver; $\vec{D}'$, $\vec{D}$ are effective dipole vectors of the receiver and the transmitter computed from the unit vectors of the satellite's ($\vec{a}',\vec{b}',\vec{c}'$) and the receiver's ($\vec{a},\vec{b},\vec{c}$) coordinate system as given in equation 3.7:

$$\vec{D}' = \vec{a}' - \vec{k}\left(\vec{k}\cdot\vec{a}'\right) - \vec{k}\times\vec{b}'$$
$$\vec{D} = \vec{a} - \vec{k}\left(\vec{k}\cdot\vec{a}\right) - \vec{k}\times\vec{b} \qquad (3.7)$$

3.4 Relativistic Clock Correction

GNSS satellites and control stations benefit from highly stable and accurate atomic clocks to provide global positioning and time transfer. The time synchronization between the satellites and receivers is utmost important for PPP. However, due to the non-negligible gravitational potential of the Earth, the relative speed differences between the satellites and the receivers and the Earth rotation effect, the clocks experience frequency shifts that need to be mitigated by relativistic corrections Δt_{rel} The relativistic correction can be divided into a constant and periodic parts as expressed in equation 3.8:

$$\Delta t_{rel} = \Delta t_{constant} + \Delta t_{periodic} \qquad (3.8)$$

The constant part of the correction arises from two factors; the gravitational field of the Earth affecting the satellite, thus, the satellite clock runs faster than the receiver clock (general relativity) and the satellite speed that a moving satellite clock tends to be slower than at one receiver at rest on the ground (i.e., special relativity). The frequency shift from the nominal frequency, i.e. f_0= 10.23 MHz, is produced by these effects is given in equations 3.9 and 3.10:

$$\frac{f'_0 - f_0}{f_0} = \frac{\Delta f}{f_0} = \frac{1}{2}\left(\frac{v}{c}\right)^2 + \frac{\Delta U}{c^2} \simeq -446.47\cdot10^{-12}\,Hz \qquad (3.9)$$

$$\Delta f = 446.47\cdot10^{-12}\cdot f_0 = 4.57\cdot10^{-3}\,Hz \qquad (3.10)$$

where v is the satellite clock velocity and ΔU is the gravitational potential difference of the satellite orbit and the geoid. The f_0' is the frequency emitted from the satellite and the f_0 is the frequency (nominal) received at the observation site. It can be seen that the satellite's frequency would be increased by $4.57\cdot10^{-3}$ Hz and thus, the satellite clock run ≈ 38 μs / day faster than the receiver's clock. In order that the receiver gets the nominal frequency, the satellite clock is corrected by decreasing the nominal oscillating frequency of the satellite by an offset Δf=$4.57\cdot10^{-3}$ Hz. This correction is done in the laboratory during modifying satellite clock oscillator frequency. As a

result, the satellite must use $f_0^{'}$ = 10.22999999543 MHz to mitigate the effects of general and special relativity. The eccentricity of each satellite orbit causes the periodic clock error that shows variation with respect to satellite's position in its orbital plane (Ashby, 2003). This correction must be applied in PPP processing (equation 3.11).

$$\Delta t_{ecc} = \frac{-2\vec{r}^{\,sat} \cdot \vec{v}^{\,sat}}{c^2} \tag{3.11}$$

where $\vec{r}^{\,sat}$ and $\vec{v}^{\,sat}$ are the satellite's radius vector and the velocity vector, respectively. Another relativistic correction is the Sagnac effect caused by the Earth rotation and receiver on the rotating Earth's surface during signal's propagation from satellite to the ground (Conley et al, 2006, p.301). The Sagnac correction term expressed by Ashby and Spilker (1996, p.623):

$$\delta t = \frac{\vec{v} \cdot (\vec{r}_R - \vec{r}_s)}{c^2} \tag{3.12}$$

where $\vec{v}$ represents the geocentric velocity vector of the receiver; $\vec{r}_R$ and $\vec{r}_S$ are geocentric vectors of the receiver and the satellite, respectively. Figure 3.5 shows the significance of the relativistic correction on the positioning. The range errors up to 30 meters and the vertical error up to 15 meters can be observed when avoiding relativistic corrections. These results were taken from the kinematic PPP solution performed on the IGS site FFMJ for day of year 148 in, 2013.

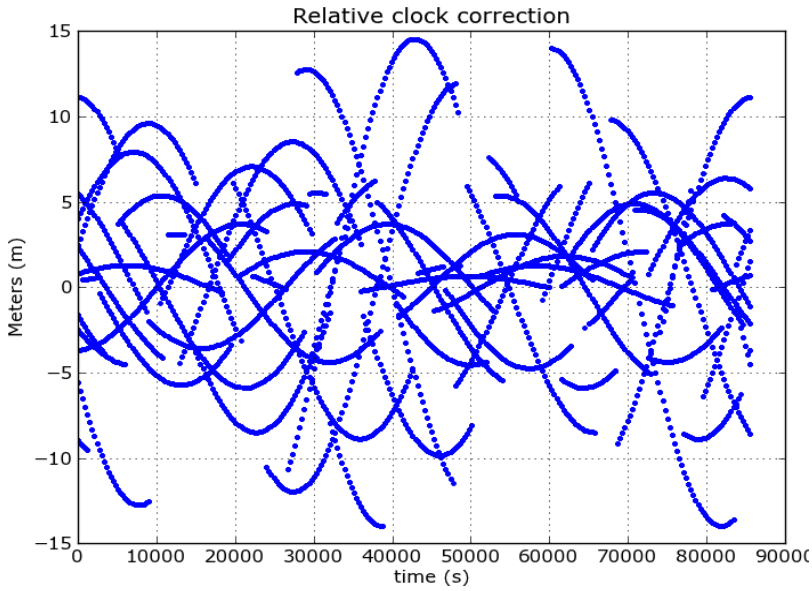

Figure 3.5 : Variation in the range due to the relativistic clock correction.

3.5 Multipath

The multipath effect occurs when a satellite-emitted signal arrives at the receiver by more than one path due to reflective surfaces around the receiver. As a result, the received signals have relative phase offsets and the phase differences that increase the measured distance and deteriorate the accuracy. The multipath affects both code and phase measurements and it is a frequency and elevation angle dependent. The signals received from low elevations are more susceptible to multipath than higher elevation observations. The magnitude of range error can reach up to several meters for code (i.e., theoretically max = 1.5 times the chip wavelength) and up to a maximum of about 5 cm (i.e. the quarter of the wavelength) for carrier phase measurements. The multipath error changes with environmental conditions and thus, there is no absolute way to eliminate it from the observations. The effect of error can be removed by selection of receiver antennas away from reflecting surfaces and reduce the effects of low elevation observations by improving antenna directivity and using choke-ring type antennas. The elevation-dependent weighting of observations can be defined during data processing in order to mitigate the effects of the multipath as well as tropospheric path delays. The code multipath effects for low elevation angle observations are depicted in Figure 3.6.

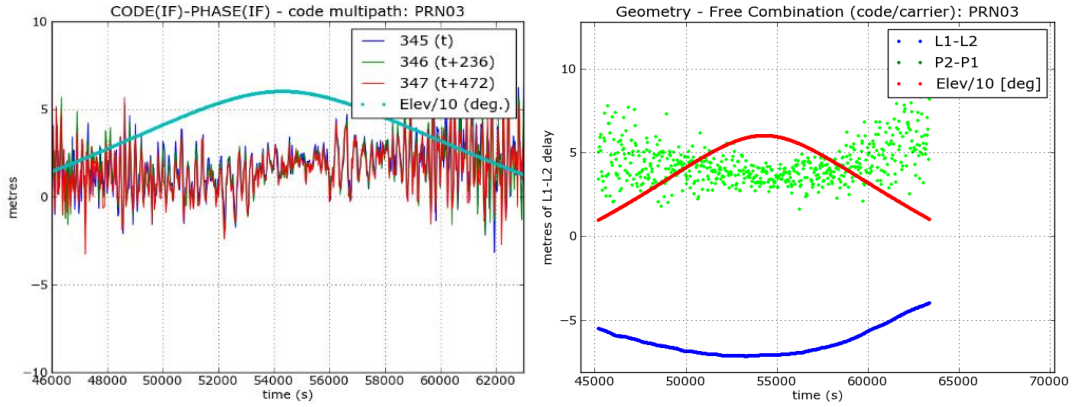

Figure 3.6 : Ionosphere free code (L_3) – phase (L_3) (left) and geometry-free (L_4) linear combinations (right).

In the left plot, representing the code multipath and noise effect, the difference of ionosphere-free linear combinations of code and phase measurements (P_3-L_3) are plotted for three consecutive sidereal days for the satellite PRN03. In the right plot, on the other hand, the multipath and noise effect of geometry-free phase and code combinations (L_1-L_2 and P_1-P_2) are depicted for the same satellite and for the day of

the year 345, in 2013. The large multipath and noise effects for low elevations are obvious for low elevations.

3.6 Antenna Phase Center Offsets and Variations

Positioning in GNSS refers to the measurements from the satellite transmitting antenna to the electrical phase center of the receiving antenna. Usually, this phase center is not a physical point, thus, it is oriented with respect to geometrical point antenna reference point (ARP) that the intersection of the vertical antenna axis with the lowest part of the antenna.

The actual electrical antenna phase center depends on elevation, azimuth, intensity and frequency of the signal and it is a function of antenna phase pattern known as phase center variations (PCVs). Since each signal defines its own phase center varying with azimuth and frequency, a mean phase center must be determined for each antenna and signal type. The difference between the ARP and the mean electrical phase center of the signal represents a phase center offset (PCO), which must be provided by the manufacturer in the 3D coordinate system.

The total antenna phase center correction consists of both PCO and PCV effects. In addition, radomes that are used at many stations for protection from environmental effects will have an impact on the antenna phase center variations. The phase center offset and variations are illustrated in Figure 3.7.

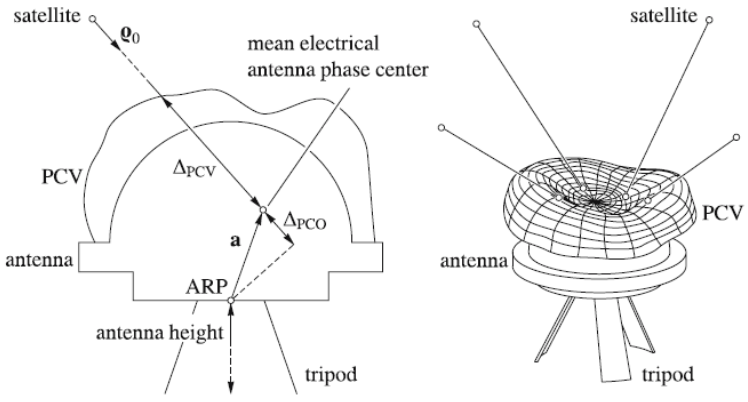

Figure 3.7 : Antenna phase center offset variations and phase patterns for the receiver (Wellenhof et al, 2008).

For PPP observations, each antenna has to be calibrated. However, the variations are difficult to model and can reach up to centimeters in the horizontal and up to

decimeters in vertical directions (Mader, 1999). The variations have an influence on site height coordinate and tropospheric path delay estimate. Until November 5, 2006, the relative calibration model (i.e., IGS_01) was used by the IGS that the field measurements are used to determine the phase center offset and the phase center variation with respect to one chosen perfect reference antenna i.e. AOAD/M_T type antenna. Without azimuth dependency and omitted radome effect, the relative model only considers elevation dependent corrections. The location of the mean phase centers of the reference antenna are determined and used as an a priori value by the test antenna for the phase center determination. The offsets between the reference antenna phase center and the test antenna phase center are then combined and mean phase center offsets used as a reference to determine the elevation dependent phase pattern by using polynomial functions. This procedure is repeated for each frequency and as a result, the antenna phase center correction is determined with respect to reference antenna phase center position. Since GPS week 1400 (November 5, 2006), the IGS has migrated to an absolute antenna phase center model based on a robotic system developed by the University of Hannover and the company Geo++. The absolute means that the phase center offset and variations are determined without using a reference antenna. The new model is both azimuth and radome dependent (Dach et al, 2015). The total antenna phase center correction applied to the measured geometric distance is expressed as:

$$\Delta\phi(\alpha, \mathrm{z}) = \Delta\phi^{'}(\alpha, \mathrm{z}) + \Delta r \cdot \mathrm{e} \tag{3.13}$$

where α and z are azimuth and zenith angle of a tracked satellite from the receiver; Δr is the mean phase center offset with respect to antenna reference point ; e is the unit vector from the receiver to the satellite and $\Delta\phi^{'}(\alpha, \mathrm{z})$ is the azimuth and elevation angle dependent phase center variation function which may be defined by spherical harmonic function as proposed by Rothacher et al. (1995):

$$\Delta\phi^{'}(\alpha, \mathrm{z}) = \sum_{n=1}^{n_{\max}} \sum_{m=0}^{n} \tilde{P}_{nm}(\cos \mathrm{z})(\mathrm{a}_{nm} \cos \mathrm{m}\alpha + \mathrm{b}_{nm} \sin \mathrm{m}\alpha) \tag{3.14}$$

where $\tilde{P}_{nm}$ are Legendre's functions; a_{nm} and b_{nm} are the coefficients of the harmonic series that can be estimated by a least squares adjustment if there are sufficient measurements of PCVs. In addition to the spherical polynomial approach, a polygon model is also a viable option that based on piecewise linear function in elevation and

azimuth. As stated by Dach et al. (2015) the polygon model interpolates the PCVs by using ANTEX file that including gridded PCVs azimuth and elevation angles derived from the robotic system. The IGS has switched to the new absolute antenna model (i.e., IGS08 - igs08.atx) since GPS week 1632 and relative antenna phase center corrections are not supported anymore. The ANTEX file igs08.atx is prepared by the IGS from robot-calibrated results and contains absolute phase center corrections (offsets and variations) for satellite and receiver antennas that compatible with the IGS08/ITRF08 reference frame. Figure 3.8 illustrates an example of the effects of the satellite antenna phase center correction that the ionosphere-free kinematic PPP solution performed at the IGS station GANP (φ=49.034; λ=20.322) which mounted with TRIMBLE NETR9 receiver and TRM55971.00 type of antenna and tracking satellite with PRN number 16.

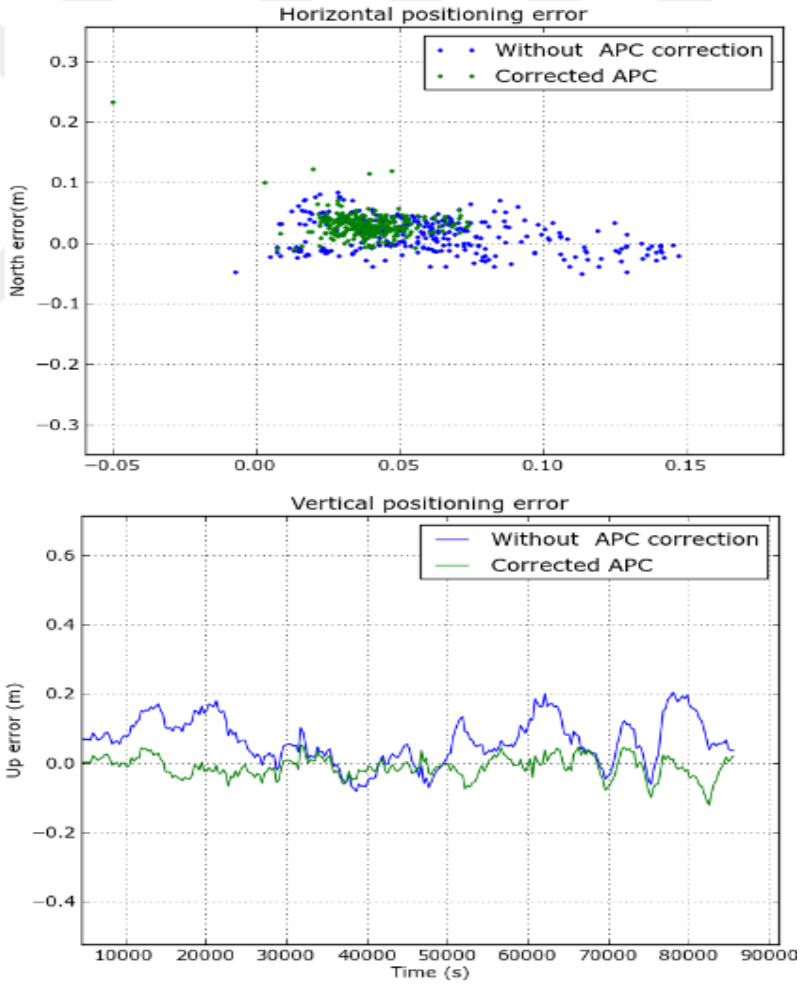

Figure 3.8 : Satellite antenna phase center corrections at the GANP station: Horizontal positioning error with and without satellite APC correction (top); Vertical positioning error with and without satellite APC correction (bottom).

The currently used model within the IGS can be found at FTP site of the IGS and designated as igs08_wwww.atx . The wwww indicates the GPS week of the last update. The relative phase center model (igs_01.atx) and the first absolute antenna phase center model igs_05.atx are not used anymore. Precise satellite coordinates and products published by the IGS refer to the mass center of the satellite, while the real-time broadcast messages and thereby, phase measurements refer to the satellites antenna phase center. Therefore, it is necessary to use phase center offset vector in order to relate the mass center and the phase center of the satellite antenna.

3.7 Instrumental Biases

Instrumental or hardware biases are significant error sources in a PPP processing and potential cause of these errors are satellite and receiver hardware (e.g., cables, antenna, filters and etc.), which are affecting both code and carrier measurements. One can separate the instrumental biases into three classes: inter-frequency biases, which are the biases between the code observables on different frequencies and intra-frequency biases (IFBs), which are the biases between two codes on the same frequency, and the inter-system biases (ISBs), which are the biases from observations of different GNSS. These biases are dependent on frequency, signal type, and receiver tracking technology.

The satellite and receiver hardware biases assimilated in the satellite and receiver clocks in addition to the time offset with respect to a GNSS system reference time of each clock as expressed in equations 3.15a and 3.15b.

$$P_{1r}^{s} = \rho_r^s + I_r^s + T_r^s + c(\delta t_r + B_{1r}) - c(\delta t^s + B_1^s) \tag{3.15a}$$

$$P_{2r}^{s} = \rho_r^s + \frac{f_1^2}{f_2^2} I_r^s + T_r^s + c(\delta t_r + B_{2r}) - c(\delta t^s + B_2^s) \tag{3.15b}$$

where B denotes the hardware delay and δt is the clock reading. The clock terms and the hardware delays in the observations can be canceled by differencing if satellite related biases (B_1^s, B_2^s) are the same for each tracked receiver on the ground. On the other hand, each GLONASS satellite transmits its unique frequency (i.e., FDMA) thus, the clock terms and additional biases cannot be eliminated by only differential techniques. The inter-system bias correction is necessary to fulfill this operation. The

code observations *C1*, *P1*, and *P2* are affected by biases of B_{C1}, B_{P1} and B_{P2}, respectively. However, these biases are not absolute and they are estimated from a global network with a mean zero condition and shifted by an arbitrary offset B_0. The estimated biases are known as Differential Code Biases (DCB) and expressed as below:

$$\begin{aligned} B_{P1} - B_{P2} &= DCB_{P1-P2} \\ B_{P1} - B_{C1} &= DCB_{P1-C1} \\ B_{P2} - B_{C2} &= DCB_{P2-C2} \end{aligned} \tag{3.16}$$

Conventionally, the IGS precise and broadcast satellite clock corrections are computed from ionosphere-free linear combination of code observables P_3. Accordingly, each clock correction includes ionosphere-free linear combination of unknown B_1 and B_2 biases i.e. $2.55 \cdot B_2 - 1.55 \cdot B_1$. Dual frequency combinations cancel out the hardware delays. However, single frequency PPP users must use the DCBs for accurate positioning and reliable time transfer. The inter-frequency bias is important when estimating the ionospheric delays with linear combinations of different frequencies and for positioning with single frequency receivers. The satellites broadcast the group delay (GD) in their navigation message for single frequency users, which is related to the inter-frequency DCB of the satellites as:

$$\tau_{GD} = -1.55 \cdot DCB_{P1-P2} + B_0 \tag{3.17}$$

For correct handling of DCBs, the receivers must be categorized by their code tracking technology (Schaer and Steingenberger, 2006):

- The *P1/P2* receivers providing *C1, P1* and *P2* code data.
- The *C1/X2 (P2)* cross-correlation receivers (e.g., Rogue and Trimble 4000) produce $C1$ and a synthetic $P2$ code derived from the sum of $C1$ and the difference between cross-correlated $P1$ and $P2$ combination $P2(X2) = C1 + (P2 - P1)$. To correct the IF linear combination and to achieve a consistency with IF satellite clocks, the $C1/X2$ or $C1/P2$ code data must be corrected by the $DCB_{P1\text{-}P2}$.
- The $C1/P2$ receivers, which are reporting $C1$ in place of $P1$, thus, the $DCB_{P1\text{-}C1}$ must be added in order to emulate *P1* code.

The inter-frequency biases ($DCB_{P1\text{-}P2}$) are by-products of estimated IGS Ionospheric Maps and PPP processing with geometry free (L_4) linear combination of code observables can produce these biases. The values of the intra-frequency biases $DCB_{P1\text{-}C1}$ estimated by the IGS Analysis centers during a global satellite clock correction estimation process with IF code observables. Monthly mean values of $DCB_{P1\text{-}P2}$ and $DCB_{P1\text{-}C1}$ for GPS and GLONASS satellites and for the IGS sites are available at CODE's FTP address (Url-6). The phase observations also contain hardware delays, which are assimilated into the unknown ambiguities in PPP solution. The assimilation destroys the integer nature of ambiguities and thus, the solution is performed with float ambiguities. In the case of a network solution of satellites and receivers, these hardware delays canceled and the process can be performed with resolved ambiguities. In case of a PPP, the hardware delays of both satellites and receivers must be modeled or mitigated in order to get fixed solutions with higher accuracy. The CODE's P1-P2 and P1-C1 DCBs files for GPS only satellites are illustrated in Figure 3.9. The DCBs and their RMS are given in nanoseconds unit. There are many ACs working on the development of techniques to provide satellite and receiver phase biases to end users in real time. With this development, PPP solutions would gain the ability to resolve ambiguities in real time and provide consistent positioning results.

CODE'S MONTHLY GNSS P1-P2 DCB SOLUTION, YEAR-MONTH 10-10

DIFFERENTIAL (P1-P2) CODE BIASES FOR SATELLITES AND RECEIVERS:

PRN / STATION NAME	VALUE (NS)	RMS (NS)
*** **********	*****.***	*****.***
G01	1.687	0.074
G02	5.109	0.029
G03	-3.014	0.017
G04	-1.817	0.022
G05	0.506	0.024
G06	-2.726	0.021
G07	1.101	0.017
G08	-3.275	0.025
G09	-2.462	0.034
G10	-4.414	0.022
G11	1.940	0.025
G12	1.719	0.027
G13	1.344	0.008
G14	-0.041	0.006
G15	0.362	0.030

CODE'S MONTHLY GPS P1-C1 DCB SOLUTION, YEAR-MONTH 10-10

DIFFERENTIAL (P1-C1) CODE BIASES FOR SATELLITES AND RECEIVERS:

PRN / STATION NAME	VALUE (NS)	RMS (NS)
*** **********	*****.***	*****.***
G01	1.425	1.536
G02	-0.298	0.003
G03	-0.919	0.005
G04	0.855	0.004
G05	1.600	0.002
G06	-0.150	0.003
G07	1.091	0.003
G08	-0.919	0.003
G09	-0.364	0.003
G10	-2.135	0.007
G11	0.081	0.002
G12	1.076	0.003
G13	1.170	0.004
G14	-0.329	0.003
G15	1.406	0.003

Figure 3.9 : CODE's differential P1-P2 (left) and P1-C1 (right) code monthly average biases and their accuracy for GPS satellites.

3.8 Atmospheric Effects on Signal Propagation

The GNSS signals propagating from satellite to receiver pass through the atmospheric regions with different state and refractivity. The atmospheric effects cause to perturbations on GNSS signal in its direction, velocity and strength. With respect to propagation the atmosphere is divided into two parts: a neutral atmosphere, i.e. namely the troposphere up to 100 km and the ionosphere from 60 to 2000 km. The inhomogeneous density of the atmospheric gasses causes to spatial and temporal changes in the refractivity. The variations in the refractivity results with an extended geometric path with respect to the vacuum (non-dispersive media) when the signal travels through the atmosphere.

The propagation delay $\Delta\rho$ computed by integration of the refractive index n of the atmospheric layers along the path from a satellite to a receiver.

$$\Delta\rho = \int_{Sat}^{Rec} (n-1)ds. \tag{3.18}$$

The refractive index *n* is determined by the ratio of the signal velocity in a medium *v* to the velocity of the signal in a vacuum *c*. According to Snell's law, an electromagnetic wave traveling from one medium with refractive index n_i to another medium with refractive index n_j changes its propagation velocity from v_i to v_j. This relation is expressed by the formula:

$$n_i \times v_i = n_j \times v_j = c \tag{3.19}$$

The variations in the refractive index for a different layer of the atmosphere cause the ray path to bend and an excess of the geometric path due to lower propagation velocity compared to vacuum. The non-dispersive medium, i.e. the troposphere, and a frequency dependent dispersive medium, i.e. the ionosphere, have to be carefully handled by modeling using either analytical models or external measurements. Most of the time they are estimated as unknown parameters by performing LSA.

With this chapter, the ionospheric path delay and its mitigation methods will be discussed while the tropospheric path delay will be discussed in the next chapter (chp. 4).

3.8.1 Fundamentals of wave propagation: phase and group velocity

The electromagnetic wave propagates in space with wavelength λ (meter) and frequency *f* (Hz) and the velocity of its phase defined as phase velocity (m):

$$v_{ph} = \lambda \cdot f \tag{3.20}$$

The GNSS phase carriers (i.e. L_1 and L_2) propagate with this velocity. On the other hand, for the group velocity we can write the formula in equation 3.21 (Wellenhof et al, 2008).

$$v_{gr} = -\left(\frac{df}{d\lambda}\right)\lambda^2 \tag{3.21}$$

This velocity corresponds for GNSS code measurements i.e. P_1 and P_2. A relation between the phase and the group velocity are derived from the differential of equation 3.20 as given below in equation 3.22:

$$dv_{ph} = fd\lambda + \lambda df \tag{3.22}$$

which can be arranged in equaiton 3.23 as:

$$\frac{df}{d\lambda} = \frac{1}{\lambda}\frac{dv_{ph}}{d\lambda} - \frac{f}{\lambda} \tag{3.23}$$

The substitution of the equation 3.23 into the equation 3.21 gives us equation 3.24:

$$\begin{aligned} v_{gr} &= -\lambda\frac{dv_{ph}}{d\lambda} + f\lambda \\ v_{gr} &= v_{ph} - \lambda\frac{dv_{ph}}{d\lambda} \end{aligned} \tag{3.24}$$

which express the relationship between group velocity and phase velocity i.e. known as Rayleigh equations. Phase and group are equal in non-dispersive media and slower than speed of light i.e. $c = 299792458\, ms^{-1}$.

The wave propagation velocity in a medium depends on the refractive index *n* of the medium as expressed in equation 3.25:

$$v = \frac{c}{n} \tag{3.25}$$

By using this expression, two different refractive indices can be defined for the group and phase (i.e. equation 3.26):

$$v_{ph} = \frac{c}{n_{ph}}; \quad v_{gr} = \frac{c}{n_{gr}} \tag{3.26}$$

Differentiation of the phase velocity with respect to λ as given in equation 3.27 yields:

$$\frac{dv_{ph}}{d\lambda} = -\frac{c}{n_{ph}^2}\frac{dn_{ph}}{d\lambda} \tag{3.27}$$

and substituting the equations 3.27 and 3.26 into the equation 3.24 gives us equation 3.28

$$\frac{c}{n_{gr}} = \frac{c}{n_{ph}} + \lambda\frac{c}{n_{ph}^2}\frac{dn_{ph}}{d\lambda} \text{ or } \frac{1}{n_{gr}} = \frac{1}{n_{ph}}\left(1 + \lambda\frac{1}{n_{ph}}\frac{dn_{ph}}{d\lambda}\right). \tag{3.28}$$

By using the approximation $(1+\varepsilon)^{-1} = 1-\varepsilon$, the equation 3.28 is inverted to equation 3.29

$$n_{gr} = n_{ph} - \lambda\frac{dn_{ph}}{d\lambda} \tag{3.29}$$

which is the modified Rayleigh Equation (Wellenhof et al, 2008). By differentiating the relation $c = \lambda f$ with respect to wavelength and frequency we get equation 3.30 as below:

$$\frac{d\lambda}{\lambda} = -\frac{df}{f} \tag{3.30}$$

and by substituting the results into the equation 3.29 gives us final equation 3.31:

$$n_{gr} = n_{ph} + f\frac{dn_{ph}}{df}. \tag{3.31}$$

3.8.2 Ionospheric refraction

The ionosphere is an uppermost layer of the Earth's atmosphere between the heights of 60 - 2000 km above the Earth's surface and contains sufficient free electrons and ions, which affecting the propagation of radio waves (Davis, 1990). The spatial distributions of electrons and ions in the atmosphere are determined by photo-chemical processes varying strongly with time, solar activity and the Earth's magnetic field. The delays because of the solar variability could reach up to 20 meters within a day due to the site's location, time of day and season. The solar activity is generally measured by the sunspot numbers, which has a direct influence on the ionosphere, and thereby, to the GNSS signals. A sunspot cycle is the time period from solar minimum to the solar maximum measured by the dark areas on the sun's surface. The sunspot numbers show an approximately 11 – year variation (i.e., min: 9 years; max: 14 years) cycle of the solar activity. This is a periodic variation of usually non-symmetric cycles. Figure 3.10 shows the daily and monthly average sunspot counts between the years of 2004 and 2016. The spatial distribution of electron and ions is closely related to solar activities and latitude dependent geomagnetic effects that both influencing the distribution and motion of the free electrons. The maximum ionospheric delay occurs in the region of about 10º North and 15º South of the geomagnetic equator during the period of maximum solar activity due to the high electron density.

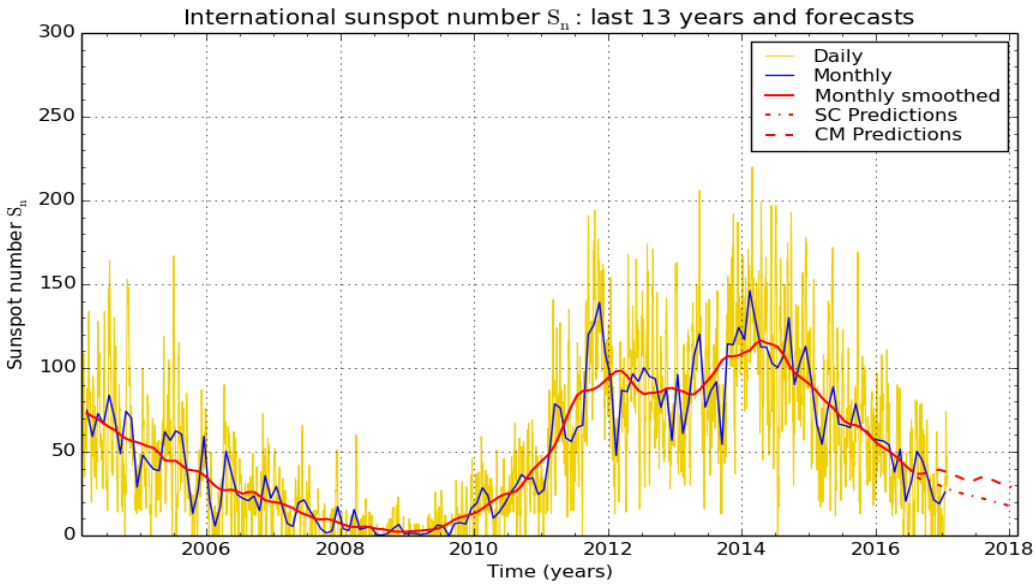

Figure 3.10 : The daily and monthly average sunspot counts from 2004 to 2017 with two different interpolation techniques in order to predict the future solar activities (SC: Standard Curves Interpolation; CM: Combining regression with Geomagnetic Index) (SIDC - Solar Influences Data Analysis Center, N.d).

The spatial distribution of electron and ions are affected by both photo-chemical processes induced by the insolation of the sun and geomagnetic effects govern the transportation and motion of the ionized atmosphere. Due to these effects, the ionosphere is classified into the four regions (*D, E, F1, and F2*) with density variations at different heights. The state of the ionosphere is defined with the electron density N_e electrons / m^3 and the regions with different electron density are shown in Table 3.1.

Table 3.1 : The ionospheric layers with different densities with respect to height (Seeber, 2003).

Layer		D	E	F1	F2
Height	(km)	$60-90$	$85-140$	$140-200$	$200-1000$
$N_e(electrons/m^3)$	Day	10^2-10^4	10^5	$5\cdot10^5$	10^6
	Night	-	$2\cdot10^3$	$5\cdot10^4$	$3\cdot10^5$

The electron density integrated along the satellite-receiver path is called a slant total electron content (STEC) and it is determined by measuring the total number of free electrons in a cylinder with a cross-sectional area of 1 m^2 and the height equal to the slant path as expressed in equation 3.32:

$$STEC = \int_R^S N_e ds. \tag{3.32}$$

STEC is measured in Total Electron Content Unit (TECU), which 1 TECU equivalent to $10^{16} electron/m^2$. As stated by Seeber (2003), the phase refractive index can be approximated by using the power series as given below (equation 3.33):

$$\begin{aligned} n_{ph} &= 1+\frac{c_2}{f^2}+\frac{c_3}{f^3}+\frac{c_4}{f^4} \\ n_{gr} &= 1-\frac{c_2}{f^2}+2\frac{c_3}{f^3}+3\frac{c_4}{f^4} \end{aligned} \tag{3.33}$$

For the GNSS signals, the first order term is nearly three orders of magnitude larger than the other terms. The coefficients c_i are independent of the carrier frequency but dependent on the quantity of the electron density n_e along the path. By cutting off the series after the quadratic term gives us equation 3.34:

$$n_{ph} = 1+\frac{c_2}{f^2} \tag{3.34}$$

and differentiating this equation gives us equation 3.35:

$$dn_{ph} = -\frac{2c_2}{f^3}df \tag{3.35}$$

and substituting 3.35 and 3.34 into 3.31 leads to equation 3.36:

$$n_{gr} = 1 - \frac{c_2}{f^2} \tag{3.36}$$

The group and phase refractive indices deviate from the unity with opposite sign (Wellenhof et al, 2008). When $n_{gr} > n_{ph}$ it is concluded that $v_{gr} < v_{ph}$. When a signal travels through the ionosphere, a carrier phase is advanced and a code is delayed due to the different velocities. Therefore, the code pseudorange is longer than the phase measurements. After introducing the estimated value for $c_2 = -40.3N_e\left[Hz^2\right]$, we obtain equation 3.37 for the phase and group indices:

$$\begin{aligned} n_{ph} &= 1 - \frac{40.3N_e}{f^2} \\ n_{gr} &= 1 + \frac{40.3N_e}{f^2} \end{aligned} \tag{3.37}$$

According to Fermat's principle (Alizadeh et al, 2013, p.40), the integral of the refractive index along the signal path gives the measured range as expressed in equation 3.38.

$$s = \int n ds \tag{3.38}$$

A delay or an advance in signal traveling through the ionosphere deviates the measured range (i.e. *S*) from the geometric range (i.e. S_0). This path length difference is called an ionosphere delay or ionospheric refraction. The difference $\Delta\rho^{ion}$ between the measured and geometric range can be written for a phase and group refractive indexes as given in equations 3.39a and 3.39b:

$$\Delta\rho_{ph}^{ion} = \int n ds - \int ds_0 = \int \left(1 + \frac{40.3N_e}{f^2}\right) ds - \int ds_0 \tag{3.39a}$$

$$\Delta\rho_{gr}^{ion} = \int n ds - \int ds_0 = \int \left(1 - \frac{40.3N_e}{f^2}\right) ds - \int ds_0 \tag{3.39b}$$

The integration for the first terms in (3.39a) and (3.39b) is approximated to the geometric range S_0 in order to simplify the solution, then, the new equations (3.40a and 3.40b) can be written as:

$$\Delta\rho_{ph}^{ion} = -\frac{40.3}{f^2}\int N_e ds_0 \tag{3.40a}$$

$$\Delta\rho_{gr}^{ion} = \frac{40.3}{f^2}\int N_e ds_0 \tag{3.40b}$$

The first order refractive index only corresponds to the electron density within the ionosphere which is almost 99.9 % of the total delay, while the second and higher order refractive indexes include bending effects and effects of the geomagnetic field. For precise positioning, these higher order terms have to be considered for low elevation observations with high electron content (Gu and Brunner, 1991). It can be deduced from the equations above, the propagation delay of GNSS signals is frequency dependent, and thus the ionosphere is often referred as dispersive media. Forming linear observation equations of different frequencies i. e. ($f = 1, 2 \ldots 3$) can eliminate the ionosphere effect up to order $f - 1$ (Petit and Luzum, 2010). For observations on GPS frequencies L_1 and L_2, the ionosphere free linear combination L_3 can be formed for both code and phase observations as:

$$L_3 = \frac{f_1^2 L_1 - f_2^2 L_2}{f_1^2 - f_2^2} \tag{3.42}$$

L_3 eliminates the first order delay which is only a few mm for PPP and relative solutions with respect to the true range. With GNSS modernization studies such as new Galileo satellites and incoming new GPS signals (L_5), the high order delays will be mitigated through linear combinations of multi-GNSS and multi-frequency observations. Despite the fact that the IGS clocks and orbits are estimated using L_3 observations with high accuracy, the effects of higher order delays and the significantly increased measurement noise of L_3 solution are usually neglected.

3.8.3 Ionosphere modeling

There are several ways to measure TEC values. TEC information is usually provided as vertical TEC (VTEC), and mapped into the slant path (STEC) via ionospheric mapping function *F(z)*, as given in equation 3.43:

$$STEC = VTEC \cdot F(z). \tag{3.43}$$

A single-layer model (SLM) is a widespread deterministic method used to get an approximation for TEC content in the ionosphere. According to the SLM, all free electrons are concentrated in an infinitesimally thin spherical shell at the height H, which is usually set between of 350-500 km where the highest electron density is expected. The geometry of the model is illustrated in Figure 3.11. The signal follows satellite - receiver path crosses the thin ionospheric layer in the ionospheric pierce point (IPP); the zenith angle at the IPP is z'; and the satellite zenith angle is z. The relationship between z' and z is given in equations 3.44, where R is 6370 km and H is the height of the single layer in km.

$$\sin z' = \frac{R}{R+H} \sin z \tag{3.44}$$

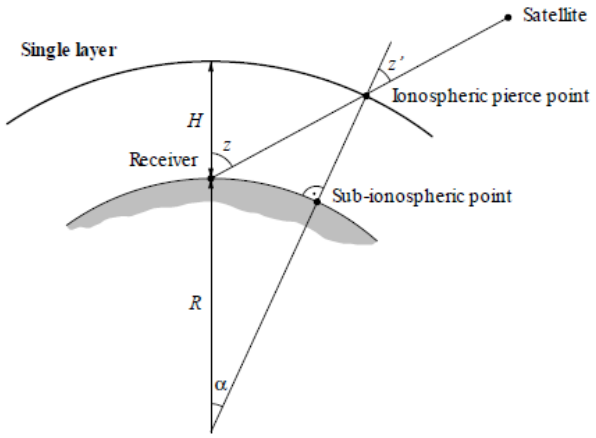

Figure 3.11 : Geometry of the Single Layer Model (SLM).

The SLM mapping function can be formed using equations 3.44, 3.43 and 3.32 and then we get the following equation (3.45):

$$F(z) = \frac{1}{\cos'} = \frac{1}{\sqrt{1-\sin^2 z}} \tag{3.45}$$

The entire vertical ionospheric refraction can be approximated by some empirical models. One of the algorithms known as Klobuchar developed in the 1980's by the Klobuchar (1986) for single frequency GPS users to mitigate about 50 % of the ionospheric delay. This model uses the ionospheric coefficients that broadcasted

within the navigation message and approximates the vertical ionospheric refraction by using vertical time delay of the code observations.

The NeQuick (De Giovanni and Radicella, 1990) model is an empirical model developed at the Aeronomy and Radiopropagation Laboratory of the Abdus Salam International Centre for the Theoretical Physics in Trieste (Italy) and the Institute for Geophysics, Astrophysics and Meteorology of the University of Graz (Austria) in order to calculate the TEC and electron density at any given location in the ionosphere. It is a three-dimensional and time-dependent model delivering electron density as a function of geographic latitude and longitude, height, monthly average values of solar activity either determined by sunspot number or by 10.7 cm solar radio flux $F_{10,7}$, and season and local time (Radicella, 2009). The Galileo project has adopted this model for positioning analyses to perform single frequency solutions. Furthermore, the prediction models like the International Reference Ionosphere (Bilitza et al. 2011), the Global Assimilative Ionospheric Model (JPL. JPL - NASA, 2011) and the Multi-Instrument Data Analyses System (MIDAS) (Mitchell and Cannon, 2002) provide significant information related to global ionospheric electron density.

Most space geodetic techniques use linear combinations of dual or multiple frequencies to eliminate the ionosphere's first order effect on propagation signal. On the other hand, the information of ionosphere refraction is valuable data on account of computing and developing the regional or global ionosphere models.

In order to extract the TEC content of the ionosphere from GNSS observations, the geometry-free linear combination L_4 can be formed, which is independent of geometric terms (i.e., clocks, troposphere, coordinates and orbits). It only contains the ionospheric delay, initial phase ambiguities, and satellite/receiver instrumental biases. As stated by Dach et al. (2015), the geometry-free linear combination for undifferenced phase and code observations are expressed as in equations 3.46a and 3.47b

$$L_4 = L_1 - L_2 = -a\left(\frac{1}{f_1^2} - \frac{1}{f_2^2}\right)\mathrm{F(z)} \cdot VTEC(\beta, S) + B_4 \tag{3.46a}$$

$$P_4 = P_1 - P_2 = +a\left(\frac{1}{f_1^2} - \frac{1}{f_2^2}\right)\mathrm{F(z)} \cdot VTEC(\beta, S) + b_4 \tag{3.46b}$$

where L_4 and P_4 are the geometry-free phase and code observables in meters, a is the constant value equal to $40.3 \cdot 10^{17} ms^{-1} TECU^{-1}$; f_1 and f_2 are the frequencies of the carriers L_1 and L_2, $F(z)$ is the ionospheric mapping function evaluated at zenith distance z, $VTEC$ is the vertical TEC in TECU unit as a function of geomagnetic latitude β and sun-fixed longitude S. B_4 is the L_4 ambiguity parameter for carrier phase, and b_4 is the constant bias due to the differential instrumental delay of the satellite and receiver L_4 linear combination. The $VTEC(\beta, S)$ represents the deterministic part of the ionosphere without short-term variations that can be estimated based on local, regional and global models and appropriate modeling functions.

The local TEC modeling for local applications is given by Dach et al. (2015) with Taylor series expansion as given in the following equation (3.47):

$$VTEC(\beta, s) = \sum_{n=0}^{n\max} \sum_{m=0}^{m\max} E_{nm} (\beta - \beta_0)^n (S - S_0)^m \tag{3.47}$$

where

- n_{max} and m_{max} are the maximum degrees of two-dimensional Taylor series expansion in latitude β and in longitude S,
- E_{nm} are the unknown local ionosphere model coefficients of the Taylor series need to be estimated, and
- β_0 and S_0 are the origin coordinates for latitude and longitude.

Despite being appropriate for local studies, it is not an efficient model for regional and global applications due to insufficient coverage of geographic space. Schaer (1999) proposed a global model with a spherical harmonic function of sun-fixed longitude, geomagnetic latitude and time in UT parameters as expressed in equation 3.48:

$$VTEC(\beta, s) = \sum_{n=0}^{n\max} \sum_{m=0}^{m\max} \tilde{P}_{nm} (\sin \beta) \left(a_{nm} \cos(ms) + b_{nm} \sin(ms) \right) \tag{3.48}$$

where

- $\tilde{P}_{nm} = N_{nm} P_{nm}$ are the normalized Legendre function from degree n to order m and N_{nm} is the normalization function, and
- a_{nm}, b_{nm} are the unknown TEC coefficients of the spherical harmonic expansion.

The daily solution of geometry-free observations (i.e., L_4 and P_4 as in equations 3.46a and 3.46b) from globally distributed GNSS stations with a sampling rate of 30 seconds and 10° elevation cut-off angles are used to derive the TEC coefficients i.e. a_{nm} and b_{nm}. The estimated coefficients are then implemented to the equation 3.48 to calculate two hourly global TEC grid maps known as GIMs. The GIM data, disseminated by the CODE periodically, can be used not only for global but also for local applications (Schaer et al, 1998). GIMs include the VTEC values and their corresponding deviations (i.e. RMS) in gridded raster format with 2-hour resolution. Expected accuracy of the GIMs is a few TECU for areas with good GNSS site coverage. The Ionosphere model Exchange format (IONEX) has been developed for the exchange of GIMs (Schaer et al, 1998) and supports two and three-dimensional TEC maps in the raster grid format where the VTEC data are represented as a function of geocentric latitude, longitude and time (i.e. UT). The information on the IONEX format can be found at the IGS Ionex pdf document (Url-7). Figure 3.12 illustrates a sample IONEX file including three-dimensional TEC maps distributed from the CODE AC.

```
     1.0            IONOSPHERE MAPS     GPS                 IONEX VERSION / TYPE
ionpgm v1.0         aiub                29-jan-96 17:29     PGM / RUN BY / DATE
example of an ionex file containing 3-dimensional tec maps  COMMENT
global ionosphere maps for day 288, 1995                    DESCRIPTION
modeled by spherical harmonics ...                          DESCRIPTION
  1995    10    15     0     0     0                       EPOCH OF FIRST MAP
  1995    10    16     0     0     0                       EPOCH OF LAST MAP
 21600                                                      INTERVAL
     5                                                      # OF MAPS IN FILE
  COSZ                                                      MAPPING FUNCTION
    20.0                                                    ELEVATION CUTOFF
double-difference carrier phase                             OBSERVABLES USED
    80                                                      # OF STATIONS
    24                                                      # OF SATELLITES
  6371.0                                                    BASE RADIUS
     3                                                      MAP DIMENSION
   200.0 800.0  50.0                                        HGT1 / HGT2 / DHGT
    85.0 -85.0  -5.0                                        LAT1 / LAT2 / DLAT
     0.0 355.0   5.0                                        LON1 / LON2 / DLON
                                                            END OF HEADER
```

Figure 3.12 : The IONEX file with 3D Ionosphere TEC maps.

4. TROPOSPHERIC PATH DELAY

4.1 Introduction

The troposphere commonly referred to as neutral atmosphere extends from the Earth's surface to about 50 km height. It contains 75 % of the total atmosphere's mass and 99 % of the water vapor. For microwave signals such as GNSS and VLBI, the troposphere is non-dispersive up to 30 GHz and being free of charged particles, which makes it impossible to mitigate effects of delays using dual frequency observation like it is in the ionosphere. The tropospheric refraction is same for code and phase signals and it delays the signals by the same magnitude. The tropospheric refraction depends on so many parameters such as observed site location, height, a line of sight, temperature, pressure, and relative humidity. Two basic approaches can be used to handle the tropospheric delays. The first approach is to estimate the delays by adjusting observation equations while the second approach uses external sources such as troposphere prediction models, water vapor radiometers, and in-situ meteorological readings to calculate the path delays.

A microwave signal experiences velocity changes as it passes through layers of different refractive indices in the troposphere. Therefore, it takes more time for the signal to reach to the receiver with respect to the vacuum. This time difference indicates tropospheric path delay in metric units and expressed as in equation 4.1:

$$\Delta\rho^{trop} = \int_s (n-1)ds \tag{4.1}$$

where n is the refractive index that is the ratio of the velocity in a respective medium to the velocity in the vacuum. In the neutral atmosphere, the refractive index is larger than 1 and getting closer to 1 with increasing height. Usually, the term refractivity i.e. N (equation 4.2) is used instead of the term refractive index.

$$N^{trop} = 10^6 (n\text{-}1). \tag{4.2}$$

So that the equation 4.1 turns into equation 4.3 as:

$$\Delta\rho^{trop} = 10^{-6}\int_s N^{trop} d_s. \tag{4.3}$$

Figure 4.1 illustrates the characteristic of the refractivity *N* as a function of height. The refractivity is a positive (+) value for the troposphere and frequency independent. On the contrary, it is negative (-) and frequency dependent for the ionosphere. The frequency and the refractivity have an opposite correlation that the refractivity decreases as the frequency increases.

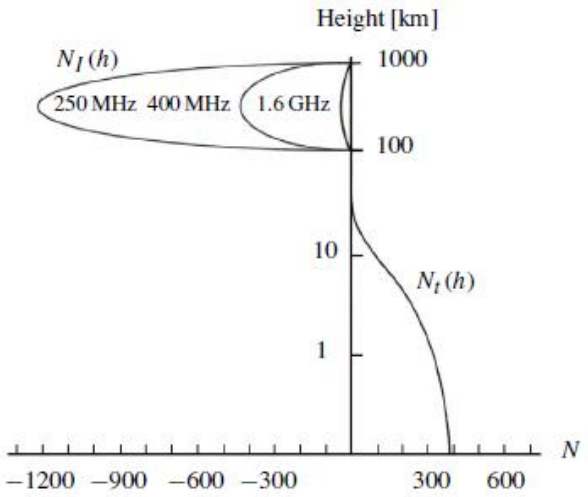

Figure 4.1 : The refractivity variation of microwave domain with respect to height for Ionosphere and Troposphere (Seeber, 2003).

4.2 Tropospheric Refraction for Microwave Signals

The refractivity in non-dispersive medium consists of three different parts: the real part i.e.N_0, real part with frequency dependency i.e. $N_{(f)}$ and imaginary part with frequency dependency i.e. $iN_f^{'}$ (Nilsson et al. 2013).

$$N = N_0 + N_{(f)} - iN'_f \tag{4.4}$$

The propagation delay of the GNSS signal in the neutral atmosphere is caused by the real part of the refractivity $\left(\text{i.e. } N_0 + N_{(f)}\right)$. The imaginary part $iN_f^{'}$, on the other hand, has none significant effect on the propagation delay of GNSS signal and thus, usually avoided in the geodetic data analyses. The real part of the refractivity can be expressed as a function of meteorological parameters of pressure, temperature, and humidity as stated by (Essen and Froome, 1951) in equation 4.5:

$$N^{trop} = k_1\left(\frac{P_d}{T}\right)Z_d^{-1} + \left[k_2\left(\frac{e}{T}\right) + k_3\left(\frac{e}{T^2}\right)\right]Z_w^{-1} + k_4\rho_{lw} \tag{4.5}$$

where k_1, k_2 and k_3 are empirically determined constants, Z_d and Z_w are compressibility factors for dry air and water vapor, respectively. The compressibility factors correspond the deviation of the atmospheric gasses from an ideal gas. The partial pressure of dry air and water vapor is represented by P_d and e, respectively, and the temperature is denoted with T.

The compressibility factor for an ideal gas is $Z=1$ and Owens (1967) expresses the formulation of the inverse compressibility factors Z_d and Z_w by using least squares fitting to thermodynamic data as shown in the equations 4.6a and 4.6b. Those values represent a non-ideal behavior of dry air and water vapor.

$$Z_d^{-1} = 1 + p_d\left[57.97\cdot10^{-8}\left(1+\frac{0.52}{T}\right) - 9.4611\cdot10^{-4}\frac{T-273.15}{T^2}\right], \tag{4.6a}$$

$$Z_w^{-1} = 1 + 1650\frac{p_w}{T^3}\left[\begin{array}{r} 1 - 0.0137\left(T-273.15\right) + 1.75\cdot10^{-4}\left(T-273.15\right)^2 + \\ 1.44\cdot10^{-6}\left(T-273.15\right)^3 \end{array}\right] \tag{4.6b}$$

There are several different estimates for the coefficients k_1, k_2 and k_3 (i.e., Smith and Weintraub, 1953; Boudouris 1963; Thayer, 1974; Bevis et al. 1994; Rüeger, 2002); see also Table 4.1.

The first term in the equation 4.5 corresponds to dry air refractivity caused by induced dipole moment of dry components. The second term represents the vapor part that includes induced dipole moment of water vapor and permanent dipole moment of water vapor molecules which all form together the significant amount of the signal delay (Thayer, 1974). Figure 4.2 displays the contribution of induced and permanent dipole moment of water vapor to the total wet refractivity The third component is the density of liquid water and it is usually ignored because of small influence on the refractivity. The dry refractivity depends only on the total density of air, whereas the vapor part depends only on the partial pressure of water vapor and the temperature.

Because of the extremely changeable mixing ratio of the partial pressures of dry air and water vapor, it is difficult to determine their values with sufficient accuracy. Thus,

we can assume a hydrostatic equilibrium where the total pressure P is expressed as the sum of the pressure of dry air and the pressure of water vapor

$$P = P_d + e \tag{4.7}$$

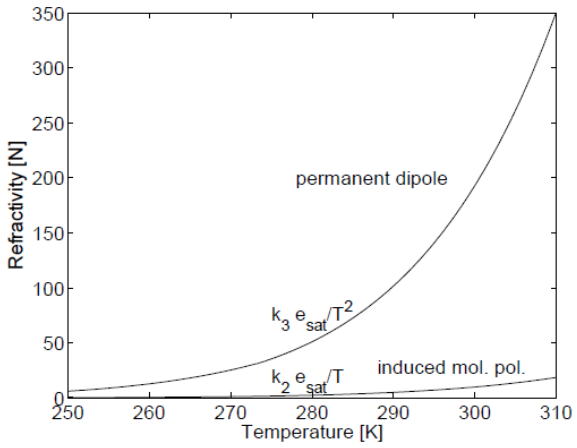

Figure 4.2 : The contribution of induced and permanent dipole moment of water vapor to the total wet refractivity (Thayer, 1974).

After applying the ideal gas law, the state equation for both dry air and water vapor, we get the following equation (4.8):

$$\begin{aligned} P_d &= \rho_d R_d T, \\ e &= P - P_d = \rho_w R_w T \end{aligned} \tag{4.8}$$

where

- P_d and e :partial pressure of dry air and water vapor $\left(N\ m^{-2}\right)$,
- R_d and R_w:specific gas constant of dry air and water vapor respectively in unit $J\ kg^{-1}K^{-1}$,
- ρ_d and ρ_w:mass density of dry air and water vapor, respectively, in unit $kg\ m^{-3}$.

With the compressibility factors, the general equation (4.9) for the ideal gas becomes:

$$P_i = Z_i \rho_i R_i T; i = d, w \tag{4.9}$$

Using the equation 4.9 and avoiding the density of the liquid water ρ_{lw}, we can reformulate the equation 4.5 as expressed in equation 4.10:

$$N = k_1 \frac{R}{M_d} \rho + k_2' \frac{e}{T} Z_w^{-1} + k_3 \frac{e}{T^2} Z_w^{-1} \tag{4.10}$$

where

- $k_2' = k_2 - k_1 \frac{M_w}{M_d}$, is a new constant ($K\ mbar^{-1}$),
- $\rho = \rho_d + \rho_w$ (total mass density) of moist air,
- M_d and M_w are the molar mass densities for the dry air and the water vapor, respectively,
- $R_d = \frac{R}{M_d}$ and $R_w = \frac{R}{M_w}$ are the specific gas constants for the dry air and the water vapor.

The first term in the equation 4.10 is the hydrostatic refractivity, which depends only on the total density of air; the second and third terms together form the wet refractivity i.e. $N_w = \left(k_2' \frac{e}{T} + k_3 \frac{e}{T^2} \right) Z_w^{-1}$, which is a function of water vapor and temperature.

According to Davis et al. (1985), the atmospheric values are given as in equation 4.11:

$$\begin{aligned} R_w &= \frac{R}{M_w} = 416.50 \qquad (J / kg \cdot K), \\ R_d &= \frac{R}{M_d} = 287.06 \qquad (J / kg \cdot K) \end{aligned} \tag{4.11}$$

where

$R = 8.31434 \pm 0.00007 \quad (Pa \cdot m^3 / K \cdot mol)$
$M_d = 28.9644 \pm 0.0014 \quad (g / mol)$ and
$M_w = 18.01528 \quad (g / mol)$

Rüeger (2002) evaluated these estimates and computed the ideal values for the constants *k1*, *k2* and *k3*. The hydrostatic refractivity mostly depends on the concentrations of the different dry gasses. Most of them, except the concentration of carbon dioxide, show almost stable characteristic. Hence, the varying coefficients must be adopted by the formulas after observing the amount of carbon dioxide concentration

in the atmosphere. The values determined for the coefficients obtained from different studies are summarized in Table 4.1.

Table 4.1 : Experimental values of coefficients used to calculate the refractivity from different publications.

Reference	k_1 $(K\ mbar^{-1})$	k_2 $(K\ mbar^{-1})$	k_3 $(10^5 K^2\ mbar^{-1})$	k_2' $(K\ mbar^{-1})$
Smith and Weintraub, 1953	77.61 ± 0.01	72 ± 9	3.75 ± 0.03	24 ± 9
Boudouris, 1963	77.59 ± 0.08	72 ± 11	3.75 ± 0.03	24 ± 11
Thayer, 1974	77.60 ± 0.01	64.79 ± 0.08	3.776 ± 0.004	17 ± 10
Bevis, 1994	77.60 ± 0.05	70.4 ± 0.08	3.739 ± 0.0012	22
Rüeger, 2002 (375 $ppm\ CO_2$)	77.6890	71.2952	3.75463	23
Rüeger, 2002 (392 ppm CO_2)	77.6900	71.2952	3.75463	23

4.3 Troposphere Modeling for GNSS Measurements

Since the IGS publishes accurate orbits and clocks, the satellite-related errors are no longer considered as the significant error source for GNSS analyses. However, the neutral atmosphere affects the propagation speed and path, which explains why it is regarded as one of the large accuracy limiting factors. Due to refractivity and velocity fluctuations in the troposphere, the actual signal path S is longer than the geometric straight path G in the atmosphere. This is one of the fundamental physical law based on Fermat's principle that the signal will follow the electrical path with minimum least travel time. The tropospheric delay $\Delta\rho^{trop}$ corresponds to the signal path excess due to the refractivity, is given as in equation 4.12:

$$\Delta\rho^{trop} = \int_S (n)ds - G = \int_S (n-1)ds + \int_S ds - G \tag{4.12}$$

or by another representations as in equations 4.13:

$$\Delta\rho^{tropo} = 10^{-6}\int_S N ds + [S - G] \tag{4.13}$$

where $[S-G]$ is the geometric bending effect that depicted in Figure 4.3. The first term on the right-hand side of equation 4.13 is the path excess caused by the delay; the second term between braces is the path excess due to the ray bending.

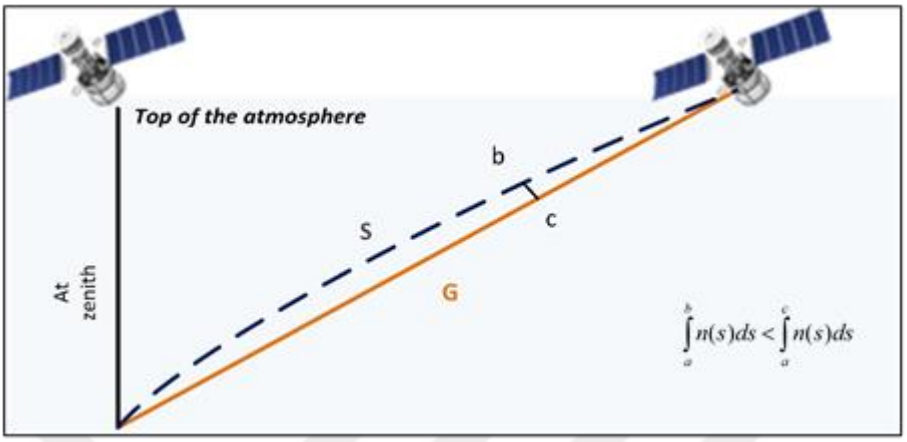

Figure 4.3 : The geometric bending effect due to the refractivity. The signal will take the S path during propagation, and since the signal propagates with a low velocity with respect to vacuum, it covers large distance than actual geometrical path G.

The total delay in equation 4.13 can be divided into a hydrostatic delay and a non-hydrostatic (i.e., wet delay) by means of the refractivity formula in the equation 4.10 and as a result, the following equations (4.14, 4.15 and 4.16) can be derived:

$$\Delta\rho^{trop} = 10^{-6}\int_S N_h ds + 10^{-6}\int_S N_w ds + S - G, \tag{4.14}$$

$$\Delta\rho^{trop} = 10^{-6}\int_S \left(\left(k_1 \frac{R}{M_d}\rho\right) Z_d^{-1}\right) ds + 10^{-6}\int_S \left(\left(k_2' \frac{e}{T} + k_3 \frac{e}{T^2}\right) Z_w^{-1}\right) ds + S - G, \tag{4.15}$$

$$\Delta\rho^{trop} = \Delta\rho_h^{trop} + \Delta\rho_w^{trop} + S - G. \tag{4.16}$$

By convention, the geometric bending effect $(S-G)$ is absorbed by the determined ZHD (Nilsson et al, 2013).

4.3.1 Zenith hydrostatic delay

The Zenith Hydrostatic Delay (ZHD) is the delay of a radio signal arriving from the zenith direction caused by the neutral atmosphere and it is computed by the integral over the hydrostatic refractivity by using equation 4.17:

$$\Delta\rho_h^z = ZHD = 10^{-6}\int_{h_0}^{\infty} N_h \, dz. \tag{4.17}$$

ZHD depends only on the total density and not on the mixing ratio of wet and dry parts. Following Davis et al. (1985), the vertical profile of the hydrostatic delay can be defined with help of hydrostatic equilibrium as expressed in equation.4.18:

$$\frac{dp}{dz} = -\rho(z)\, g(z) \tag{4.18}$$

where $g(z)$ is the gravity along the vertical coordinate of the site. Integration of the equation 4.18 from the receiver antenna h_0 to the infinity (∞) yields the pressure P_0 at the receiver antenna by using the following equation (4.19):

$$P_0 = \int_{h_0}^{\infty} \rho(z)\, g(z)\, dz = g_{eff} \int_{h_0}^{\infty} \rho(z)\, dz. \tag{4.19}$$

The effective (i.e., mean) gravity acceleration g_{eff} is computed at the center of mass of the vertical column of the atmosphere above the site and may be used instead of height dependent gravity $g(z)$. The effective mean formula (4.20) is given below as:

$$g_{eff} = \frac{\int_{h_0}^{\infty} \rho(z) g(z) dz}{\int_{h_0}^{\infty} \rho(z) dz} \tag{4.20}$$

and the ZHD is calculated with measured surface pressure P_0 and the mean gravity as in equation 4.21 given below:

$$\Delta\rho_h^z = 10^{-6} k_1 \frac{R \cdot P_0}{M_d \cdot g_{eff}}. \tag{4.21}$$

The mean gravity acceleration i.e. g_{eff} is both height and latitude dependent and approximated by Saastamoinen (1972) and Davis et al. (1985) as in equation 4.22:

$$g_{eff} = 9.7840\left(1 - 0.00266\cos(2\varphi) - 0.28 * 10^{-6} h\right) \tag{4.22}$$

where φ is the latitude of the station and h is the ellipsoidal height above the geoid; g_m = 9.7840 is the gravity acceleration at the center of the mass, and $f(\varphi,h)=1-0.00266\cos(2\varphi)-0.28*10^{-6}h$ is the function of latitude and height, provides gravity acceleration for any given location. By using the equations 4.21 and 4.22 and substituting the constant values k_1, R and M_d, the zenith hydrostatic delay can be formulated in meters unit as in equation 4.23:

$$ZHD=0.0022768\frac{P_0}{f(\varphi,h_0)}. \tag{4.23}$$

Being able to calculate ZHD by processing only station coordinates and surface pressure information, makes the Saastamoinen model (1972) one of the widely used troposphere models used in GNSS studies. However, it must not be forgotten that poor pressure readings produce an error in the path delay estimates and coordinates. An error of 1hPA in the pressure readings causes an approximately error of 2.3 mm in the hydrostatic delay.

4.3.2 Extraction of meteorological parameters

Most of the space geodetic techniques need measurements of surface meteorological parameters. However, most GNSS sites do not have meteorological sensors and thus NMW or prediction function derived data is utilized to obtain a priori troposphere parameters. Analytical models are adopted as a priori meteorological data in the absence of surface measurements and numerical weather models. Berg (1948) suggested one primitive type of height dependent analytical model that using standard atmosphere values (i.e. equation 4.24) for pressure, temperature, and relative humidity as:

$$\begin{aligned} P &= P_0(1-0.0000226\cdot(h-h_0))^{5.225} \\ T &= T_0-0.0065\cdot(h-h_O) \\ R_h &= R_{h_0}\cdot e^{-0.0006396\cdot(h-h_O)} \end{aligned} \tag{4.24}$$

where P, T and R_h are pressure in millibars, the temperature in Celsius, and humidity (%) above the sea surface, respectively, that all defined for a specific height. The corresponding standard atmosphere values for sea surface are given as:

$$h_0 = 0\ meter,$$
$$P_0 = 1013.25\ millibar,$$
$$T_0 = 18^{\circ}\ Celsius,$$
$$R_0 = 50\ \%.$$

There are also sophisticated models that handle the tropospheric delays, particularly, the ZHD. Global prediction models, which do not need to deploy any meteorological sensors to measure meteorological data are practical options in this regard. For instance, Collins and Langley (1997) proposed a hybrid neutral atmosphere model for Wide Area Augmentation System (WAAS) users. This model, called UNB, developed at the Department of Geodesy and Geomatics Engineering, University of New Brunswick, Canada. The UNB was developed based on the derivation of the neutral atmosphere delays by adapting a look-up table with annual means and cosine amplitudes of atmospheric parameters, which are based on 1966 U.S. standard atmosphere data. Derived atmospheric data (e.g., pressure, humidity and temperature) are then used to compute zenith hydrostatic and non-hydrostatic delays by using Saastamoinen (1972) model. The most recent version of the UNB model is UNB3m which was developed by Leandro et al. (2006) to improve its performance for modelling the wet delays. UNB3m uses relative humidity (%) instead of water vapor pressure and as a matter of fact, the humidity must be converted to water vapor pressure in anyway to be used for zenith delay computation. The model uses day of the year, height and latitude as input parameters.

Table 4.2 : Look up table of UNB model (Leandro et al, 2006).

Mean						Amplitude					
Lat (º)	*P* mbar	*T* (*K*)	*WVP* mbar	*β* Km^{-1}	*λ* (-)	*Lat* (º)	*P* (*mbar*)	*T* (*K*)	*WVP* mbar	*β* Km^{-1}	*λ* (-)
15	*1013.25*	*299.6*	*26.31*	*6.30e-3*	*2.77*	*15*	*0.00*	*0.00*	*0.00*	*0.00*	*0.00*
30	*1017.25*	*294.1*	*21.79*	*6.05e-3*	*3.15*	*30*	*-3.75*	*7.00*	*8.85*	*0.25e-3*	*0.33*
45	*1015.75*	*283.1*	*11.66*	*5.58e-3*	*2.57*	*45*	*-2.25*	*11.00*	*7.24*	*0.32e-3*	*0.46*
60	*1011.75*	*272.1*	*6.78*	*5.39e-3*	*1.81*	*60*	*-1.75*	*15.00*	*5.36*	*0.81e-3*	*0.74*
75	*1013.00*	*263.6*	*4.11*	*4.53e-3*	*1.55*	*75*	*-0.50*	*14.50*	*3.39*	*0.62e-3*	*0.30*

The look-up table (i.e., Table 4.2) consists of one-year average of meteorological parameters: pressure (P), temperature (T), water vapour pressure (WVP), temperature

lapse rate (β), and water vapour pressure height factor (λ) along with their amplitudes which all tabulated at five latitude bands with respect to the equator. The table values are interpolated with a linear function to derive parameters for any location and day of year.

The annual average of meteorological parameters for a particular latitude (φ) is computed as given in equation 4.25:

$$Mean_{\varphi} = \begin{cases} Mean_{15}, if\ \varphi \le 15 \\ Mean_{75}, if\ \varphi \ge 75 \\ Mean_i + \dfrac{(Mean_{i+1} - Mean_i)}{15} \cdot (\varphi - Lat_i), if\ 15 < \varphi < 75 \end{cases} \quad (4.25)$$

where φ stands for the latitude of the observing site in degrees, $mean_{\varphi}$ is the average value for a meteorological parameter of interest and i is the index for the closest latitude in the table to the latitude of interest. Likewise, the amplitude, i.e. Amp_{φ}, can be computed as expressed in equation 4.25:

$$Amp_{\varphi} = \begin{cases} Amp_{15}, if\ \varphi \le 15 \\ Amp_{75}, if\ \varphi \ge 75 \\ Amp_i + \dfrac{(Amp_{i+1} - Amp_i)}{15} \cdot (\varphi - Lat_i), if\ 15 < \varphi < 75 \end{cases} \quad (4.25)$$

This procedure must be repeated for each meteorological parameter individually. Mean and amplitude values are then used to compute meteorological parameters for a specific day of year and latitude.

$$X_{\varphi, doy} = Mean_{\varphi} - Amp_{\varphi} \cdot \cos((doy - 28)\frac{2\pi}{365.25}) \quad (4.27)$$

The origin of the variation of the year starts on January 28. The predicted meteorological values are then used to compute a priori hydrostatic and non-hydrostatic delays. The mapping function of Niell (1996) and the UNB3m work collaboratively to model the troposphere.

The empirical Global Pressure and Temperature (GPT) model developed by Boehm et al. (2007) is represented by a spherical harmonic up to degree and order nine. GPT provides meteorological data, i.e. pressure, temperature, lapse rate, and water vapor pressure at anytime, anywhere. The pressure and temperature parameters in the GPT model are derived from 3 years (i.e., 1999 - 2002) of global 15° x 15° grids of monthly mean profiles and 23 isobaric levels from the European Centre for Medium-Range Weather Forecasts (ECMWF) 40 years reanalysis data (ERA40, Uppala et al, 2005). These values are determined by using mean vertical profiles and interpolation methods. First, the pressure values on the surface of the Earth (i.e., P_h) are reduced to mean sea level. Likewise, the temperature data are also reduced to mean sea level by considering a linear decreasing of temperature with height as expressed in the equation 4.29.

$$P_h = P_{h_0} \cdot (1 - 0.0000226 \cdot (h - h_0))^{5.225}, \tag{4.28}$$

$$\frac{\partial T}{\partial h} = -0.0065^{\circ} C / m. \tag{4.29}$$

As a result, 36 monthly mean values of the pressure and temperature data at mean sea level are determined for each point on the grid. The annual mean and the annual amplitude for each meteorological parameter at each grid point are estimated with the least squares adjustment by fitting 36 monthly average values to the equation 4.30.

$$Mean = Mean_0 + Amp \cdot \cos\left(\frac{doy - 28}{365.25} 2\pi\right) \tag{4.30}$$

The zero phase is set to the day of year 28, just like the UNB model. The next step is expanding the mean and the amplitudes of each of the four-grid point into spherical harmonics up to degree and order nine as illustrated in the equation 4.31.

$$Mean_0 \ or \ Amp = \sum_{n=0}^{9} \sum_{m=0}^{n} P_{nm}(\sin\varphi) \cdot \left[A_{nm} \cos(m\lambda) + B_{nm} \sin(m\lambda)\right] \tag{4.31}$$

Where P_{nm} are the Legendre polynomials, φ and λ are the latitude and the longitude of interest, respectively; B_{nm} and A_{nm} are the polynomial coefficients determined with the LSA. *Mean* and *Amp* values, which determined in the equation 4.31, are used in the equation 4.30 to derive meteorological data at the observed site. Since the

orthometric heights derived from a global model include errors, the GPT adopts the ellipsoidal heights instead. (Boehm et al, 2007). The GPT uses site coordinates and day of year as input parameters, thus it does not need any external data source, which makes it easy to implement into the GNSS software packages.

The UNB3m and the GPT are both limited models that representing annual variations with a coarse spatial resolution. Consequently, short time variations in the atmosphere cannot be detected via analytical models that make them partly inefficient for real-time atmosphere monitoring during extreme weather events (Boehm et al. 2009).

Some weakness of the GPT model are compensated by a new model called GPT2 (Lagler et al, 2013; GPT2(w) - Böhm et al, 2015). The coarse resolution of the GPT (≈ 15°), which is insufficient to reflect the meteorological changes due to large height variations, is partly improved by adopting global 5° x 5° resolution grids. In addition, the GPT2 provides semi-annual harmonics that are more convenient to deal with very wet and very dry regions. The GPT2 is produced based on 10 years (2001-2010) of global monthly mean profiles for meteorological parameters of ERA Interim data (Dee et al, 2011). The phase is not fixed on January 28 as in the UNB and GPT, but estimated this time. The elevations of the GPT2 points are based on ETOPO5 land and seafloor elevations of 5-minute latitude and longitude grid. The latest analyses show that the GPT2 model improved previous GPT results almost 40 % in terms of station height differences in comparison to solutions using local pressure measurements and VMF1 mapping functions (Böhm et al, 2015). The GPT2 can produce the hydrostatic and wet mapping function coefficients for the VMF1, which are slightly worse than the ECMWF grid files.

ECMWF is an operational service carrying out scientific and technical research to improve Earth meteorological monitoring and disseminating numerical weather predictions to its contributors. The Institute of Geodesy and Geophysics (IGG) at the Vienna University of Technology provides zenith hydrostatic delays derived from the ECMWF data. In contrast with the GPT, the a priori ZHDs, which are derived from the ECMWF by numerical integration through pressure levels, is more accurate for short term and inter-seasonal variations. The IGG disseminated the ZHDs and ZWD data along with hydrostatic and non-hydrostatic mapping functions' coefficients (a_h, a_w) by global 2.0° x 2.5° grids known as VMF1 global grids (VMFG) (Boehm et al, 2009) file with a temporal resolution of 6 hours (i.e., 00:00, 06:00, 12:00, and 18:00

UTC). All grids data for a specific day can be retrieved the following day at 23:00 UTC. The latency is sufficient in order to conduct a lot of applications, however, for studies related to real-time or near real-time atmosphere monitoring it is beneficial to receive these parameters in real-time. Since the height data of the global grids derived from Digital Elevation Models (DEMs), the ZHD values computed based on these grids must be reduced to the station height by extrapolation (Steigenberger et al, 2009). Table 4.3 displays some basic properties of analytical models and numerical weather model derived from the ECMWF.

Table 4.3 : Some properties and availability of meteorological data from different sources (Böhm et al, 2009).

P, T, R_H	**Local Records**	**ECMWF**	**GPT**	**UNB3m**
Availability	At sites	All (Interpolation)	All	All
Time Span	Per observation	Since 1994	Unlimited	Unlimited
Spatial Resolution	Per site	2.0 x 2.5°	Spherical harmonics	Interpolation 5 Lat. bands
Time resolution	Per observation	6 h	Annual	Annual

4.3.3 Zenith wet delay

The derivation of a model for ZWD is far more challenging than one for the zenith hydrostatic delay. Highly variable and unpredictable water vapor amount in the low atmosphere with respect to time and speed is the main reason for that challenge. Furthermore, a surface temperature and water vapor content around the site can not reveal the behavior of the air masses above sites. Zenith wet delays may reach about few millimeters at the poles and 40 cm above the equatorial regions. Despite the fact that there are many empirical models available to model wet delays, the highest accuracy is expected when they are estimated as unknown parameters in the data adjustment. Still, due to lack of an appropriate alternative, some empirical models can be introduced to obtain initial values.

ZWD can be formulated as in equation 4.32:

$$ZWD = 10^{-6} \int_{h_0}^{\infty} N_w \, dz \tag{4.32}$$

in which the wet refractivity N_w can be expressed as the following equation (4.33):

$$N_w = k_2^{'} \frac{e}{T} + k_3 \frac{e}{T}. \tag{4.33}$$

Saastamoinen (1972) calculated the wet delay empirically as a function of water vapor pressure e_0 and temperature T_0 by using the following equation (4.34)

$$ZWD = 0.0022768\left(1255 + 0.05T_0\right)\frac{e_0}{T_0} \tag{4.34}$$

Askne and Nordius (1987) assumed a constant lapse rate (λ) and developed a wet delay model (i.e. equation 4.36) using mean temperature T_m and the partial pressure of water vapor e_0 derived from the model of Smith (1966) as given in equation 4.35.

$$e = e_0(\frac{P}{P_0})^{\lambda+1}, \tag{4.35}$$

$$ZWD = 10^{-6}\left(k_2^{'} + k_3 / T_m\right)\frac{R_d}{\left(\lambda+1\right)g_m}e_0 \tag{4.36}$$

where R_d is the specific gas constant of dry air, the constant λ variates with the season and site location and usually ranges between 1 and 5, and g_m is the gravitational acceleration. Another empirical model was developed by Mendes (1999) assuming a linear relation between ZWD and partial water vapor pressure as in equation 4.37:

$$ZWD \approx \frac{0.217e}{T}. \tag{4.37}$$

The water vapor pressure and temperature at the surface must be known in any case to use any of the empirical models mentioned above to model ZWD.

4.4 Slant Delay Models

The slant tropospheric delay is the total atmospheric delay along the signal path from the satellite to the receiver. The slant delay can be obtained either from external measurements such as ray-tracing through NWMs, radiosonde measurements, and WVR or estimated from GNSS observations. The radio signals usually arrive at the receiver from slant directions and delays are often modeled as the sum of the dry and wet delays that each of them is the product of zenith values and corresponding mapping

functions. According to Rothacher (1992), it is recommended to use different mapping functions for the dry and wet part of the delay as in equation (4.37) below:

$$\Delta\rho^{trop} = \Delta\rho_h^z \cdot mf_h(e) + \Delta\rho_w^z \cdot mf_w(e) \tag{4.37}$$

An elevation (e) dependent hydrostatic (i.e., $mf_h(e)$) and wet (i.e., $mf_w(e)$) mapping functions express the ratio of slant delays to delays in the zenith direction. The ZHDs are calculated with an accuracy better than 1 mm, but the accurate slant delay determination is prone to error due to imperfections of mapping functions and usually neglected azimuthal asymmetries. In addition, since the troposphere parameters are estimated together with the receiver clock parameters and the station coordinates, large correlations between these unknowns cause to incorrect estimations. De-correlation between the troposphere delays and the height estimates can be ensured by observing the satellites with low elevation angles. The accuracy of the mapping functions is crucial regarding mapping delays from low angles. Any large error in the mapping function reveals itself in the estimated zenith delay increases the station height uncertainty. Several researchers (Niell et al, 2001; Boehm et al, 2004) defined the rule of thumb that the station height error is approximately one-fifth of the delay error at 5° and at lower elevations.

4.4.1 Mapping functions

Mapping functions are used to relate the slant atmospheric delay coming from any direction to the zenith direction delay. The hydrostatic $mf_h(e)$ and wet $mf_w(e)$ mapping functions, respectively, are used to accomplish this task. Nowadays, several and well-established mapping functions are available, however, that to a first order all mapping functions may be approximated by using equation 4.38:

$$mf_h(e) \approx mf_w(e) \approx \frac{1}{\sin(e)} \tag{4.38}$$

where e is the elevation angle measured from the horizon to the satellite. In this approximation, the curvature of the Earth is neglected by assuming a flat and evenly stratified atmosphere and the thinner the atmosphere gets; the approximate mapping function gets closer to *1 / sine*. This mapping function is appropriate for high elevation angle observations (i.e., > 20°). The fundamental of mapping functions is based on

Saastamoinen (1972) cosecant model that avoids the earth curvature. It was developed for high elevations and causes an error of about 0.1 m in the range correction at a minimum elevation angle of 10°. In a parallel with the Saastamoinen, expressions for tropospheric corrections were derived and published by Marini (1972) who was the first one came up with the idea to use continued fractions with constants i.e. *a, b* and *c* as expressed in equation 4.39 below:

$$mf_{h,w}(e) = \cfrac{1}{\sin e + \cfrac{a}{\sin e + \cfrac{b}{\sin e + \cfrac{c}{\sin e + \ldots}}}} \tag{4.39}$$

The continued fractions have advantages over models with Taylor expansions, i.e. the Saastamoinen model that they fit for nearly the whole range of zenith angles. Marini verified his model with respect to standard atmosphere model, but not with real meteorological data. He found an agreement with standard atmosphere model almost 0.3 % down to elevation angle 1°. However, the verification with radiosonde data revealed large standard deviation of range corrections from 20 mm in zenith to 200 mm at 10° elevation angles (Niell, 1996).

Chao (1974) developed the first mapping function which uses continued fractions with two terms *a* and *b*. After evaluation of two-year radiosonde data, he used different coefficients for the dry (a_h) and the wet part (a_w) and replaced the second term in the equation 4.39, *sin(e)*, by *tan(e)* to get unity in the zenith direction.

The CfA-2.2 mapping function (Davis et al, 1985) was designed to achieve sub-centimeter accuracy down to 5° elevation angle. By fitting 57 ray-tracing through the standard atmosphere data with elevation angles between 5 ° and 90°, the coefficients a, b, and c were calculated as a function of pressure, water vapor pressure, a temperature at the Earth's surface, temperature gradients, and a height of the troposphere. With this model, the standard deviation of the range corrections shows improvement of nearly 90 % with respect to Chao's mapping function. Ifadis (1986) developed a hydrostatic mapping function that can be used down to 2° elevation. He ray-traced the real weather profiles from various sites distributed over large areas of the world and with different climatic conditions.

The MTT (i.e., MIT Temperature) mapping function was developed by Herring (1992) as a function of latitude, height, and site temperature. The MTT represents the elevation angle dependence of the tropospheric delay down to 3° with an RMS of a less than 0.2 mm. Apart from Davis et al. (1985), Herring did not use the standard atmosphere model, but determined expressions for the dry (a_h, b_h, c_h) and wet coefficients (a_w, b_w, c_w) with ray-tracing radiosonde data at ten locations, in the US, located near VLBI stations. The ray tracing methods were performed at sixteen elevation angles between 3° and 90°. The MTT mapping functions are based on a slightly changed continued fraction as expressed in equation 4.40:

$$mf_{h,w}(\varepsilon) = \frac{1+\dfrac{a_{h,w}}{1+\dfrac{b_{h,w}}{1+c_{h,w}}}}{sin\varepsilon+\dfrac{a_{h,w}}{sin\varepsilon+\dfrac{b_{h,w}}{sin\varepsilon+c_{h,w}}}}. \tag{4.40}$$

The strong dependence of mapping functions like those of CfA-2.2, MTT, and Ifadis to surface temperatures, which are far from representing the behavior of the upper troposphere, cause an error in the hydrostatic mapping functions. Therefore, Niell (1996) aimed at developing New Mapping Functions (NMF) to produce mapping functions that are independent of surface meteorological parameters. The NMF is based on a form shown in the equation 4.40 and the input parameters to determine the coefficients are DoY, station latitude, and station height. Therefore, the NMF has been widely used in GNSS campaigns due to its simple solution that does not need an external data to derive a mapping function. Niell used ray-tracing method to nine temperature and relative humidity profiles of the US Standard Atmosphere. One for north latitudes of 15° for the whole year, and two for north latitudes of 30°, 45°, 60°, and 75°, for the months January and July down to 3°. As a result, he retrieved the dry and the wet coefficients of the mapping functions that almost covering the northern hemisphere as illustrated in Table 4.4. Additionally, the height correction for the hydrostatic NMF is introduced because of the fact that mapping functions' values increase with an altitude, i.e. the atmosphere above the site becomes flatter. The Isobaric Mapping Function IMF (Niell, 2000) was introduced to determine mapping

functions coefficients (a_h and a_w) by favor of NWMs' 6-hour resolution data while the coefficients *b* and *c* are derived from empirical functions.

Table 4.4 : Coefficients of the Niell hydrostatic and wet mapping functions (Niell, 1996).

coeff.	$\varphi = 15^\circ$	$\varphi = 30^\circ$	$\varphi = 45^\circ$	$\varphi = 60^\circ$	$\varphi = 75^\circ$
a_{avg}	1.2769934e-3	1.2683230e-3	1.2465397e-3	1.2196049e-3	1.2045996e-3
b_{avg}	2.9153695e-3	2.9152299e-3	2.9288445e-3	2.9022565e-3	2.9024912e-3
c_{avg}	62.610505e-3	62.837393e-3	63.721774e-3	63.824265e-3	64.258455e-3
a_{amp}	0.0	1.2709626e-5	2.6523662e-5	3.4000452e-5	4.1202191e-5
b_{amp}	0.0	2.1414979e-5	3.0160779e-5	7.2562722e-5	11.723375e-5
c_{amp}	0.0	9.0128400e-5	4.3497037e-5	84.795348e-5	170.37206e-5
a_{wet}	5.8021897e-4	5.6794847e-4	5.8118019e-4	5.9727542e-4	6.1641693e-4
b_{wet}	1.4275268e-3	1.5138625e-3	1.4572752e-3	1.5007428e-3	1.7599082e-3
c_{wet}	4.3472961e-2	4.6729510e-2	4.3908931e-2	4.4626982e-2	5.4736038e-2

Niell used the dependency of the hydrostatic mapping function with the atmospheric thickness and examined a relation between the mapping function coefficients and the geopotential height of constant pressure levels (isobaric levels). He found that a level of 200 hPa is one of the appropriate to represent the thickness of the atmosphere. He determined the coefficients *b* and *c* using empirical functions while the coefficient "a" was obtained from the re-analyses data of numerical weather models. Furthermore, to extract the wet coefficients, Niell proposed to use a coarse ray-trace at 3.3° initial elevation angle through numerical weather models. Böhm and Schuh (2004) developed the Vienna Mapping Functions (VMF) based on a rigorous ray tracing through ECMWF weather model. The VMF was developed to compensate some weak parts of IMF, e.g. the coarse vertical resolution is improved by interpolation, and the atmospheric bending effect is considered as a part of the hydrostatic mapping function. A ray tracing was carried out at an initial elevation angle of 3.3° and the hydrostatic and the wet coefficients are computed. The coefficient *a* was determined from the ray trace data while the coefficients *b* and *c* were extracted from the empirical functions

using the day of the year and site latitude as inputs. Due to the strong correlation between the coefficients *a*, *b* and *c* any imperfection in functions determining the *b* and the *c* causes in errors in the determination of the coefficient *a*. Thus, mapping functions and delays will be erroneous as well as station height estimates (e.g., a miscalculation of the VMF coefficients *b* and *c* in the Antarctica region resulted with discrepancies up to 4 mm in the mean station height). Böhm et al. (2006a) upgraded VMF to Vienna Mapping Function 1 (VMF1) by compensating some inefficiencies of the coefficients *b* and *c* and by recalculating the coefficient *a*. The $a_{h,w}$ coefficients were determined from ray tracing through pressure levels of ECMWF data. The coefficients $b_{h,w}$ and $c_{h,w}$ on the other hand, are derived empirically from 1-year ECMWF data in least squares fit. These coefficients are provided with 6 hours temporal resolution (00, 06, 12, and 18 UTC) as site specific or by global grids of 2.5° x 2.0° (VMFG) from FTP site of the IGG. The VMFG can be used to calculate coefficients for the location of interest with the agreement of 1.0 and 2.0 mm in the horizontal and vertical position component, respectively, in comparison to the site-specific VMF1 (Kouba, 2008). Using data from numerical weather models with 6-hour resolution is the main drawback of the VMF1 model because its implementation to GNSS software packages gets complicated.

The objective of the Global Mapping Function (GMF; Boehm et al. 2006b) is to provide a mapping function parameter that available globally with spherical harmonics expansion up to degree and order 9. The GMF is an empirical mapping function developed from 3 years of ECMWF 40 years data (ERA40; Uppala et al. 2005). The coefficients $b_{h,w}$ and $c_{h,w}$ were computed similarly to the VMF1 whereas the coefficients $a_{h,w}$ were determined using 312 grid points and 36 monthly mean profiles of pressure, temperature, and humidity data. Hence, at each of the 312 grid points, 36 monthly values for the coefficient *a* were determined for both: hydrostatic and wet mapping functions. Using the height correction of Niell (1996), the hydrostatic coefficients were reduced to the mean sea level heights. The annual means a_0 and amplitudes (*A*) are then estimated by fitting these monthly-reduced values to the sinusoidal function, i.e. equation 4.41, in which the phases referred to January 28.

$$a = a_0 + A \cdot \cos\left(\frac{doy - 28}{365.25} 2\pi\right). \tag{4.41}$$

The estimated mean values a_0 and amplitudes A at each grid points are expanded into spherical harmonic up to degree and order 9 in a least squares fit as in equation 4.42.

$$a_0 \text{ or } A = \sum_{n=0}^{9}\sum_{m=0}^{n} P_{nm}(\sin\varphi)\cdot\left[A_{nm}\cos(m\lambda) + B_{nm}\sin(m\lambda)\right] \tag{4.42}$$

where φ is the site latitude, P_{nm} is the Legendre polynomials; B_{nm} and A_{nm} are the spherical polynomial coefficients derived from the least squares adjustment. The hydrostatic and wet mapping function coefficients $a_{h,w}$ are available at any site and for any day of year. Having similar characteristics with the GPT, GMF's ability to account short-term variations within a short period is limited. On the contrary, the GMF reflects seasonal variability and agrees well with the VMF1 in this respect. Despite being dependent on the ECMWF data, the VMF1 is still the most consistent and accurate mapping function for geodetic applications. The mapping functions for the GMF and the VMF1, which computed on May 16, 2013 at 5º elevation angle at mean sea level, are compared in Figure 4.4. Due to the frequently updated ECMWF data (i.e., four times a day), the hydrostatic and wet mapping functions of the VMF1 are much more sensitive to changes in the atmosphere within a day.

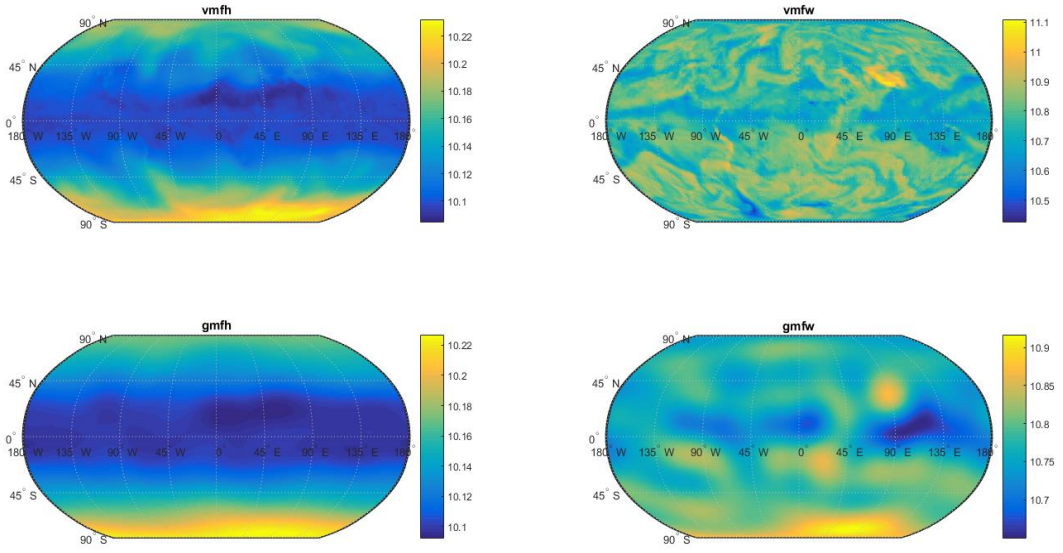

Figure 4.4 : The hydrostatic and wet mapping functions comparison among the VMF1 and GMF for DOY: 136, 2013 at 5º elevation angle at mean sea level.

4.4.2 Azimuthal Asymmetry and Horizontal Gradients

Up until now, the mapping functions and tropospheric path delays were discussed by assuming horizontally layered and azimuthal symmetric atmosphere. However, the

thickness of the atmosphere is not equal everywhere and increases from polar to the equatorial regions. The path toward the equator is longer than the path toward the pole, in particular for low elevation observations. Moreover, the signal will interact with regions, which include different water vapor density and atmospheric conditions due to the azimuthal asymmetry.

Parameterization of horizontal gradients and estimate them via LSA is a valid way to overcome these asymmetries. The station coordinate repeatability may be considerably improved by this measure, as shown by Rothacher and Beutler (1998) and Meindl et al. (2004). One way to model the asymmetry is to assume a tilted atmosphere as given in Figure 4.5.

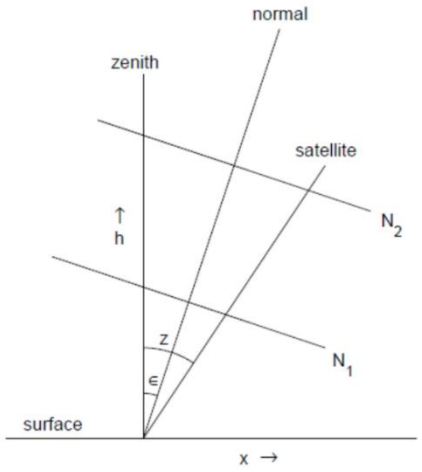

Figure 4.5 : Tilting of the tropospheric zenith (MacMillan, 1995).

In the tilted atmosphere, the refractivity *N* is expressed as function (equation 4.43) of height *H* and horizontal position $\vec{x}$.

$$N(\vec{x},h) = N(0,h) + \nabla\vec{N} \cdot \vec{x}. \tag{4.43}$$

where *N(0, h)* is the refractivity above the site, $\vec{x}$ is the horizontal position vector; and $\nabla\vec{N}$ is the linear horizontal gradient vector of refractivity at height *h*. The dot in the equation 4.43 denotes the inproduct multiplier. The gradient vector is given by equation 4.44:

$$\nabla\vec{N} = \frac{\partial N}{\partial \vec{x}}|_{\vec{x}=0} . \tag{4.44}$$

The elevation (e) and azimuth (a) dependent total tropospheric delay in an azimuthal asymmetric atmosphere may be defined as the sum of the symmetric delay and the correction term owing to azimuthal asymmetry as expressed in equations 4.45 and 4.46:

$$ZTD(a,e) = 10^{-6}\int_0^{\infty} N(s)\,ds = 10^{-6}\int_0^{\infty} N(0,h)\,ds + 10^{-6}\int_0^{\infty}\left(\nabla\vec{N}\ .\vec{x}\right)ds, \tag{4.45}$$

$$ZTD(a,e) = ZTD_0(e) + 10^{-6}\int_0^{\infty}(\nabla\vec{N}\cdot\vec{x})ds. \tag{4.46}$$

where $ZTD_0(e)$ is the symmetric delay that neglecting gradients.

The basic relations between the North (i.e G_n) and the East (i.e G_e) direction gradients and tilted atmosphere were given by Niell et al. (2001) and by MacMillan (1995) who proposed to use the simple model as given in equation 4.47.

$$\Delta\rho(a,e) = m_f(e)(\Delta\rho_z^{trop} + \cot(e)\left(G_n\cos(a) + G_e\sin(a)\right). \tag{4.47}$$

The gradients must be estimated in GNSS data adjustment along with station coordinates, clocks and wet delays, in particular when observing at low elevation angles. On the other hand, there is no need to apply a priori gradients if no constraints are specified beforehand on the estimates.

4.5 GNSS METEOROLOGY

4.5.1 The role of water vapor

Water vapor is a significant parameter for meteorological applications like weather forecasting. It enters the atmosphere by evaporation, changing its own state into liquid water and forming clouds by condensation and return to the earth surface by precipitation. During the evaporation and condensation, the heat energy redistributed quickly because of the fast moving water through the atmosphere. Water vapor is also one of the most important greenhouse gases that stands for more than 80 % of the total greenhouse effect that its molecules absorb long wave infrared radiation radiated back from the Earth's surface and prevent the radiation from escaping into outer space. As a result, the absorbed energy warms the atmosphere and the surface of the Earth. Due to the strong relation with temperature, an increase of the water vapor by 5-7 % results

in an increase of temperature of 1 K (Trenberth et al, 2003). In order to carry out short-term weather forecast analysis, the highly variable water vapor must be modeled accurately in real time. Today, a number of techniques available to use for extraction of atmospheric water vapor.

4.5.2 Measurement techniques of water vapor

Absolute humidity (ρ_v) is a measure of the actual amount of water vapor in a given volume of air. Thus, the integrated water vapor content (IWV (kg/m^2) of the atmosphere above an observed station is closely related with absolute humidity as given by equation 4.48:

$$IWV = \int_0^\infty \rho_v(h)\,dh = \frac{1}{R_w}\int_0^\infty \frac{p_w}{T(h)}\,dh \tag{4.48}$$

where the height above the site h (zenith) defined in meters, R_W is the specific gas constant of water vapor and determined as $461.522 \pm 0.008\,\mathrm{J/kg\,.\,K}$, T_h is the absolute temperature in Kelvin, p_w is the partial pressure of water vapor in hPa. Another parameter to reflect the amount of water vapor is the PWV, which is identical to the height of an equivalent column of liquid water in the air above of the observing site and can be expressed as in equation 4.49:

$$PWV = \frac{IWV}{\rho_W}. \tag{4.49}$$

IWV corresponds to Integrated Water Vapor in the zenith direction and ρ_w is the density of liquid water that is equal to $1000 \pm 0.002\ \mathrm{kg/m^3}$. The atmospheric water vapor content can be measured with balloon-borne instruments such as radiosonde network or via aircraft and satellite-based measurements (e.g., GNSS, Remote Sensing techniques).

4.5.2.1 Radiosondes

A radiosonde is a tool suspended below of small weather balloon filled with hydrogen or helium gas and joined with a radio transmitter to measure the vertical profile of IWV and to collect information about refractivity field of the atmosphere. During ascending period, the radiosonde transmits data received by equipped sensors on temperature, pressure, humidity, and wind to the receiving station on the ground. From

a technical aspect, a radiosonde provides only pressure, temperature, and humidity but when the position of the radiosonde is tracked through GPS or Radio Detecting and Ranging (RADAR), the strength and direction of winds can be determined by tracking the position of the balloon, which is known as Rawinsonde measurements. Most of the radiosonde observations are taken at 00:00, 00:06, 12:00 and 18:00 UTC from about 2,700 upper air stations around the world. The Integrated Global Radiosonde Archive (IGRA) is a part of the National Oceanic and Atmospheric Administration (NOAA) and collects radiosonde data from stations around the world and share the data free of charge via HTTP or FTP protocols (Url-8). The earliest data is older than a hundred years, and the recent is downloadable almost in near real time. All IGRA data is provided in plain ascii text files, which include information about pressure, temperature, geopotential height, relative humidity, wind speed, and direction as shown in Figure 4.6. All radiosonde data gathered from distributed stations worldwide take an instantaneous picture of the atmosphere and thus, become significant input for real time and near real time weather forecast applications. Radiosonde has offered long and continuous time series for almost sixty years; however, its measurements are limited considering sensor instability, low traceability, and lower spatial and temporal resolution.

10393 Lindenberg Observations at 00Z 25 May 2013

PRES hPa	HGHT m	TEMP C	DWPT C	RELH %	MIXR g/kg	DRCT deg	SKNT knot	THTA K	THTE K	THTV K
1000.0	80									
996.0	115	9.6	6.3	80	6.04	310	6	283.1	300.0	284.1
951.0	497	8.8	0.8	57	4.28	0	13	286.0	298.4	286.8
947.0	532	8.5	0.8	58	4.29	5	14	286.0	298.4	286.8
925.0	725	6.6	0.6	66	4.34	0	12	286.1	298.6	286.8
871.0	1215	2.2	-0.8	81	4.16	349	12	286.4	298.5	287.1
851.0	1403	1.0	-6.0	60	2.88	345	12	287.1	295.6	287.6
850.0	1412	1.0	-6.0	60	2.89	345	12	287.2	295.7	287.7
834.0	1564	0.0	-5.7	65	3.00	330	12	287.7	296.6	288.2
819.0	1710	-0.9	-5.5	71	3.11	333	13	288.2	297.5	288.8
812.0	1778	-0.9	-9.9	50	2.23	334	13	288.9	295.7	289.3
807.0	1827	-1.3	-8.8	57	2.44	335	14	289.1	296.4	289.5
792.0	1977	-2.4	-5.5	79	3.21	310	14	289.4	298.9	289.9
791.0	1987	-2.5	-5.3	81	3.27	310	13	289.4	299.1	290.0
773.0	2169	-3.9	-6.3	83	3.10	310	10	289.8	299.0	290.3
758.0	2323	-5.1	-7.2	85	2.95	324	7	290.1	299.0	290.6
722.0	2704	-8.0	-8.7	95	2.77	0	0	291.0	299.3	291.5
721.0	2715	-8.1	-8.7	95	2.76	6	1	291.0	299.4	291.5
710.0	2834	-7.3	-10.6	77	2.41	75	10	293.2	300.6	293.6
705.0	2889	-6.9	-11.5	70	2.26	75	12	294.2	301.2	294.6
700.0	2945	-7.3	-9.3	86	2.71	75	14	294.4	302.7	294.9
697.0	2979	-7.5	-9.4	86	2.71	75	14	294.6	302.9	295.1
696.0	2990	-7.5	-9.4	86	2.71	75	14	294.6	302.9	295.1
694.0	3012	-7.5	-14.5	57	1.80	76	13	294.9	300.5	295.2
680.0	3171	-8.9	-10.0	92	2.64	79	12	295.0	303.2	295.5
675.0	3228	-9.2	-10.3	92	2.60	80	12	295.3	303.3	295.8
656.0	3449	-10.4	-11.6	91	2.42	65	12	296.4	303.9	296.9
654.0	3472	-10.5	-11.7	91	2.40	68	12	296.5	304.0	297.0
650.0	3520	-10.5	-15.3	68	1.80	74	11	297.1	302.8	297.4
639.0	3651	-11.1	-12.4	90	2.32	90	11	297.8	305.1	298.2
624.0	3834	-12.1	-17.1	66	1.61	113	10	298.7	303.9	299.0
616.0	3932	-12.6	-17.0	70	1.65	125	10	299.2	304.5	299.5
608.0	4031	-13.1	-16.9	73	1.68	135	10	299.7	305.1	300.0
590.0	4260	-14.3	-16.6	83	1.77	140	12	300.9	306.6	301.2

Figure 4.6 : IGRA file sample collected from Lindenberg radiosonde station located in Germany.

Pressure (*P*), temperature (*T*) and partial pressure of water vapor (*e*) from the radiosonde data are utilized to compute PWV as determined by Bevis et al. (1992) as in equation 4.50 where the water vapor density can be expressed with equation 4.51.

$$PWV = \frac{1}{\rho_W}\left(h_{i+1} - h_i\right)\cdot\left(\rho_v^{i+1} + \rho_v^i\right)/2, \tag{4.50}$$

$$\rho_v = \frac{e}{R_v \cdot T}. \tag{4.51}$$

where the variable ρ_v corresponds the water vapor density, ρ_w is the liquid water density, *i + 1* and *i* represent the top and bottom of each vertical layer for height and for water vapor density, *T* is the temperature and *e* is the partial pressure of water vapor and $R_v = 461.525 JK^{-1}kg^{-1}$ is the specific gas constant of water vapor.

4.5.2.2 Water vapor radiometer

Water Vapor Radiometer (WVR) is a radio technique that is used to obtain the wet delay of the troposphere. It observes the thermal radiation from the sky at microwave frequencies near the water vapor spectral line (i.e., 22.235 GHz) where the reduction in the intensity of electromagnetic radiation due to the water vapor is relatively higher. The reduction of electromagnetic radiation will depend upon frequency, temperature, pressure, humidity, and liquid water content in the atmosphere.

The brightness temperature T_B defined as a measurement of the radiance of the microwave radiation traveling through the atmosphere, expressed in units of the temperature of an equivalent black body. The brightness temperatures, measured at different microwave frequencies, are used to derive wind, vapor, and cloud and rain products in meteorological applications and calculated from the equation of radiative transfer as given in the following equation (4.52).

$$T_{bf} = T_{bg}^{e^{-\tau(f)}} + \int_0^\infty T(h)\alpha(f,h)e^{-\tau(f,h)}dh \tag{4.52}$$

where T_{bg} is the cosmic background temperature and equals to 2.7 K; α is the total attenuation due to water vapour, oxygen and, liquid water while the opacity $\tau(f,h)$ is given by equation 4.53 as below:

$$\tau(f,h) = \int_0^h \alpha(h', f)dh' \tag{4.53}$$

The brightness temperature varies with temperature, pressure, humidity, and liquid water content in the atmosphere. These meteorological parameters are also much or less sensitive to different frequencies. In order to extract the water vapor content, the frequency close to the 22.23 GHz is the most proper one while for the retrieval of the pressure or the temperature, 60 and 120 GHz frequencies are much more sensitive.

The sensitivity of frequency for different meteorological parameters also changes with an altitude, e.g., water vapor content close to the earth surface is captured much well by frequencies that are more sensitive to ground vapor content. Contrary, some frequencies are much more convenient to capture the high altitude water vapor content. Therefore, using radiometer measurements of different frequencies for different heights could be utilized to estimate the atmosphere humidity profile above the site. Tropospheric zenith wet delay and integrated water vapor then can be derived from the humidity profile. The need for multiple channels to obtain the radiometric humidity profile of the atmosphere, however, is an expensive process. Furthermore, finding the optimum set of radiometric water vapor channels to estimate IWV by passing through the atmosphere is extremely difficult.

By using brightness temperatures at two different frequencies, the wet delay can be calculated (Jarlemark, 1997) as in equation 4.54:

$$\Delta L_w = k[(f1/f2)^2 T_{bf1}^{'} - T_{bf2}^{'} - T_{bg,ox}] \tag{4.54}$$

where T'_{bf1} and T'_{bf2} are linearized brightness temperature that can be obtained from the opacity (τ) and linearized effective temperature (T'_{eff}); $T_{bg,ox}$ is the contribution coming from oxygen and from cosmic microwave background and k is the retrieval coefficient modeled by function of temperature, pressure and humidity.

One disadvantage with radiometers except being expensive is: they are not operable during rainy weather. Moreover, due to the large antenna beam width of radiometers, observations are limited to elevation angles of higher than 15° in order to prevent antennas to collect scattering radiation from the ground.

4.5.2.3 Very long baseline interferometry (VLBI)

The possibility to infer the water vapor amount in the air from space geodetic observations has been demonstrated during the last 25 years. Very Long Baseline Interferometry (VLBI) is the space geodetic technique determines the reference frame for the Earth and provides information about the motions of the solid Earth and measures Earth's orientation changes due to gravitational changes and redistribution of the Earth's angular momentum. VLBI uses radio telescopes distanced by up to thousands of kilometers on the earth surface and measures the time difference between the arrivals at two telescopes of radio signals emitted from far away radio source quasars. The time delay is dependent on the baseline length between the radio telescopes and angular separation between radio source. The signal coming from the radio source arrive at different radio telescopes at different times. Using the time delays, some unknown parameters such as telescope positions, earth orientation and rotation parameters and ZWDs along with horizontal delay gradients can be estimated from many quasars observed with a global network of radio telescopes.

VLBI determines the inertial reference frame (i.e., ICRF) defined by the quasars coordinates and the precise positions of the antenna in the TRF (i.e., ITRF2008). In VLBI, the hydrostatic delays, which are generally computed based on Saastamoinen (1972), are introduced to the VLBI observations as the a priori troposphere (ZHD) while the ZWDs and horizontal gradients are estimated with the LSA as seen in GNSS. All time-dependent parameters such as tropospheric delays and gradients use a piecewise continuous linear functions in order to form a design matrix of the adjustment.

The main findings of the multi-technique comparisons of ZTD estimates conducted during Continuous VLBI Campaign 2008 (IVS-CONT08) shows that the biases between VLBI and GNSS collocated sites are below 5 mm as depicted in Figure 4.7 and the median standard deviations of differences are within 4 mm (Teke, 2011). The comparisons with GNSS are promising, however, the VLBI is not a convenient method to monitor water vapor content, for both at global and at local scale, because of a low number of telescopes (i.e., less than 150) and few number of sessions per year (between 20 – 30). Furthermore, most of the VLBI telescopes are located in the Northern Hemisphere that reduces the spatial resolution of derived water vapor.

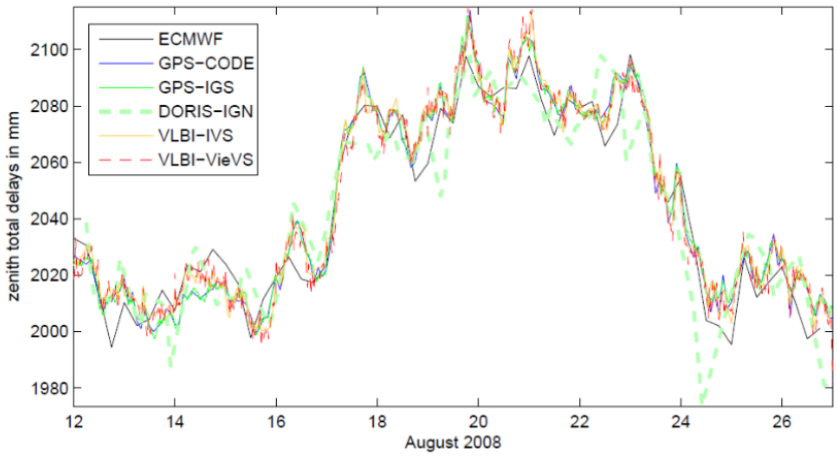

Figure 4.7 : Intra / inter-technique comparison of tropospheric zenith path delay during the IVS-CONT08 campaign for co-located site HartRAO – Hartebeesthoek / South Africa (Teke, 2011).

4.5.2.4 GNSS

Since the introduction of GNSS Meteorology in the 1990s, GNSS has been recognized as a cost-effective approach to determine water vapor amount in the atmosphere. Atmospheric water vapor shows sharp variations both temporally and spatially due to heat circulation, the wind and other effects like atmospheric turbulences and it must be measured with a high accuracy to produce consistent inputs to be assimilated by NWMs.

Traditional methods such as radiosonde and WVR are not competent in terms of spatial and temporal resolution in comparison to the continuous and dense GNSS having more than 400 stations worldwide. Under the assumption of highly accurate orbits and clocks used in the analyses, ZWD estimates of GNSS measurements provide an accuracy within ± 5 mm. PWV, which is approximately 0.16 of ZWD can fluctuate by more than 15 %, due to latitude and seasonal changes (Fölsche, 1999). Based on this information, if the accuracy of ZWD estimates is about ± 5 mm, the PWV derived from the ZWDs have an accuracy of about ± 1 mm and it is a good approximation in order to use the ZWDs in the weather or climate related studies.

Several regional and global projects have been performed in order to prove the contribution of assimilation of GNSS ZWDs into the NWMs for meteorological applications. COST-716 project (Elgered et al. 2005), TOUGH (Vedel, 2006), and E-GVAP, WAVEFRONT in Europe, BALTEX in Baltic Sea, and MAGIC in Mediterranean. In all these projects and others, the zenith wet delay values were used

to improve NWMs' quality of the weather monitoring systems.

The wet delays used to derive a precipitable water vapor representing the total mass of water vapor in an atmospheric column with the unit area. Following the equations 4.53 and 4.54 give the empirical relation between the ZWD and the PWV by Bevis et al. (1992) we get the following equations (4.55 and 4.56) that used for conversion:

$$PWV = \kappa \cdot \Delta \rho_w^z \tag{4.55}$$

$$PWV = \frac{10^{-6} M_W}{\rho R(k_2^{'} - k_1 \frac{M_W}{M_D} + \frac{k_3}{T_m})} \cdot ZWD \tag{4.56}$$

where κ is the unitless conversion factor, k_2' and k_3 are empirical constants defined by Rüeger (2002) and listed in the Table 4.1, R_w is the specific gas constant for water vapor $\left(\approx R/M_W\right)$; M_W is the molar mass of water vapor, R defines the universal gas constant, q_W is the density of liquid water in $\left(kg/m^3\right)$ and T_m is the integrated mean temperature computed from vertical profiles of the water vapor pressure *(e)* and observed surface temperature *T*.

The formulation used for calculating integrated mean temperature along a path from site to the top of the troposphere is given below as in equation 4.57.

$$T_m = \frac{\int_s^\infty \frac{e}{T} ds}{\int_s^\infty \frac{e}{T^2} ds} \tag{4.57}$$

Such temperature data either derived from radiosonde or calculated from operational NWMs (e.g., ECMWF reanalysis data) (Wang et al. 2005). In absence of this data, the empirically derived model by i.e., Bevis et al. (1992) (equation 4.58) can be used:

$$T_M \approx 70.2 + 0.72 T_0 \tag{4.58}$$

where T_0 is the earth surface temperature.

This empirical formula was found by Bevis et al. (1992) after 2-year measurements of more than 8000 profiles of radiosonde launches at 13 stations covering the area

between latitudes of 17° and 65° in the northern hemisphere. Standard deviation is ± 4.70 K and with accurately known ZWDs and surface temperature, the PWV can be derived with an average error less than 4 %. The sensitivity of GNSS PWV relatively to the uncertainty of conversion factor κ has been estimated by Bevis et al. (1994) to be of the order of 1 or 2 %.

5. CENTRAL EUROPEAN FLOODING

At the end of May and the beginning of June in 2013, a large area in the Central Europe experienced high precipitation amounts, as can be seen from Figure 5.1, due to severe rains. Several places received as much as normal monthly precipitation within just one or two days. The excess of precipitation resulted in high levels in European rivers such as Rhine, Elbe, and Danube. Water levels of the Danube in Budapest exceeded their highest point in at least 100 years. Thousand people had to be evacuated from places in Germany, Czechia, and Austria.

Figure 5.1 : Flooding effect on Passau near the Danube River – Geromany (left), Dresden near the Elbe River - Germany (right) on June 2, 2013 (European Reanalyses and Observations for Monitoring – EURO4M, 2013).

Precipitation amounts during late May and early June reached values over 100 mm in the area covering Switzerland, Austria, southern and eastern Germany and Czechia. The highest amount was observed in the last two days of May and first two days of June as illustrated in Figure 5.2. Elbe and Danube, which are the two main river basins in the region and reached values of 93 mm and 74 mm for 10-day accumulated precipitation amounts as can be seen in Figure 5.3. For many regions in central Europe, the weather in May 2013 preceding the flooding had been one of the wettest in last 100 years. Austria saw twice as much rainfall as average during the month (Update Starkregen und Rückblick Mai - ZAMG, 2013). Germany experienced record level of soil moisture prior to rains. (SMOS Maps Record Soil Water before Flood, 2013).

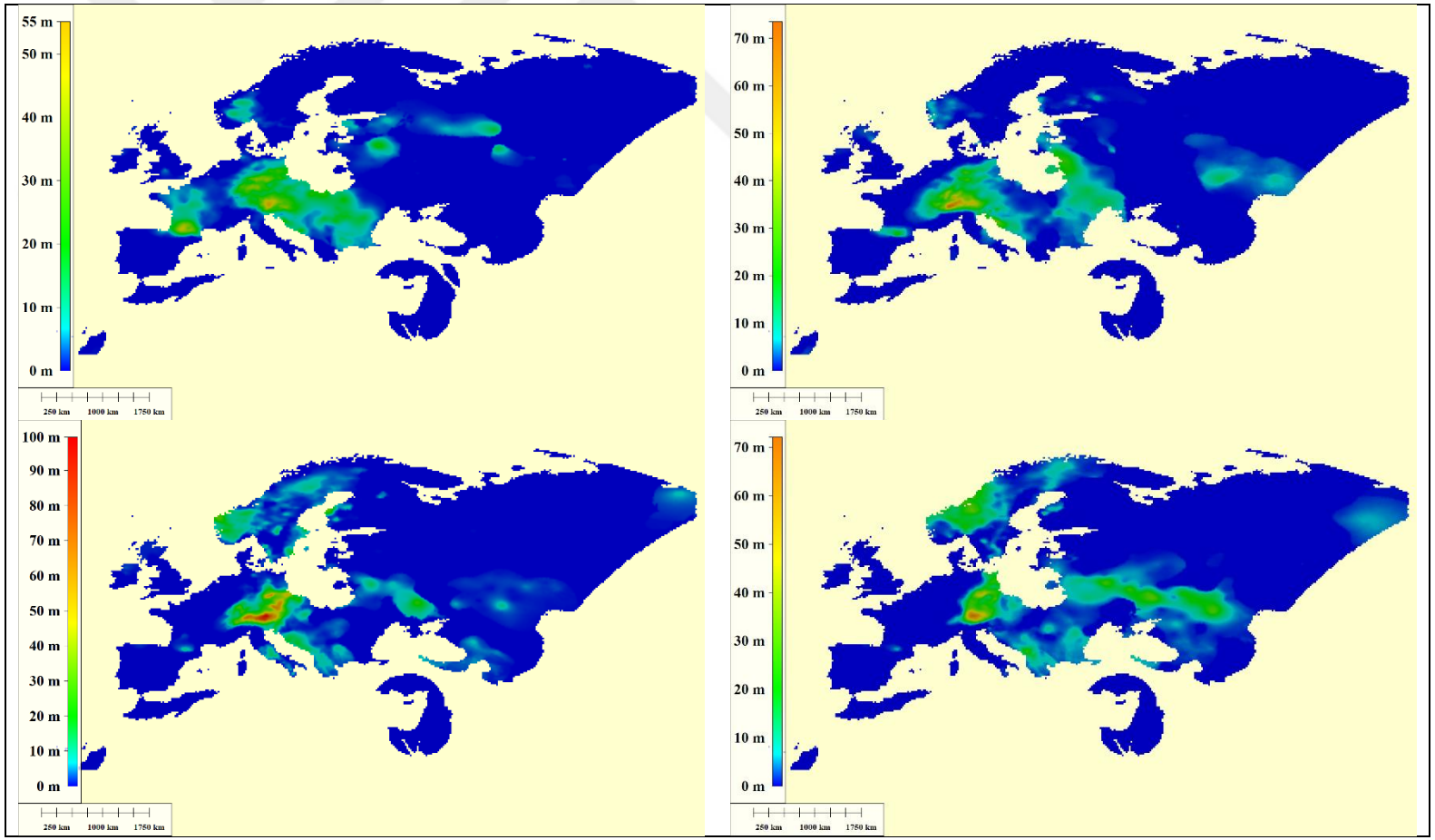

Figure 5.2 : Daily precipitation amounts in the period 30 May – 2 June (From upper left to lower right). Gridded precipitation maps derived from E-OBS dataset (ASCII) by Global Mapper.

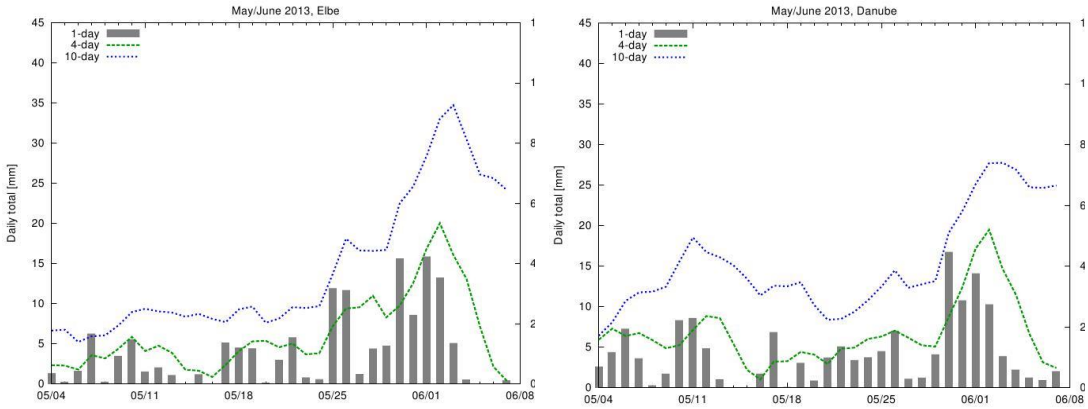

Figure 5.3 : Time series of 1-, 4- and 10-day accumulated precipitation amounts for the river basins of the Elbe (left) and the Danube west of 20° E (right) (European Reanalyses and Observations for Monitoring – EURO4M, 2013).

Since extreme weather passages are usually associated with variations of the water vapor, the zenith tropospheric delays, which are closely related to the water vapor, were monitored during the extreme period. Thus, observations of 11 IGS sites, which were selected from the affected area, were processed by GNSS PPP for the period from May 20 to June 10, 2013.

Table 5.1 lists the IGS sites from the region in the central Europe where the severe weather conditions were experienced.

Table 5.1 : IGS sites selected for monitoring the atmosphere during severe weather.

Site	Latitude	Longitude	Height	Receiver Type	Antenna Type	Location
FFMJ	50.09057	8.66496	178.213	JPS LEGACY	LEIAR25.R4	Germany
GANP	49.03471	20.32293	746.0138	TRIMBLE NETR9	TRM55971.00	Slovakia
GOPE	49.913705	14.78562	592.598	TPS NETG3	TPSCR.G3	Czech Rep
GRAZ	47.06713	15.49348	538.279	LEICA GRX1200+GNSS	LEIAR25.R3	Austria
LEIJ	51.35398	12.37410	178.394	JPS LEGACY	LEIAR25.R3	Germany
POTS	52.37929	13.06609	144.417	JAVAD TRE_G3TH DELTA	JAV_RINGANT_G3T	Germany
PTBB	52.29619	10.45974	130.230	ASHTECH Z-XII3T	ASH700936E	Germany
WARN	54.16978	12.10142	50.739	JPS LEGACY	LEIAR25.R3	Germany
WROC	51.11320	17.06204	180.808	LEICA GR25	LEIAR25.R4	Poland
WTZR	49.14419	12.87891	666.012	LEICA GRX1200+GNSS	LEIAR25.R3	Germany
ZIMM	46.87709	7.46527	956.335	TRIMBLE NETRS	TRM29659.00	Switzerland

All of these IGS stations are equipped with a dual-frequency GNSS (i.e., GPS, GLONASS and GALILEO) receiver and distributed in the area as displayed in Figure

5.4. The baseline lengths between the two closest stations in the area varies between 150 km and 1500 km, which is not an ideal distribution to perform a GNSS Network solution due to fact that baseline solutions presents meaningful result for weather monitoring if only a dense GNSS network is established (e.g., < 5 km). PPP observations, on the other hand, give significant information above the observed site alone, thus, densified campaigns are needed in order to interpret large-scale weather events.

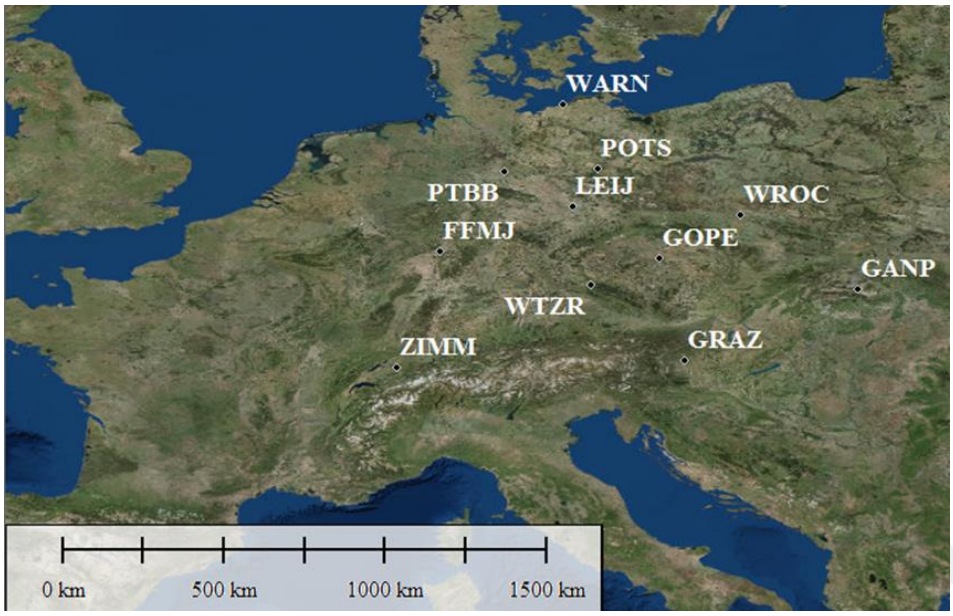

Figure 5.4 : Observed IGS sites for performing the GNSS Meteorology experiment during severe weather conditions.

The stations of GOPE, PTBB, ZIMM, WARN and WTZR that are located in the region are also equipped with pressure and temperature sensors offering in-situ meteorological data that can be used in the calculation of a priori tropospheric delays (i.e., ZHD).

In addition to the tropospheric path delays, the site coordinates, the receiver clocks, and the phase ambiguities were also parameterized and estimated in the PPP solutions. A number of GNSS software and programming languages were used in this regard. The PPP campaigns were processed with both UNIX/Linux and MS-Windows operating systems. The BERNESE GNSS v.5.2 (Dach et al, 2015) was the main platform the processes were performed for its highly advanced LSA solution and improved extensions for handling each parameter in the observation equations. In addition to the Bernese, the MatLab environment was also used to derive the a priori ZHD and ZWD parameters by processing the analytical troposphere models and their

corresponding mapping functions. A large number of executable programs that are written in the languages Fortran and C were created in order to be used in the pre-processing and validation phases of the atmosphere modeling. The gLAB GNSS v4.2 (Sanz et al, 2012), an advanced educational processing package for GNSS data processing developed under ESA Contract by the research group of Astronomy and Geomatics (gAGE) from the Universitat Politecnica de Catalunya (UPC), was employed for its ability to perform with a KF processing for epoch-wise estimation. With this study, relatively elementary troposphere solutions in the KF of the gLAB has been improved with the global and up-to-date analytical and numerical weather models and their corresponding mapping functions. Thus, the Kalman and the LSA solutions from two different platforms were evaluated and compared to each other.

5.1 Methodology and PPP Processing

The steps being followed in the PPP solution summarized as below:

- Data preparation step for collecting necessary products e.g. RINEX daily observation files, precise orbits, and clocks, antenna files for receiver and satellites. In addition, global grids and tabular files for a number geophysical models such as solid earth tides, ocean loading, atmosphere loading, tectonic movement and nutation models are also gathered in this phase.
- Pre-processing step to detect the cycle slips, outliers and removing bad satellites. Synchronizing the receiver clock with the GNSS time and code smoothing,
- Parameterization of unknowns, modeling the neutral atmosphere with the a priori troposphere; constraining the unknown parameters with determined sigma values,
- Parameter estimation with the LSA; producing the daily normal equation files for each daily solution per each site.
- Combination of daily NEQ files and processing all daily observation in one-step solution; parameter estimation for the unknowns.
- Conversion of the ZWD estimates to the PWV and verifying the results with external sources and intra-technique solutions.

In the data preparation step, the daily 30-second RINEX v.2.11 and v.3.00 observation data of the selected dual frequency IGS sites were downloaded from "The Crustal Dynamics Data Information System (CDDIS)" FTP site (Url-9) (see Appendix B). The RINEX version supports not only the GPS data, but also the GLONASS and GALILEO data. The new version RINEX v.3.00, which handles multiple GNSS observations, was not available during the campaigns performed in 2013. The daily IGS Final precise orbits (i.e., standard product 3 – sp3), EOPs and satellite clock corrections were downloaded from FTP servers of CODE (Url-6) and CDDIS. The latter one distributes ephemerides data of the GPS and the GLONASS in separate product files (i.e., IGS and IGL, respectively), whereas the CODE publishes the combined GPS / GLONASS orbits and clocks. The IGS Rapid and Ultra-rapid satellite products were also downloaded from the IGS to investigate the real and near real-time performance of the PPP solutions. A high rate, i.e. 5 sec. and 30 sec., satellite clocks were additionally used in the solutions to improve the PPP's accuracy.

The ephemeris orbits, which are in the ECEF coordinate system were first transformed to the celestial system and interpolated by adjusting a 10-degree Lagrange polynomial that fulfilling the equations of motion based on a physical model of the forces acting on the satellites for specifying the positions of the satellites in a polynomial representation at any epochs. A set of EOPs, which is required for the transformation between the ECEF and the Celestial system, must be consistent with the precise orbits and, usually must be stemmed from the same analysis center (e.g., IGS or CODE). The satellite clocks are necessary to synchronize the receiver clocks with the GPS time. Clock corrections for each observation epoch can be determined by either fitting the several hours (e.g., 12) precise satellite clock by a low degree polynomial (e.g., 2^{nd} degree) or by applying high rate satellite clock corrections from the precise clock files (e.g., IGS:30 sec or CODE: 5 sec). In addition, unaltered satellite clock corrections from precise orbit files with an interval of 15-minutes are also available; however, using this data is rather harmful due to the significant data reduction. Moreover, a high accuracy is met only for the observation epochs that matching with the tabulated epochs in the precise file. It is crucial that the set of precise orbits, EOPs and satellite clocks be consistent with each other, thus it is recommended to use product set generated from the same analysis center.

Antenna phase center file (PCV_COD.I14), ANTEX files (I14.ATX) and DCBs for code and phase observations (P1-P2 DCB and P1-C1 DCB) extracted from the CODE's FTP site (Url-6). The Nutation Model "IAU2000R06" and sub-daily pole model "IERS2010XY" were applied to the solutions as suggested by the IERS Conventions (Petit and Luzum, 2010). NNR–NUVEL–1A (DeMets et al. 1994) model was selected regarding the plate motions and another remarkable site displacement effect caused by ocean tidal loading compensated for by the FES2004.BLQ model generated at the CODE. Atmospheric tidal loading effects were corrected by using the so-called "grdinterp" FORTRAN subroutine corresponding to the atmospheric tidal model developed by Ray and Ponte (2003).

In the pre-processing step, first, the receiver clock inconsistencies were investigated by the epoch-differences of the ionosphere-free linear combinations (L_3, P_3) between the phase and code observations. Daily RINEX files were processed arc by arc, where an arc usually represents a pass of a single satellite and the phase and the code observations from both frequencies were screened in order to detect the cycle slips, outliers, and bad data on RINEX level. The Melbourne – Wubbena (MW) (Melbourne, 1985; Wubbena, 1985) and the geometry-free (L_4, P_4) linear combinations of dual frequencies were used to spot the jumps between the phase and code measurements and to determine the size of the cycle slips, respectively. The bad observations, which were not detected by the MW, were identified by the differences between the ionosphere-free linear combinations of code and phase data (L_3 - P_3). Finally, code observations were smoothed using the code and carrier phase data of cleaned arc observations. Ionosphere-free LC of dual frequency measurements eliminates the first order ionospheric refraction while remaining unknowns such as the receiver clock corrections, the coordinates, the site-specific tropospheric delays, and the phase ambiguities must be estimated. The a priori coordinates, which were propagated from the ITRF14 frame coordinates to the observation epoch via velocity files, were not constrained in the first PPP solution. The troposphere parameters were parameterized as a continuous piecewise linear function with a resolution of 1-hour while the receiver clocks, were set up as single-epoch parameters and estimated as a random-walk process. Ambiguities were parameterized as constant parameters until the new ambiguities were determined for the receiver – satellite pair. The parameterization procedure is completely different with the KF approach. Tropospheric path delays,

coordinates, and initial ambiguities were modeled as random-walk whereas receiver clocks were modeled as white noise in the Kalman filter. Each unknown parameter was estimated epoch-wise (i.e., 300 seconds).

The dry part of the troposphere was accounted for by the a priori troposphere calculated by the Saastamoinen (1972). Input pressure data was derived either from the analytical models of GPT (≈GPT2) and UNB or from the ECMWF daily published analyses data (i.e., VMFG). The wet part was estimated by the LSA (or KF) adjustment and added to the a priori ZHD to obtain the total delay. Models and mapping functions were processed in the parameter estimation phase are given below:

- ECMWF derived VMFG and the corresponding mapping functions of dry and wet VMF1,
- GPT (≈GPT2) analytical prediction model and the corresponding mapping functions of dry and wet GMF,
- UNB analytical model and its collaborative mapping functions of dry and wet Niell (NMF).

The PPP solutions which differ only in the employed a priori troposphere models and mapping functions were assessed based on their atmosphere monitoring performance with respect to IGS troposphere results, relative GNSS results and direct atmosphere measurements i.e. radiosonde data. The parameter adjustment phase consists of three sequential PPP solution. The first ionosphere-free run was performed to generate the observation residuals in order to remove outliers and bad observations. The second run was performed with the cleaned data in order to produce a priori parameters for the unknowns. During these runs the elevation mask was set up for 5° and none constraints (relative or absolute) were defined for the coordinates and troposphere parameters.

The third LSA, which used the a priori parameters determined earlier, was performed to generate the daily normal equation files (NEQs). The coordinates were loosely constrained (i.e., 10 cm sigma) in the X, Y and Z directions, the elevation mask was set up for 5°, the ZHDs were derived from analytical and numerical weather models; the ZWDs were estimated for 1-hour resolution along with horizontal gradients that were estimated per 12 hours. The relative constraints of 1.0 cm and 10.0 cm were specified for ZWDs and gradients, respectively. Real value phase ambiguities were determined and pre-eliminated before saving the NEQ files.

In the last step, the daily NEQ files were combined to generate the final solution which includes a large number of parameter types (i.e., coordinates, troposphere, receiver clock corrections) of three weeks sequential PPP solutions. This time the coordinates were tightly constrained (1.0 cm sigma). The relative a priori sigma for the ZWDs and gradients were specified as 5.0 mm and 1.0 cm, respectively. The unknowns $(\Delta X, \Delta Y, \Delta Z, c\delta t, Tr_{zwd}, G_n, G_e)$ in the final estimation step were nothing but the corrections to the a priori parameters (coordinates, receiver clocks, and modeled ZHD). The flow chart of the PPP campaign that is followed in the study is displayed in Figure 5.5.

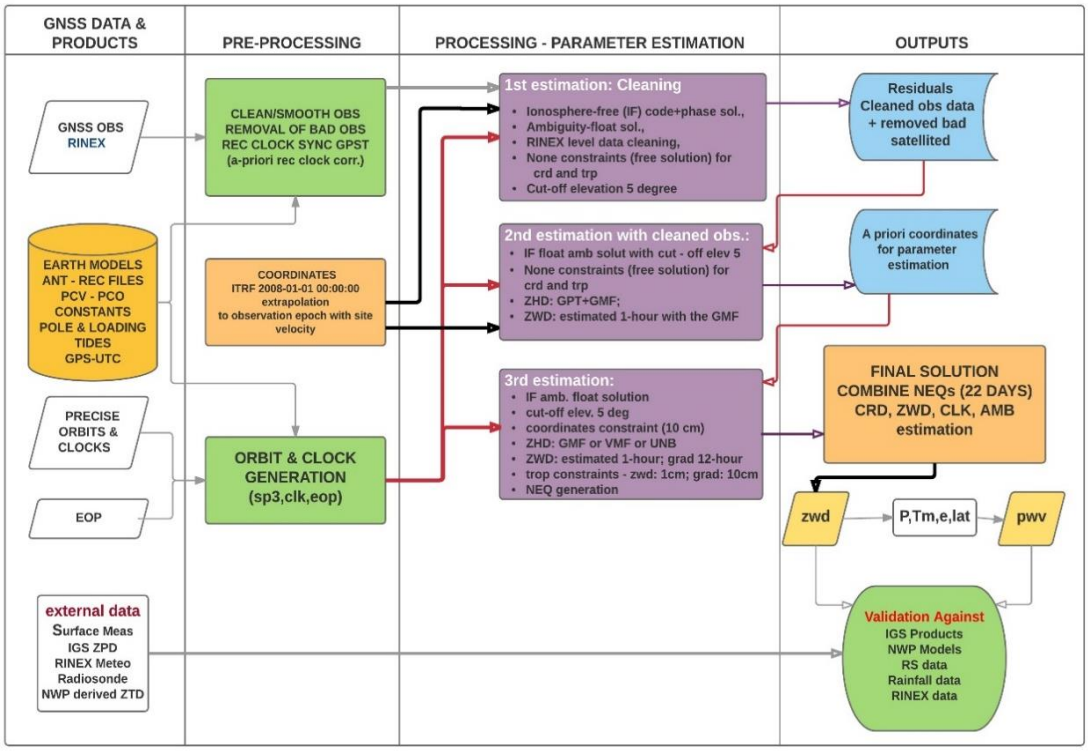

Figure 5.5 : The scheme presenting the data processing steps in order to estimate ZWDs.

The slant total delay $\Delta\rho_r^s$ can be modeled by hydrostatic (i.e. $\Delta\rho_h^z$) and non-hydrostatic components ($\Delta\rho_w^z$), which can both be expressed by their individual zenith delays and the corresponding mapping functions ($m_h(\varepsilon),\ m_w(\varepsilon)$) as expressed in equation 5.1. The gradients ($G_n,\ G_e$) are also part of the delays when considering azimuthal asymmetries (Dach et al, 2015).

$$\begin{aligned}\Delta\rho_r^s(t,\varepsilon,\alpha) \;=\; & \Delta\rho_h^z\, m_h(\varepsilon) \;+\; \Delta\rho_w^z\, m_w(\varepsilon) \\ & + m_f(e)(\Delta\rho^z + \cot(e)(G_n\cos(a) + G_e\sin(a))\end{aligned} \tag{5.1}$$

where $\Delta\rho_h^z\, m_h(\varepsilon)$ is the NWM or analytical function derived a priori ZHD; $\Delta\rho_w^z\, m_w(\varepsilon)$ is estimated ZWD and $+ m_f(e)(\Delta\rho^z + \cot(e)(G_n\cos(a) + G_e\sin(a))$ corresponds to the horizontal East and North gradients estimated to mitigate effects caused by azimuthal asymmetric troposphere.

5.2 Zenith Wet Delays

The zenith wet delays of 11 IGS sites were estimated using an ionosphere-free linear combination of dual frequency phase and code observations (L_3 and P_3) at a minimum elevation angle of 5°. A sequential least squares adjustment was utilized to estimate the ZWDs along with other unknowns including tropospheric gradients. The ZWDs and gradients were modeled as random walk process. Since the tropospheric delays are much more sensitive to observations at lower elevation than other estimated parameters, elevation dependent weighting must be applied to de-correlate the strong correlation between the troposphere, coordinates and receiver clocks. The elevation dependent weighting defined by Dach et al. (2015) as $w(z) = \cos^2(z)$, where z is the zenith angle of the satellite, was implemented into the observations of the normal equations. It must not be forgotten that any error or miscalculation in the a priori ZHDs and the mapping functions will introduce an error in the height coordinates and the ZWDs.

Figure 5.6 illustrates the time series of the wet delays and their solution accuracy (i.e., RMS) at the 11 IGS sites in the central Europe for the period from May 20 to June 10, 2013. The results were illustrated for all applied troposphere models both analytical function and NMW derived and corresponding mapping functions. The results were validated against the IGS Final troposphere, i.e., ZPD, products.

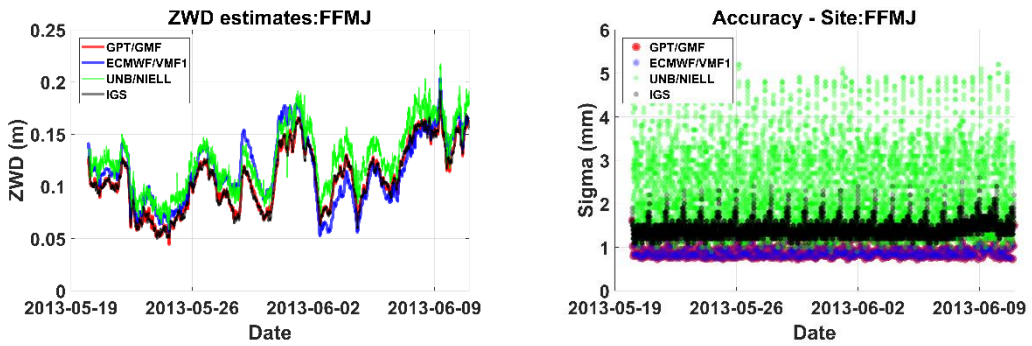

Figure 5.6 : The estimated ZWDs and RMS values of the solution; The IGS ZPDs used for validation.

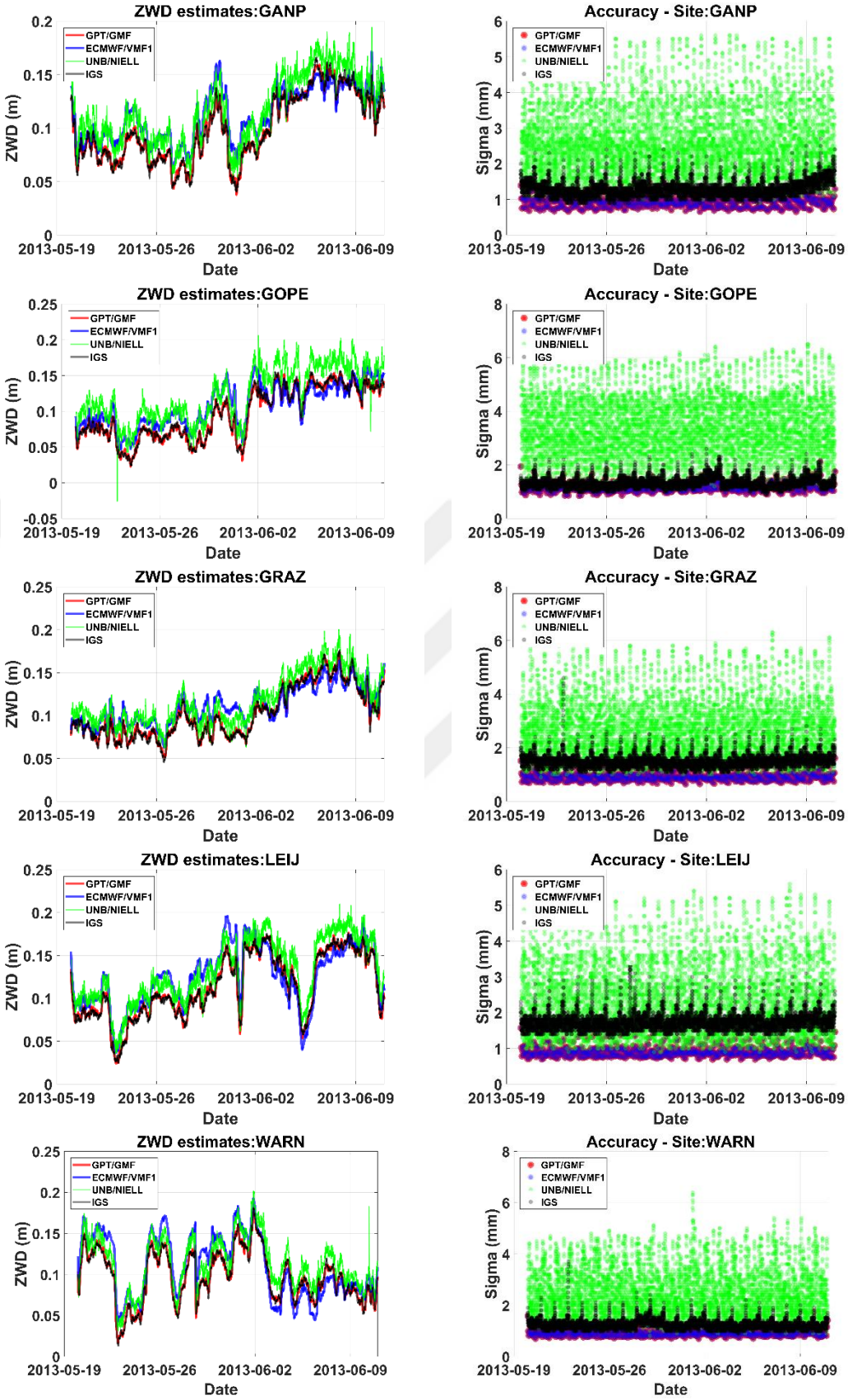

Figure 5.6 (continued): The estimated ZWDs and RMS values of the solution; The IGS ZPDs used for validation.

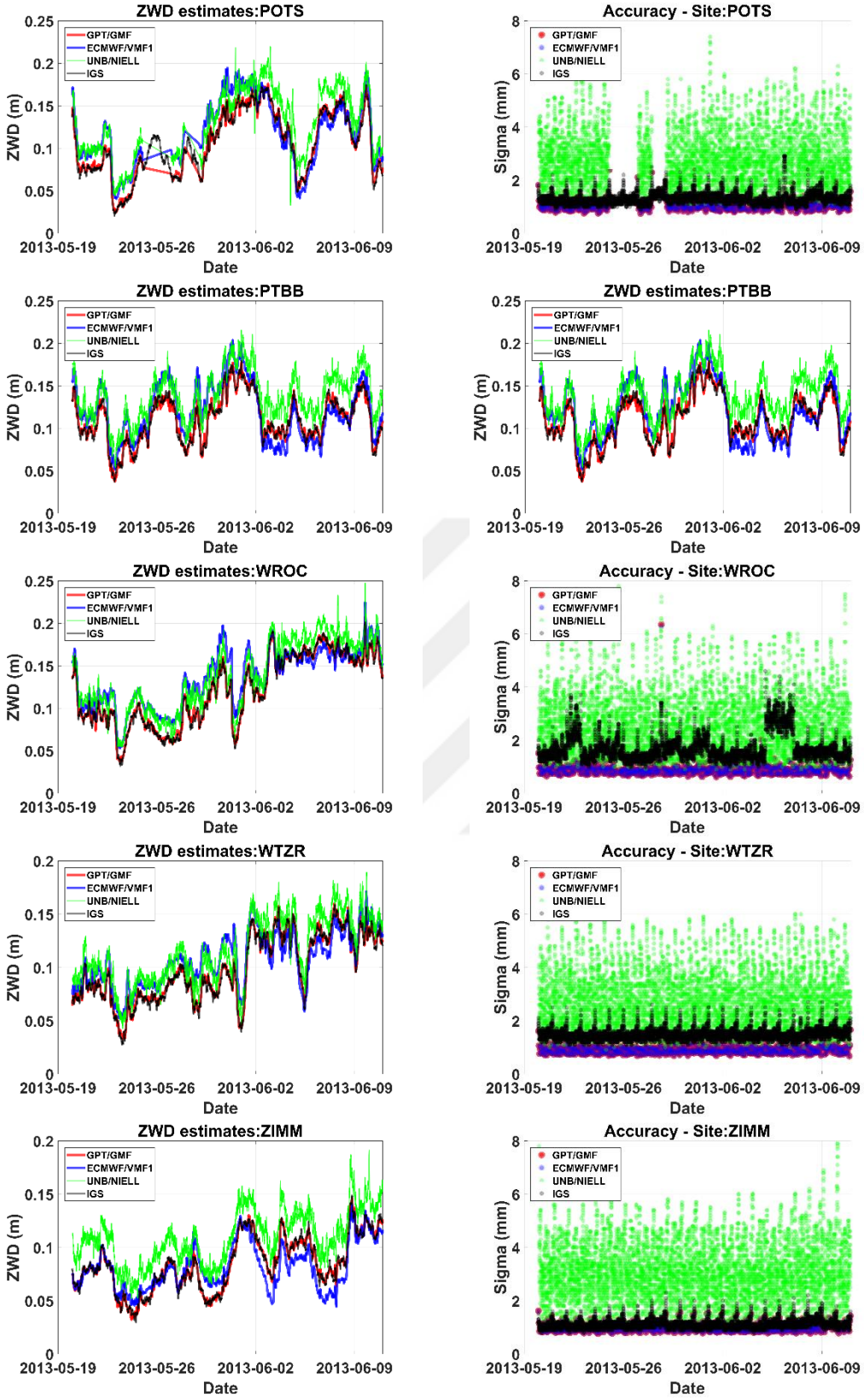

Figure 5.6 (continued): The estimated ZWDs and RMS values of the solution; The IGS ZPDs used for validation.

The results from the time series revealed that the sudden changes in the air humidity are detected by the GNSS signal, but, the 1-hour resolution and the tight relative constraints in the ZWDs prevented to capture the shorter variations less than 1-hour thus, the formal errors of the estimates elevated. In addition, data gaps in the RINEX, bad observations, and incorrectly modeled errors e.g., satellite clock interpolation errors or orbit interpolation errors can also increase the formal errors of the estimates. The higher deviations experienced at the day boundaries are the result of using 24-hour orbital batches and processing daily solutions with the daily satellite products and daily RINEX observation files. Even though the spherical harmonic GPT and the look-up table of the UNB3m are both analytical models, available at any time and location, they give only annual means and amplitudes for the phase set for January 28; hence, these empirical models are not sufficient for monitoring hydrostatic delay variations of a short period. Comparisons have already been performed by Boehm et al. (2009), Tesmer et al. (2007), Vey et al. (2006), and Tregoning and Herring (2006) who found that systematic differences between constant ZHDs and NWP-derived ZHDs introduce systematic station height biases of up to 10mm, in particular in northern latitudes (i.e., Antarctica). The ECMWF data offer short-terms as well as inter-seasonal variations as showed in Figure 5.7.

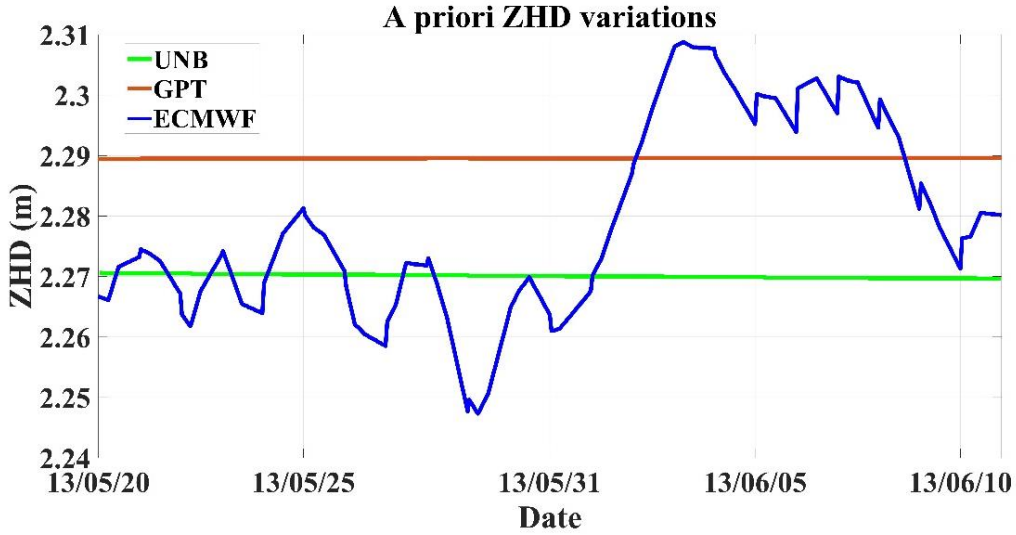

Figure 5.7 : ZHD derived from the GPT (red), the UNB (green) and the ECMWF (blue).

The scatter comparison in Figure 5.8 showed that the PPP ZWDs using the a priori models of the GPT (or the GPT2) agreed better with the IGS Final ZPD products. Since the IGS was using the Saastamoinen and the GPT2 / GMF pair to model the

troposphere in 2013 (i.e., the ECMWF / VMF1 pair has recommended since 2014); the ZWD results remained closer to the GPT2 ones.

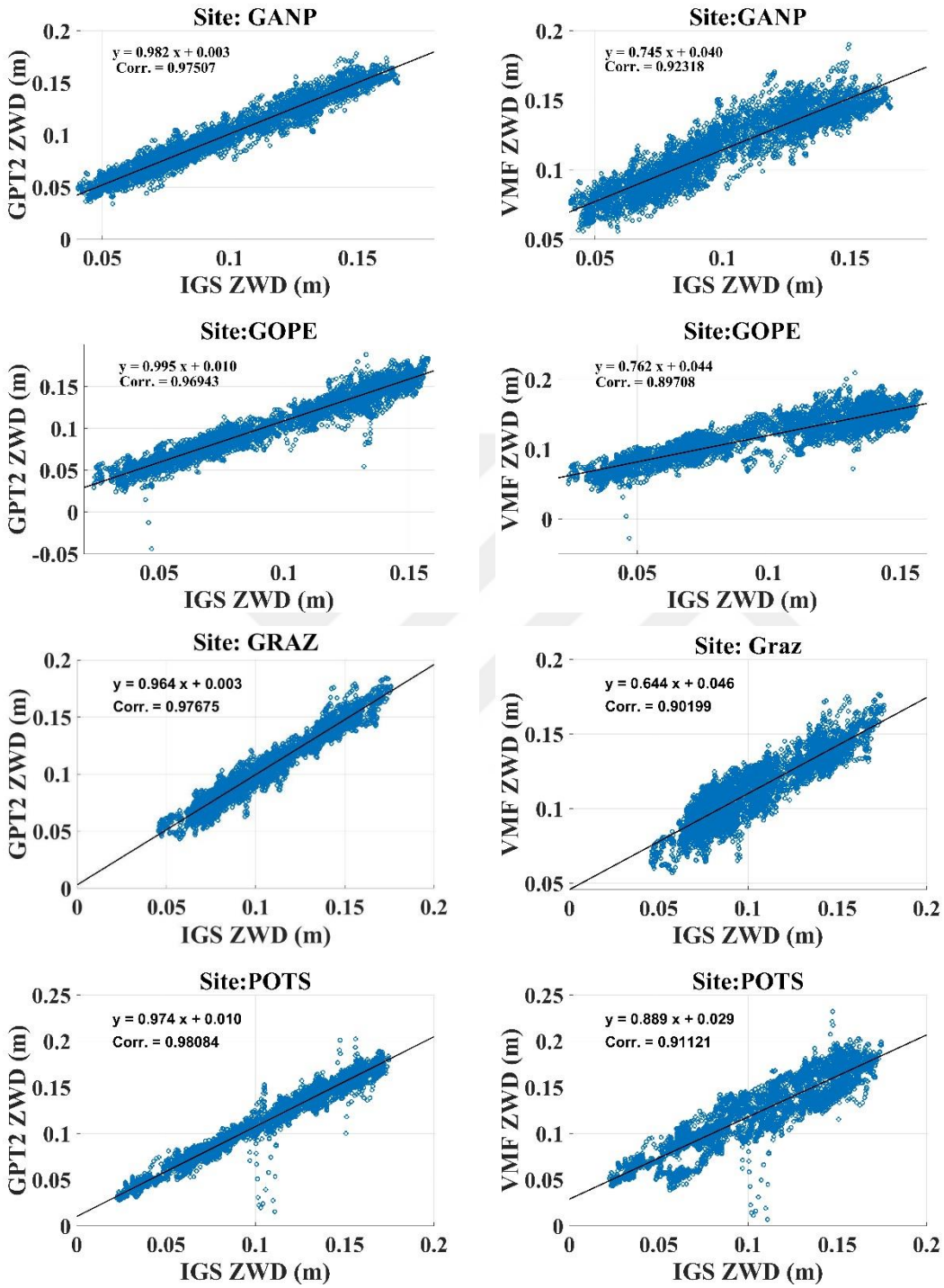

Figure 5.8 : Scatter plot of the PPP ZWDs (GPT2 and VMF1 grid) data with respect to the IGS ZWD data.

It is noted that the range of differences between the IGS ZWDs and PPP ZWDs deviates from -10.0 mm to +6.0 mm for the GPT2 model. The RMS values of the differences were found to be 6.3 mm (minimum) and 14.2 mm (maximum) for the

GRAZ and PTBB stations, respectively. The differences between the PPP VMF1 and the IGS ranges from – 20.9 to -6.7 mm while the RMS values remain between 19.0 - 26.4 mm. The largest discrepancies against the IGS were detected for the PPP solutions using the UNB model where the differences larger than 20.0 mm were detected with the RMS values of bigger than 25 mm. The mean differences of the ZWD estimates between the PPP using GPT2 and the PPP using VMF1 were found to be around 1.0 - 1.5 cm. The GPT2 - UNB average differences were in the range of 1.5 - 2.0 cm. Table 5.2 presents the mean differences, RMS of the differences and the correlation coefficients for the ZWD estimates.

Table 5.2 : Statistical information for the ZWD differences from different PPP solutions and IGS products.

	Mean Differences (mm)					
Site	IGS-GPT	IGS-VMF1	IGS-UNB	GPT-VMF1	GPT-UNB	VMF1-UNB
ganp	-1.1	-14.6	-17.7	-13.4	-16.6	-3.1
gope	-9.1	-20.9	-27.0	-11.7	-17.9	-6.2
graz	5.0	-9.3	-15.6	-9.8	-16.1	-6.3
wroc	-4.6	-14.8	-17.4	-14.3	-16.9	-2.6
pots	-7.3	-17.2	-24.5	-9.9	-17.1	-7.3
wtzr	6.1	-8.7	-17.0	-9.3	-17.7	-8.4
zimm	-7.7	-6.7	-24.9	9.7	-17.2	-18.2
leij	-7.5	-10.4	-18.1	-9.6	-17.3	-7.7
ptbb	-10.6	-19.0	-28.1	-8.4	-17.5	-9.1
	RMS of Differences (mm)					
ganp	7.1	19.2	19.0	16.9	16.5	10.6
gope	12.9	26.3	28.5	17.7	17.9	14.6
graz	6.3	16.8	16.8	15.4	16.1	13.4
wroc	7.2	21.4	18.8	19.5	16.9	13.7
pots	10.5	23.7	25.6	18.0	17.1	16.9
wtzr	6.3	17.2	18.1	15.8	17.6	15.2
zimm	9.5	15.2	25.5	12.0	17.2	21.5
leij	6.7	18.7	19.2	17.7	17.3	16.9
ptbb	14.2	26.4	29.6	17.7	17.4	18.2

Table 5.2 (continued): Statistical information for the ZWD differences from different PPP solutions and IGS products.

	Correlation Coefficients					
Site	IGS-GPT	IGS-VMF1	IGS-UNB	GPT-VMF1	GPT-UNB	VMF1-UNB
ganp	0.97507	0.92317	0.97475	0.95871	0.99996	0.95844
gope	0.96943	0.89708	0.96892	0.94076	0.99998	0.94071
graz	0.97674	0.90199	0.97643	0.93765	0.99997	0.93684
wroc	0.98455	0.93580	0.98484	0.95312	0.99998	0.95318
pots	0.98084	0.91121	0.98085	0.92346	0.99994	0.92162
wtzr	0.97924	0.88134	0.97896	0.91593	0.99996	0.91583
zimm	0.97438	0.83864	0.97290	0.87789	0.99967	0.88256
leij	0.98371	0.90701	0.98387	0.91488	0.99997	0.91387
ptbb	0.94439	0.83676	0.94373	0.88535	0.99992	0.88160

Although the largest ZWD differences were observed for the GPT - UNB, the linear dependence of the estimates for these analytical models were comparatively higher in comparison to GPT - VMF1 and UNB - VMF1. This dependence can be certainly attributed to use yearly averages of the pressure data for the a priori ZHD calculation that later affect the ZWD estimations. The positioning results of the PPP campaigns were also assessed and residuals from the CODE's weekly SINEX coordinates in the North, East and Up components were illustrated in Table 5.3.

Table 5.3 : Mean positioning residuals (mm) of the PPP solutions differing in used troposphere model.

Site	GPT - IGS			VMF1 - IGS			UNB – IGS		
	N	E	U	N	E	U	N	E	U
ffmj	5.0	-5.5	-12.1	4.9	-5.5	-9.8	4.9	-5.5	-9.9
ganp	3.5	3.7	-11.8	3.5	3.7	-9.1	3.5	3.7	-10.6
gope	2.7	-9.7	-36.2	2.7	-9.8	-34.6	2.7	-9.8	-35.2
graz	8.8	7.5	-19.4	8.8	7.4	-16.7	8.8	7.4	-18.3
wroc	6.9	4.8	-18.3	6.8	4.9	-15.4	6.9	4.9	-16.2
pots	1.0	-1.5	-17.8	1.0	-1.6	-15.8	1.0	-1.6	-15.5
wtzr	4.8	1.4	-18.0	4.8	1.4	-15.4	4.8	1.4	-16.2
zimm	4.2	-2.1	-23.4	4.2	-2.1	-21.9	4.2	-2.1	-22.5
leij	7.8	-3.3	-19.8	7.7	-3.3	-17.7	7.7	-3.3	-17.7
ptbb	-0.5	1.8	-34.4	-0.5	1.8	-33.6	-0.5	1.8	-33.6

It is obvious that the positioning residuals in the north and the east directions are quite similar regardless of employed troposphere model. The residuals remained within ± 1 cm for the East and the North, whereas the differences in the Up directions are larger that up to ± 4 cm compared to the CODE's reference coordinates. If the troposphere parameters and the heights are estimated together, formal errors may increase due to large correlations among these parameters. Lowering the cut-off elevation angle with elevation dependent weighting is one approved solution to de-correlate the unknown parameters. The impact of uniformly distributed high elevation satellites and used a priori troposphere model along with the mapping functions must be investigated in this regard.

The convergence periods of the PPP campaigns were evaluated and almost all solutions reached to cm level accuracy after half an hour. It was revealed that there is no significant improvement in the convergence time caused by applying a different troposphere model either analytical or NWM derived. The convergence periods at GRAZ for the day of year 151 in 2013 were illustrated in Figure 5.9 where all three troposphere models were processed sequentially. Mean convergence values for the PPP sessions processed with the GPT / GMF are listed in Table 5.4.

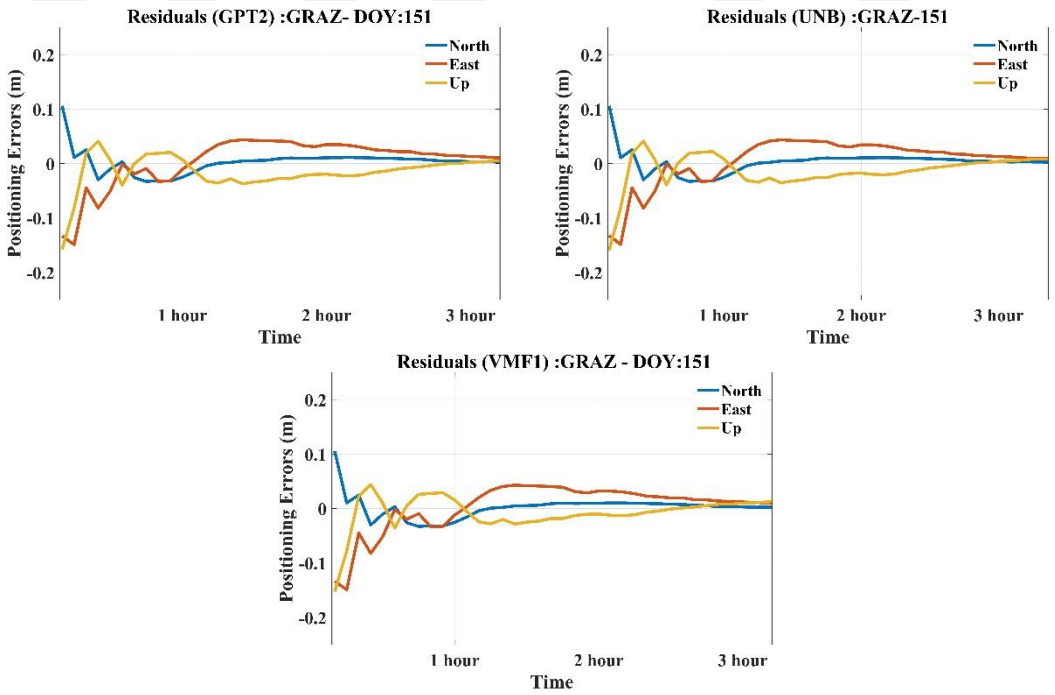

Figure 5.9 : GRAZ station positioning results and convergence periods under different atmosphere models; the coordinate set of CODE's weekly SINEX solutions were used as reference data.

Table 5.4 : Mean convergence (minutes) of the daily PPP solutions that using GPT/GMF troposphere model.

Site	FFMJ	GANP	GOPE	GRAZ	WROC	POTS	WTZR	ZIMM	LEIJ	PTBB
Mean (min)	31.0	32.0	32.5	30.6	30.4	27.7	30.6	32.0	30.4	36.1

In order to detect potential jumps and outliers and to measure the consistency between each daily campaign, the repeatability between the daily coordinates were investigated. First, unknown coordinates were estimated with the least squares adjustment and daily NEQ files were generated. The NEQ files from independent daily sessions were combined and processed in the multi-session solution. As a result, all coordinate parameters associated with the same station were combined to produce one single set of coordinates. Coordinate residuals of the daily solutions against to the combined solution (i.e., single set of coordinates) were computed in the North, East and Up directions. The RMS values of the repeatability were illustrated in Table 5.5. The repeatability analyses were performed for two independent PPP solutions: one with the GPT and the other with the VMF1 troposphere model, separately. The computed residuals and the RMS values help us to recognize problems for each station or in the NEQ files. The findings are consistent with the results of Steigenberger et al. (2009) who avoided atmospheric loading corrections during PPP processing.

Table 5.5 : The RMS of the positioning repeatability for the static PPP solution with respect to the atmosphere models of both GPT and VMF1.

Site	Day	Repeatability RMS (mm) GMF			Repeatability RMS (mm) VMF1		
		N	**E**	**U**	**N**	**E**	**U**
FFMJ	22	1.33	2.30	4.07	1.35	2.33	4.08
GANP	22	0.85	1.74	3.48	0.89	1.73	3.79
GOPE	22	0.83	1.31	3.51	0.83	1.32	4.25
GRAZ	22	0.71	1.52	3.38	0.74	1.52	2.89
LEIJ	22	0.53	2.25	3.93	0.54	2.27	4.42
POTS	19	0.86	1.21	3.34	0.85	1.22	4.55
PTBB	22	1.02	1.85	3.63	1.03	1.84	3.69
WARN	22	0.79	1.76	3.94	0.75	1.77	3.91
WROC	22	0.61	3.41	3.90	0.68	3.40	3.96
WTZR	22	0.81	1.36	2.99	0.82	1.41	4.18
ZIMM	22	0.89	1.22	2.97	0.90	1.22	3.18

5.2.1 Validation of PPP results with differential GNSS

In this part of the study, the estimated PPP ZWD parameters were compared to the estimates from the double differenced network solution performed for the same sites. Baselines between the selected sites were created by considering the number of common observations, i.e. obs – max strategy Dach et al. (2015), for the associated stations. From all possible combinations, a set of baselines with maximum common observations were chosen. Forming baseline based on the baseline length is the simplest criterion and it generally advised to use short baselines that speed up ambiguity by assuming that both sites observe the same satellites. Unlike the PPP where the code observations were screened solely, a single difference phase observations were also screened in the Network solution to detect outliers and cycle slips and correct them in a relative manner. This procedure is advised if users have accurate and high-rate satellite clocks.

The network solution was performed with same elevation angle (5°), same relative constraints for coordinates and troposphere as specified in the PPP solution. Analytical GPT2 / GMF and NWM derived ECMWF / VMF1 troposphere models were used. The wet delays were estimated with a time resolution of 1-hour. Double differenced ambiguities were estimated by differencing single difference ambiguities between receivers so they can be fixed to integer values immediately. Figure 5.10 shows the comparison of the ZWD estimates between the PPP and the relative GNSS solutions at stations: FFMJ, GANP, GOPE, GRAZ, WROC, POTS, WTZR, ZIMM, PTBB and LEIJ.

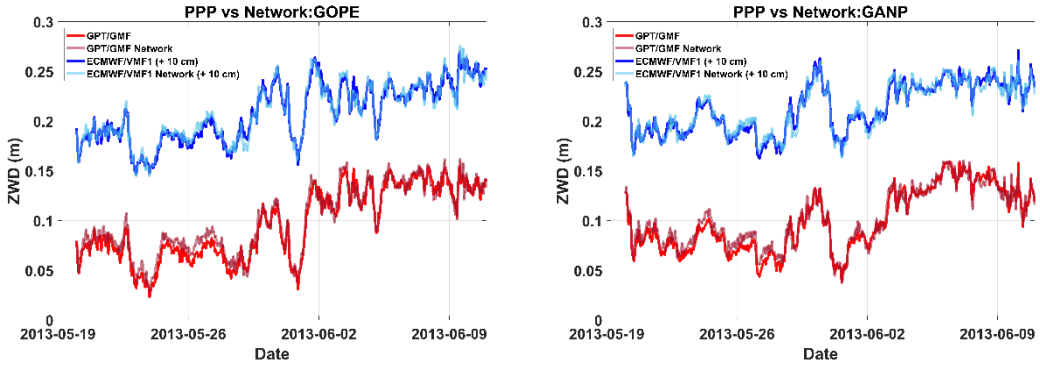

Figure 5.10 : Comparison of ZWD estimates derived from PPP and Network solution for stations: FFMJ, GANP, GOPE, GRAZ, WROC, POTS, WTZR, ZIMM, PTBB, LEIJ.

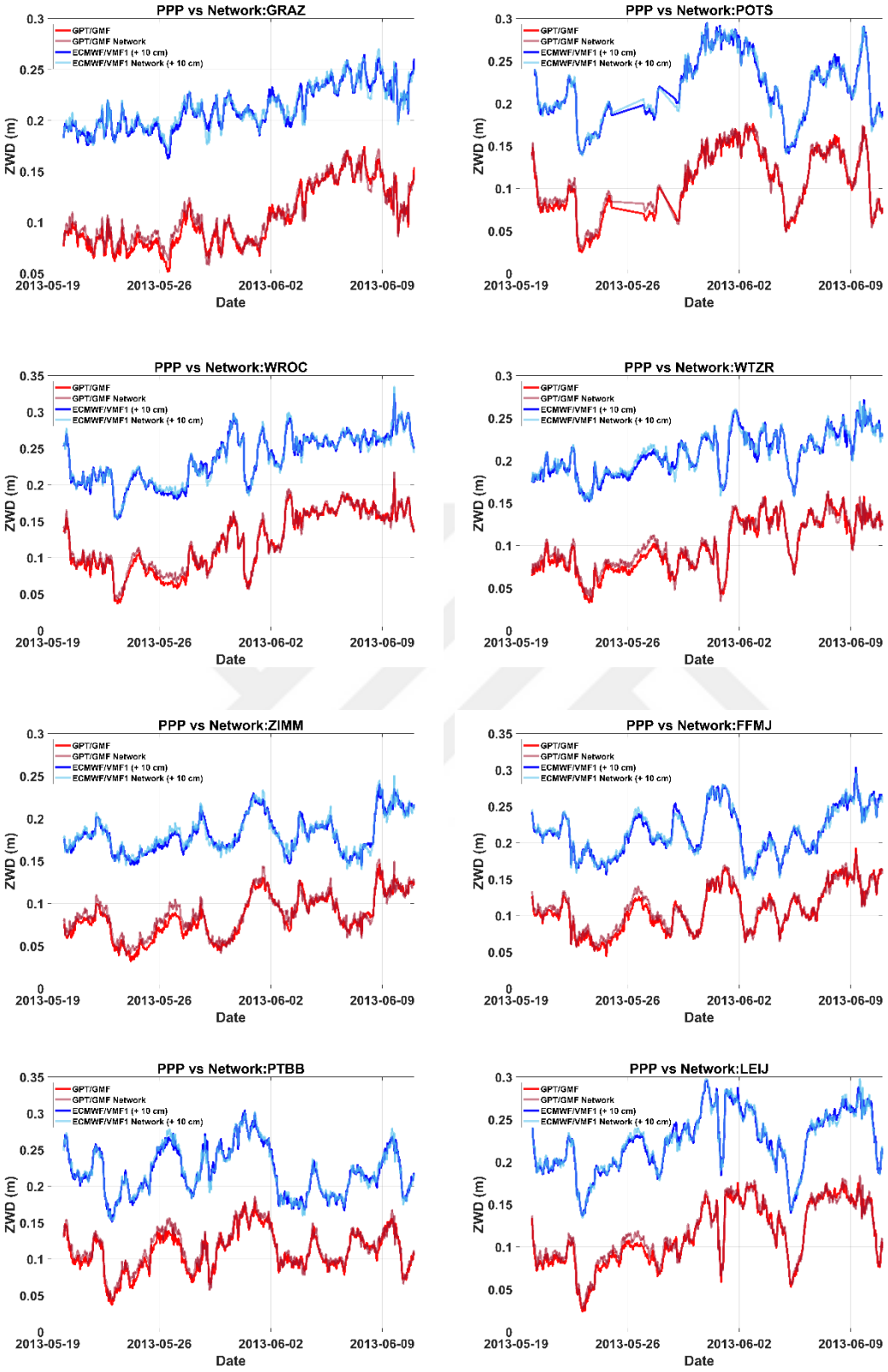

Figure 5.10 (continued): Comparison of ZWD estimates derived from PPP and Network solution for stations: FFMJ, GANP, GOPE, GRAZ, WROC, POTS, WTZR, ZIMM, PTBB, LEIJ.

Table 5.6 summarizes the mean differences, median differences, mean standard deviations, and maximum differences of the estimates between the PPP and relative solutions. The mean differences of the ZWD estimates between the PPP and Network remain in the range of ± 4.5 mm and ± 1.0 cm for the solutions using the GPT2 and VMF1 models, respectively. The mean formal errors are about ± 2 mm for the double difference ZWD estimates that are higher compared to the formal errors i.e. ± 1.5 mm of the PPP ZWDs. The higher formal errors for the relative solutions could be associated with the max - observation baseline selection strategy, which degrades the number of observables, used in the solutions that data processing is only performed for common observables between station/satellite pairs.

Table 5.6 : Mean (mm), Max (mm) and RMS (mm) of the differences between the PPP and the Network solutions.

PPP vs Network (GPT/GMF)					
Station	Mean diff	Median diff	Max diff	std.dev(PPP)	std.dev(Net)
FFMJ	-3.3	-3.7	15.3	0.9	1.5
GANP	-2.9	-3.1	19.4	0.9	1.5
GOPE	-4.2	-4.4	15.5	1.2	1.6
GRAZ	3.4	-3.5	13.9	0.9	1.5
WROC	-2.7	-2.9	14.8	0.9	1.4
POTS	-3.0	-3.0	14.9	1.1	1.5
WTZR	-3.1	-3.4	13.1	0.9	1.4
ZIMM	-4.1	-4.4	15.6	1.0	1.8
LEIJ	-3.0	-3.2	17.7	0.9	1.4
PTBB	-4.5	-4.8	17.2	1.5	1.9
WARN	-3.0	-3.3	17.7	0.9	1.6
PPP vs Network (ECMWF/VMF1)					
FFMJ	-0.6	-1.1	15.7	0.9	1.5
GANP	-0.1	-0.4	21.1	0.9	1.5
GOPE	-0.6	-1.0	16.5	1.2	1.6
GRAZ	-1.0	-1.4	15.6	0.9	1.5
WROC	-0.15	-0.4	15.2	0.9	1.4
POTS	-0.27	-0.3	15.5	1.1	1.4
WTZR	-0.6	-0.1	15.6	0.9	1.4
ZIMM	-1.0	-1.5	16.0	1.0	1.8
LEIJ	-0.3	-0.6	18.4	0.9	1.4
PTBB	-0.5	-1.2	18.8	1.5	1.9
WARN	0.2	-0.1	18.7	0.9	1.5

Successful PPP or Network sessions are deducible from the a posteriori RMS errors that stand for an overall accuracy of the whole solution. A posteriori RMS error of about 1.0 - 1.5 mm is acceptable if an elevation dependent weighting is applied. Higher values indicate bad data, failure of preprocessing steps or low-quality receivers used in the solution. If a processing is performed without elevation dependent weighting, the expected RMS values are about 2.0 - 2.5 mm. Table 5.7 lists the a posteriori RMS errors of the PPP and Network solutions for 10 consecutive days (i.e., doy:145 - 154, in 2013).

Table 5.7 : A-posteriori sigma of the PPP and Network solution for each day (a-priori sigma of unit weight = 1.0 mm).

DoY	145	146	147	148	149	150	151	152	153	154
PPP (mm)										
GPT/GMF	0.9	0.9	0.9	1.0	1.0	0.9	1.0	0.9	1.0	1.0
ECMWF/VMF1	0.9	0.8	0.9	1.0	1.0	0.9	1.0	0.9	0.9	1.0
Network (mm)										
GPT/GMF	1.3	1.3	1.3	1.4	1.4	1.3	1.4	1.4	1.4	1.4
ECMWF/VMF1	1.3	1.3	1.3	1.4	1.4	1.3	1.4	1.4	1.4	1.4

5.2.2 Orbits and clocks comparison

The GNSS combined orbit/clock products come in various flavors, from the Final, Rapid to the URP. These orbits/clocks differ mainly in their varying latency and the extent of the tracking network used for their computations. Today, the highest precision GNSS orbits are available through the IGS and its ACs. The IGS Final orbits and clocks are currently combined from up to eight contributing IGS ACs, using six, largely independent, software packages (i.e., BERNESE, GAMIT, GIPSY, EPOS (Gendt et al, 1999) and PAGES (Schenewerk et al, 2000)). The IGS Final orbits and clocks are usually available before the thirteenth day after the last observation. The rapid orbit/clock product is combined 17 hours after the end of the day of interest. The latency is mainly due to the varying availability of tracking data from stations of the IGS global tracking network, which use a variety of data acquisition and communication schemes, as well as different levels of quality control.

A near RT IGS product i.e. the IGS URP is generated since March 2000. These near RT orbits are delivered since April 19, 2004, four times a day at 3, 9, 15, and 21 UTC

with an average delay of about 6 hours. The first 24 hours in the files are based on the data of more than 200 IGS stations delivering hourly data, the following 24 hours are extrapolated from the first part and may be used for real-time applications. The consistency between orbits, clocks and earth orientation parameters is a prerequisite for PPP analyses. Figure 5.11 shows the time series of the wet delays for the period from May 20 to June 10, 2013 (i.e., DoY 140 -161) at the IGS station FFMJ where the both GNSS processing techniques PPP and relative GNSS were performed. Figure 5.11 shows the ZWDs estimated by processing IGS Final, Rapid and URP products and the accuracy of the estimates.

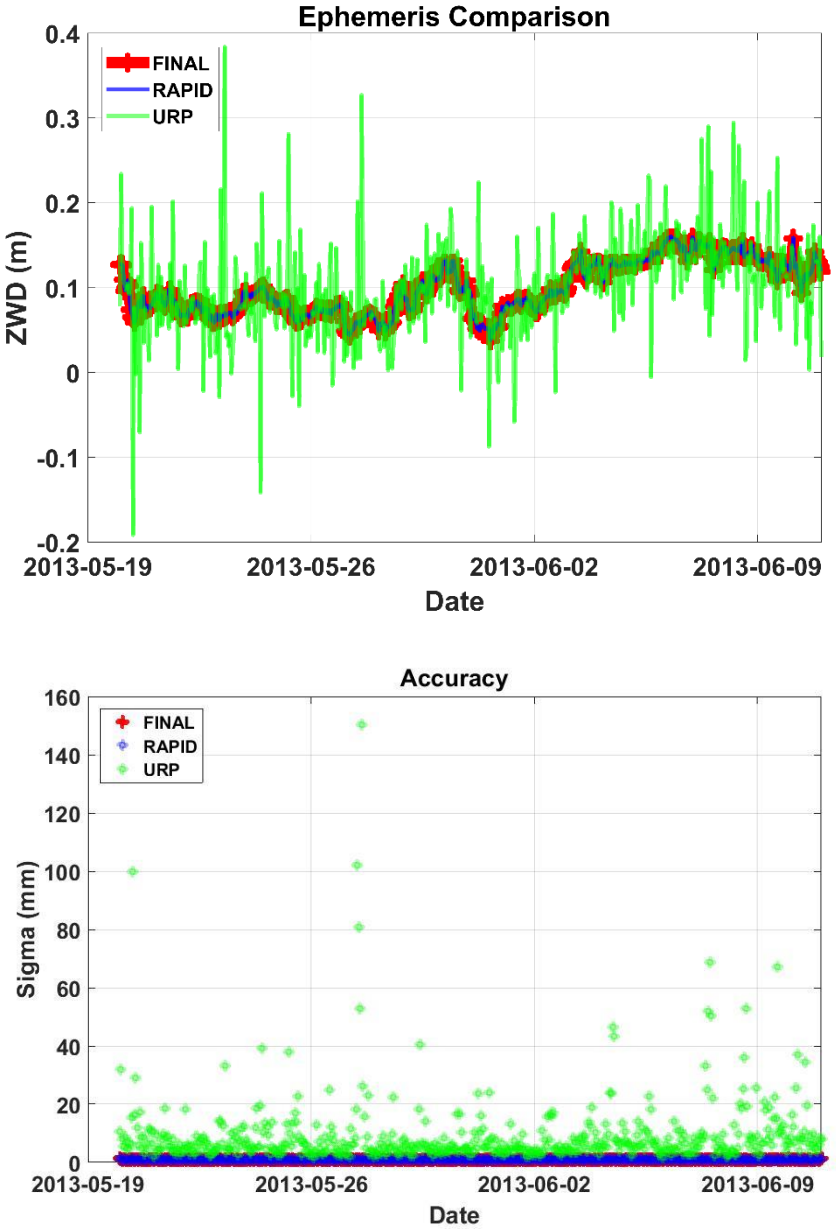

Figure 5.11 : PPP ZWD solutions for station GANP using IGS Final, Rapid and URP (up) and their solution accuracy (mm) (bottom).

The mean ZWD differences between the PPP solutions using the Final ephemeris and Rapid ephemeris are in the range of ±1 mm with the RMS of 1.8 mm, whereas the differences and RMS errors increase to ± 8 cm and 13.0 cm for the PPP Final and PPP URP comparison. Based on these results; the Rapid products that disseminated after 17 hours of the last observation are compatible with the IGS Final products and second, highly inconsistent nature of the IGS URP's clocks and orbits it is challenging to obtain precise and accurate estimates. Contrary, IGS URP can offer sufficient accuracy if it is processed within a network solution. The average differences were reduced to ± 6.0 mm (with RMS of 8.0 mm) with respect to the PPP Final solutions when the IGS URP products were processed in the Network GNSS solution.

5.2.3 Analysis center comparison

The ZWD parameters, which were estimated by processing individual orbits from three different ACs, were evaluated to reveal the impact of using different product sets coming from different sources. Therefore, the precise ephemeris orbits and clocks that downloaded from the IGS, CODE and GFZ were processed with the observations from three IGS sites GANP, POTS and GRAZ for the time period from May 20 to June 5 in 2013. Table 5.8 presents the mean ZWDs differences between the ACs individual solutions.

Table 5.8 : Mean wet delay differences at POTS, GANP and GRAZ sites due to processing GNSS products from different AC

Mean ZWD diff	POTS	GANP	GRAZ
IGS – COD (mm)	1.3	1.2	1.0
IGS – GFZ (mm)	1.8	1.4	1.1
GFZ – COD (mm)	2.5	1.7	1.5

It can be noticed that the ZWD differences are almost negligible and range from 1.0 mm to 2.5 mm on average. In addition, the average RMSs of the individual PPP solutions at the three stations are below 1.0 mm for the GFZ and between 1.0 – 2.0 mm for the IGS and CODE. During the experiment conducted in 2013, the GFZ was offering orbits and clocks for three GNSS system GPS, GLONASS and GALILEO, and thus it provided more accurate results than the CODE, which was offering GPS and GLONASS support, and the IGS that provided GPS-only products. With the advent of the Multi-GNSS Experiment (MGEX) project, signals from the different systems will allow users to perform highly accurate analyses.

5.2.4 Clock Comparison

The satellite clock corrections with respect to GPS time may be extracted from three sources: from broadcast messages, from IGS precise orbit files, and from IGS clock RINEX files. The Clock RINEX format has been defined by Ray and Gurtner (1999) for exchanging clock corrections to GPS system time not only for satellites but also for receivers with a higher sampling than available in the IGS precise orbit files (i.e., 30 seconds instead of 15 minutes).

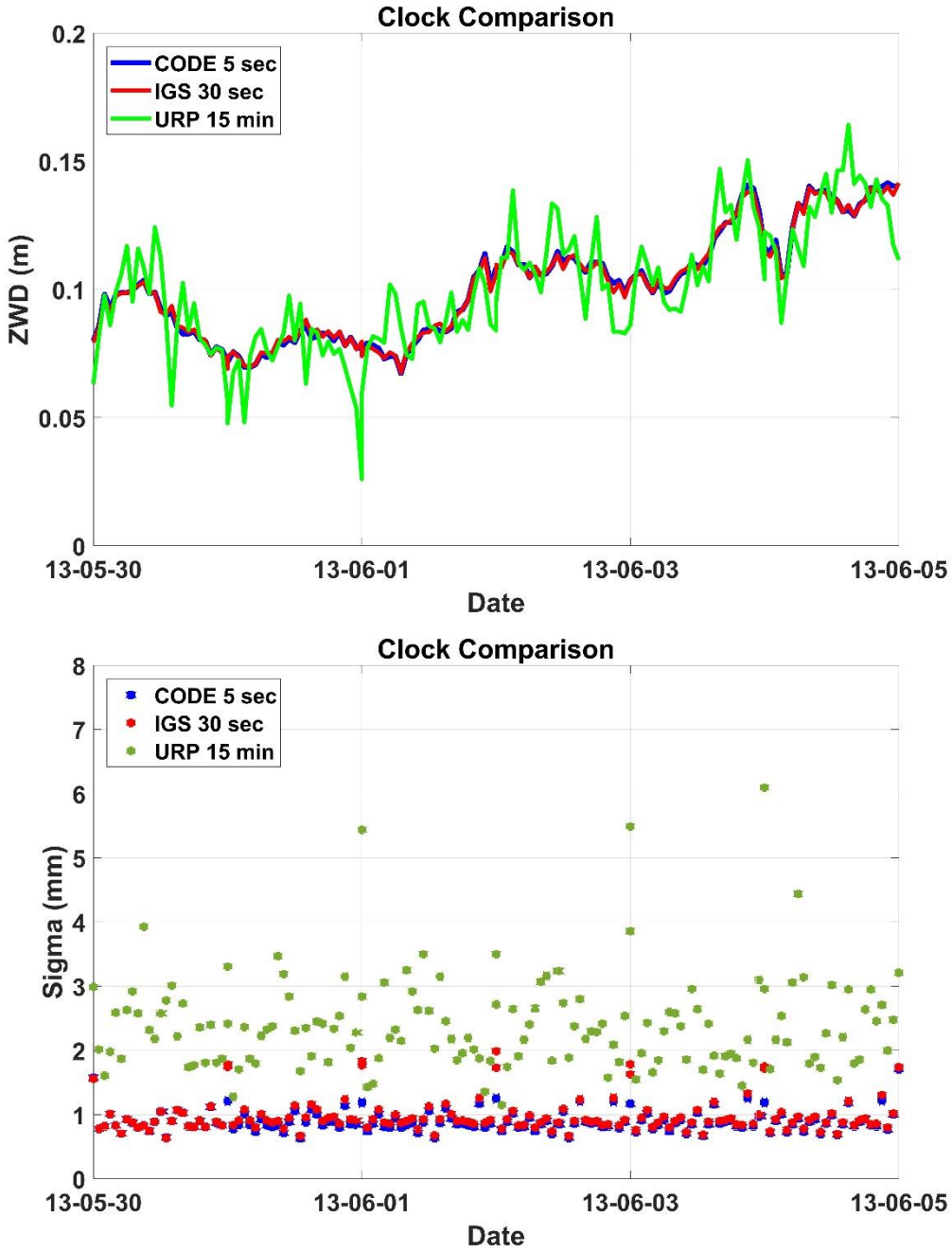

Figure 5.12 : ZWD estimates (up) and RMSs of the solutions at the site GRAZ where the PPP was performed with different clocks.

Clock RINEX files available from the IGS and contain clock values sampled every 5 minutes or 30 seconds while the satellite clocks in the sp3 file are sampled for every 15 minutes. In addition, the CODE analysis center provides final clock correction data with a 5-second time resolution (i.e., for processing the high-resolution observation data). A higher clock correction rate is in particular useful in case of a comparable observation data rate. Comparison of the wet delays provided from different clock products showed that the IGS clock of 30 seconds gave almost similar results to the CODE's 5 seconds clock product. On the other hand, the satellite clocks with 15 minutes resolution in the precise ephemeris files were rather harmful due to the significant data reduction.

As illustrated in Figure 5.12, the mean differences in the ZWDs due to processing the CODE's clock instead the IGS remained in several millimeters; the RMS of the differences are below 2 mm. The high inconsistencies (i.e., < 4 cm) detected when using 15 minutes interval clocks due to the fact that the clocks are only reliable at the sampled epochs (i.e., every 15 minutes). The interpolation of the low sampling clocks raised the RMS values of the estimates i.e. 3-4 times bigger RMS values were noticed compared to the high rate clocks.

5.2.5 Cut-off elevation angles and parameter spacing

Observations at a low elevation angle are more influenced by tropospheric refraction and multipath effects than observations with high elevation angle. In addition, large correlations between troposphere path delays and station height can be reduced by lowering the angle in the data analyses, however, the azimuthal asymmetries are essential in this context to improve the positioning accuracy. On the contrary, observations at higher elevation angle reduce the number of available observations, degrade the geometry and as a result, formal errors increase.

Figure 5.13 shows the mean RMS values of the ZWDs obtained from individual PPP campaigns between May 30 - June 6, 2013. Each PPP solution processed with three different cut-off elevation angle: 3°, 10°, and 20°, respectively. It can be noticed from the results that the RMS values of the wet delays are two times higher at the high elevations in comparison to the lower observations no matter which troposphere model is applied in the analyses.

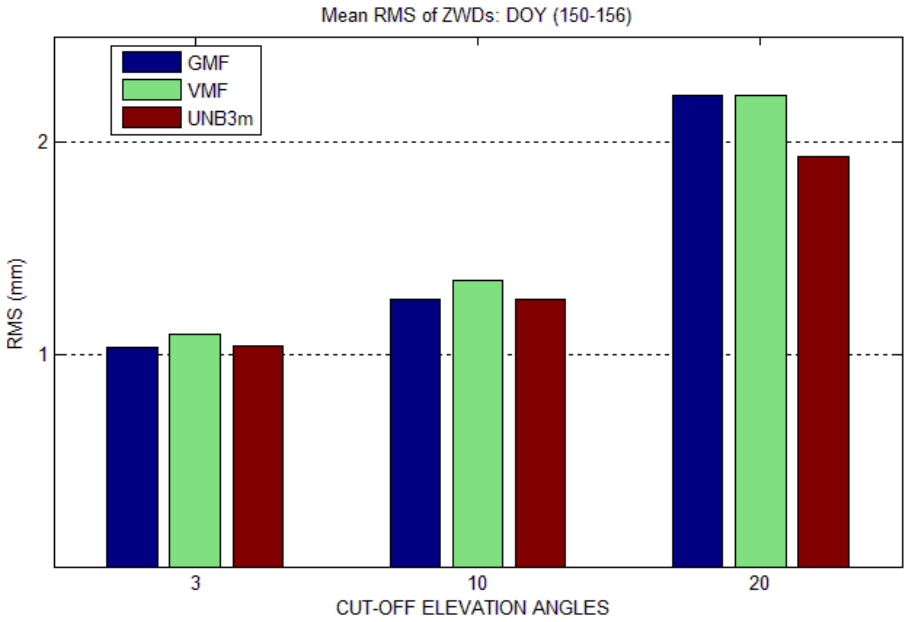

Figure 5.13 : RMS values for the wet delay estimates at different cut-off elevation angles: 3°, 10°, 20°.

Parameter spacing may be specified for all time-dependent piece-wise linear parameters such as ZWD. A time interval between the estimates is crucial since the parameters are estimated at spaced time so-called nodal points. The linear function is used to model the parameters between nodal points. Figure 5.14 illustrates two independent PPP solutions processed with a 1-hour and 15 minutes parameter spacing, respectively.

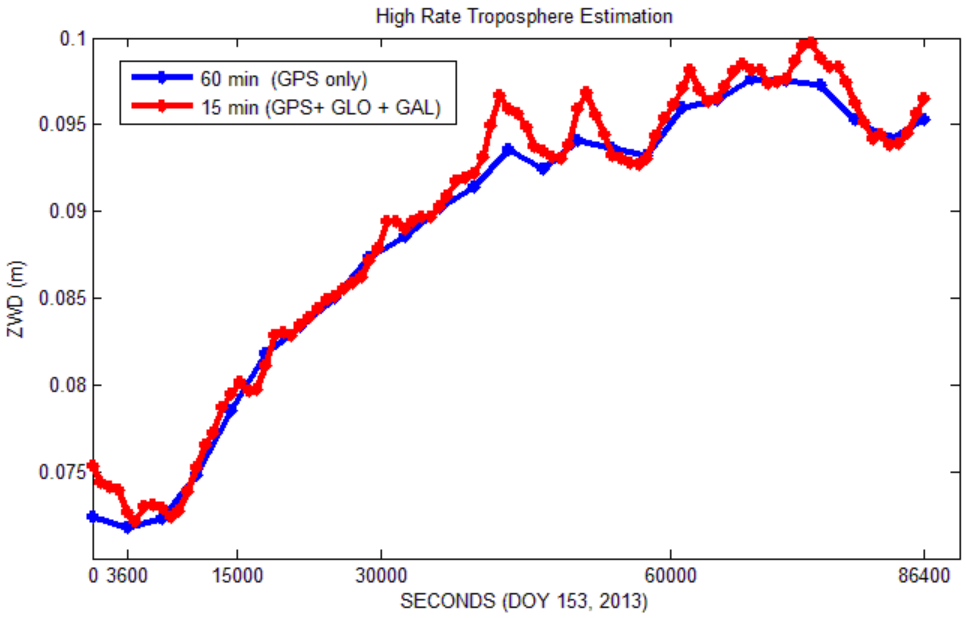

Figure 5.14 : The ZWDs estimated with different time resolution; IGS site GANP on June 2, 2013.

The results indicate that the estimates with the 15 minutes interval are more sensitive to catch the short time atmospheric variations than the solutions with coarser parameter spacing i.e. 60 minutes. Because the water vapor is highly variable with time and space, using parameter intervals longer than 2 or 3 hours will cause formal errors of the estimates to increase. On the other hand, there are limitations for the path delays estimated less than one hour that higher RMS values might be observed due to a large number of unknowns and correlation between parameters.

5.2.6 Baseline length comparison

The relationship between ZWDs and baseline lengths for relative GNSS solutions was investigated by processing the baselines formed with the three IGS sites: POTS, ZIMM and LEIJ. POTS was selected as the station whose wet delay parameters were a major concern. The reference stations were determined as "ZIMM" with 732.812 km, "GOPE" with 299.500 km and "LEIJ" with 123.639 km away with respect to the POTS station. The troposphere was modeled with the VMF1 while relative sigma between subsequent epochs was specified as 5 mm. The wet delays were estimated with 1-hour resolution on May 30, 2013. Figures 5.15 shows the RMS comparison of the ZWD estimates. It can be concluded that there is an inverse correlation between the accuracy of the estimates and the baseline length.

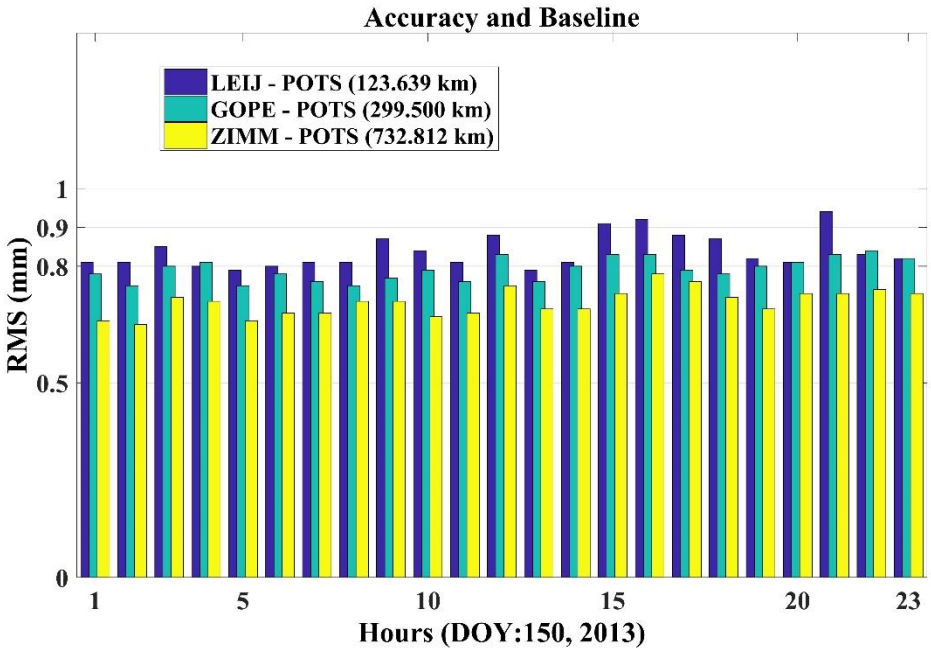

Figure 5.15 : RMS values of the ZWD estimates at the IGS site POTS processed by the network solutions with different baseline lengths.

It is difficult to separate and resolve the absolute troposphere parameters for short baselines that at each endpoint the satellites' geometry, elevation angles, and mapping functions are almost identical. For longer baselines, the correlation between both endpoints falls and the tropospheric delays can be estimated with higher accuracy. Table 5.9 summarizes the overall accuracy of the solutions with respect to used baseline lengths. A posteriori RMS of the Network solutions and the residuals of the estimated coordinates against the CODE's weekly SINEX coordinates were also illustrated in the table.

Table 5.9 : The statistics derived from the network solutions with different baseline lengths.

Baseline	Bas. Length (km)	RMS of Solution (mm)	Obs.	CODE - GNSS		
				ΔX (mm)	ΔY(mm)	ΔZ(mm)
ZIMM - POTS	732.812	1.1	3336	-5.1	-1.1	5.9
GOPE - POTS	299.500	1.2	8120	-10.2	6.9	1.7
LEIJ - POTS	123.639	1.5	7093	-6.7	5.8	5.0

5.2.7 Epoch-wise kinematic coordinates

Kinematic positions are epoch-wise parameters that are estimated for each observation epoch with other unknowns (e.g., troposphere and clocks) and they are very sensitive to the quality other parameters in the observation equation. In this part of the study, the correlation between kinematic coordinates and tropospheric refraction was investigated.

The kinematic coordinates were validated with the IGS reference coordinates (ITRF 2008-01-01 00:00:00) extrapolated to the observation epoch: June 2, 2013, 00:00:00. The positioning residuals of the estimated coordinates for the POTS site in the North, East and Up components with respect to applied GPT/GMF troposphere model were shown in Figure 5.16. The wet delays were also added to the graphs to reveal if there exists a correlation between the epoch-wise coordinates and the tropospheric refraction.

The station displacement of kinematic POTS station in the North and the East direction are below ± 2 cm for the GPT/GMF and the ECMWF/VMF1 while the vertical positioning shows discrepancies up to ± 5 cm for both models. The largest residuals are observed within ± 10 cm in the Up component with the UNB model. De-correlation between the ZWD and the height can be established by using low elevation angles (<

10°) with good a priori ZHD models. The mean residuals of the estimated coordinates and the standard deviations of the residuals are listed in Table 5.10.

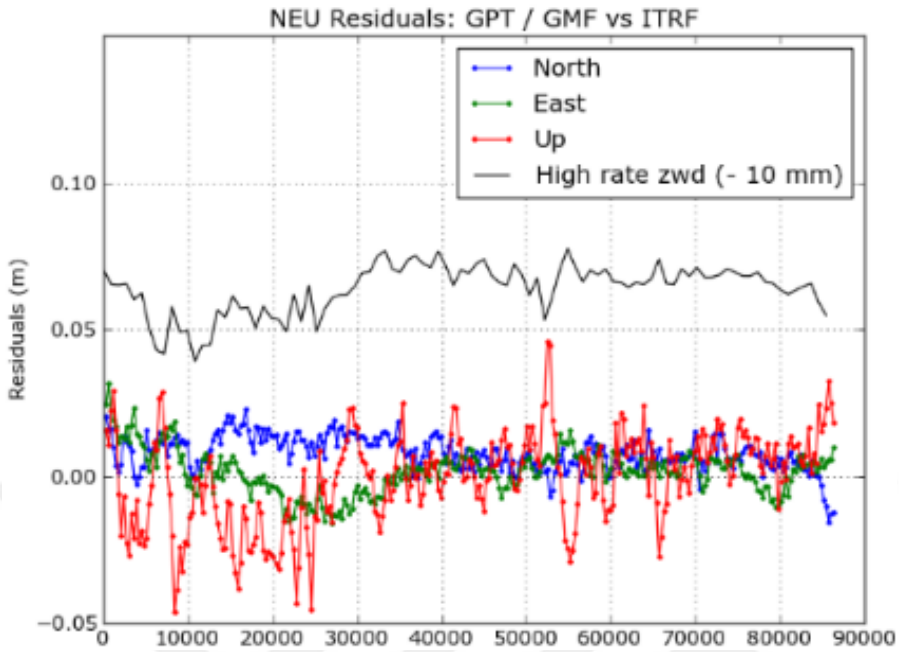

Figure 5.16 : POTS inematic receiver North, East and Up residuals to nominal a priori position (ITRF2008 – epoch: June 2, 2013).

Table 5.10 : The mean positioning residuals and standard deviations of the residuals of the kinematic coordinates with respect to the three troposphere models.

Unit: (mm)	GPT/GMF		ECMWF/VMF1		UNB/NIELL	
	Mean	St.Dev	Mean	St.Dev	Mean	St.Dev
North	8.0	10	8.1	9.9	-5.8	13.4
East	1.8	7.7	2.5	7.3	17.3	3.7
Up	-0.6	15.8	-1.8	15.1	13.0	30.0

5.3 Monitoring PWV with GNSS PPP

This part of the study addresses post - processed monitoring of the PWV with PPP observations. Due to the fact that tropospheric wet delay is well correlated to the quantity of water vapor integrated along the signal path, the wet delay estimates from the GNSS measurements can be used to quantify the atmospheric water vapor or the PWV which plays a crucial role in weather events. The GNSS observations from six IGS stations, which located in the region affected from a severe weather, were processed with PPP and network GNSS campaigns separately in order to monitor the weather variations between in May and June of 2013. The GNSS sites were picked

based on the criteria that radiosonde stations within 50 km distance of the IGS site are available.

The hourly PWV data were introduced from the hourly estimated wet delays and using the conversion formula, i.e. the equation 4.54, developed by Bevis et al., (1992). The conversion factor between the ZWD and the PWV must be determined for each site and each estimation epoch. The reference data to verify the PPP derived PWVs were extracted from the radiosonde sites' readings. The radiosonde profile data is available at the National Ocean and Atmospheric Administration's (NOAA) - Integrated Global Radiosonde Archive (IGRA) (Url-8) where temperature, pressure and humidity data along the flight path is tabulated with respect to altitude.

The IGS stations (white) and the co-located or close radiosonde sites (i.e., yellow) used in the analyses are expressed in Figure 5.17. For an accurate comparison, the radiosonde sites must be close enough to the GNSS site that both sites, therefore, could have almost similar atmospheric conditions and variations over time. The radiosonde sites Ganovce, Wroclaw, Praha, and Graz are co-located, whereas the sites Lindenberg and Payerne are within 70 km from the GNSS sites POTS and ZIMM, respectively. The IGS and the radiosonde sites used in the experiment are listed in Table 5.11.

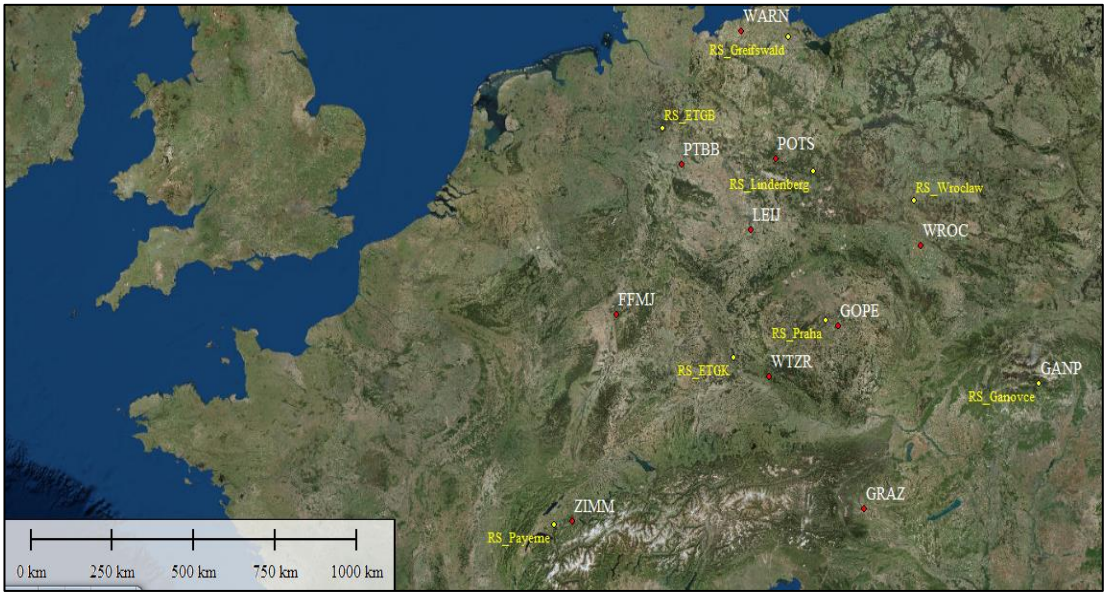

Figure 5.17 : IGS and RS sites used in the PWV monitoring during the 3-week period (20 May – 10 June 2013).

In the cases where the GNSS site is located above the radiosonde site, the only measurements above the height level of the GNSS site were considered. On the

contrary, for the cases where the GNSS site is below the radiosonde, the radiosonde readings were extrapolated linearly.

Table 5.11 : The IGS and the radiosonde sites used in the analyses.

IGS				Radiosonde			
Site	Lat	Long	H	Site	Lat	Long	H
wroc	51.1130	17.0610	181.0	wroclaw	51.1131	16.8811	119.6
ganp	49.0344	20.3227	745.2	ganovce	49.0333	20.3167	703.0
gope	49.9136	14.7855	592.6	praha	50.0078	14.4469	302.0
graz	47.0669	15.4933	538.3	graz	46.9931	15.4392	340.0
pots	52.3791	13.0658	144.4	lindenberg	52.2167	14.1167	112.0
zimm	46.8769	7.46527	956.7	payerne	46.8117	6.9425	490.0

Figure 5.18 illustrates the time series of the PPP PWVs with respect to the radiosonde reference data for the observed stations. The mean differences between the PPP solutions, which processed with the GPT/GMF, and the Radiosonde data at the six IGS sites range from 1.43 to 3.99 mm. The mean differences differ from 0.63 to 2.48 mm when the ECMWF/VMF1 model is employed and from -1.78 to 1.88 mm for the UNB / Niell model. The PPP PWV parameters estimated from the PPP solutions using the ECMWF/VMF1 troposphere model offered more consistent and accurate results against the radiosonde data while the biggest deviations were experienced for the PPP solutions using the UNB / Niell model.

Similarly, the same site observations were processed by the Network GNSS by forming baselines between the stations. The estimated ZWDs then converted to the PWVs in order to reveal the improvement of the water vapor monitoring with respect to the radiosonde measurement. The findings proved that the GNSS solutions both the PPP and the Network are more accurate in terms of water vapor monitoring if the ECMWF/VMF1 is used in the data analyses.

The maximum differences are found at the site POTS, i.e., 12.28 mm, 10.71 mm, and 13.57 mm for the GPT, VMF1, and UNB, respectively. Since the radiosonde site Lindenberg, which was specified to validate the PPP results obtained at POTS, is approximately 70 km away from the site, and thus slightly different water vapor estimates were observed due to the long distance between two sites. Table 5.12 provides overall statistics resulting from a comparison of the GNSS sessions and the radiosonde data. In addition to the mean, the table includes median, standard deviations, root mean squares and maximum values for the differences of the ZWDs.

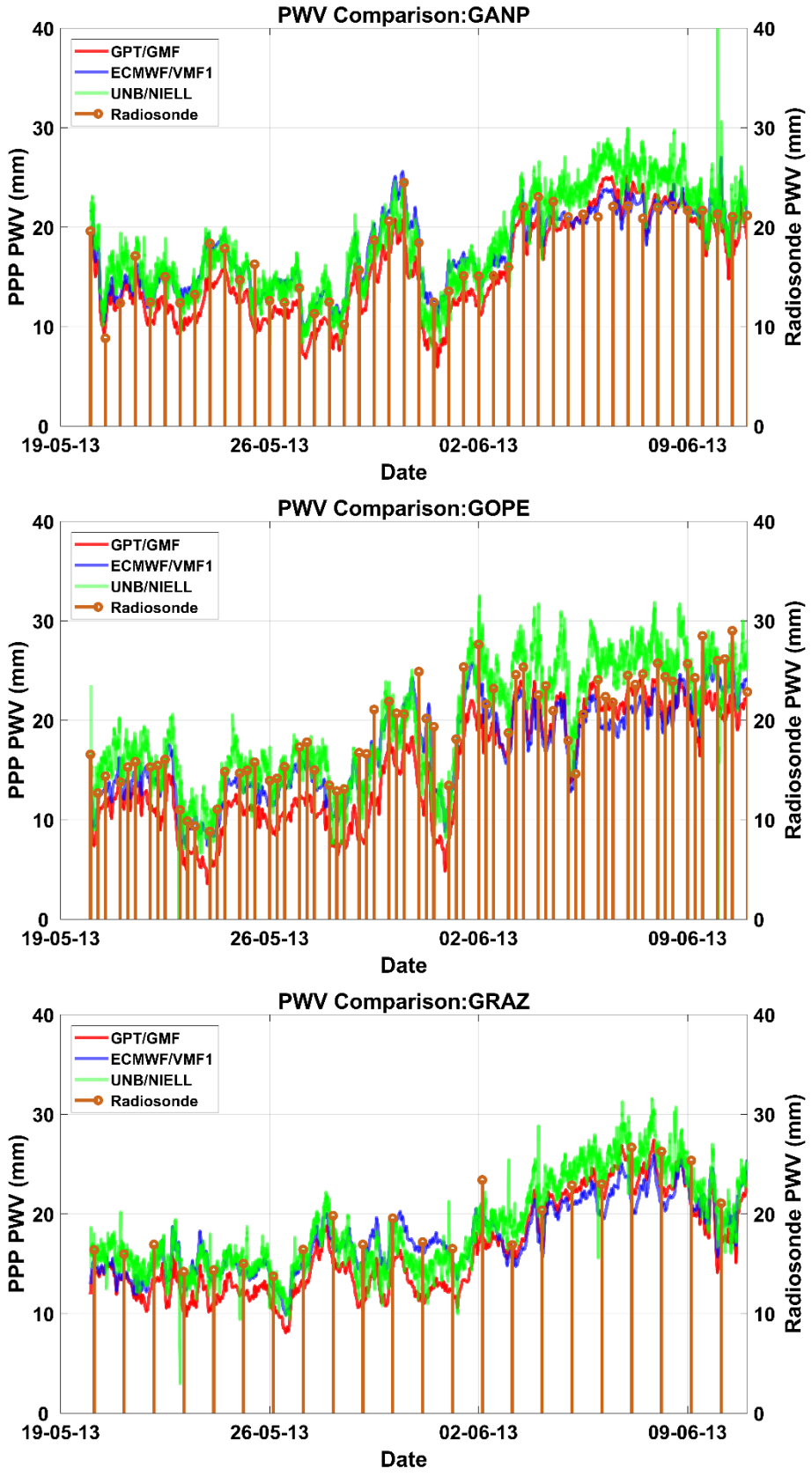

Figure 5.18 : PWV differences between the radiosonde data, the PPP solutions and the relative solutions with respect to different troposphere models at six IGS sites: GANP, GOPE, GRAZ, POTS, WROC and ZIMM.

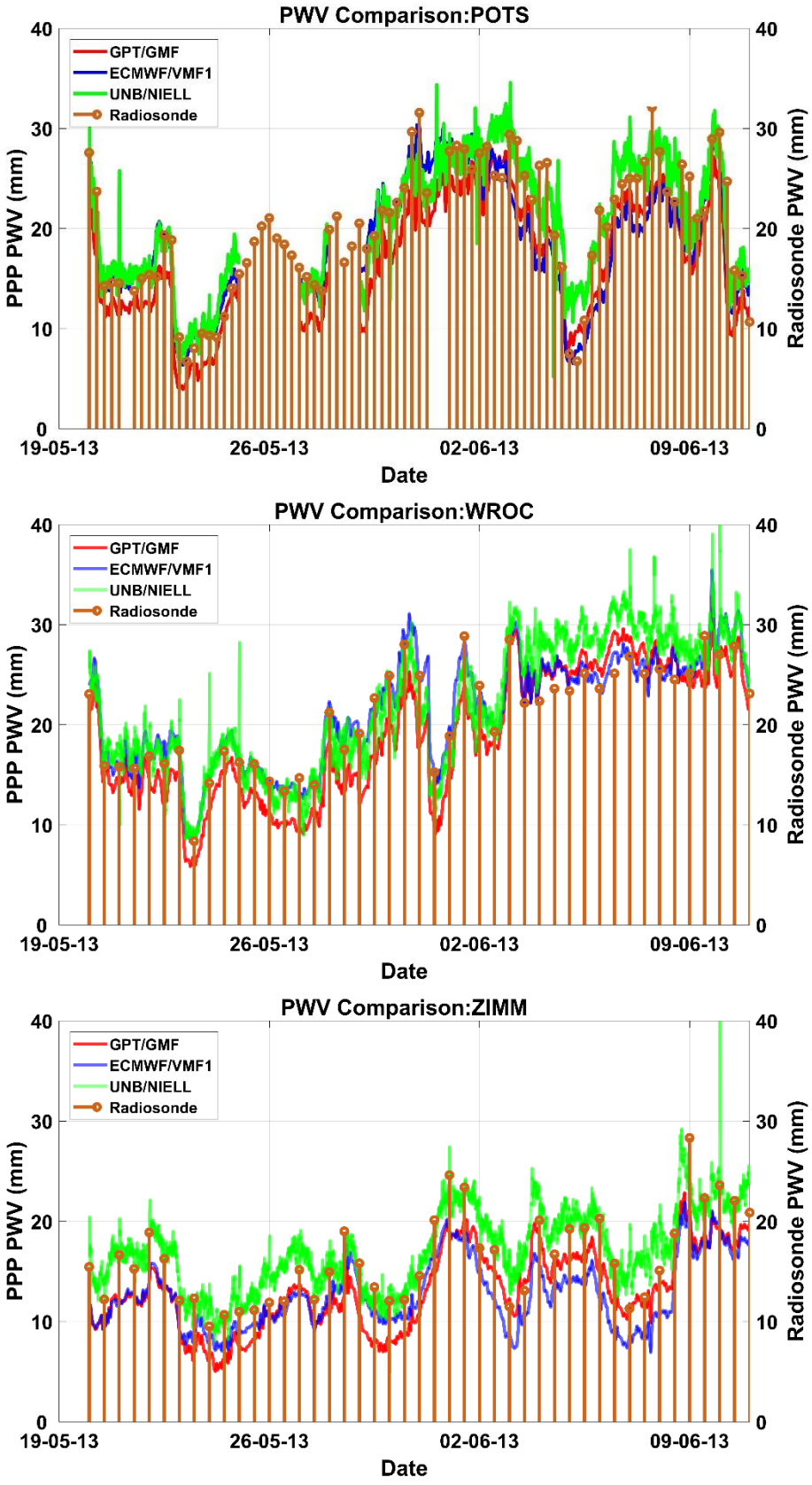

Figure 5.18 (continued): PWV differences between the radiosonde data, the PPP solutions and the relative solutions with respect to different troposphere models at six IGS sites: GANP, GOPE, GRAZ, POTS, WROC and ZIMM.

Table 5.12 : Data statistics of the PPP and Network GNSS derived PWVs with respect to the Radisonde data.

	RS – PPP (GPT)	RS – PPP (VMF1)	RS – PPP (UNB)	RS – DD (GPT)	RS – DD (VMF1)
			WROC		
Mean Bias (mm)	1.84	-0.44	0.34	1.30	-0.57
Median (mm)	2.01	-0.42	-0.54	1.41	-0.75
std (mm)	2.67	1.05	5.67	2.61	1.29
rms (mm)	3.22	1.13	5.62	2.89	1.40
Max diff (mm)	7.24	2.66	7.63	7.24	2.66
			GANP		
Mean Bias (mm)	1.43	-0.63	-0.58	1.01	-0.58
Median (mm)	1.81	-0.84	-0.85	1.16	-0.69
std (mm)	2.00	1.29	3.16	2.24	1.76
rms (mm)	2.44	1.42	3.18	2.43	1.84
Max diff (mm)	6.51	3.82	7.41	6.51	3.82
			GOPE		
Mean Bias (mm)	3.99	2.09	0.04	3.43	2.11
Median (mm)	3.82	1.84	0.46	3.15	2.07
std (mm)	2.51	1.64	4.08	2.63	1.81
rms (mm)	4.70	2.65	4.05	4.31	2.78
Max diff (mm)	11.84	6.72	9.33	11.84	6.72
			GRAZ		
Mean Bias (mm)	3.69	2.48	1.78	3.31	2.45
Median (mm)	3.85	2.10	2.05	3.27	1.79
std (mm)	1.54	1.38	1.82	2.04	2.00
rms (mm)	3.99	2.82	2.52	3.87	3.14
Max diff (mm)	6.66	5.48	4.97	6.66	5.48
			POTS		
Mean Bias (mm)	3.74	1.87	1.01	3.23	1.82
Median (mm)	3.53	1.08	0.23	3.05	1.03
std (mm)	2.95	3.27	4.38	3.03	3.26
rms (mm)	4.75	3.75	4.47	4.42	3.72
Max diff (mm)	12.28	10.71	13.57	12.28	10.71
			ZIMM		
Mean Bias (mm)	3.07	3.52	-1.88	2.37	3.30
Median (mm)	3.15	3.24	-0.12	2.69	3.31
std (mm)	1.91	1.54	7.67	2.11	1.74
rms (mm)	3.61	3.84	7.81	3.16	3.72
Max diff (mm)	6.86	8.01	5.72	6.86	8.01

The IGS releases its final tropospheric products, namely zenith path delays, for a large number of GNSS sites on a daily basis with a latency around three weeks so they can be treated as reference data for individual GNSS campaigns. The PWVs derived from the GNSS PPP and Network sessions were also verified with the IGS Final ZPD products. The ZPD values were extracted from the "US Naval Observatory" (USNO) AC where they are estimated with the BERNESE GNSS software by processing the ionosphere-free linear combination of the observations with a sampling interval of 300 seconds, at minimum elevation cut-off angle of 7° and by modeling the troposphere with the GPT/GMF model. The root mean square error of the USNO's PWVs are at the mm (i.e., < 2.0 mm) level.

In order to avoid biases generated due to the interpolation of the ZPDs, only the IGS values at the matching epochs with the PPP or Network were used for the validation. Due to the latest developments, a large number of IGS ACs adopt the ECMWF/VMF1 model to estimate the total ZPD in their solution. However, in 2013, the USNO AC, as well as many other ACs, was using the Saastamoinen (1972) formula, GPT derived pressure data and dry GMF to calculate a ZHD. Therefore, the validation in this part was carried out by considering the conventions were effective in 2013 that were recommending to use the GPT/GMF model to derived a tropospheric refraction. In addition, the IGS ACs generally estimate ZPD values with the PPP rather than the network solutions.

The requested IGS ZWDs were derived by subtracting the calculated ZHDs from the total ZPDs. Using the Bevis et al. (1994) equations 4.55 and 4.56, the ZWDs converted to the PWV for each defined epoch. Figure 5.19 displays the differences between the PWV values derived from both the GNSS PPP and Network sessions and the reference PWV values calculated from the IGS Final troposphere products i.e. ZPD at the GANP site from May 20 to June 10, 2013. The solid horizontal black line represents the reference ZPD data while each dot symbolizes the difference from the reference; each color corresponds to the applied GNSS measurement technique and used troposphere model in the analyses.

The mean differences between the IGS PWV and GNSS PPP are -0.38 mm for the GPT and 1.65 mm for the VMF1 while the RMS values are 0.74 mm and 2.52 mm, respectively. The RMS values deteriorate, i.e. 0.91 mm for the GPT and 2.73 mm for the VMF1, when employing the GNSS Network solution.

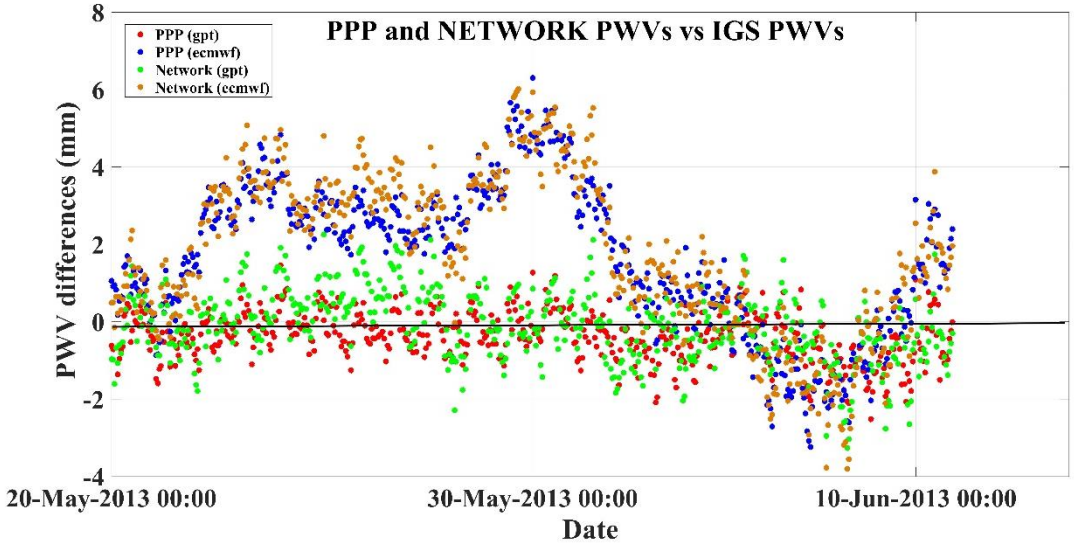

Figure 5.19 : Discrepancies between the PPP PWVs (gpt: red and ecmwf: blue), Network PWVs (gpt: green and ecmwf: brown) and the PWV derived from the IGS USNO AC (solid black line) at the GANP station.

These decreases in the RMS values are expected because the IGS ZPDs are nothing but the products of a PPP solution, and so they are expected to be more compatible with another PPP session performed at the same site. In this regard, the validation of the PPP's results with the IGS ZPDs is an intra-technique comparison that both PWV products are utilized by using almost same models, inputs, and by applying the same measurement technique. Table 5.13 shows the cross-comparison statistics between the IGS Final products, PPP and Network session results.

Table 5.13 : PWV cross-comparison between the IGS, PPP and Network solutions.

Site: GANP	IGS - PPP (GPT)	IGS - PPP (ECMWF)	IGS - Net (GPT)	IGS – Net (ECMWF)
Mean Bias (mm)	-0,38	1,65	-0,11	1,80
St.Dev (mm)	0,63	1,91	0,91	2,05
RMS (mm)	0,74	2,52	0,91	2,73
Max Diff (mm)	1,46	6,30	2,25	6,01

The large RMS values, noticed in the table for the PPP sessions using the ECMWF/VMF1, depend on frequently updated (i.e., each six hours within a day) meteorological data and thus a variation in the a priori ZHD values of the VMFG. PWV data derived from solutions using these updated VMFG data naturally vary from PWVs which are provided from solutions e.g. IGS ZPD, PPP with GPT/GMF using an annual averaged meteorological data to model the troposphere.

5.3.1 Real-time water vapor monitoring with IGS URP products

Monitoring precipitable water vapor using the GNSS has been investigated since 1990's and a remarkable progress has been achieved for post-process monitoring studies. However, it still remains a challenging subject to accomplish real-time solutions from which many climate studies may benefit from. To be used in the NWM analyses, a PWV data must be obtained within less than an hour and the only way to fulfill this condition is carrying out processes without delays, working with a small amount of data and using accurate orbits and clocks that published in real time. URP orbits and clocks are the only data available in the real-time within the IGS product set. URP orbits are updated 4 times in a day and are valid for a 48-hour period. The first 24 hours are based on actual observations and the second 24 (i.e., predicted part) hours extrapolated from the first part. The predicted half accuracy is less than 10 cm and 5 ns by means of orbits and clocks, respectively, which is a significant degradation in accuracy compared to Final orbits and clocks (i.e., < 5 cm and < 0.1 ns). IGS URP products offer reliable solution if only they are processed within a network-based GNSS session since the errors and biases that absorbed in satellite clocks and orbits can be mitigated by differencing. The performance evaluation of the URP products in troposphere monitoring has been assessed at the IGS stations GRAZ and WTZR. Figure 5.20 shows the PWV values estimated from the URP utilized PPP and Network sessions versus the PWV values derived from the Final IGS ZPD products.

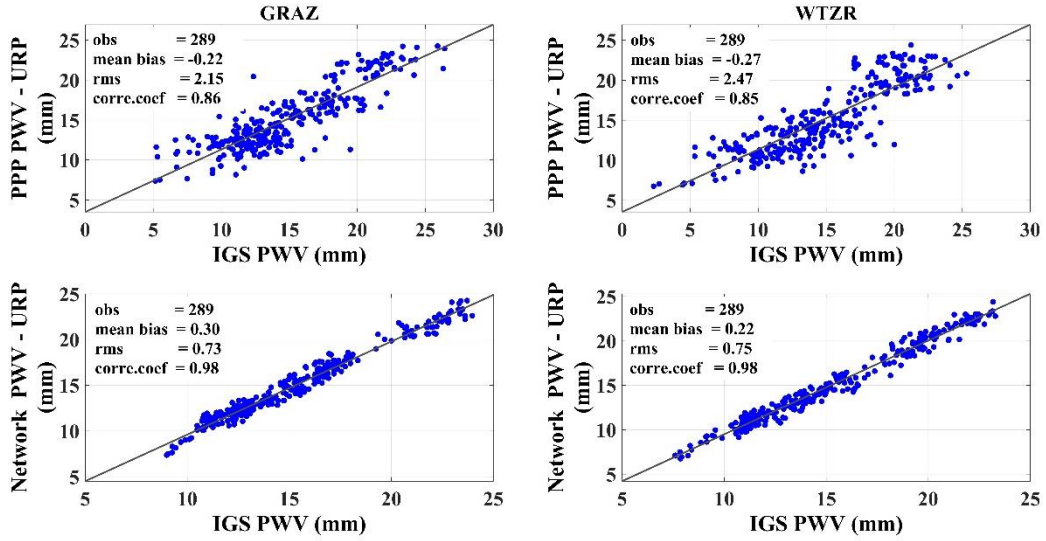

Figure 5.20 : Scatter plot comparison between PWVs derived by PPP and Network sessions with the URP and PWVs generated from IGS Final troposphere products.

For each GNSS solution, the troposphere was modeled with the GPT / GMF as a random walk, with 1-hour resolution. The upper part of the scatter plot in figure 5.20 shows the PPP results against the IGS data while the lower part illustrates the Network solution with respect to the IGS. It can be concluded that the differences from the IGS data are significantly larger for the PPP sessions compared to the Network solutions. The same conclusion can be inferred by comparing the RMS values of the differences and the correlation coefficients between the estimates. The mean RMS values of the differences between the PPP and IGS reference data are about 2.15 mm and 2.47 mm for GRAZ and WTZR, respectively. The mean RMS of the differences for the relative solutions offers an improvement of about 30 - 35 %, i.e. 0.73 mm and 0.75 mm for the GRAZ and WTZR stations, respectively. The comparatively bad results of the PPP can be attributed to inconsistency of the interpolated URP clocks, which disturbed the PWV estimates in the end, whereas the relative solutions canceled almost all biases related to the satellite and receiver. In summary, it is not a viable option to use the predicted part of the URP products, particularly interpolated clocks for PPP based RT atmospheric studies where a high accuracy is needed. The coherent way to use these products in RT PPP is to process only the epochs of each 15 minutes' data without interpolate the data. The PWVs derived from the PPP and the Network sessions that processing IGS URP products were further compared to co-located radiosonde derived PWVs where the results are demonstrated in Figure 5.21 and Figure 5.22. It is obvious the improvement due to cancelled satellite and receiver related errors within the network.

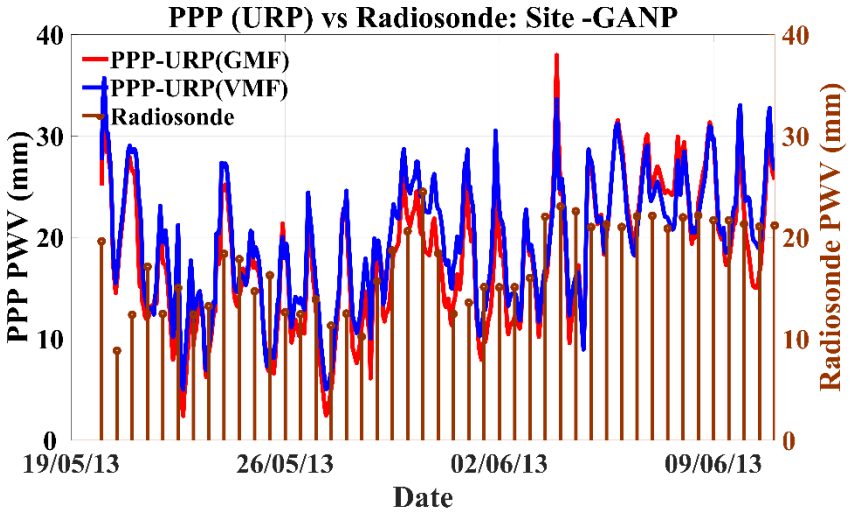

Figure 5.21 : PWV comparison between the Radisonde data and the PPP session using the URP products at GANP.

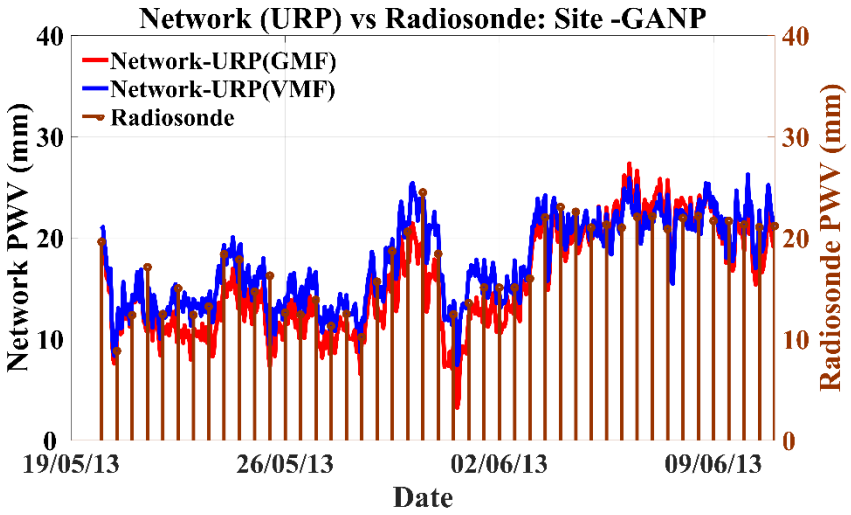

Figure 5.22 : PWV comparison between the Radisonde data and the Network session using the URP products at GANP.

Table 5.14 lists the mean PWV differences and RMS of the differences for the radiosonde derived PWV and the GNSS (i.e., PPP and Network) derived PWVs using GPT/GMF and ECMWF/VMF1 troposphere models in order.

Table 5.14 : Mean differences, RMS values and maximum detected differences of GNSS solutions (PPP and Network) and radiosonde readings for all relevant sites.

Product: IGS Ultra-Rapid	RS – PPP (GMF)	RS – NET (GMF)	RS – PPP (VMF1)	RS – NET (VMF)
		WROC		
Mean Diff. (mm)	1.48	1.61	-0.53	-0.29
RMS (mm)	8.10	3.07	7.57	1.22
Max Diff (mm)	19.35	7.94	16.40	3.56
		GANP		
Mean Diff. (mm)	2.45	1.05	0.33	-0.57
RMS (mm)	7.46	2.45	6.96	1.83
Max Diff (mm)	18.21	6.21	16.91	4.34
		GOPE		
Mean Diff. (mm)	8.27	3.51	5.65	2.20
RMS (mm)	22.07	4.33	19.32	2.85
Max Diff (mm)	>30.00	11.23	>30.00	7.30
		GRAZ		
Mean Diff. (mm)	3.38	3.40	2.27	2.56
RMS (mm)	7.18	3.91	5.98	3.23
Max Diff (mm)	13.80	7.19	13.43	6.78
		POTS		
Mean Diff. (mm)	2.42	3.43	0.99	2.00
RMS (mm)	13.24	4.51	13.87	3.76
Max Diff (mm)	>30.00	12.33	>30.00	12.97

6. REAL-TIME SERVICES FOR PPP

The atmospheric water vapor has been monitored with GNSS since the 1990's when the first studies were proposed by Bevis et al. (1992), Rocken et al. (1997a and 1997b) and Tregoning et al. (1998). However, a large number of studies have been carried out are PP Network GNSS solutions which are not adequate to respond to real-time requests. Thus, most recent studies have focused on up-to-date GNSS monitoring applications, like now-casting weather systems which necessitate the production of a real time meteorological data. Using URP products is one alternative to accomplish the task as discussed in the previous chapter; however, the URP's accuracies particularly interpolated clocks reduce the reliability of the estimates. Even though clocks and orbits related errors can be canceled by differencing observations with a network solution, analyses will struggle this time to cope with a long computational time and strong correlations come with a relative approach. PPP methods differ from relative methods in that only a single receiver is necessary that removing the need for a user to set a local reference station. However, a sparse CORS network is still required for streaming necessary corrections for a real-time PPP solution. Moreover, one huge weakness of PPP over relative GNSS techniques; the large convergence time that reducing the performance of a real-time positioning, remains in the observations. Long convergence time is a consequence of hard-to-determine undifferenced satellite / receiver hardware delays and must be mitigated before carrying out real-time (RT) PPP applications.

The advent of the IGS Real-Time Pilot Project in 2007 has elevated PPP as a potentially practical alternative to the differential GNSS technique for real-time applications (Ge et al., 2008). The real-time orbit and clock correction to the broadcast ephemerides via data streams from a global network of high-quality GNSS receivers have been provided since April 1, 2013, by IGS Real-Time Services (RTS). The IGS RTS is a partnership of with NRCan, BKG, and ESA/ESOC. The IGS RTS network consists of globally 196 real tracking stations as depicted in Figure 6.1, multiple data centers, and 10 real-time analyses centers (RTAC) around the world. The correction

streams are combined solutions of real-time products published by a number of IGS RT Analyses Centre that makes the streams more reliable and stable. The IGS RTS product availability is at least 95 % that makes it possible to perform real-time PPP applications.

The real-time orbit and clock corrections to the broadcast ephemerides are streamed in the Radio Technical Commission for Maritime services / State Space Representation (RTCM / SSR) format using Networked Transport of RTCM via Internet Protocol (NTRIP). The NTRIP is a differential GNSS data streaming protocol over the Internet via RTCM-104 message format. Ephemerides and corrections are broadcasted within ITRF08. NTRIP broadcasters are established worldwide for sharing the data received from GNSS stations and streaming space state corrections to client users who requested those data. EUREF-IP (i.e., www.euref-ip.net), IGS-IP (i.e., www.igs-ip.net), MGEX.IGS-IP (i.e., mgex.igs-ip.net) and PRODUCTS (i.e., products.igs-ip.net) are most widely used NTRIP casters supported by BKG and allow real-time access to the GNSS data streams. IGS RTS also allows users to access to real-time broadcast ephemeris (i.e., RTCM3EPH) data and code biases to correct pseudoranges disseminated by the RTS.

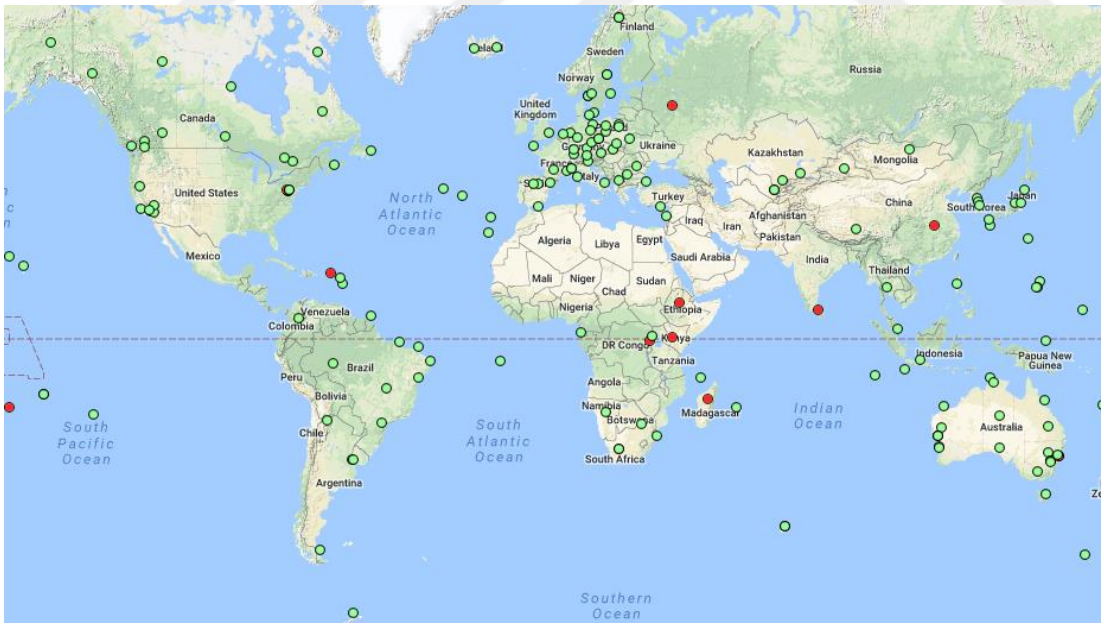

Figure 6.1 : RTS stations distributed worldwide (green: operational, red: no data received for last 10 days) (Url-11, 14.10.2017).

Users must use an NTRIP client application to retrieve a real-time GNSS data after registering to the IGS RTS system. There are a limited number of open source client

applications such as BKG NTRIP Client (BNC) and Real-time Kinematic Library (RTKLIB). The BNC platform has been created by BKG (BKG, 2013) and it is a multi-stream and open source program written under GNU General Public License (GPL), designed to receive, decode and process GNSS products and data from one / multiple NTRIP Broadcaster(s) and can manage a real-time analysis of PPP solution from these streams. Today, the BNC supports all existing GNSS systems (GPS, GLONASS, GALILEO, QZSS, and BDS). Streams could be observations, ephemeris or satellite orbits/clocks. Although it has been developed as a real-time tool, the BNC can run in offline mode as a post-processing software.

BNC enables users to use their own set of configurations regarding the objectives by manipulating configuration file within the application. Configuration options are usually specified via graphical user interface. For example, the flowchart of static PPP solution displayed in Figure 6.2 is one of the sample configuration used to estimate precise SP3 orbits and RINEX clock files by feeding the broadcast ephemeris with

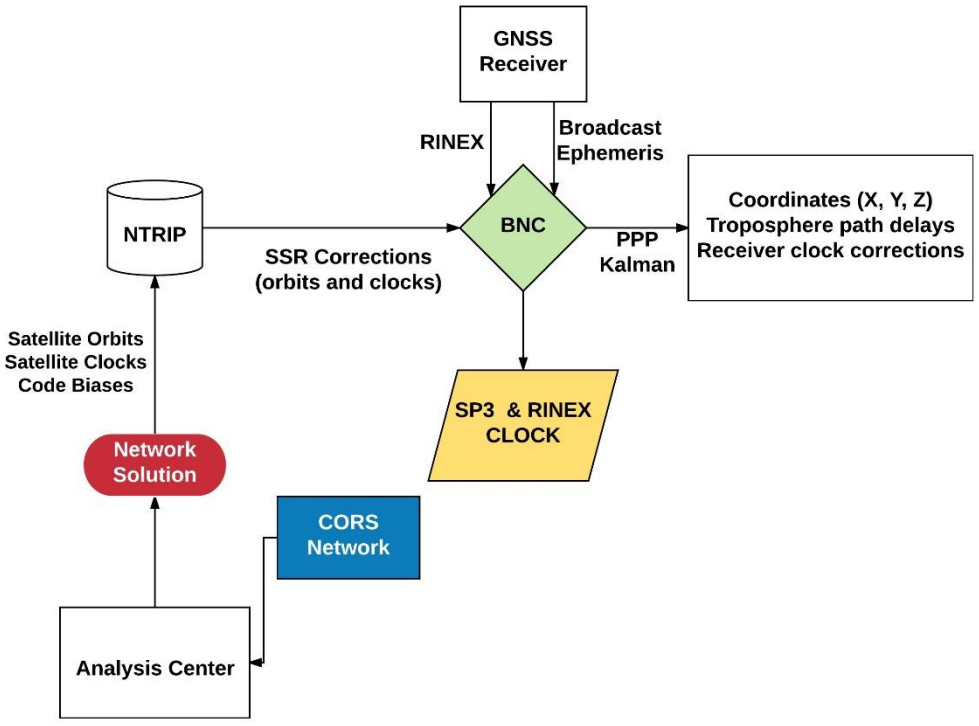

Figure 6.2 : The flowchart of BNC using the real-time correction streams and broadcast ephemeris to produce precise epehmeris orbits (sp3) and clocks (rinex clock).

real-time clock and orbit correction streams. The broadcast correction stream is referred to satellite APC whereas the ephemeris orbits are referred to satellite CoM;

hence the recent ANTEX file is necessary for correcting observations for antenna phase center offsets and variations when producing precise orbits with RTCM SSR messages.

6.1 RTCM DATA and Products

6.1.1 Broadcast ephemeris and observations

IGS RTS disseminates two streams offering the ephemeris data. Incoming ephemeris is first verified and then uploaded to NTRIP caster with 5 seconds repetition rate. The RTCM3EPH is a broadcast ephemeris stream that encoded in RTCM v3 for GPS, GLONASS, and Galileo satellites and is generated from the global IGS RTS Network. The RTCM3EPH01 is another broadcast ephemeris stream for GPS-only solutions and is also generated from the real-time IGS global network. Table 6.1 lists the two casters streaming real-time broadcast ephemeris.

Table 6.1 : Broadcast Ephemeris Streams

Caster IP:Port	Mountpoint	GNSS	Messages	AC
products.igs-ip.net:2101	RTCM3EPH	GPS+GLO	1019 1020 1019	BKG
mgex.igs-ip.net:2101	RTCM3EPH-MGEX	GPS+GLO+GAL	1020 1045 1046	BKG

Real-time RINEX observation data of more than 190 sites are available through RT distribution centers as listed in Table 6.2.

Table 6.2 : NTRIP Broadcasters which provide real-time observation (Weber et al., 2016).

Caster IP:Port	Operator	Country	Register for access	Remarks
www.igs-ip.net:2101	BKG	Germany	Registration	Primary broadcaster for IGS observations
products.igs-ip.net:2101	BKG	Germany	Registration	Primary broadcaster for IGS products

RTS corrections are distributed in the form of unique SSR messages, depending on supported GNSS and type of corrections. The official products include corrections to the GPS only and GPS / GLONASS combined satellite orbit and clocks such as the products, named as IGS01 and IGS02, include corrections only for the GPS satellites while the product assigned at IGS03 contains corrections for GPS and GLONASS.

The IGS RT Pilot project aims to reach a real-time orbit accuracy that higher than IGS Ultra Rapid predicted part and 0.3 ns station/satellite clock accuracy. The satellite position is attributed to the ionosphere-free phase center of the antenna which broadcast corrections will be added on. The correction streams defined in Table 6.3 are available through analyses performed in the network of EUREF and IGS.

Table 6.3 : RTCM v3 streams of ephemeris corrections to support RT PPP (Weber et al., 2016).

Caster	Stream	Ref	GNSS	Messages	Orbit	AC & SW
products.igs-ip.net:2101	IGS01	APC	GPS	1059,1060	IGS Ultra Rapid	SE Combination RETINA
products.igs-ip.net:2101	IGS02	APC	GPS	1057,1058,1059	IGS Ultra Rapid	KF Combination BNC
products.igs-ip.net:2101	IGS03	APC	GPS GLO	1057,1058,1059 1063,1064,1065	CODE Ultra Rapid	KF Combination BNC
products.igs-ip.net:2101	CLK91	APC	GPS GLO	1059,1060 1065,1066	CODE Ultra Rapid	CNES PPP-Wizard + BNC
http://178.33.109.250:2101	CLK93	APC	GPS	1059,1060	IGS Ultra Rapid	CNES PPP-Wizard + BNC

6.2 Real Time Satellite and Clock Correction Calculations

The real-time orbit corrections are given in the Earth Centered Inertial (ECI) reference system in the along-track, cross-track and radial components. On the other hand, broadcast ephemeris streams (RTCMEPH v3) are expressed in the Earth Centered Earth Fixed (ECEF) coordinate system. Thus, real-time corrections must be transformed from the inertial system to the terrestrial system to use these corrections with the ephemeris products.

The real-time correction in the celestial reference system for the current epoch can be described as in equation 6.1:

$$\begin{bmatrix} \Delta_{along} \\ \Delta_{cross} \\ \Delta_{radial} \end{bmatrix}_{T,\,ECI} = \begin{bmatrix} \Delta_{along} \\ \Delta_{cross} \\ \Delta_{radial} \end{bmatrix}_{T_0,\,ECI} + \begin{bmatrix} \hat{\Delta}_{along} \\ \hat{\Delta}_{cross} \\ \hat{\Delta}_{radial} \end{bmatrix} (T - T_0) \tag{6.1}$$

where Δ_{along}, Δ_{cross} and Δ_{radial} are the along-track, cross-track and radial corrections, sequentially. T_0 and T are the issue of data (IOD) and current epoch respectively, and $\hat{\Delta}_{along}$ $\hat{\Delta}_{cross}$ $\hat{\Delta}_{radial}$ are the correction rates of along - track, cross-track and radial components. By using the transformation matrix *R*, whose specifications can be found in the IERS Conventions (Petit and Luzum, 2010), the corrections defined in the ECI system transformed into the ECEF system as expressed in equation 6.2.

$$\begin{bmatrix} \Delta_{along} \\ \Delta_{cross} \\ \Delta_{radial} \end{bmatrix}_{T,\,ECEF} = R \times \begin{bmatrix} \Delta_{along} \\ \Delta_{cross} \\ \Delta_{radial} \end{bmatrix}_{T,\,ECI} \tag{6.2}$$

Finally, the correction streams in the ECEF system subtracted from the broadcast ephemeris in order to find satellite coordinates (X, Y, Z) in the Cartesian ECEF coordinate system as in equation 6.3:

$$\begin{bmatrix} X \\ Y \\ Z \end{bmatrix}_{T,\,ECEF} = \begin{bmatrix} X \\ Y \\ Z \end{bmatrix}_{T,\,BRD} - \begin{bmatrix} \Delta_{along} \\ \Delta_{cross} \\ \Delta_{radial} \end{bmatrix}_{T,\,ECEF} \tag{6.3}$$

The broadcast navigation message delivers the clock data in the form of polynomial coefficients c_0, c_1 and c_2 in the specific reference epoch (t_0) to derive satellite clock offset to the current epoch as given in equation 6.4:

$$t_{corr} = c_0 + c_1 (t - t_0) + c_2 (t - t_0)^2 \tag{6.4}$$

where t_{corr} is the real time clock corrections to the broadcast ephemeris clocks. By subtracting t_{corr} from the correction of broadcast ephemeris gives us the precise satellite clock corrections.

6.3 Real Time Ambiguity Resolution

The greatest restricting factor in delivering a RT PPP solution with corrected orbits and clocks is the convergence time, i.e. the time needed to reach a cm level positioning accuracy. Traditional PPP method uses float solutions, for which long observation time is required (30 min to hours) in static mode. A number of methods have been developed in order to reduce this time such as using a real-time wide area ionospheric correction model as proposed by Juan et al. (2012), introduce un-calibrated phase delays (UPDs) estimated from ground-based network offered by Ge et al. (2011) and implement regional satellite clocks estimated from augmented network as suggested by Laurichesse et al. (2009). The mutual points of these developments are that they are all based on dual-frequency linear combinations and network supported solutions. Currently, several IGS RTS agencies publish their own combined orbit and clock corrections derived from both single epoch and KF solutions. For example, CNES developed a method using a global network to produce orbits and clocks that help to resolve ambiguities in several minutes (PPP-Wizard, (CNES, 2013)). The CNES's PPP approach for resolving ambiguities starts with Melbourne-Wübbena (MW) linear combination for fixing the between satellites wide-lane (WL) ambiguities for each receiver in the network and then, the ionosphere-free phase combination is used to fix the remaining narrow-line (NL) ambiguities with the help of a network solution. During the fixing procedure, the KF estimates the ionosphere-free corrections of the satellite clocks associated with the integer phase combinations and thus can fix the NL ambiguities immediately at the receiver. A KF is then executed in both modes that one PPP solution with resolved ambiguities and the second one with the float ambiguities. The differences between the fixed and float orbits and clocks are streamed as corrections that received from the receiver at the user side to fix the carrier phase ambiguity. With the help of these integer clocks' streams and WL biases provided in real time, user can fix the carrier phase ambiguities and can reach to centimeter level accuracy within a short of time (Laurichesse, 2011). The CNES streams corrections for GPS and GLONASS via RTCM v3 SSR messages 1059 and 1060, sequentially. Besides IGS01, IGS02 and IGS03 streams from the IGS, the CNES makes CLK91, CLK92 and CLK93 streams available for users who requested to use orbits and clocks for a real-time solution with ambiguity fixing ability. The flowchart showing the principle of the CNES RT ambiguity resolved PPP solution is depicted in Figure 6.3.

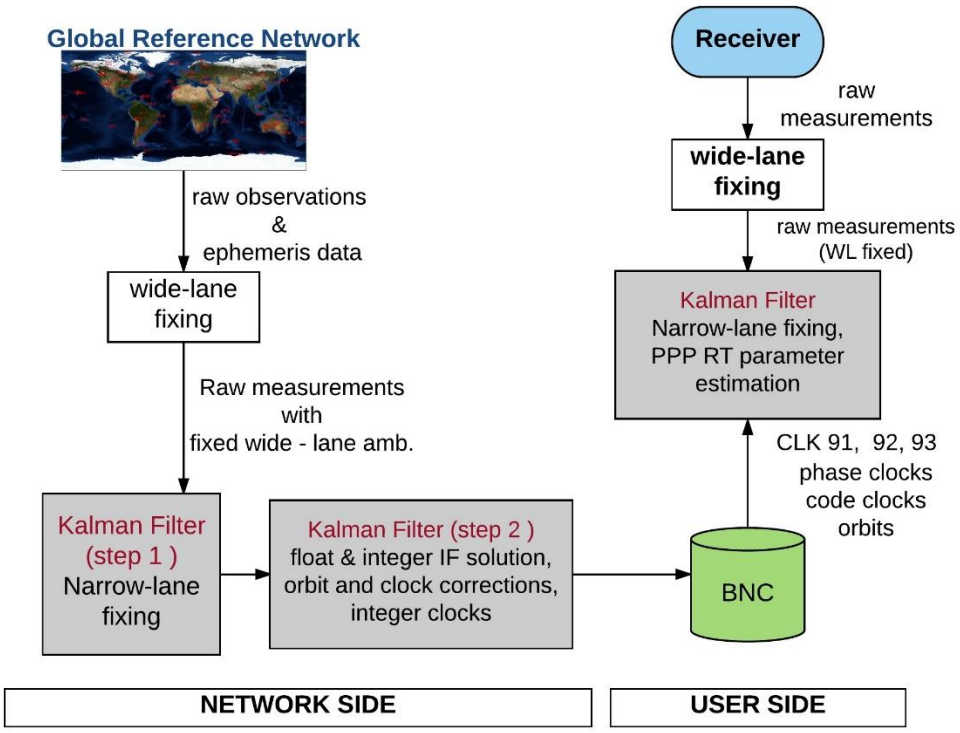

Figure 6.3 : Diagram of RT PPP solution with fixed ambiguity as developed by CNES PPP-Wizard Project (Laurichesse et al, 2011).

6.4 IGS RTS versus CODE final ephemeris

In order to evaluate the accuracy of the IGS RTS correction streams, the precise ephemeris orbits and clocks, which were generated by using the broadcast ephemeris the CNES's correction stream CLK91, were compared with the CODE's Final orbits and clocks with a nominal accuracy of 2.5 cm and 75 picoseconds, separately. In the CNES solution, the satellite orbits coordinate vector $r(t)$ and velocity vector $\dot{r}$ are first calculated based on broadcast ephemeris derived from a global network of reference stations. The real time broadcast corrections which are encoded as RTCM v3 SSR messages calculated in the KF and are then applied to the broadcast orbits (i.e., equation 6.5) and clocks (i.e., equation 6.6).

$$r(t)_{corrected} = r(t) - [e_{radial}\ e_{along}\ e_{cross}] \cdot \gamma Orb \tag{6.5}$$

where $r_{corrected}$ is the corrected coordinate vector $e_{radial} = \dot{r}/|r|$, $e_{along} = r \times \dot{r}/|r \times \dot{r}|$, $e_{cross} = e_{radial} \times e_{alond}$ and γOrb is the SSR orbit correction vector in radial, along-track, and cross track components. The clock corrections are applied to the broadcast clocks as expressed in equation 6.6:

$$dt^{s}_{SSR} = dt^{s} + \gamma Clk/c \tag{6.6}$$

where dt^{s}_{SSR} is the corrected clocks; $\gamma Clk = C_0 + C_1(t - t_0) + C_2(t - t_0)^2$ is the clocks correction obtained from KF as previously expressed by the equation 6.4, t is the broadcast clock time, t_0 is the reference time of clock correction message and c_0, c_1 and c_2 are clock correction coefficients in the SSR messages. The orbital differences refer to the orbital coordinate system were compared for matched epochs only and the RMS values of the orbit and clock differences are calculated for all 31 GPS satellites for 20 consecutive days from May 20th, 2013 to June 10th, 2013. The mean discrepancies in the orbital system for each observed GPS satellites between the two orbits are illustrated in Figure 6.4. The same differences are also displayed in the ECEF Cartesian system in Figure 6.5.

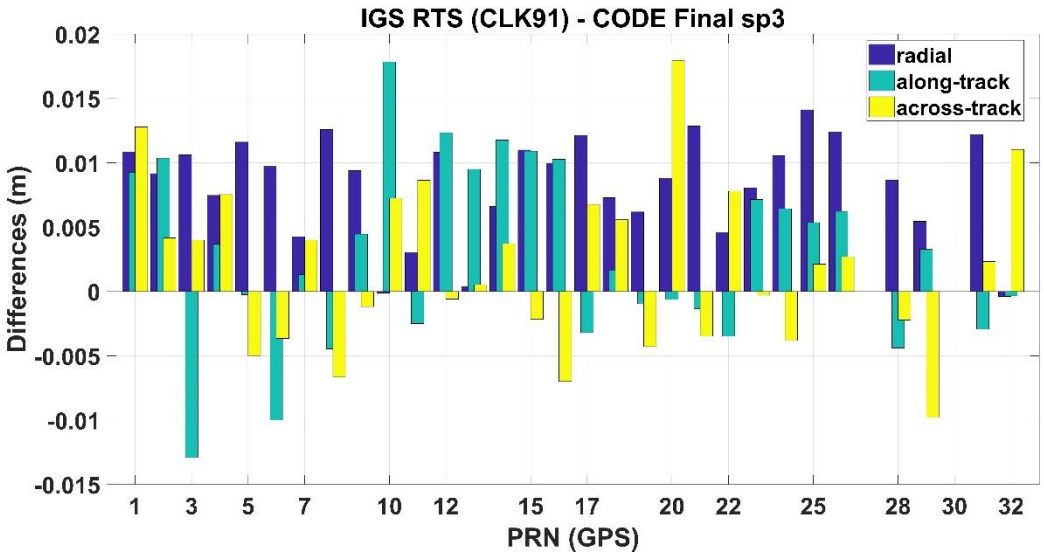

Figure 6.4 : Mean differences in radial, along-track and across-track directions between the IGS RTS (CLK91) and CODE Final ephemeris.

The potential errors in GNSS are projected on the line of sight distance between satellite and receiver. SISRE (Signal in Space Range Error) which refers to line of sight error associated with satellite and receiver can be computed by using equation 6.7. As can be derived from Table 6.4, the mean SISRE value of the IGS RTS against the CODE Final products is 0.50 m with RMS of 0.68 that outperforms the IGS URP's SISRE accuracy that is bigger than 0.8 m.

$$SISRE = \sqrt{(radDiff - clkDiff)^2 + (crossDiff^2 + alongDiff^2)/49} \tag{6.7}$$

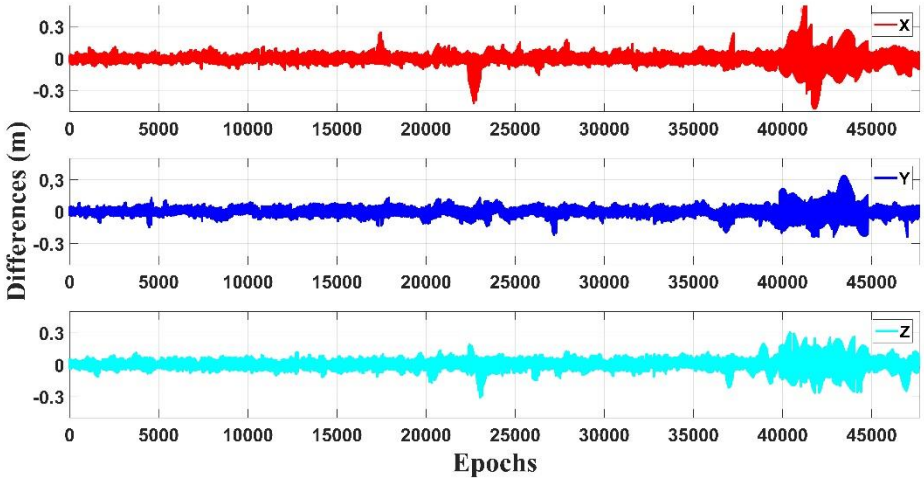

Figure 6.5 : X,Y and Z residuals of the IGS RTS (CLK91) with respect to the CODE Final ephemeris product.

Table 6.4 : Orbits and Clocks comparison between IGS RTS (CLK 91) and CODE Final ephemeris products for 21 consequtive days in 2013.

Doy	Obs	Sisre (m)			3D Orbit (m)			Clock (m)		
		mean	rms	st.dev	mean	rms	st.dev	mean	rms	st.dev
140	2591	0.327	0.462	0.326	0.031	0.035	0.017	0.242	0.464	0.395
141	2453	0.364	0.530	0.386	0.036	0.040	0.018	0.073	0.531	0.526
142	2399	0.417	0.541	0.345	0.035	0.039	0.016	-0.192	0.540	0.505
143	1107	0.815	0.863	0.283	0.047	0.051	0.021	0.733	0.864	0.458
144	2216	1.233	1.344	0.534	0.042	0.047	0.020	1.174	1.348	0.662
145	Corrupt Data									
146	Corrupt Data									
147	1593	0.409	0.615	0.459	0.040	0.045	0.019	0.284	0.619	0.550
148	2700	0.395	0.556	0.391	0.044	0.048	0.020	0.222	0.559	0.513
149	1718	0.551	0.651	0.345	0.042	0.046	0.018	0.513	0.658	0.412
150	2878	0.619	0.758	0.437	0.044	0.050	0.024	0.514	0.764	0.565
151	2700	0.599	0.894	0.664	0.048	0.054	0.025	0.075	0.894	0.891
152	Corrupt Data									
153	2594	0.432	0.616	0.438	0.059	0.071	0.040	-0.069	0.615	0.611
154	2618	0.289	0.565	0.486	0.044	0.051	0.025	-0.024	0.566	0.565
155	2860	0.369	0.635	0.517	0.039	0.044	0.021	-0.081	0.636	0.630
156	2349	0.279	0.427	0.323	0.037	0.043	0.021	-0.101	0.427	0.415
157	1335	0.518	0.655	0.400	0.047	0.052	0.023	0.328	0.659	0.572
158	2844	0.410	0.814	0.703	0.045	0.052	0.025	0.147	0.818	0.804
159	Corrupt Data									
160	Corrupt Data									
161	2859	0.515	0.651	0.398	0.053	0.064	0.035	0.066	0.657	0.654

In comparison to the CODE's orbits, a three - dimensional orbital accuracy value of 4.95 cm is obtained for the real-time products with accuracies of 1.7 cm, 3.8 cm and 2.55 cm for radial, along-track, and cross-track orbital components, respectively. The blank areas in the graph represent the periods with bad satellite data that removed from the observations. Thus, it is highly advised to perform a quality check before using real-time orbits and clocks. With the overall accuracy of 2.28 ns (0.684 m in range) for clocks, the IGS RTS provided much better results than the IGS URP's clocks (i.e., RMS: 3.0 ns). The mean clock differences between IGS RTS and CODE are displayed in Figure 6.6.

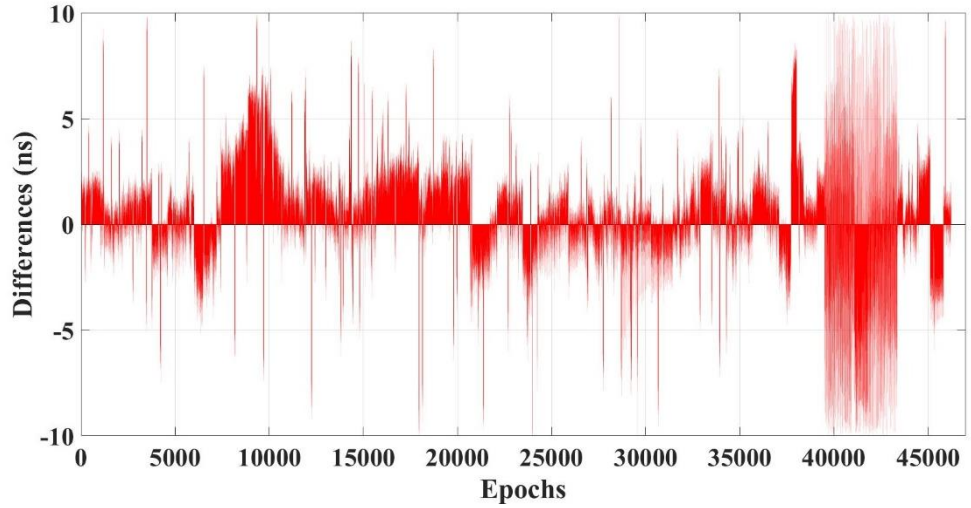

Figure 6.6 : Clock differences between the IGS RTS and CODE Final.

6.5 PPP Solutions using Real Time Platforms and Products

The BNC uses observations from static and rover receivers by processing a dual frequency code-only or code and phase data in the ionosphere-free linear mode. The observation can be extracted from the casters defined in Table 6.2 or directly pulled from a receiver itself via serial, Bluetooth or internet connection. When a receiver has none or limited access to a broadcast ephemeris data or receives the data with a rather low sampling rate, streams offering RTCMEPH can be extracted from casters in Table 6.2. A bad or outdated data detected within a broadcast message is eliminated from solutions immediately. An algorithm adopted by the BNC is sensitive to potential cycle slips and outliers whose effects are mitigated by using MW and geometry free linear combinations. A processing filter used in the BNC estimates receiver coordinates,

troposphere zenith delays, receiver clock corrections, GPS – Glonass time offsets and ionosphere – free phase ambiguities (float).

Site coordinates and troposphere parameters are estimated with white noise sigmas, which are generally specified as 1.0 m and 1.0 cm, respectively. The algorithm executed in the solution corrects solid earth tides and phase windup effects but it is insensitive to satellite APC variations that can reach up to about 2.0 cm in an extreme case. Streams carrying real-time broadcast corrections and a broadcast ephemeris are both referred to the satellite's APC, thus it is must for users to apply a file including antenna phase center offsets and variations for receivers and satellites to correct the observations. IGS provides a file known as ANTEX for this purpose and in addition, to relate a satellite mass center with a phase center that is a mandatory process when using precise ephemeris orbits. Loading effects produced by ocean and atmosphere are avoided in BNC's solutions, however, particularly the ocean, can cause a positioning error of about 10.0 cm in coastal areas. Moreover, deformations caused by polar tides are also neglected, despite they may exceed 2 centimeters. From a scientific point of view, the PPP algorithm inside the BNC is weaker than its partly counterparts e.g. GAMIT, BERNESE or GIPSY where all the avoided effects mentioned above are implemented in the data analyses.

The performance of BNC's RT positioning, regarding accuracy and convergence period, has been evaluated by processing two different streams IGS03 and CLK91 that the latter has an ability for fixing ambiguities. The analyses were performed for 5 days period 14 – 19 November in 2016. RTCM v3 RINEX observations, broadcast data stream, i.e. RTCM3EPH, and correction streams, i.e. IGS03 and CLK91 were all processed in the static ionosphere-free PPP solution with 1-second estimation rate. Daily observations were divided into the 4 pieces with 6-hour observation data per one piece that allowed assessing a convergence period of the solution 4 times within a day. Positioning results of the RT PPP sessions' conducted at three IGS sites (GRAZ, POTS and FFMJ) were verified with the post-process PPP sessions in which final ephemeris files from CODE's was used. Figure 6.7 displays the positioning errors and RMS of the RT PPP solution at FFMJ site. CODE's positioning results were used for comparison.

Real-time ambiguity fixing procedure developed by the CNES consists of wide-lane and narrow lane ambiguity determination in order by using single-difference

observations between all satellites in a network. As stated by Geng et al., (2010), for large-scale networks single differences are not observable for all sites during the full pass.

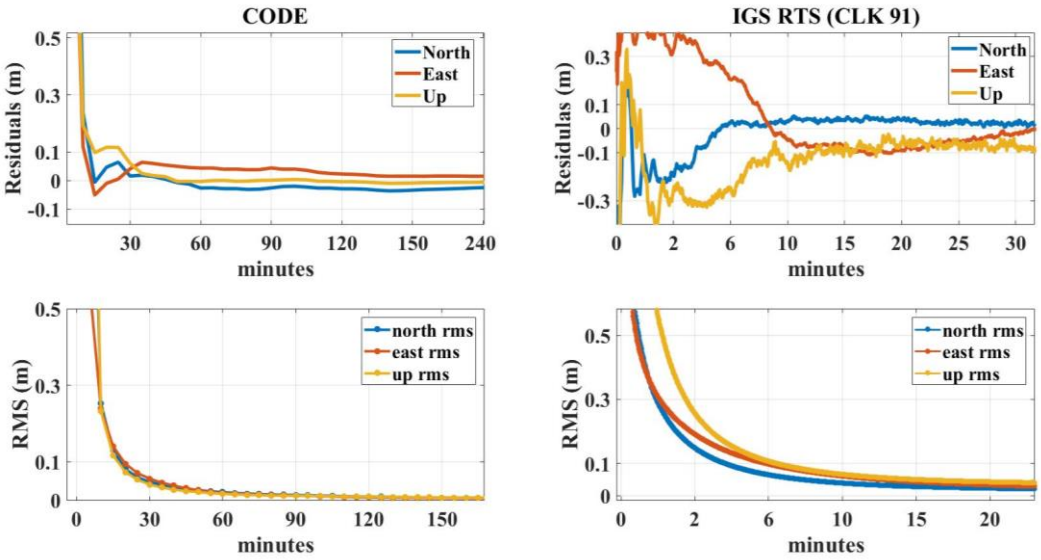

Figure 6.7 : Positioning and convergence performance of the real-time integer PPP solution (right) with respect to CODE's Final PPP results (left).

Therefore, a real-time PPP offers better results for a small-scale network where these between satellite observables can be tracked by all sites within the network. Contrary to the wide-lane delays, which are stable and precisely estimated due to their long wavelength, the time needed to estimate the variable narrow-line phase delays is approximately 15 minutes. Due to this time delay, most users generally ignore the first 15 and 20 minutes of data flow and assess the results produced after this period. Table 6.5 provided the overall statistics relevant to the performance of the float PPP solution using IGS03 correction stream, fixed PPP solution using CLK91 correction stream and post-process float PPP solution used CODE's final products. Coordinates obtained from the individual solutions were verified by the CODE's weekly SINEX file.

Table 6.5 : RMS values and convergence times of RT PPP positioning with ambiguity float (IGS03), ambiguity fixed (CLK91) and post-process float PPP solutions (CODE) that all are validated through CODE's weekly coordinates.

IGS03 - RT PPP amb – float (cm)				CLK91 – RT PPP amb – fixed (cm)				Post Process PPP CODE Final amb – float (cm)			
N	E	U	t (s)	N	E	U	t (s)	N	E	U	t (s)
3.2	3.0	4,8	1200	2.2	2.0	4.2	420	1.0	0.7	1.1	1500

The mean convergence time at the site FFMJ is about 1200 sec for the float solution using IGS03 and 1500 sec for the post process float PPP solution. The time spent on the convergence for the PPP solution using CLK91 stream is about 420 seconds considering the fast resolution of the narrow-lane ambiguities. Using integer phase clocks in the PPP session improved the RMS values averagely 31 %, 30 % and 12.5 % in the North, East and Up components, respectively, in comparison to the float IGS03 positioning results.

Using NTRIP platforms such as BNC and RTKLIB for RT PPP analyses brings about some inefficiencies regarding atmosphere monitoring. Ignoring the effects caused by ocean loading, atmosphere loading and polar tides that the former has a strong influence on the tropospheric path delays, in addition, not correcting the ranges due to satellite antenna variations, i.e. maximum: 2 cm may influence the tropospheric estimates and cause large differences with respect to IGS Final and individual post-process results. Moreover, the path followed by the BNC to handle the tropospheric delay is insufficient that the standard atmospheric values instead in-situ measurements are used to calculate a priori ZHD and only one total mapping function, corresponding to both dry and wet delays, is adopted. The troposphere is modeled by using equation 6.8 as expressed by Weber at al. (2016).

$$T_{(Z)} = T_{apr(z)} + \frac{dT}{\cos(z)} \tag{6.8}$$

where $T_{(Z)}$ is the total zenith path delay, $T_{apr(z)}$ is the a priori troposphere model computed by Saastamoinen (1972) and standard atmosphere data, and the remaining part is an elevation dependent correction to the a priori troposphere, estimated in the KF as a white noise. The total mapping function for mapping the slant delays into the zenith direction is given in equation 6.9.

$$mf = \frac{1}{\sin e} \tag{6.9}$$

In order to show the weakness of the BNC's troposphere solution, the tropospheric path delays of three IGS site were estimated by performing a RT PPP session between DoY 319 and DoY 324, 2016. The RINEX data from sites FFMJ locates in Frankfurt - Germany, GRAZ is from Graz-Austria and POTS in Berlin – Germany were

processed with the broadcast ephemeris that corrected by the RTCM SSR corrections from IGS03 and CLK91 streams.

The real-time ZTDs estimated from the PPP IGS03 (i.e., ambiguity-float) and PPP CLK91 (i.e., ambiguity-fixed) were compared with the PP PPP troposphere estimates at three IGS sites GANP, GRAZ and FFMJ. The results are illustrated in Figure 6.8 where the estimates from IGS01 are depicted by the blue, the CLK91 by the red and the reference post-process ZPDs by the black.

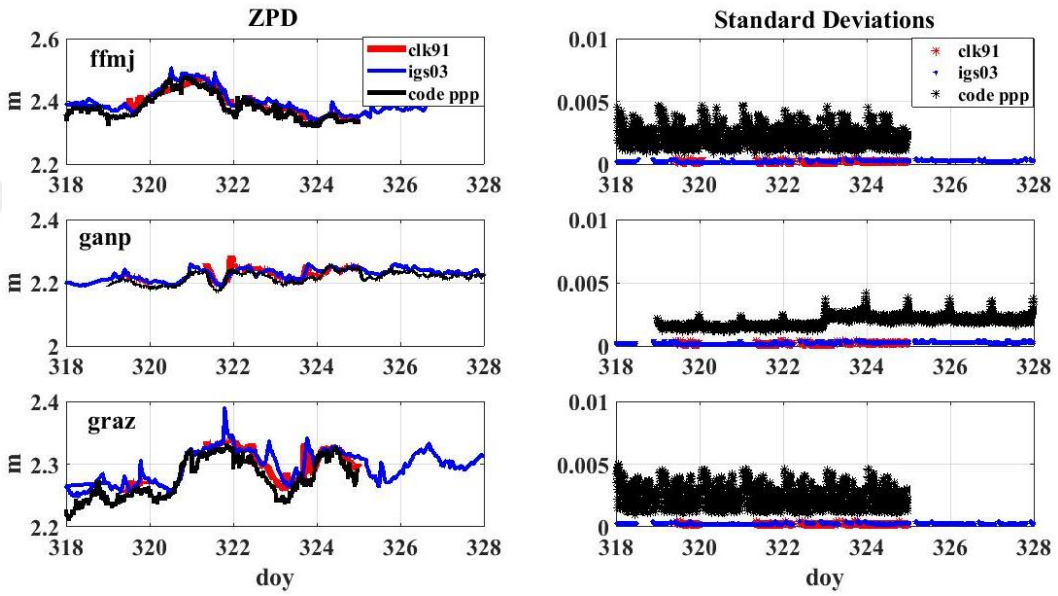

Figure 6.8 : ZTD time seriescomparison between an ambiguity fixed RT PPP (CLK91), an ambiguity float RT PPP (IGS03) and ambiguity float PP PPP (CODE) solutions.

Using the CODE as the reference, five-day averages of the ZPD differences are in the range from -1.0 to - 3.0 centimeters for the IGS03 solutions and from -0.1 to -3.0 centimeters for the CLK91 solutions. The RMS values of the ZPD differences range from 1.0 cm to 3.6 cm for the IGS03 and from 0.7 cm to 2.3 cm for the CLK91 solutions. The large differences associated with the weak solution adopted in the RT solution can be reduced by employing comparatively modern troposphere models.

The comparison of convergence times of the ZPD estimates, as illustrated Figure 6.9, shows that the solutions using the ambiguity fixed streams, i.e. CLK91 reach to mm level RMS accuracy much faster than the RT PPP solutions using the ambiguity float stream, i.e. IGS03. However, the differences between the RMSs decrease to insignificant values after several epochs (e.g., 10 minutes). Table 6.6 lists the average differences and RMS of the RT PPP solutions (CLK91 and IGS03) and PP PPP

solutions. PPP sessions generally lack of adequate real-time solutions because of unresolved ambiguities whose integer nature is destroyed by unmodeled hardware biases of satellites and receivers. On the other hand, upgraded algorithms developed to estimate precise satellite clocks and being able to pull hardware related biases in real time from NTRIP correction streams like CNES's CLKxx, users can successfully resolve phase ambiguities in PPP observations and reach to desired accuracy faster, i.e., several minutes.

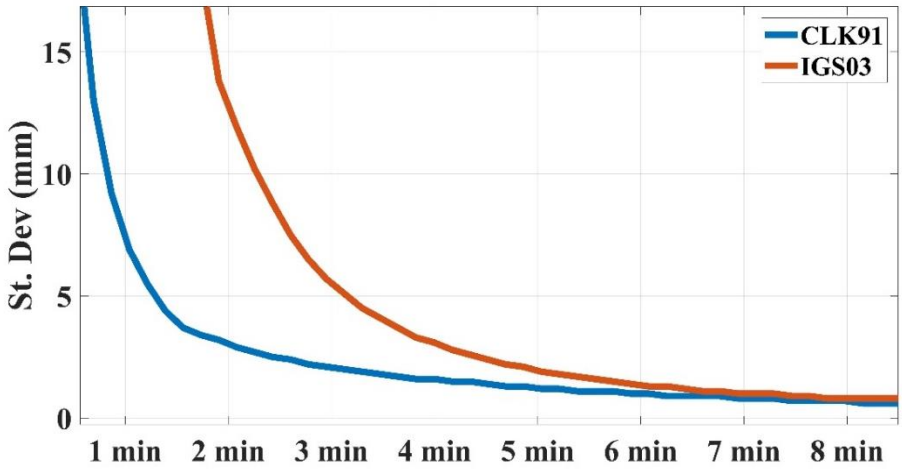

Figure 6.9 : Convergence performance of the IGS RTS streams (CLK91 vs IGS03) in terms of estimated troposphere path delays.

Table 6.6 : Statistical comparison of average differences and RMS of the differences between RT PPP troposphere and PP PPP troposphere.

	ppp vs rts (IGS03) ffmj		ppp vs rts (CLK91) ffmj		ppp vs rts (IGS03) graz		ppp vs rts (CLK91) graz		ppp vs rts (IGS03) ganp		ppp vs rts (CLK91) ganp	
DOY	mean	rms	mean	rms	mean	rms	mean	rms	mean	rms	mean	rms
319	-13.0	17.7	-17.0	21.0	-19.1	21.6	-11.7	12.2	-18.0	19.5	-16.0	16.5
321	-28.0	30	-28.0	30	-15.2	18.9	-10.7	11.6	-12.1	18.5	-16.4	23.7
322	-17.1	21.4	-9.6	14.6	-26.0	31.0	-18.3	19	-12.4	16.5	-16.3	16.7
323	-27.5	29.6	-19.8	22.1	-30.0	36.2	-15.8	20.6	-24.6	26.7	-13.5	15.5
324	-15.9	18.7	-7.9	10.8	-14.0	19.4	-10.0	12.4	-4.0	10.0	-1.0	7.0

6.6 Real-Time Water Vapor Monitoring with IGS RTS

In this part of the study, the PWV data derived from RT PPP solutions were validated with the co-located radiosonde sites' readings. Using the ratio factor given in the equations 4.55 and 4.56, the estimated ZWDs were converted to the PWVs. Contrary to the previous RT PPP sessions that were carried out with the BNC's algorithms; a

more robust approach has been developed to improve the performance of the real-time atmosphere monitoring. This approach starts with the utilizing broadcast ephemeris information and real time correction streams to generate precise orbits and clocks in IGS format, i.e., sp3. Four correction streams "IGS01" (i.e., GPS), "IGS03" (i.e., GPS plus GLONASS), "CLK91" (i.e., GPS) and the "CLK93" (i.e., GPS+GLONASS) were pulled from the casters offered by the BKG and CNES ACs. It is crucial to specify a sampling interval for the output precise products that if the pulled streams have different sampling interval, only epochs that match to the defined sampling interval must be used. The correction streams were combined based on given weights (i.e., CLK91: 0.4, IGS03: 0.3, CLK93:0.2 and IGS01:0.1). A mean three-dimensional orbits per each epoch were determined from combined streams, the satellites that exceed the average orbits by 0.5 meters were removed from the solution and the combination process started from the beginning. The satellite clocks were derived from an adjustment process where an individual clock from each stream is defined as observation in the adjustment and represented by a linear function of three parameters: stream specific offset, satellite specific offset and clock correction, which is the combined clock correction. The combined corrections were then applied to the Broadcast Ephemeris stream i.e. RTCM3EPH pulled from the IGS to produce daily precise satellite orbits files with 5-minutes interval and RINEX clock files with sampling rate of 5-seconds. The produced files are software independent plain orbits and clocks in IGS format (sp3 and RINEX clk) and enable carrying out RT PPP to determine the state of the troposphere. When combining the streams from different ACs, the ANTEX file must be used to relate the antenna phase center to the satellite mass center where the precise ephemeris orbits are referred to. To demonstrate the efficiency of the produced precise orbits and clocks in real time, RT PPP sessions were carried out at the six IGS sites (“WROC”, “GANP”, “GOPE”, “GRAZ”, “POTS” and “ZIMM”), which are the same sites used in the PP sessions in the previous chapter and listed in Table 5.11. The daily RINEX observations of the sites were processed with the combined orbits and clocks through batch mode in the Bernese v5.2 from May 20 to June 10, 2013. Some weak parts of the BNC's solution were upgraded with stronger pre-processing and parameter estimation abilities of the Bernese. In addition, some models neglected in the previous BNC's NTRIP solution were added to the solution. The deformations caused by changing mass distributions due to ocean loading were corrected by the FES2014 (Carrere et al., 2015) containing station specific coefficients

of the loading effect. The S1/S2 atmospheric tidal loading corrections were produced for the IGS sites by extracting corrections from global grids (Petrov and Boy, 2004). Real-time ERPs, nutation (i.e., IAU2000R06) and sub-daily pole model (i.e., IERS2010XY) are the models adopted. Moreover, antenna phase center eccentricities and variations of satellite and receiver antennas were extracted from the PCV_COD.I08 of CODE. In case of missing antenna offsets due to new-launched satellites with unknown data, frequently updated CODE's I08.ATX was also implemented in the analyses. The flowchart being followed to derive zenith wet delays and precipitable water vapor from real-time PPP analyses illustrated in Figure 6.10.

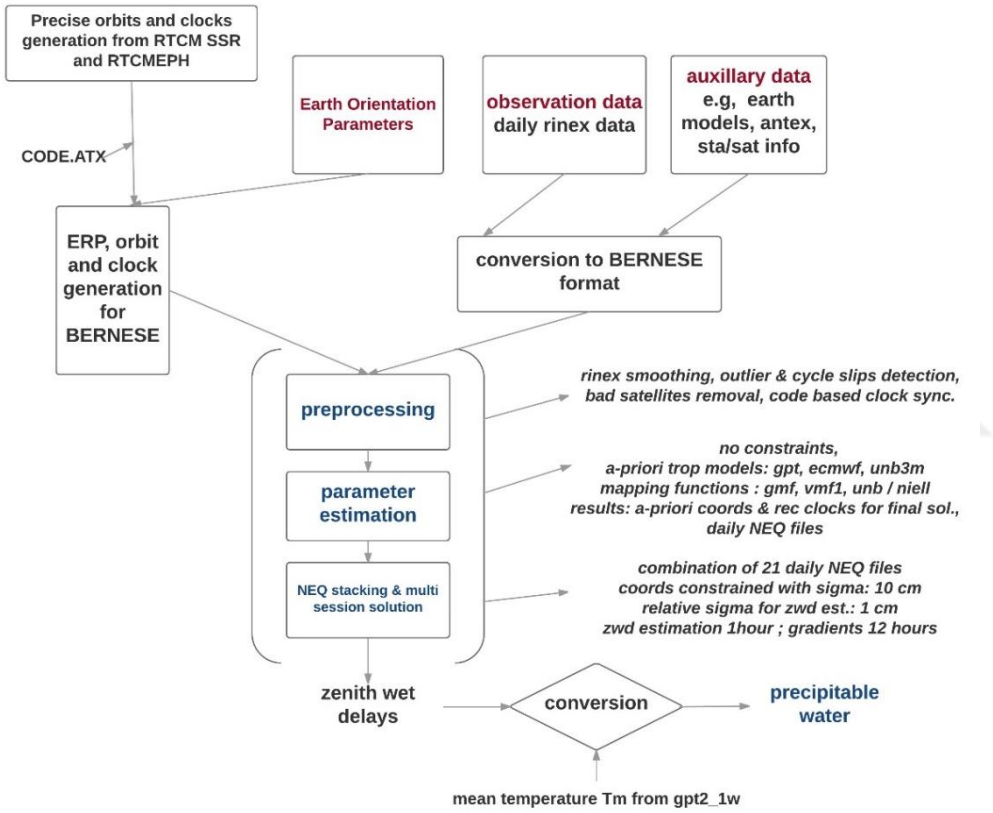

Figure 6.10 : The architecture of the real time PPP session performed within the BERNESE 5.2.

The steps followed in the solution are almost similar to the PP PPP where the first phase started with examining the RINEX data and the satellite products in order to detect cycle-slips and outliers. The standard least-squares adjustment was performed to check the prefit residuals to remove bad observations and problematic satellites. The follow-up estimation was performed with the cleaned ionosphere-free observations without specifying any constraints, and, daily NEQ files, which consist of the a priori estimates of coordinates, clocks, and troposphere (ZHD), were generated. The final

step includes the combination of all the NEQs, stacking the parameters and estimation of coordinates, epoch-wise ZWDs and receiver clocks by employing LSA procedure for each site. In order to measure their performances in real time, all the three troposphere modeling approach GPT / GMF, UNB / Niell and ECMWF / VMF1 were used sequentially for each individual RT PPP session as that has been done for the PP PPP analyses in the previous chapter. In addition, a cut-off elevation angle was setup as 5° during the whole process. The a priori ZHD calculated by the Saastamoinen using the pressure data derived from the GPT, UNB and VMF1 added to the observations, whereas the unknown ZWDs were estimated with a priori sigma of 1.0 cm and with a resolution of 1-hour. The mean temperature of water vapor (T_M), which is essential for converting the wet delays into the precipitable water, was derived by executing the FORTRAN subroutine (gpt2_1w.f) developed by Böhm et al. 2015 Figure 6.11 shows the real-time estimated PWV time series at the five IGS stations and co-located radiosonde readings from May 20 to June 10, 2013. Moreover, the Global Precipitation Climatology Project (GPCP), under the National Center Atmospheric Research (NCAR), offers daily rainfall estimates (mm) on a 1-degree grid over the globe. GPCP precipitation data generated from microwave, infrared, and sounder data of precipitation-related satellites, and precipitation gauge analyses (Huffman et al., 2016). The daily-accumulated precipitation data derived from the GPCP was also added to the figure as the indicator for measuring the performance of the RT PWVs in catching the precipitation events.

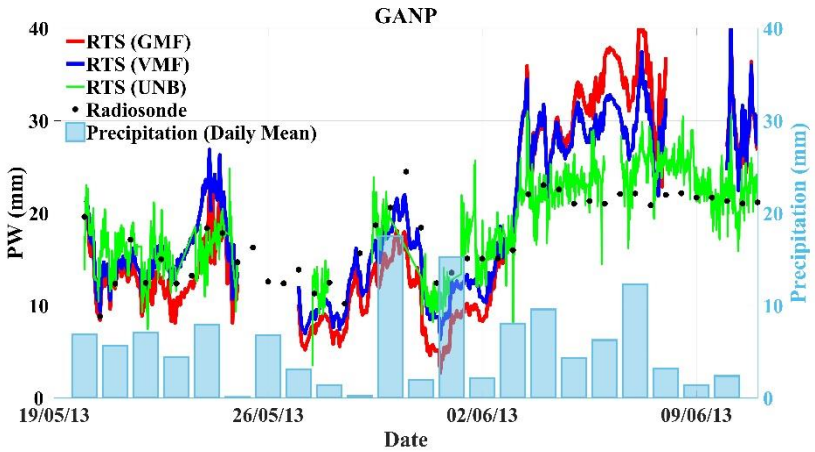

Figure 6.11 : RT PPP derived PWV and radiosonde time series at the sites GANP, GOPE, GRAZ, POTS, WROC and accumulated daily precipitation recorded at the sites.

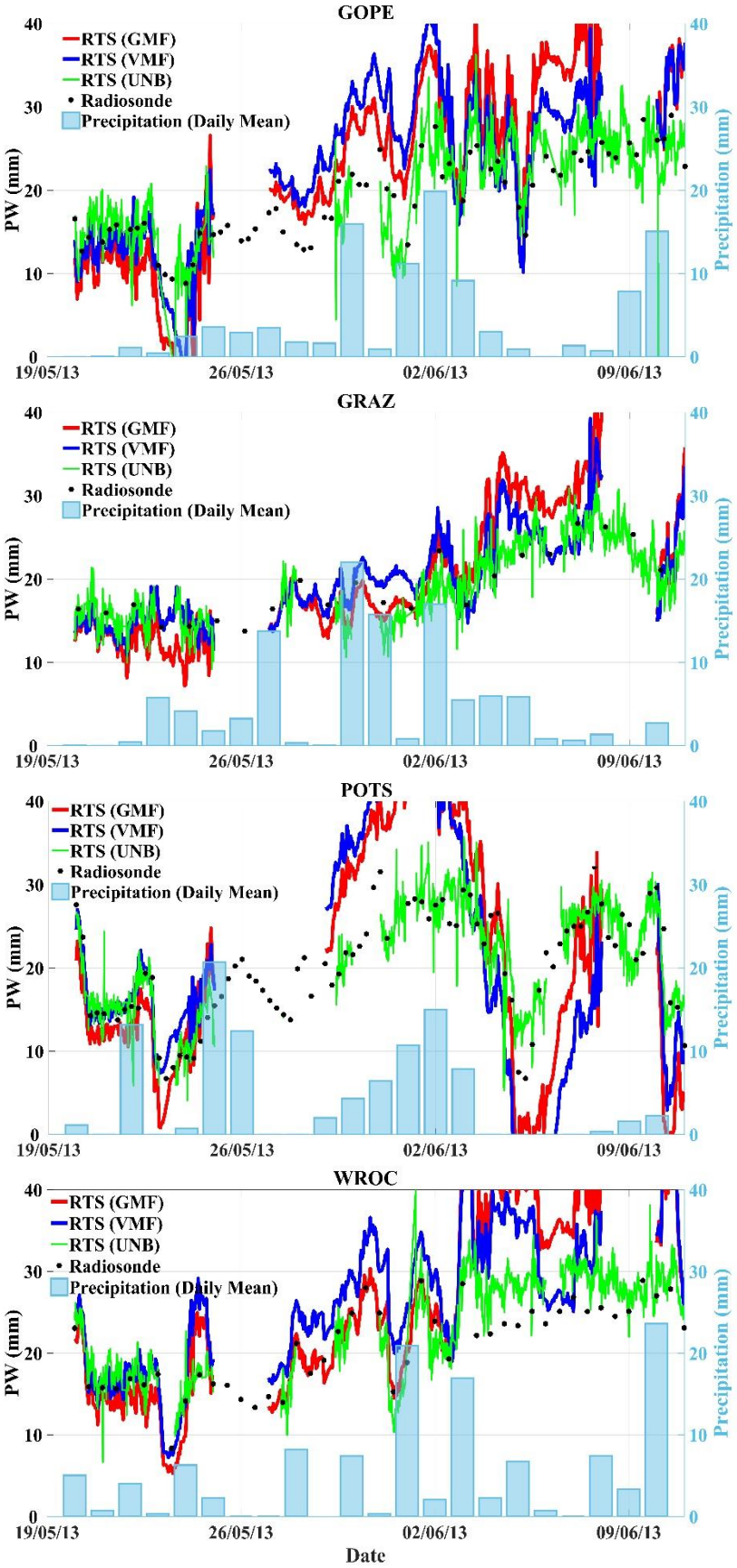

Figure 6.11 (continued): RT PPP derived PWV and radiosonde time series at the sites GANP, GOPE, GRAZ, POTS, WROC and accumulated daily precipitation recorded at the sites.

As expressed in the Figure (6.11), RT PWV estimates for the first week of the session generally range between 10.0 mm and 20.0 mm, while sharp increases and decreases due to the variability in humidity can be observed almost for all sites for the period starting with May 27. The severe weather event that mostly showed its effect between May 28 and June 4 is also caught by the PWV's time series. At the site GANP, there are two scenes of intense precipitation event recorded on May 29 and June 1, both were initiated immediately after a remarkable rise in PWV, followed by a sharp decrease while the accumulated rainfall rates decrease to several millimeters as well. The same pattern is also observable at GOPE on May 29, June 1 and June 2 when the accumulated PWV values reach to more than 35 mm that immediately followed by the severe rain (i.e., around 20 mm/day). After the rain stops, the PWVs decrease remarkably due to reduced amount of the water vapor in the atmosphere. By assessing the rainfall events and associated PWV peaks, it noted that the water vapor accumulation first started in the southern regions (GRAZ) and moved to the northern areas (WROC, POTS). Based on the analysis, the RT PPP derived PWV time series are generally compatible with the GPCP's daily-accumulated precipitation records, however, it is not easy to state that after each accumulated PWV peak there will be a precipitation event. The highest PWV values were experienced for the period between July 5 and July 10 at GOPE, GRAZ and WROC, but no precipitation event recorded at all.

As shown in Table 6.7, the verification of the RT PPP derived PWV with the co-located radiosonde sites shows that the mean PWV differences vary from -0.45 mm to 3.31 mm for the RT PPP sessions using the VMF1, from 1.69 mm to 4.13 mm for the GPT and from -0.95 mm to 1.53 mm for the UNB. Regarding the differences from the radiosonde data, the PWV values derived by the PPP sessions using the UNB model are found to be more scattered than the sessions using the GPT and VMF1. In addition, almost all solutions remain within an average 4.55 mm in standard deviation while the best agreement is detected with 2.9 mm for the RT PPP session using the VMF1 model at the station GANP. The large differences from the radiosonde are inevitable due to the accuracy of a priori troposphere model, bad RINEX data or poor satellite products. Specifying a threshold to remove epochs with large biases (i.e., larger than 10 mm) reduces the largest mean deviation from 4.55 mm to 2.80 mm at WROC using the UNB, from 3.59 mm to 2.70 mm at GRAZ using the VMF1 and from 3.69 to 2.61 at

GRAZ again, but using the GPT. The solutions using analytical models show more improvement after the threshold is specified. To sum up, the PWV values derived from the RT PPP, using the ECMWF/VMF1 to model the troposphere, are more compatible with respect to the radiosonde derived PWV values.

Table 6.7 : The statistics of the PW differences between the PPP solutions and the Radiosonde data for each GNSS site co-located with the radiosonde sensor.

	RS – RTS PPP Mean Bias (mm)			RS – RTS PPP Std. Dev (mm)		
Site	VMF1	GPT	UNB	VMF1	GPT	UNB
GANP	0.19	1.89	-0.41	2.91	3.43	4.38
GOPE	1.72	2.36	-0.15	3.42	4.10	4.01
GRAZ	3.31	4.13	1.53	3.59	3.69	2.67
WROC	-0.45	1.69	-0.95	3.42	3.78	4.55
POTS	1.83	3.03	0.09	3.86	3.55	3.87

Besides validation with the radiosonde data, the RT PPP derived PWV values have also been verified by the PWV values of the post-process PPP solutions. According to the results illustrated in Figure 6.12, the average PWV differences between the RT PPP and post-process PPP are remained within ± 3.0 mm for all sessions, regardless of used troposphere model is applied. The largest RMS is detected at GRAZ site about 2.77 mm for the VMF1 while the lowest one is observed at WROC with 1.16 mm for the GPT.

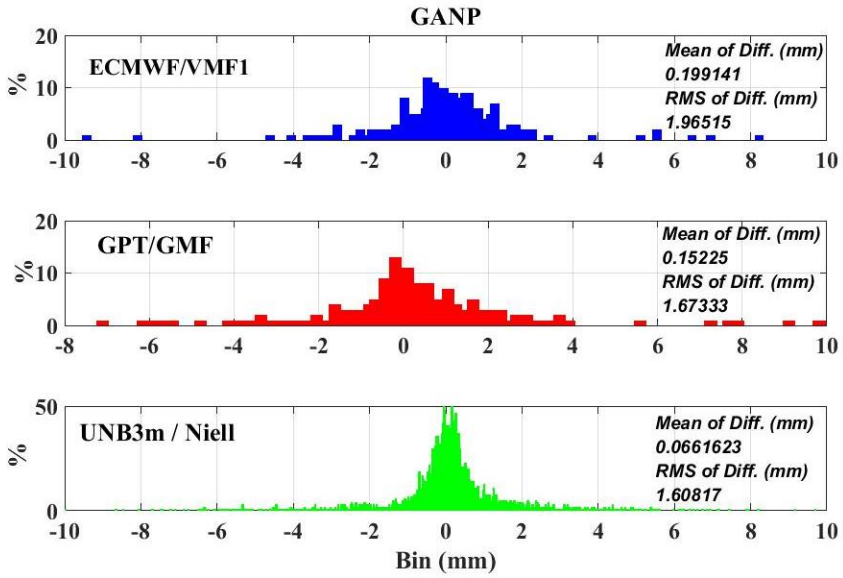

Figure 6.12 : The mean and RMS values of the PW differences between the real time and post-process PPP.

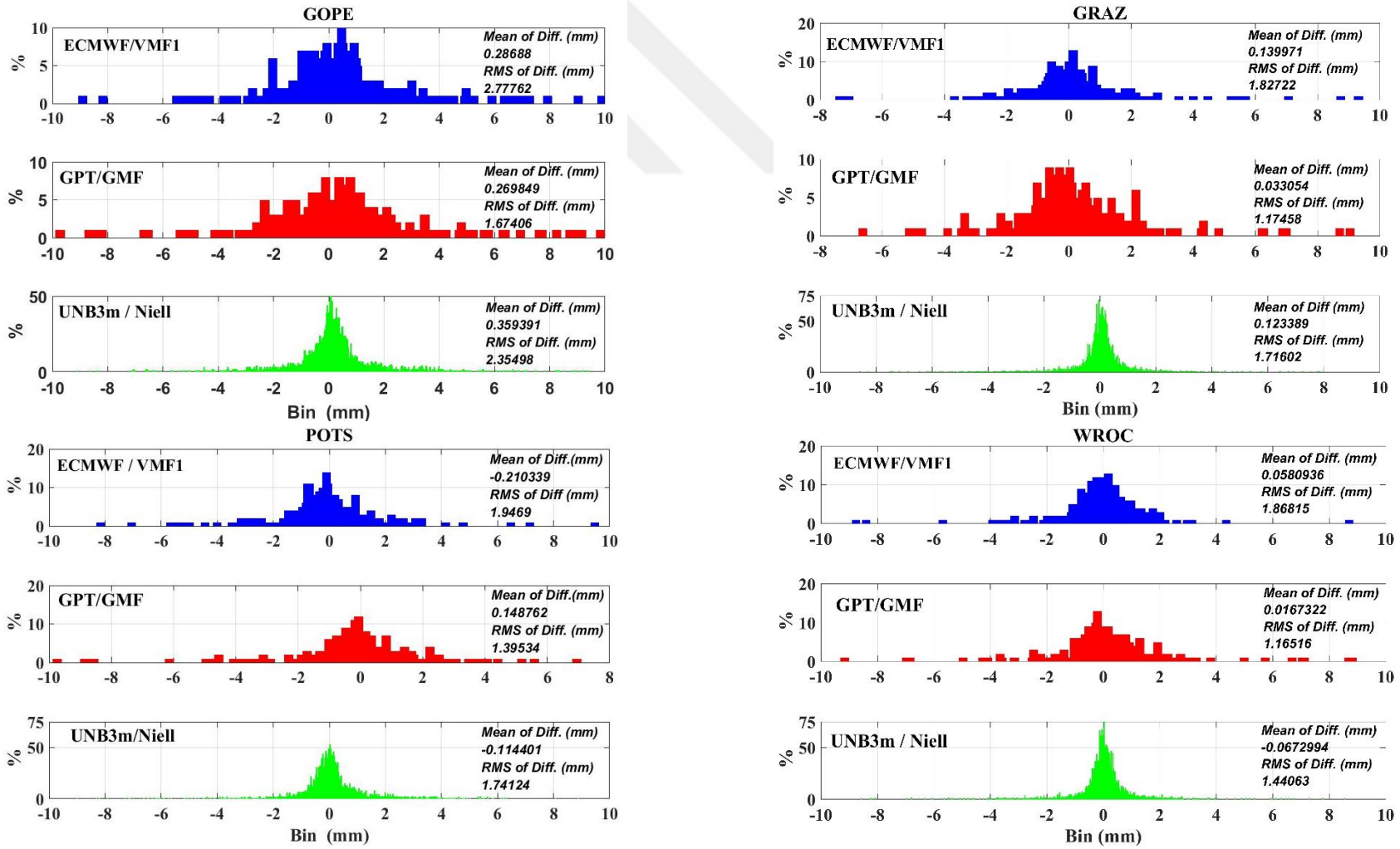

Figure 6.12 (continued): The mean and RMS values of the PW differences between the real time and post-process PPP.

6.7 Validation of RT PPP Derived PWV with MODIS derived PWV

Moderate Resolution Imaging Spectroradiometer (MODIS) is a remote sensing instrument located on the U.S. Terra and Aqua satellites for monitoring the Earth and delivering a variety of data that can be used for land, ocean and atmospheric sciences with a spatial resolution between 250 meters and 1 kilometers depending on the selected bands. Terra and Aqua satellites observe the Earth within 1 to 2 days with 36 spectral bands (i.e., range: 0.4 µm - 14.4 µm) and swath dimensions of 2330 km (cross-track) by 10 km (along-track). A near infrared (NIR) bands are generally used for clear land areas and clouds over land and ocean during daytime and the data are generated at the 1 km spatial resolution. An infrared (IR) bands are used for both day and night time with a 1km pixel resolution and extracted data are specified as Level-2 products such as aerosol, water vapor, cloud, atmospheric profile, cloud mask and joint atmosphere products. The water vapor products and precipitation data derived from the Terra and Aqua platforms are saved in Level - 2 files i.e. MOD05_L2 and MYD05_L2, respectively. The Level – 3 Modis Atmosphere Global Joint Products (i.e., MOD08) are derived from Level – 2 products (i.e., MOD04, MOD05, MOD06 and MOD07) and contains daily / eight-day / monthly degree grid mean values of atmospheric water vapor and other atmospheric parameters. Ability to extract the amount of precipitable water vapor in the atmosphere makes MODIS images essential sources for climate studies and real-time weather forecasting. Atmospheric water vapor is extracted with the solar retrieval algorithm that detects an attenuation of reflected solar radiation by clouds and surfaces in the MODIS NIR channels. The underlying principle for retrieval atmospheric water vapor depends upon differential absorption approach. One absorption band is compared to a close band without or with few absorption (Albert et al, 2005). The difference is then used to produce water vapor within the atmospheric column. The ratios of water vapor absorbing channels 17, 18 and 19 with the atmospheric window channels 2 and 5 provide the water vapor transmittance that is removed from the partial effects of reflectance variations due to wavelengths. The column water vapor amount is calculated with the help of radiative transfer formulations and look-up tables. In Table 6.8, the positions and widths of these channels are illustrated. The product is only produced for areas where there is a reflection in the NIR. The IR precipitable water products are generated by MOD07

atmospheric profiles and stored as a new layer within MOD05_L2 and MYD05_L2 files for convenience.

Table 6.8 : Positions and widths of five MODIS near-IR channels used in the water vapor extraction.

Channel	Position	Width
2	0.865	0.04
5	1.240	0.02
17	0.905	0.03
18	0.936	0.01
19	0.940	0.05

The product files of the Aqua and Terra are distributed in Hierarchical Data Format for Earth Observing System (HDF-EOS) with 13 gridded parameters where the water vapor are stored as a short integer to reduce the size of the files. The exact value is found as expressed in equation 6.10 by multiplying these short integers with the scale factors and subtracting the offsets that all given within the product set.

$$PW_{real} = scale \times \left(PW_{stored} - offset \right) \tag{6.10}$$

The water vapor products from MODIS can be ordered and downloaded without a fee from the Atmosphere Archive & Distribution System (LAADS) Distributed Active Archive Center (DAAC) web service (Url-10) by specifying a time range and spatial boundaries of a requested area.

In this part of the study, the RT PPP derived PWV estimates were compared with the MODIS NIR derived PWV data at five IGS sites (GANP, GOPE, GRAZ, POTS and WROC) for three weeks long period i.e. May 20 – June 10, 2013. Since a retrieval of water vapor above lands is likely under cloud-free pixel environment only, the cloud mask algorithm of NASA, coherent with the MOD05_L2 products, was implemented where the MODIS data is available and data extraction was performed only for the clear pixels that are geographically matching the relevant IGS sites. MODIS Re-Projection Tool Swath (MRTSwath) was introduced to transform 366 MODIS Level-2 images to a georeferenced gridded image (i.e., GeoTIFF). The geolocation files, which are needed to georeference each NIR pixel to its related Earth coordinates, were also extracted from the LAADS FTP site (Url-10).

Table 6.9 introduces the comparison results between the daily mean PPP PW estimates (post-process and real-time) and the daily mean PW data retrieved from the MODIS products. A comprehensive statistics regarding the PWV comparison are provided in two aspects: mean differences and standard deviations of the differences. It can be concluded that the PPP solutions with VMF1 troposphere model, processed in either real-time or post-process mode, agree better with the MODIS NIR water vapor data, whereas the PPP solutions with GMF model show larger residuals.

Table 6.9 : Statistical comparison between the MODIS PWV and GNSS PPP (post-process and real-time).

(units = mm)	GANP		GOPE		GRAZ		POTS		WROC	
	Post-process									
	mean	std	mean	std	mean	std	mean	std	mean	std
modis vs ppp (gmf)	6.05	2.47	4.83	1.48	1.83	1.92	3.52	2.07	4.43	2.29
modis vs ppp (vmf1)	4.87	2.70	3.48	1.62	1.47	1.62	2.89	2.04	2.15	2.80
	Real-time									
	mean	std	mean	std	mean	std	mean	std	mean	std
modis vs ppp (gmf)	6.08	2.96	5.01	2.08	2.19	2.01	5.02	4.21	3.28	4.48
modis vs ppp (vmf1)	4.80	3.03	3.79	1.43	1.85	1.58	3.61	3.25	1.02	4.25
	MODIS vs Radiosonde									
	mean	std	mean	std	mean	std	mean	std	mean	std
	4.54	3.97	2.28	2.51	-0.5	1.41	3.92	4.99	3.35	2.07

Assessing the PWV differences, the agreement between the MODIS and the GNSS PPP at all stations remains within 4.25 mm in terms of standard deviations. Apart from an adopted processing mode, either post-process or real-time, the PPP sessions using ECMWF / VMF1 to model the troposphere agree better with the MODIS data at almost all sites. Comparison between the MODIS data and the radiosonde data revealed the mean differences and their deviations certainly increase at three sites GANP, GOPE and GRAZ with respect to the MODIS – GNSS comparison. In overall, the MODIS data agrees with the radiosonde data in the range of 1.41 – 4.99 mm that is comparatively worse than the GNSS PPP. During the analysis, an overestimated MODIS – PPP and MODIS - Radiosonde differences detected for some epochs can be attributed to three main reasons: low sampling rate, bad interpolated data and a large number of unknown pixels (i.e., NaN) observed during 21 days long period. Therefore, it is recommended to use much longer time series that the average biases will smooth after a while and it would be easier to detect outliers from larger dataset showing Gaussian distribution.

7. CONCLUSIONS AND RECOMMENDATIONS

7.1 Conclusions

The main goal of this research was to investigate the performance of GNSS PPP in troposphere monitoring during extreme weather conditions. Since GNSS has significant advantages over traditional methods such as radiosonde, water vapor radiometer and remote sensing measurements such as low maintenance expense, weather condition independent, continuous data stream and high spatial coverage, it has been used since the 1990s for the meteorological studies, and particularly for monitoring atmospheric water vapor. Atmospheric water vapor is a greenhouse gas and the fundamental parameter having a strong influence on climate events and transports a large amount of energy in the atmosphere. Therefore, the tracking and monitoring ability of the GNSS in highly variable water vapor delivers a significant amount of information associated with rainfall, evaporation and convection processes. In this study, using the connection between zenith wet delay estimates and precipitable water vapor content, the atmospheric variations in the lower neutral atmosphere were monitored in both post-process and real-time mode to evaluate the performance of the PPP method during an extreme weather event. To accomplish this task, the daily observation data of 11 IGS sites and ephemeris products obtained from different IGS ACs were processed in a static mode using the GNSS software Bernese v5.2. MatLab Laboratory platform and a number of programs written in FORTRAN and C were additionally used during the analyses.

The error mitigation methods in PPP play a crucial role in leading up high accuracy applications. A Network GNSS using a double differencing approach has been widely used for post-process and real-time atmosphere monitoring considering most of the errors are canceled or mitigated by the differencing. However, a hardware cost and a necessity of using at least two receivers to perform a differential solution, dual frequency single receiver solution, i.e. PPP, which utilizing precise orbits and clocks from the IGS, has become an effective alternative for meteorological studies. PPP enables to estimates coordinates, tropospheric path delays, receiver clocks and float

ambiguities with adequate accuracy after proper modeling of error sources such as the ionospheric refraction, which can almost be eliminated with ionosphere-free combinations, antenna phase center variations, phase wind-up, differential system biases, relativity, and station displacement effects, e.g., Solid earth tides, ocean loading, atmospheric loading and tectonic movements. The focus should be on the phase biases of satellites and receivers that decrease the accuracy of PPP solutions by being absorbed by the phases and thus destroy the integer nature of the ambiguities.

The propagation delay consists of two parts: the hydrostatic component including dry gases and the non-hydrostatic part changing with water vapor concentration. The hydrostatic component, i.e. a priori ZHD, can be predicted with a high accuracy with surface pressure measurements and applying Saastamoinen troposphere model while the hard-to-predict wet part is generally estimated by data adjustment. Modeling the troposphere in the GNSS observation model requires to use meteorological data and a number of ways can be followed to extract the data, such as numerical weather prediction models, radiosonde readings, data of remote sensing satellites, in-situ measurements, etc. In this study, it was assumed that there were none in-situ meteorological readings and a priori troposphere model, i.e. ZHD was modeled by using inputs obtained from three different models to derive a needed meteorological data: a spherical harmonic and an analytical model of GPT (≈ GPT2), an analytical UNB, and NWM (i.e., ECMWF) derived VMF1 global grids. The a priori ZHD calculated based on these models is generally based on yearly averages that do not account for sub-yearly variations that affected the estimates of wet delays afterwards due to mis-modeled ZHD and other propagating error sources. In order to reveal the potential of the PPP ZWDs in weather monitoring; the severe precipitation period between late May and the beginning of June was assessed by observing GNSS data of 11 IGS sites distributed within the affected area in the Central Europe. The PPP sessions were performed in a static mode by processing IGS and CODE's precise ephemeris satellite products, and by using IERS recommended models to mitigate geophysical effects. The analyses were performed comparatively by employing both strategies: least-squares adjustment in the Bernese and Kalman filter developed in C and FORTRAN to estimate the tropospheric delays. The mean differences between the two strategies at 11 IGS sites in terms of ZWD estimates were found to be around 2.00 mm with the RMS of 1.0 cm level. It has been shown that the mean differences in the

wet delay estimates caused by using different a priori model can reach to over 2.0 cm in extreme cases with RMS errors larger than 2.0 cm. The ZWD estimates at 11 IGS sites were additionally validated with the wet delays derived from the IGS Final ZPD products. The agreement of the PPP ZWDs with the IGS ZWDs in terms of RMS accuracy is found to be in the range of ± 1, ±2 and ± 3 cm for the GPT / GMF, ECMWF/VMF1 and UNB3m / Neill troposphere models, respectively. The PPP estimated site coordinates provide discrepancies up to 1.0 cm in the North and East components while the discrepancies in the Up components are up to 4.0 cm with respect to the CODE's weekly mean coordinates that distributed in the SINEX format. The large differences in the Up component can be attributed to the un-modeled troposphere and receiver clocks. Regardless of the used a priori troposphere model and associated mapping function, the mean convergence time needed to reach a cm level accuracy in the positioning is found about 30 - 60 minutes for all post-process PPP solutions. On the other hand, a network based GNSS sessions at the same sites gave more consistent results than PPP with the IGS data that can be accounted for two reasons: the mitigation of satellite and receiver related errors by using short baselines and an immediate phase ambiguity resolution. However, the formal errors of the ZWD estimates for the Network solution at several sites were found to be higher than the PPP's errors. The baseline creation strategy, i.e., observation – maximum , which is based on assuming two closest sites observing common observations from the same satellites, dramatically reduces the number of observations processed, and thus increase the formal errors of the whole solution as seen in the Network analysis. In addition, the mean ZWD differences between the Network GNSS and PPP GNSS sessions using the VMF1 model were found to be 5 times lower than the sessions using the GMF.

Comparison of the ZWD estimates of the PPP sessions applying different IGS ephemeris products revealed that the IGS Rapid orbits and clocks, provided with 13-hour latency, offer highly consistent results with the IGS Final products, while the Ultra-rapid products reduce the accuracy of the estimates due to the extrapolated orbits and inconsistent clocks. Using the IGS Ultra-rapid products in atmospheric monitoring can lead to reliable results if only they are processed within a GNSS Network solution where all receiver/satellite related errors are cancelled.

In order to see the PPP's reliability in monitoring water vapor variations the wet delays were validated against the radiosonde data of the co-located sites. The ZWD estimates, which only differ in the applied a priori troposphere model and associated mapping function, were converted to the precipitable water vapor by using the conversion factor between these two parameters. The derived PWV values were then validated against the radiosonde readings for matching epochs. According to the analysis results, the PPP derived PWV processing the VMF1 global grids agree better with the radiosonde derived PWV in terms of average differences and RMS of the differences, whereas the largest discrepancies and deviations are observed for the PPP sessions applying the UNB model.

After the IGS launched its real-time service and started sharing real-time broadcast corrections from multiple streams via NTRIP client applications such as the BNC and RTKLIB, the PPP has been successfully used for water vapor monitoring in real-time. Moreover, a limitation emerging from unmodeled receiver and satellite hardware biases, which are considered the main cause of phase ambiguities, can be overcome by using streams that including these biases that are offered by IGS ACs in real time, and thus a convergence of solutions can be reduced to several minutes. In this study, the performance of the real-time precise orbits that were generated by combining the broadcast ephemeris and correction streams pulled from the NTRIP casters were checked against the CODE's Final orbits and clocks. The primary results showed that the RTS orbits and clocks are far superior to the IGS Ultra-rapid products because of their improved orbits and more consistent clocks. It has been shown that the PWV estimates, derived from the real-time PPP sessions using these real-time precise ephemeris products with the VMF1 troposphere model yield a better agreement with both: the post-process PPP estimates and radiosonde readings at co-located sites. The highest uncertainties of the estimates were observed for the RT PPP sessions with the UNB3m / Niell troposphere solution. Furthermore, a high correlation between the recorded precipitation rates on the ground and the precipitable water estimates of the RT PPP sessions was revealed by investigating the time series of the estimates and precipitation events that most of the recorded precipitation events happen immediately after a remarkable increase in the PWV, followed by a sharp decrease when the rain stops. In the last phase of the study, the MODIS retrievals of water vapor variations were evaluated to verify the GNSS results. It is observed that the RMS values of the

PWV differences between MODIS and post-process PPP are found to be around 2.0 mm, whereas these values increase to 4.0 mm when the real time PPP is performed.

7.2 Recommendations

The observation data used in this study were selected from a large area in the central Europe that the distances between the sites are considerably larger. Since the neutral atmosphere is susceptible to short-range water vapor variations, using denser site distribution (i.e., 5 - 10 km) would allow catching the sharp increases and decreases in the water vapor better regarding precipitation regimes during severe weathers.

A large number of the GNSS sites used in the analyses did not have a meteorological sensor on-board back in 2013 for collecting data that could provide a significant information concerning atmospheric variations in the region. In addition, using RINEX meteorological data, which is disseminated along with observations by the IGS, will enhance the reliability of the estimates since they are derived from actual sensor readings with a high sampling rate.

Estimates derived from regional troposphere models can lead users to enhance monitoring ability of the PPP by offering realistic a priori troposphere parameters with less uncertainty. As a result, not only ZWD estimates but also heights are expected to be improved.

GNSS modernization phase, including upcoming GALILEO and new GPS civil signals, will offer a great number of observations and good satellites geometry that will improve ZWD estimates. The ionosphere-free linear combinations used in the PPP solutions to mitigate the effects caused by ionospheric refraction, but unfortunately they also prevent to use an external ionospheric state information generated from network solutions that can offer solutions that reduce the convergence time dramatically. Local augmentation of PPP solutions with the regional ionosphere models should be assessed in terms of potential benefits in troposphere monitoring and positioning. Furthermore, future works will study the possibility of using single frequency devices in atmospheric monitoring and accurate real-time weather forecasting, thus the necessities in order to achieve this aim must be investigated.

REFERENCES

Albert, P., Bennartz, R., Preusker, R., Leinweber, R., and Fischer, J. (2005). Remote Sensing of Atmospheric Water Vapor Using the Moderate Resolution Imaging Spectroradiometer. *J. Atmos. Ocean. Tech., 22*, 309–314, doi:10.1175/JTECH1708.1, 2005.

Alizadeh, M.M., Wijaya, D.D., Hobiger, T., Weber, R., Schuh, H. (2013). Atmospheric effects in space geodesy. In: Böhm, J. and Schuh, H. (eds). *Ionospheric effects on microwave signals*. Springer, *Vol. 1*, 35–71.

Ashby, N. and Spilker, Jr. J. (1996) Introduction to Relativistic Effects on the Global Positioning System. In B.W. Parkinson., J.J. Spilker Jr., P. Axelrad. and P. Enge. *Global Positioning System: Theory and Applications* Volume 1, American Institute of Aeronautics and Astronautics, Inc., Washington, DC, *Vol. 1*, 623-715.

Ashby, N., (2003). Relativity in the Global Positioning System. Living Reviews in Relativity. Retrieved January 11, 2015, from http://relativitylivingreviews.org/Articles/lrr-2003-1/download/lrr-200 31Color.pdf.

Askne, J., and Nordius. H., (1987). Estimation of tropospheric delay for microwaves from surface weather data. *Radio Science, 22*, 379–386.

Baby, H.B., Gol´e. P., and Lavergnat. J., (1988), A model for the tropospheric excess path length of radio waves from surface meteorological measurements. *Radio Science, 23*, 1023–1038.

Banville, S., Santerre1, R., Cocard, M. and Langley, R. (2008). Satellite and Receiver Phase Bias Calibration for Undifferenced Ambiguity Resolution. *Proceedings Institute of Navigation.* National Technical Meeting. San Diego, CA, USA.

Berg, H. (1948) *Allgemeine Meteorologie.* Dümmlers Verlag, Bonn.

Bevis, M., Businger, S., Herring, T. A., Anthes, R., Rocken, C. and Ware, R. H. (1992). GPS meteorology: Remote sensing of atmospheric water vapor using the global positioning system. *Journal of Geophysical Research* (D), *97*, 15787– 15801.

Bevis, M., Businger, S., Chiswell, S., Herring, T. A., Anthes. R., Rocken. C., and Ware, R. H. (1994), GPS meteorology: Mapping zenith wet delays onto precipitable water. *Journal of Applied Meteorology, 33*, 379–386.

Bilitza, D., McKinnell, L. A., Reinisch, B. and Fuller-Rowell, T. (2011). The International Reference Ionosphere today and in the future. *J. Geod., 85*, 909–920.

Bisnath, S., Gao, Y. (2008). Current State of Precise Point Positioning and Future Prospects and Limitations. *Observing Our Changing Earth*, 615–623. doi: 10.1007/978-3-540-85426-5_71.

BKG. (2013). BKG Ntrip Client (BNC) Version 2.11 manual, Federal Agency for Cartography and Geodesy, Frankfurt, Germany.

Boehm, J. and Schuh, H. (2004). Vienna Mapping Functions in VLBI analyses. *Geophysical Research Letters, Vol. 31*.

Boehm, J., Werl, B. and Schuh, H. (2006a). Troposphere mapping functions for GPS and VLBI from ECMWF operational analysis data. *Journal of Geophysical Research, Vol. 111*.

Boehm, J., Niell, A., Tregoning, P. and Schuh, H. (2006b). Global Mapping Function (GMF): A new empirical mapping function based on numerical weather model data. *Geophysical Research Letters*, *33*(7). doi:10.1029/2005gl025546.

Boehm, J., Heinkelmann, R. and Schuh, H. (2007). Short Note: A global model of pressure and temperature for geodetic applications. *Journal of Geodesy, Vol. 81*, 679 - 683.

Boehm. J, Kouba. J, and Schuh, H. (2009). Forecast Vienna mapping functions 1 for real-time analysis of space geodetic observations. *J. Geodesy*, *83*(5), 2009. doi:10.1007/s00190-008-0216-y.

Böhm, J., Möller, G., Schindelegger, M., Pain,G., Weber, R. (2015). Development of an improved blind model for slant delays in the troposphere (GPT2w), *GPS Solutions*. doi:10.1007/s10291-014-0403-7.

Boudouris, G. (1963). On the index of refraction of air, the absorption and dispersion of centimeter waves in gases. *J. Res. Natl. Bur. Stand., 67*D, 631–684.

Carrere, L., Lyard, F., Cancet, M., Guillot, A., Picot, N. (2015). FES 2014, a new tidal model on the global ocean with enhanced accuracy in shallow seas and in the Arctic region. *In EGU General Assembly 2015*. 12-17 April 2015 in Vienna, Austria.

Chao, C. C. (1974). The troposphere calibration model for mariner mars 1971. Technical Report 32–1587, NASA JPL, Pasadena, CA, 1974.

Chen, G. and Herring, T. (1997). Effects of atmospheric azimuthal asymmetry on the analysis from space geodetic data. *Journal of Geophysical Research, Vol. 102*, 20489-20502.

Chen, K. and Gao, Y. (2005). Real-Time Precise Point Positioning Using Single Frequency Data. *Proceedings of ION GNSS*, September 13-16, Long Beach, CA. 1514-1523.

CNES. CNES PPP Demonstrator (PPP-Wizard Project), (2013). Retrieved June, 2015 from http://www.ppp-wizard.net/caster.html.

Collins, J.P. and Langley, R.B. (1998). "The Residual Tropospheric Propagation Delay: How Bad Can It Get?" *Proceedings of ION GPS-98, 11th International Technical Meeting of the Satellite Division of The Institute of Navigation*, Nashville, TN, 15-September 18, 729-738.

Collins, J.P. and Langley, R.B. (1997). A Tropospheric Delay Model for the User of the Wide Area Augmentation System. Final contract report for Nav Canada, Department.of Geodesy and Geomatics Engineering Technical Report No. 187, University of New Brunswick, Fredericton, N.B., Canada.

Conley, R., Cosentino, R., Hegarty, C. J., Kaplan, E. D., Leva, J. L., de Haag, M. U., and Van Dyke, K. (2006). In *Understanding GPS: Principles and Applications,* ed. E. D. Kaplan & C. J. Hegarty (2nd ed.; Boston, MA: Artech House), 301

Dach, R., Lutz, S., Walser, P., Fridez, P. (Eds)**.** (2015). Bernese GNSS Software Version 5.2. User manual, Astronomical Institute, University of Bern, Bern Open Publishing. DOI: 10.7892/boris.72297; ISBN: 978-3-906813-05-9.

Davis, J. L., Herring, T.A., Shapiro, I.I., Rogers, A.E.E. and Elgered. G. (1985). Geodesy by radio interferometry: Effects of atmospheric modeling errors on estimates of baseline length. *Radio Sci.*, *20*(6), 1593–1607. doi:10.1029/RS020i006p01593.

Davis, K. (1990). Ionospheric Radio. *IEE Electromagnetic Waves Series.* 31, Peter Pergrinus Ltd., London.

Dee, D.P. et al. (2011). The ERA-Interim reanalysis: configuration and performance of the data assimilation system. Q.*J.R. Meteorol. Soc., 137*, 553–597. doi:10.1002/qj.828.

DeMets, C., Gordon, R. G., Argus, F.D. and Stein, S. (1994). Effect of recent revisions to the geomagnetic reversal time scale on estimates of current plate motions. *Geophysical Research Letters, 21* (20), 2191–2194.

Elgered, G., Plag, H.P., van der Marel, H., Barlag, S. and Nash, J. (2005). *Exploitation of ground based GPS for operational numerical weather prediction and climate applications*. COST action 716: Final Report. European Union, Brussels, Belgium.

Essen, L. and Froome, K. D. (1951). The Refractive Indices and Dielectric Constants of Air and its Principal Constituents at 24 GHz. *Proc. of the Physical Society* (London), Section B, *64*, 862-875.

European Reanalyses and Observations for Monitoring – EURO4M. (2013). RetrievedMay15,2014fromhttp://cib.knmi.nl/mediawiki/index.php/Central_European_flooding_2013.

Fölsche, U. (1999). *Tropospheric water vapor imaging by combination of space-borne and ground-based GNSS sounding data*. (Ph.D. Thesis) Univ. Graz, Graz, Austria.

gLAB: GNSS-Lab Tool (v4.2). [Computer Software]. Research Group of Astronomy and Geomatics. ESA / UPC.

Gao, B.C. and Kaufman, Y. J. (2003).Water vapor retrievals using Moderate Resolution Imaging Spectroradiometer (MODIS) near-infrared channels, *J. Geophys. Res.-Atmos., 108*, 4389, doi:10.1117/12.154909.

Gao, Y. and Shen, X. (2001). Improving Ambiguity Convergence in Carrier Phase-Based Precise Point Positioning. *Proceedings of ION GPS-2001*, Salt Lake City, Utah, USA, September 11-14.

Gao, Y., Chen, K. and Shen, X. (2003). Real-Time Kinematic Positioning Based on Undifferenced Carrier Phase Data Processing. *Proceedings of ION NTM.* Jan.22 - 24, Anaheim, California. 362-368.

Ge, M., Gendt, G., Rothacher, M., Shi, C., Liu, J. (2008) Resolution of GPS carrier-phase ambiguities in precise point positioning (PPP) with daily observations. *Journal of Geodesy 82*(7), 389–399.

Ge, M., Dousa, J., Li, X., Ramatschi, M., Wickert, J. (2011), A Novel Real-Time Precise Positioning Service System: Global Precise Point Positioning with Regional Augmentation, *in: Proceedings of the 3rd Int. Colloquium - Galileo Science*, 31 August - 2 September 2011, Copenhagen, Denmark

Gendt, G., Dick, G., Söhne, W. (1999). GFZ Analysis Center of IGS — Annual Report 1998. In: Gowey K, Neilan R, Moore A (eds) 1998 IGS Technical Reports, IGS Central Bureau, Pasadena, 79–87.

Geng, J. et al. (2010). Towards PPP-RTK: Ambiguity resolution in real-time precise point positioning. *J. Adv. Space Res.* http://dx.doi.org/ 10.1016 /j.asr. 2010.03.030.

De Giovanni, G. and Radicella, S. (1990). An Analytical Model of the Electron Density Prole in the Ionosphere. *Advances in Space Research. 10*(11), 27-30.

GPS: The Global Positioning System. *(2002). Retrieved March 03, 2017, from http://www.gps.gov/systems/gps/modernization/sa/data.*

Gu, M. and Brunner, F.K. (1991). Theory of the two frequency dispersive range correction. *Manuscripta Geodaetica, vol. 15*, 357-361.

Herring, T.A. (1992). Modeling atmospheric delays in the analysis of space geodetic data. In J.C. De Munk and T. A. Spoelstra, editors, *Symposium on Refraction of Transatmospheric Signals in Geodesy*. 157–164. Netherlands Geod. Comm., Delft.

Herring, T., King, R. W., Floyd, M. A., McClusky, S. C. (2015). GAMIT manual Documentation for the GAMITGPS Analysis Software, Release 10.06.

Hopfield, H.S. Two-quartic tropospheric refractivity profile for correcting satellite data. *J. Geophys. Res.*, *74*, 4487–4499, 1969. doi:10.1029/JC074i018p04487.

Huffman, G. J., Bolvin, D. T. and Adler, R. F. (2016). *GPCP Version 1.2 One-Degree Daily Precipitation Data Set*. Research Data Archive at the National Center for Atmospheric Research, Computational and Information Systems Laboratory. https://doi.org/10.5065/D6D50K46. Accessed: 11.08.2017.

BeiDou-SIS-ICD. (2016). Technical report. BeiDou Navigation Satellite System Signal in Space. Interface Control Document. Retrieved 05.08.2017, from http://www.beidou.gov.cn/attach /2016/11/07/21212.pdf.

Ifadis, I. (1986). The atmospheric delay of radio waves: Modeling the elevation dependence on a global scale. Tech. Rep. 38L, School of Electrical and Computer Engineering, Chalmers University of Technology, Göteborg.

Jarlemark, P. O. J. (1997). *Analysis of temporal and spatial variations in atmospheric water vapor using microwave radiometry*. (Ph.D. Thesis). Tech. Rep. 308, School Electrical Computer Engineering, Chalmers Univ. Tech., 1997. Göteborg, Sweden.

JPL. JPL – NASA. (2011). Gaim introduction. Retrieved May, 2014. from http://iono.jpl.nasa. gov/gaim/intro.html.

Juan, J., Hernandez-Pajares, M. and Sanz, J. (2010). Precise Real Time Orbit Determination and Time Synchronization (PRTODTS). TN2 & TN3: GPS PRTODTS Design and Validation Documents, v0.0. ESA report (ESA ITT AO/1-5823/08/NL/AT), ESOC/ESA, Noordwijk, The Netherlands.

Juan, M., Hernandez-Pajares, M., Sanz, J., Ramos-Bosch, P., Aragon-Angel, A., Orus, R., Ochieng, W., Feng, S., Coutinho, P., Samson, J. and Tossaint, M. (2012). Enhanced Precise Point Positioning for GNSS Users. IEEE Transactions on Geoscience and Remote Sensing PP, *99*, 1-10.

Klobuchar, J. (1986). Design and characteristics of the GPS ionospheric time-delay algorithm for singlefrequency users. In *PLANS'86 - Position Location and Navigation Symposium*, pages 280–286, Las Vegas, Nevada, 4–7 November.

Kouba, J. and Héroux, P. (2001). GPS Precise Point Positioning Using IGS Orbit Products. *GPS Solutions,Vol.5*, No.2, 12-28.

Kouba, J. (2008). Implementation and testing of the gridded vienna mapping function 1 (VMF1). *J. Geodesy*,82(4–5):193–205, 2008. doi:10.1007/s00190-007-0170-0.

Kouba, J. (2009) A Guide to using International GNSS Service (IGS) products, Natural Resources Canada, http://igscb.jpl.nasa.gov/ components/usage.html (accessed December 2015).

Lagler, K., Schindelegger, M., Böhm, J., Krásná, H., Nilsson, T. (2013): GPT2: Empirical slant delay model for radio space geodetic techniques. - *Geophysical Research Letters*, *40*(6), 1069-1073.

Laurichesse, D. and Mercier, F., (2007). Integer Ambiguity Resolution on Undifferenced GPS Phase Measurements and Its Application to PPP. *Proceedings of the 20th International Technical Meeting of the Satellite Division*, Institute of Navigation. Fort Worth, TX, USA.

Laurichesse, D., Mercier, F., Berthias, J.P., Broca, P., Cerri, L. (2009)..Integer Ambiguity Resolution on Undifferenced GPS Phase Measurements and its Application to PPP and Satellite Precise Orbit Determination", *Navigation, Journal of the institute of Navigation*, Vol. 56, N° 2.

Laurichesse, D. (2011) The CNES real time PPP with un-differenced integer ambiguity resolution demonstrator, *Proceedings of the 24 th*e *International Technical Meeting of The Satellite Division of the Institute of Navigation 2011*, Portland, USA, 654-662.

Leandro, R. F., Santos, M.C. and Langley, R.B. (2006). UNB neutral atmosphere models: Development and performance. In National Technical Meeting of The Institute of Navigation, Monterey, California, 18–20 January, 564–573.

MacMillan, D. (1995). Atmospheric gradients from very long baseline interferometry observations. *Geophysical Research Letters, Vol. 22*, 1041-1044.

Mader, G. (1999). GPS antenna calibration at the National Geodetic Survey. *GPS Solutions*. *3*(1), 50-58.

Marini, J. (1972). Correction of satellite tracking data for an arbitrary tropospheric profile. *Radio Science, Vol. 7*, 223-231.

McCarthy, D. and Petit, G., (2004). IERS Conventions (2003). *IERS Technical Note 32*. IERS Convention Center, Frankfurt am Main.

Meindl, M., Schaer, S., Hugentobler, U. and Beutler, G. (2004). Tropospheric Gradient Estimation at CODE: Results from Global Solutions. *Journal of The Meteorological Society of Japan - J METEOROL SOC JPN*. *82*. 331-338. 10.2151/jmsj.2004.331.

Melbourne, W. G. (1985). The case for ranging in GPS based geodetic systems. In Goad, C., editor, *Proceedings of the 1*st *International Symposium on Precise Positioning with the Global Positioning System*, 373–386, US Department of Commerce, Rockville, Maryland, 1985.

Mendes, V. B. (1999). *Modeling of the neutral-atmosphere propagation delay in radiometric space techniques.* (Ph.D. Thesis). Department of Geodesy and Geomatics Engineering Tech. Report No. 199, University of New Brunswick, Fredericton, New Brunswick, Canada, 1999. General definitions of IWV, relative humidity etc.

Mikhail, E.M. and Ackermann, F. (1976). Observation and Least Square, IEP-A Dun- Donnelley Publisher, New York.

Mitchell, C.N., and Cannon, P.S. (2002). Multi-instrumental data analysis system (MIDAS) imaging of the ionosphere. Technical report, University of Bath, United States Air Force European Office of Aerospace Research and Development.

Navigation Centre of Excellence*. (2006, June 6). Retrieved from http://www.navcen.uscg.gov/cgsic/meetings/summaryrpts/46thMeeting /16%20CGSIC%0Constellation%20Status.ppt.*

Niell, A.E. (1996), Global mapping functions for the atmosphere delay at radio wavelengths, *Journal of Geophysical Research (B), 101*, 3227–3246.

Niell, A.E. (2000), Improved atmospheric mapping functions for VLBI and GPS, *Earth Planets Space*, *52*, 699–702.

Niell, A. E., Coster, A. J., Solheim, F.S., Mendes, V. B., Toor, P. C., Langley, R. B. and Upham, A.C. (2001) Comparison of measurements of atmospheric wet delay by Radiosonde, Water Vapor Radiometer, GPS, and VLBI. *J. Atmos. Oceanic Technol.,18*(6):830-850, doi:10.1175/15200426(2001)018<0830:COMOAW>2.0.CO;2.

Nilsson, T., Böhm, J., Wijaya, D.D., Tresch, A., Nafisi, V., Schuh, H. (2013). Atmospheric Effects in Space Geodesy. In: Böhm J Schuh H (eds), Path delays in the neutral atmosphere. Springer Atmospheric Sciences, 73–136. Springer, Berlin Heidelberg.

Owens, J. C. (1967). Optical refractive index of air: Dependence on pressure, temperature and composition. *Appl. Opt.*, *6*(1), 51–59, 1967.

Petit, G. and Luzum, B. (2010). IERS Conventions. IERS Technical Note 36, Bundesamt für Kartographie und Geodäsie, Frankfurt am Main, 2010. http://www.iers.org/IERS/ EN/Publications/TechnicalNotes/tn36.html. Accessed May, 2015.

Petrov, L. J. and Boy, P. (2004). Study of the atmospheric pressure loading signal in very long baseline Interferometry observations, *J. Geophys. Res*., *109*, B03405, doi:10.1029/2003JB002500.

Povalyaev, A. (2013) New Structure for GLONASS Navigation Message. *GPS World, 24*(11), 36.

Radicella, S. M. (2009). The Nequick model genesis, uses and evolution. *Annals of Geophysics, 52* (3/4), 417–422.

Ray, J. and Gurtner, W. (1999): "RINEX Extensions to Handle Clock Information". ftp://igscb.jpl.nasa.gov/igscb/data/format/rinex_clock.txt.

Ray, R. D. and Ponte, R. M. (2003). Barometric tides from ECMWF operational analyses. *Annales Geophysicae*, *21*(8), 1897–1910, 2003. doi: 10.5194/angeo-21-1897-2003.

Rocken, C., Van Hove, T. and Ware, R. (1997a). Near real-time sensing of atmospheric water vapor, *Geophysical Research Letters*, *24*, 3221-3224.

Rocken, C., Anthes, R. Exner, M., Ware, R., Feng, D., Gorbunov, M., Herman, B., Hunt, D., Kuo, Y.H., Schreiner, W., Sokolovskiy, S. and Zou, X. (1997b). Verification of GPS/MET data in the neutral atmosphere, *Journal of Geophysical Research 102*, 29849-29866.

Rothacher, M. (1992). Orbits of satellite systems in space geodesy. *Geod-Geophys. Arb. Schweiz, Vol. 46*. Schweizerische Geodatische Kommision.

Rothacher, M., Schaer, S., Mervart, L., Beutler, G. (1995). Determination of antenna phase center variations using GPS data. Gendt G. and Dick G. (eds) Proc 1995 IGS Workshop, GeoForschungs Zentrum Potsdam, Potsdam, 205–220.

Rothacher, M. and Beutler, G. (1998). The role of GPS in the study of global change. *Physics and Chemistry of the Earth, 23*(9-10):1029–1040.doi: 10.1016/S0079-1946(98)00143-8.

Rüeger, J. M. (2002). Refractive index formulae for radio waves. In *Proc. XXII FIG International Congress*, Washington DC, USA. FIG. URL http://www.fig.net/pub/fig_2002/ procmain.htm. Accessed April 2015.

Saastamoinen, J. (1972). Atmospheric correction for the troposphere and stratosphere in radio ranging of satellites, The use of artificial satellites for geodesy, *Geophys. Monogr. Ser., 15*, 247–251.

Sanz, J., Rovira-Garcia, Adria., Hernandez, M., Juan, J., Ventura-Traveset, J., Lopez, C., Hein, G. (2012). The ESA/UPC GNSS-Lab Tool (gLAB): An advanced educational and professional package for GNSS data processing and analysis. Retrieved May 18, 2015. Available from http://gage.upc.edu/glab-download.

Sanz, S.J., Hernandez. P. M., Juan, Z.M. (2013). GNSS Data Processing – Vol. I: Fundamentals and Algorithms. European Space Agency (ESA). Nordwijk, The Netherlands. Available at: http://bit.ly/1QV4KAL. Accessed on 12 January, 2015.

Schaer, S., Gunter. W., and Feltens. J. (1998). Ionex: The ionosphere map exchange format version 1. . *Proceeding of the IGS AC Workshop*. In In J. M. Dow, J. Kouba, and T. Springer (Eds.), pages 233–247, DaRMStadt, Germany.

Schaer, S. (1999). *Mapping and predicting the Earth's ionosphere using the Global Positioning System.* (Ph.D. Thesis). Bern University, Switzerland, 1999.

Schaer, S. and Steigenberger, S. (2006). Determination and Use of GPS Differential Code Bias Values. *IGS Analysis Centre Workshop*, Darmstadt, Germany.

Schenewerk, M., Dillinger, W. and Hilla, S. (2000), Online documentation for the PAGES suite of processing software, http://www.ngs.noaa.gov/ GRD/GPS/DOC/toc.html. Accessed on 15 February, 2015.

Seeber, G., (1993). *Satellite Geodesy: Foundations, Methods, and Applications*. Walter de Gruyter,, Berlin, Germany.

SIDC - Solar Influences Data Analyses Center (N.d), retrieved (June, 2016), from http://sidc.oma.be/silso/

Slater, J. A., Willis, P., Beutler, G., Gurtner, W., Lewandowski, W., Noll, C., Weber, R., Neilan, R. E. and Hein. G. (1999). The International GLONASS Experiment (IGEX-98): Organization, preliminary results and future plans. In *Prodeedings of the ION GPS-99*, Nashville, Tennessee, September.

Smith, E.K., and Weintraub, S. (1953), The constants in the equation for atmospheric refractive index at radio frequencies, in Proc. IRE *41*, 1035–1037.

Smith, W.L. (1966), Notes on the relationship between total precipitable water and surface dew point, *Journal of Applied Meteorology*, *5*, 726–727.

SMOS maps record soil water before flood. (2013). Phys.org - News and Articles on Science and Technology. Retrieved October 14, 2016, from https://phys.org/news/2013-06-smos-soil.html.

Strategic Plan 2013-2016. (2012). Retrieved May 13, 2017, from https://kb.igs.org/hc/en-us/articles/201747733-Strategic-Plan-2013 2016.

Steigenberger, P., Boehm. J., and Tesmer. V. (2009). Comparison of GMF/GPT with VMF1/ECMWF and implications for atmospheric loading. *J. Geodesy, 83*, 943–951, 2009. doi:10.1007/s00190-009-0311-8.

Teke, K. (2011). *Sub-daily parameter estimation in VLBI data analysis*. (Ph.D. Thesis). Vienna University of Technology, Vienna, Austria. Grafisches Zentrum HTU GmbH, ISSN 1811-8380.

Tesmer, V., Böhm, J., Heinkelmann. R. and Schuh. H. (2007). Effect of different tropospheric mapping functions on the TRF, CRF and position time-series estimated from VLBI. *J. Geodesy*, *81*(6–8), 409–421, 2007. doi:10.1007/s00190-006-0126-9.

Thayer, G. D. (1974). An improved equation for the radio refractive index of air. *Radio Sci., 9*(10):803–807.

Tregoning, P., Boers, R., O'Brien, D., and Hendy, M. (1998). Accuracy of absolute precipitable water vapor estimates from GPS observations, *J. Geophys. Res.-Atmos., 103*, 28701–28710.

Tregoning, P. and Herring, T.A. (2006). Impact of a priori zenith hydrostatic delay errors on GPS estimates of station heights and zenith total delays. *Geophys Res Lett 33*(L23303). doi:10.1029/ 2006GL027706

Trenberth, K.E., Dai, A., Rasmussen, R.M. and Parsons, D.B. (2003). The changing character of precipitation, *Bull Amer Meteor Soc.*, *84*(9), 1205–1217, doi:10.1175/BAMS-84-9-1205.

Update Starkregen und Rückblick Mai ZAMG*. (n.d). (in German). Retrieved 7 June 2013 from http://www.zamg.ac.at/cms/de/aktuell.*

Uppala, S.M. et al. (2005) The ERA-40 re-analysis, *Quarterly Journal of the Royal Meteorological Society, 131*, doi:10.1256/qj.04.176, 2961-3012.

Url-1<*http://www.igs.org/network*>, data retrieved 15.10.2016.

Url-2< *http://gaps.gge.unb.ca.*>, data retrieved 14.08.2016.

Url-3< *https://magicgnss.gmv.com*>, data retrieved 14.08.2016.

Url-4< *http://www.geod.nrcan.gc.ca/online_data_e.php*>, data retrieved 14.08.2016.

Url-5< *ftp://hpiers.obspm.fr/iers/eop*>, data retrieved 12.12.2016.

Url-6< *ftp://ftp.unibe.ch/aiub/CODE/*>, data retrieved 10.08.2016.

Url-7< *ftp://ftp.igs.org/pub/data/format/ionex1.pdf*>, data retrieved 12.04.2015

Url-8< *ftp://ftp.ncdc.noaa.gov/pub/data/igra* >, data retrieved 10.10.2015.

Url-9< *ftp://cddis.gsfc.nasa.gov/gnss/data/daily*>, data retrieved 15.10.2016.

Url-10<*https://ladsweb.nascom.nasa.gov*>, data retrieved 12.10.2016.

Url-11< *http://www.igs.org/network?network=rts*>, data retrieved 14.10.2017.

Vedel, H. (2006). Targeting optimal use of GPS humidity measurements in meteorology: Final report of the TOUGH project, 2006. URL http://web.dmi.dk/pub/tough/. Accessed May 2016.

Vey, S., Dietrich, R., Fritsche, M., Rülke, A., Rothacher, M., Steigenberger, P. (2006) Influence of mapping function parameters on global GPS network analyses: comparisons between NMF and IMF. *Geophys Res Lett 33*:L01814. doi:10.1029/2005GL024361.

Wang, J., Zhang, L. and Dai, A. (2005). Global estimates of water-vapor-weighted mean temperature of the atmosphere for GPS applications. *J. Geophys. Res.*, *110*(D21101), 2005. doi:10.1029/2005JD006215.

Weber, G., Mervart, L., Stürze, A., Rülke, A. and Stöcker, D. (2016). BKG Ntrip Client, Version 2.12. *Mitteilungen des Bundesamte für Kartographie und Geodäsie, Vol. 49*, Frankfurt am Main.

Wellenhof, H. B., Lichtenegger, H., Wasle, E. (2008): *GNSS - Global Navigation Satellite Systems (GPS, Glonass, Galileo and more)*, Springer, Wien, New York.

Wijaya, D. D., Böhm, J., Krasna, H., Karbon., Schuh, H. (2013). Atmospheric effects in space geodesy. In: Böhm, J. and Schuh, H. (eds). *Atmospheric Pressure Loading*. Springer, *Vol. 1*, 137–157.

Willis, P., Slater, J.A., Gurtner, W., Noll, C., Beutler, G., Weber, R., Neilan, R., He, G. (2000). In J. Slater, C. Noll, K. Gowey (Eds.), The GLONASS IGEX-98 Campaign: From its Genesis to Its Realization, *International GLONASS Experiment IGEX-98, IGEX Workshop Proceedings*, IGS Central Bureau, Nashville, Tennessee, 3-9.

Wooden, W. (1985). H. NAVSTAR Global Positioning System In Goad, C., editor, *Proceedings 1st International Symposium on Precise Positioning with the Global Positioning System, Vol. 1*, pages 403–412, US Department of Commerce, Rockville, Maryland, 1985. April 15-19. *Vol 1*, 23-32.

Wu, J., Wu, S., Hajj, G., Bertiguer, W. and Lichten, S. (1993). Effects of Antenna Orientation on GPS Carrier Phase Measurements. *Manuscripta Geodaetica*. *18*, 91-98.

Wubbena, G. (1985). Software developments for geodetic positioning with GPS using TI 4100 code and carrier measurements. In Goad, C., editor, *Proceedings First International Symposium on Precise Positioning with the Global Positioning System*, 403–412, US Department of Commerce, Rockville, Maryland, 1985.

Zumberge, J.F., Heflin, M.B., Jefferson, D.C., Watkins, M.M., Webb, F.H. (1997): Precise point positioning for the efficient and robust analysis of GPS data from large networks. *Journal of Geophysical Research, 102*(B3): 5005–5017.

APPENDICES

APPENDIX A: Least Squares Adjustment vs. Kalman Filter
APPENDIX B: URL Lists for GNSS Data and Products

APPENDIX A: Least Squares Adjustment vs. Kalman Filter

The aim of this part is to illustrate an example of a step-by–step solution of a PPP session that is based on code-only observations. The unknowns i.e. receiver coordinates (X, Y, and Z), receiver clock offsets (δt) and tropospheric zenith wet delays (ΔT_{wet}^{z}) were estimated by applying two different strategies: the least squares adjustment and the Kalman filter.

The daily observation data at "GRAZ" station, which was collected with a LEICA GRX1200 receiver, with LEIAR25.R3 antenna in GRAZ, Austria on June 3, 2013, was processed with precise ephemeris orbit "cod17430.pre" and rinex clock "cod17430.clk" files in static mode in order to estimate the unknowns.

The inputs and some settings that specified in the solution are given as below:

- Pseudoranges ($receiver_K$ - $satellite_J$): ρ_K^J (J=1, 2, 3,....,n; n>=4)
- Epochs: 9000sec, 9300sec and 9600sec.
- Precise ephemeris orbits: cod17430.pre.
- Precise ephemeris clocks: cod17430.clk.
- Earth Orientation Parameters: cod17427.erp.
- Antenna file: ANTEX08.atx.
- A priori positions: RINEX header records.
- Elevation mask: 5°.
- Data decimation: 300 seconds
- A priori troposphere: Saastamoinen with Niell dry mapping function.
- Observed satellites: GPS, GLONASS and GALILEO.

Unknowns:

- Receiver position (X, Y, Z)
- Receiver clock offset (Δt_{rec})
- Troposphere zenith wet delays (ΔT_{wet}^{z})

Appendix A1: Least Squares solution

For each satellite in view the ionosphere-free pseudorange observations can be defined as in equation (A 1.1):

$$C_K^J = \rho_K^J + c\left(dt_K + dt^J\right) + mf_{hyd}\Delta T_{hyd}^z + mf_{wet}\Delta T_{wet}^z + \varepsilon \qquad \text{(A 1.1)}$$

The code and phase measurements for three consecutive epochs are summarized in Table A.1 as below. The table are tabulated based on the field contents on top of the table.

Table A.1 : Input RINEX Measurements.

Input	Year	DoY	Sec	GNSS	PRN	Arc_length	C1	P1	P2	L1	L2
1	2	3	4	5	6	7	8	9	10	11	12
INPUT	2013	153	9000.00	GPS	17	235	22558577.9900	22558577.9900	22558573.6300	22558580.1611	22558577.586
INPUT	2013	153	9000.00	GPS	13	26	24372976.9980	24372976.9980	24372973.9180	24372976.7352	24372969.464
INPUT	2013	153	9000.00	GPS	11	300	22188160.2920	22188160.2920	22188155.4920	22188159.0171	22188153.807
INPUT	2013	153	9000.00	GPS	20	300	20251549.6260	20251549.6260	20251544.6860	20251557.3070	20251557.099
INPUT	2013	153	9000.00	GPS	31	219	22829456.7280	22829456.7280	22829452.0280	22829465.4014	22829467.480
INPUT	2013	153	9000.00	GPS	23	166	22158556.7940	22158556.7940	22158550.7340	22158564.1527	22158557.773
INPUT	2013	153	9000.00	GPS	32	300	20796290.0420	20796290.0420	20796286.0820	20796292.2950	20796290.378
INPUT	2013	153	9000.00	GPS	14	300	25168977.5340	25168977.5340	25168975.3340	25168972.9293	25168966.772
INPUT	2013	153	9000.00	GPS	1	300	20568154.4040	20568154.4040	20568153.2640	20568155.3098	20568154.818
INPUT	2013	153	9300.00	GPS	17	245	22523220.6100	22523220.6100	22523215.9300	22523222.6852	22523220.136
INPUT	2013	153	9300.00	GPS	13	36	24155131.9800	24155131.9800	24155129.1800	24155132.1433	24155124.981
INPUT	2013	153	9300.00	GPS	11	310	22372139.0520	22372139.0520	22372134.3320	22372137.4311	22372132.157
INPUT	2013	153	9300.00	GPS	20	310	20205593.0660	20205593.0660	20205588.1260	20205600.7260	20205600.514
INPUT	2013	153	9300.00	GPS	31	229	22800710.5080	22800710.5080	22800705.8680	22800719.1804	22800721.261
INPUT	2013	153	9300.00	GPS	23	176	21996537.8740	21996537.8740	21996531.6140	21996545.7121	21996539.495
INPUT	2013	153	9300.00	GPS	32	310	20868853.1220	20868853.1220	20868849.3220	20868855.4334	20868853.497
INPUT	2013	153	9300.00	GPS	14	310	25367693.0320	25367693.0320	25367690.8920	25367687.6798	25367681.347
INPUT	2013	153	9300.00	GPS	1	310	20655049.7640	20655049.7640	20655048.6840	20655050.6552	20655050.132
INPUT	2013	153	9600.00	GPS	17	255	22499051.3100	22499051.3100	22499046.5300	22499053.4431	22499050.917
INPUT	2013	153	9600.00	GPS	13	46	23939582.9220	23939582.9220	23939579.9420	23939583.3207	23939576.311
INPUT	2013	153	9600.00	GPS	11	320	22561274.7300	22561274.7300	22561270.1500	22561272.9520	22561267.614
INPUT	2013	153	9600.00	GPS	20	320	20166526.1460	20166526.1460	20166521.1460	20166533.7130	20166533.495
INPUT	2013	153	9600.00	GPS	31	239	22783150.7500	22783150.7500	22783146.2500	22783159.6063	22783161.675
INPUT	2013	153	9600.00	GPS	23	186	21840666.6360	21840666.6360	21840660.2360	21840674.8711	21840668.801
INPUT	2013	153	9600.00	GPS	32	320	20946810.0220	20946810.0220	20946806.2420	20946812.2680	20946810.312
INPUT	2013	153	9600.00	GPS	14	320	25567552.9100	25567552.9100	25567550.8900	25567546.7902	25567540.177
INPUT	2013	153	9600.00	GPS	1	320	20750827.3420	20750827.3420	20750826.4020	20750828.1982	20750827.641

Using the code pseudorange measurements the ionosphere-free linear combinations are formed based on the formula (i.e., equation A 1.2) as expressed below:

$$C_{L3} = \frac{f_1^2 P_1 - f_2^2 P_2}{f_1^2 - f_2^2} \qquad \text{(A 1.2)}$$

Then, prefit residuals are computed as given by equation (A 1.3):

$$\text{Prefit}_{rec}^{sat} = C_K^J\left[\text{measured}\right] - C_K^J\left[\text{modelled}\right] \qquad \text{(A 1.3)}$$

where the $C_K^J[\text{measured}]$ are obtained from the ionosphere-free combination of the code measurements (i.e., equation A 1.2) whereas the $C_K^J[\text{modelled}]$ are the sum of the modelled terms (i.e., equation A 1.4) such as atmosphere propagation, relativistic effects, clocks and instrumental delays.

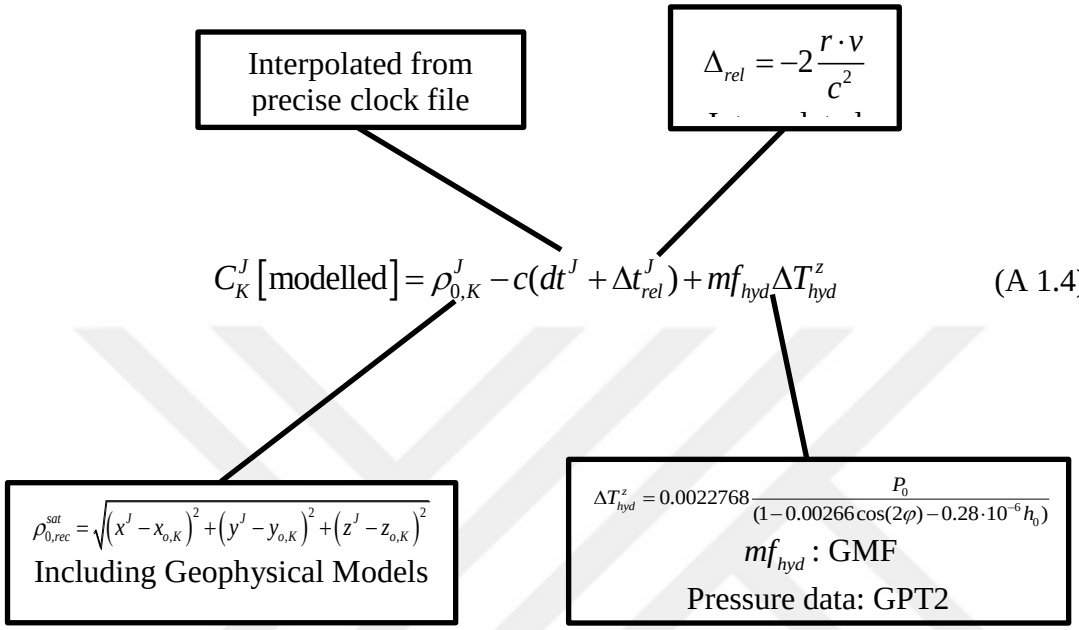

Linearising the satellite-receiver geometric range ρ around the a priori receiver position (x_0, y_0, z_0) we can write a non-linear measurement equation as a linear system(i.e., equation A 1.5) as below:

$$\begin{aligned} &C_K^J - \rho_{0,K}^J + cdt^{sat} + \Delta rel^{sat} - mf_{hyd}\Delta T_{hyd}^z = \\ &\frac{x_0 - x^{sat}}{\rho_{0,K}^{sat}}\Delta x_K + \frac{y_0 - y^{sat}}{\rho_{0,K}^{sat}}\Delta y_K + \frac{z_0 - z^{sat}}{\rho_{0,K}^{sat}}\Delta z_K + cdt_K + mf_{wet}\Delta T_{wet}^z \end{aligned} \quad \text{(A 1.5)}$$

The unknown vector to be determined is given by equation A 1.6 as:

$$\hat{x} = \left(\Delta x_K, \Delta y_K, \Delta z_K, cdt_k, \Delta T_{wet}^z\right) \quad \text{(A 1.6)}$$

where the coordinates are considered as constants (i.e., fixed receiver), clock offsets are modelled as white noise with zero mean, and the troposphere parameters are modelled as random – walk. The previous system of navigation equation can be written in matrix notation (i.e., equation A 1.7) as

$$\begin{bmatrix} \text{Prefit}^1 \\ \text{Prefit}^2 \\ \cdots\cdots\cdots \\ \text{Prefit}^n \end{bmatrix} = \begin{bmatrix} \frac{x_0 - x^{sat1}}{\rho_{0,K}^{sat1}} & \frac{y_0 - y^{sat1}}{\rho_{0,K}^{sat1}} & \frac{z_0 - z^{sat1}}{\rho_{0,K}^{sat1}} & 1 & mf_{wet}^{sat1} \\ \frac{x_0 - x^{sat2}}{\rho_{0,K}^{sat2}} & \frac{y_0 - y^{sat2}}{\rho_{0,K}^{sat2}} & \frac{z_0 - z^{sat2}}{\rho_{0,K}^{sat2}} & 1 & mf_{wet}^{sat2} \\ \cdots\cdots & \cdots\cdots & \cdots\cdots & \cdots & \cdots \\ \frac{x_0 - x^{satn}}{\rho_{0,K}^{satn}} & \frac{y_0 - y^{satn}}{\rho_{0,K}^{satn}} & \frac{z_0 - z^{satn}}{\rho_{0,K}^{satn}} & 1 & mf_{wet}^{satn} \end{bmatrix} \bullet \begin{bmatrix} \Delta x_K \\ \Delta y_K \\ \Delta z_K \\ cdt_{rec} \\ \Delta T_{wet}^z \end{bmatrix} \quad \text{(B 1.7)}$$

Prefit residuals for the three epochs: 9000, 9300 and 9600 seconds are tabulated below in Table A.2 before fitting the unknown parameters to the linear model.

Table A.2 : Prefit Resdiuals obtained from the solution.

GNSS	PRN	Obs	Prefit	Measures (m)	Model	x_pd	y_pd	z_pd	t_pd	Mf wet	el	az
5	6	7	8	9	10	11	12	13	14	15	16	17
PREFIT	9000.00	GPS 17	PC 1.3803	22558584.7294	22558583.3490	-0.3385	0.6951	-0.6342	1.0000	1.78168	34.059	-66.592
PREFIT	9000.00	GPS 13	PC 2.7591	24372981.7588	24372978.9997	-0.8807	0.2451	0.4053	1.0000	4.15366	13.698	-150.973
PREFIT	9000.00	GPS 11	PC 2.4222	22188167.7115	22188165.2893	-0.8712	-0.4902	0.0245	1.0000	1.55269	40.026	161.759
PREFIT	9000.00	GPS 20	PC 3.1477	20251557.2619	20251554.1142	-0.6110	0.1173	-0.7829	1.0000	1.04932	72.346	-65.633
PREFIT	9000.00	GPS 31	PC 1.6181	22829463.9929	22829462.3748	0.0513	-0.8769	-0.4780	1.0000	2.09442	28.414	77.507
PREFIT	9000.00	GPS 23	PC 2.3288	22158566.1611	22158563.8323	-0.9981	0.0607	-0.0119	1.0000	1.52984	40.752	-154.587
PREFIT	9000.00	GPS 32	PC 3.1025	20796296.1631	20796293.0605	-0.4036	-0.4052	-0.8203	1.0000	1.06455	69.924	55.432
PREFIT	9000.00	GPS 14	PC 0.6824	25168980.9346	25168980.2522	0.6294	-0.5137	-0.5831	1.0000	8.61388	6.157	41.837
PREFIT	9000.00	GPS 1	PC 2.1070	20568156.1661	20568154.0591	-0.7856	-0.4168	-0.4572	1.0000	1.07941	67.862	149.408
PREFIT	9600.00	GPS 17	PC 2.8045	22499058.6986	22499055.8941	-0.4008	0.7011	-0.5897	1.0000	1.7670	34.563	-71.889
PREFIT	9600.00	GPS 13	PC 2.9455	23939587.5283	23939584.5828	-0.9101	0.2455	0.3338	1.0000	3.6231	17.961	-149.719
PREFIT	9600.00	GPS 11	PC 3.0042	22561281.8094	22561278.8052	-0.8601	-0.4996	0.1030	1.0000	1.6314	35.452	162.002
PREFIT	9600.00	GPS 20	PC 3.9234	20166533.8746	20166529.9513	-0.5925	0.0408	-0.8045	1.0000	1.0 39	76.055	-55.084
PREFIT	9600.00	GPS 31	PC 1.7235	22783157.7058	22783155.9823	0.0880	-0.8394	-0.5364	1.0000	2.0647	29.186	72.447
PREFIT	9600.00	GPS 23	PC 3.0319	21840676.5287	21840673.4968	-0.9941	0.0515	-0.0950	1.0000	1.4619	45.458	-153.295
PREFIT	9600.00	GPS 32	PC 3.3506	20946815.8649	20946812.5143	-0.3672	-0.4724	-0.8013	1.0000	1.0786	66.009	61.442
PREFIT	9600.00	GPS 1	PC 2.3754	20750828.7950	20750826.4196	-0.8051	-0.4547	-0.3808	1.0000	1.0998	62.876	150.700
PREFIT	9900.00	GPS 17	PC 1.6516	22486134.9877	22486133.3361	-0.4304	0.7042	-0.5647	1.0000	1.759	34.599	-74.596
PREFIT	9900.00	GPS 13	PC 1.7426	23726719.8228	23726718.0803	-0.9229	0.2456	0.2965	1.0000	3.212	20.120	-149.029
PREFIT	9900.00	GPS 11	PC 2.4004	22755156.8658	22755154.4655	-0.8527	-0.5028	0.1416	1.0000	1.720	33.197	162.133
PREFIT	9900.00	GPS 20	PC 2.7497	20134410.1237	20134407.3740	-0.5837	0.0017	-0.8120	1.0000	1.030	77.771	-48.053
PREFIT	9900.00	GPS 31	PC 0.7578	22776914.2931	22776913.5353	0.1079	-0.8193	-0.5631	1.0000	2.044	29.376	69.898
PREFIT	9900.00	GPS 23	PC 1.6817	21691239.4687	21691237.7870	-0.9895	0.0462	-0.1366	1.0000	1.401	47.829	-152.612
PREFIT	9900.00	GPS 32	PC 2.2673	21029987.7029	21029985.4355	-0.3501	-0.5054	-0.7887	1.0000	1.094	64.052	64.065
PREFIT	9900.00	GPS 1	PC 0.9462	20855347.5186	20855346.5723	-0.8134	-0.4712	-0.3411	1.0000	1.123	60.389	151.363

where x_pd, y_pd and z_pd are the partial derivatives of X, Y and Z coordinates' corrections, respectively. The *t_pd*, is the partial derivative of the receiver clock correction and mf_{wet} is mapping function for the wet component. Using conversion formula (i.e., equation A 1.8) from ECEF (x, y, z) to Local (e, n, u) coordinates we get

$$\begin{bmatrix} \text{Prefit}^1 \\ \text{Prefit}^2 \\ \cdots\cdots\cdots \\ \text{Prefit}^n \end{bmatrix} = \begin{bmatrix} -\cos(el)^1 \sin(az)^1 & -\cos(el)^1 \cos(az)^1 & -\sin(el)^1 & 1 & mf_{wet}^1 \\ -\cos(el)^2 \sin(az)^2 & -\cos(el)^2 \cos(az)^2 & -\sin(el)^2 & 1 & mf_{wet}^2 \\ \cdots\cdots & \cdots\cdots & \cdots & \cdots & \cdots \\ -\cos(el)^n \sin(az)^n & -\cos(el)^n \cos(az)^n & -\sin(el)^n & 1 & mf_{wet}^n \end{bmatrix} \bullet \begin{bmatrix} \Delta e_K \\ \Delta n_K \\ \Delta u_K \\ cdt_{rec} \\ \Delta T_{wet}^z \end{bmatrix} \quad \text{(A 1.8)}$$

where el and az are elevation and azimuth angle of the satellites in view, respectively. The navigation equation for the epoch 9000 sec is illustrated in matrix form (i.e., equation A 1.9) as:

$$\begin{bmatrix} 1.3803 \\ 2.7591 \\ 2.4222 \\ 3.1477 \\ 1.6181 \\ 2.3288 \\ 3.1025 \\ 0.6824 \\ 2.1070 \end{bmatrix} = \begin{bmatrix} 0.760278 & -0.329128 & -0.560046 & 1 & 1.78168 \\ 0.471421 & 0.849521 & -0.236804 & 1 & 4.15366 \\ -0.239692 & 0.727272 & -0.643135 & 1 & 1.55269 \\ 0.276253 & -0.125122 & -0.952905 & 1 & 1.04932 \\ -0.858707 & -0.190261 & -0.475839 & 1 & 2.09442 \\ 0.325092 & 0.684241 & -0.652786 & 1 & 1.52984 \\ -0.282664 & -0.194764 & -0.939238 & 1 & 1.06455 \\ -0.663166 & -0.740748 & -0.107253 & 1 & 8.61388 \\ -0.191781 & 0.324388 & -0.926279 & 1 & 1.07941 \end{bmatrix} \cdot \begin{bmatrix} \Delta e_K \\ \Delta n_K \\ \Delta u_K \\ cdt_{rec} \\ \Delta T_{wet}^{z} \end{bmatrix} \quad \text{(A 1.9)}$$

The basic linearized GNSS measurement equation can be written as:

$$y = Gx \;\rightarrow\; G^T W y = G^T W G x \;\rightarrow \hat{x} = (G^T W G)^{-1} G^T W y \quad \text{(A 1.10)}$$

The matrix form in the equation A 1.9 can be written in the form (i.e., M matrix) as below, which is more convenient for matlab or octave coding.

Table A.3 : Prefit Resdiuals and design matrix components for the unknowns.

Epoch=9000	Prefit	$-\cos(el)\sin(az)$	$-\cos(el)\cos(az)$	$-\sin(el)^1$	1	mf_{wet}
	O-C	east	north	up	clock	zwd
9000	1.380	0.76027	-0.32912	-0.56004	1	1.7816
9000	2.759	0.47142	0.84352	-0.23680	1	4.1536
9000	2.442	-0.23969	0.72727	-0.64313	1	1.5526
9000	3.147	0.27625	-0.12512	-0.95290	1	1.0493
9000	1.618	-0.85870	-0.19026	-0.47583	1	2.0944
9000	2.328	0.32509	0.68424	-0.65278	1	1.5298
9000	3.102	-0.28266	-0.19476	-0.93923	1	1.0645
9000	0.682	-0.66316	-0.74074	-0.10725	1	8.6138
9000	2.107	-0.19178	0.32438	-0.92627	1	1.0794

The unknowns then can be derived by executing the code (i.e., equation A 1.11) below via Octave or Matlab:

$$\begin{aligned} &y = M(:,2); \quad G = M(:,3:7); \\ &W = \sigma^2 * eye(length(y), length(y)); \quad \%where\ \sigma = sigma = 1 \\ &\hat{x} = inv(G' \cdot W \cdot G) \cdot G' \cdot W \cdot y \end{aligned} \quad \text{(A 1.11)}$$

The unknown parameters for three subsequent epochs are tabulated in Table A.3 as below:

Table A.4 : Estimated unknowns for each observed epoch.

Epoch(sec)	East_corr(m)	North_corr(m)	Up_corr(m)	Clock_corr(m)	Wet delay(m)
9000	0.1716	0.7408	-2.0928	0.6133	0.0808
9300	0.2919	0.1842	-2.2598	-0.0195	0.2182
9600	0.6102	0.1573	-3.5178	-0.6047	0.6385

Appendix A2: Kalman Filter

The state vector to be determined is given by $\hat{x} = \left(\Delta x_K, \Delta y_K, \Delta z_K, cdt_k, \Delta T_{wet}^z\right)$ where the coordinates are parameterized as constants (i.e. fixed receiver), the clock offset can be modelled as white noise with zero mean and the wet delays can be modelled as random-walk. Under this conditions initial state vector, transition and process noise matrices are determined as below.

Filter configuration

- İnitialization: $\hat{x}(0) = \begin{pmatrix} 0 & 0 & 0 & 0 & 0 \end{pmatrix}$
- Process Noise, transition matrices and initial covariance matrix

Transition matrix

$$\Phi = \begin{bmatrix} 1 & 0 & 0 & 0 & 0 \\ 0 & 1 & 0 & 0 & 0 \\ 0 & 0 & 1 & 0 & 0 \\ 0 & 0 & 0 & 0 & 0 \\ 0 & 0 & 0 & 0 & 1 \end{bmatrix}$$

Process noise matrix

$$Q = \begin{bmatrix} 1e8 & 0 & 0 & 0 & 0 \\ 0 & 1e8 & 0 & 0 & 0 \\ 0 & 0 & 1e8 & 0 & 0 \\ 0 & 0 & 0 & 9e8 & 0 \\ 0 & 0 & 0 & 0 & 1e\text{-}4 \end{bmatrix}$$

Initial covariance matrix

$$P(0) = \begin{bmatrix} 1e8 & 0 & 0 & 0 & 0 \\ 0 & 1e8 & 0 & 0 & 0 \\ 0 & 0 & 1e8 & 0 & 0 \\ 0 & 0 & 0 & 1e8 & 0 \\ 0 & 0 & 0 & 0 & 0.25 \end{bmatrix} \quad \text{(A 2.1)}$$

- Measurement covariance matrix: $R = \sigma_y^2 I$ where $\sigma_y = 1\,m$.

Using the prefit residuals vector, design matrix illustrated in the equation A 1.8 and the configuration parameters defined in the equation A 2.1; the unknowns for the epochs 9000, 9300 and 9600 can be computed via the Kalman filter as expressed in equations A 2.2, A 2.3, A 2.4 and A 2.5:

For t=300 sec

Predict

$$x(t^-) = \Phi \cdot x(0)$$
$$P(t^-) = \Phi \cdot P(0)\Phi^T + Q$$

Update (A 2.2)

$$P(t) = \left[G(t)^T \cdot R(t^-)^{-1} \cdot G(t) + P(t^-)^{-1} \right]^{-1}$$

$$x(t) = P(t)\left[G(t)^T \cdot R(t)^{-1} \cdot y(t) + P(t^-)^{-1} \cdot x(t^-) \right]$$

For t=9000 sec

Predict

$$x(9000^-) = \Phi \cdot x(8700)$$
$$P(9000^-) = \Phi \cdot P(8700) \cdot \Phi^T + Q$$

Update (A 2.3)

$$P(9000) = \left[G(9000)^T \cdot R(9000^-)^{-1} \cdot G(9000) + P(9000^-)^{-1} \right]^{-1}$$
$$x(9000) = P(9000)\left[G(9000)^T \cdot R(9000)^{-1} \cdot y(9000) + P(9000^-)^{-1} \cdot x(9000^-) \right]$$

For t=9300 sec

Predict

$$x(9300^-) = \Phi \cdot x(9000)$$
$$P(9300^-) = \Phi \cdot P(9000) \cdot \Phi^T + Q$$

Update (A 2.4)

$$P(9300) = \left[G(9300)^T \cdot R(9300^-)^{-1} \cdot G(9300) + P(9300^-)^{-1} \right]^{-1}$$
$$x(9300) = P(9300)\left[G(9300)^T \cdot R(9300)^{-1} \cdot y(9300) + P(9300^-)^{-1} \cdot x(9300^-) \right]$$

t=9600 sec

Predict

$$x(9600^-) = \Phi \cdot x(9300)$$
$$P(9600^-) = \Phi \cdot P(9300) \cdot \Phi^T + Q$$

Update (A 2.5)

$$P(9600) = \left[G(9600)^T \cdot R(9600^-)^{-1} \cdot G(9600) + P(9600^-)^{-1} \right]^{-1}$$
$$x(9600) = P(9600)\left[G(9600)^T \cdot R(9600)^{-1} \cdot y(9600) + P(9600^-)^{-1} \cdot x(9600^-) \right]$$

The Kalman results computed via Octave or Matlab then compared with the results of the LSA solution in the Table A.4. Table A.5 illustrates the corrections estimated from the Kalman filter solution.

Table A.5 : Estimated unknowns for each epoch by using Kalman filter.

Epoch(sec)	East_corr(m)	North_corr(m)	Up_corr(m)	Clock_corr(m)	Wet delay(m)
300	-0.0089	0.7257	2.6824	2.4535	-0.3263
		….			
9000	0.1716	0.7408	-2.0928	0.6133	0.0808
9300	0.2919	0.1842	-2.2598	-0.0195	0.2182
9600	0.6102	0.1573	-3.5178	-0.6047	0.6385

APPENDIX B: URL List for GNSS Data and Products

URL address list of GNSS data used in the study are tabulated below where keywords in a URL address are given as below:

&YR year (4 digits: 2010 - 2099)	&gwgps week (0001 - 9999)
&yryear (2 digits: 10 - 99)	&gpd weekday (0 - 6)
&mnmonth (01- 12)	&minminutes (00 - 59)
&dmday of month (01 - 31)	&ststation name (lower case)
&hrhours (00 - 23)	&STstation name (upper case)
&hchour code(a - x)	&doyday of year (001 -365)

Table B.1: WEB addresses for GNSS RINEX Observation data.

AC: CDDIS	Address
IGS RINEX	ftp://cddis.gsfc.nasa.gov/gps/data/daily/&YR/&doy/&yrd/&st&doy0.&yrd.Z
NAV (GPS)	ftp://cddis.gsfc.nasa.gov/gps/data/daily/&YR/&doy/&yrn/brdc&doy0.&yrn.Z
NAV (GLO)	ftp://cddis.gsfc.nasa.gov/gps/data/daily/&YR/&doy/&yrg/brdc&doy0.&yrg.Z
RINEX HR	ftp://cddis.gsfc.nasa.gov/gps/data/hourly/&YR/&doy/&hr/&st&doy&hc.&yrd.Z
NAV HR	ftp://cddis.gsfc.nasa.gov/gps/data/hourly/&YR/&doy/&hr/&st&doy&hc.&yrn.Z
NAV HR (GLO)	ftp://cddis.gsfc.nasa.gov/gps/data/hourly/&YR/&doy/&hr/&st&doy&hc.&yrg.Z
RINEX High Rate	ftp://cddis.gsfc.nasa.gov/gps/data/highrate/&YR/&doy/&yrd/&hr/&st&doy &hc&min.&yrd.Z
NAV High Rate	ftp://cddis.gsfc.nasa.gov/gps/data/highrate/&YR/&doy/&yrn/&hr/&st&doy &hc&min.&yrn.Z
NAV High Rate (GLO)	ftp://cddis.gsfc.nasa.gov/gps/data/highrate/&YR/&doy/&yrn/&hr/&st&doy &hc&min.&yrg.Z
MGEX RINEX	ftp://cddis.gsfc.nasa.gov/gps/data/campaign/mgex/daily/rinex3/&YR/&doy /&yro/&st&doy0.&yro.Z
MGEX NAV	ftp://cddis.gsfc.nasa.gov/gps/data/campaign/mgex/daily/rinex3/&YR/&doy /&yrp/brdm&doy0.&yrp.Z
MGEX NAV (GLO)	ftp://cddis.gsfc.nasa.gov/gps/data/campaign/mgex/daily/rinex3/&YR/&doy /&yrg/&st&doy0.&yrg.Z
MGEX NAV (GAL)	ftp://cddis.gsfc.nasa.gov/gps/data/campaign/mgex/daily/rinex3/&YR/&doy /&yrl/&st&doy0.&yrl.

Table B.1 (continued): WEB addresses of GNSS RINEX Observation data.

AC: IGN	Address
RINEX	ftp://igs.ensg.ign.fr/pub/igs/data/&YR/&doy/&st&doy0.&yrd.Z
NAV	ftp://igs.ensg.ign.fr/pub/igs/data/&YR/&doy/brdc&doy0.&yrn.Z
NAV (GLO)	ftp://igs.ensg.ign.fr/pub/igs/data/&YR/&doy/brdc&doy0.&yrg.Z

Table B.2: WEB addresses of GNSS Precise Ephemeris Products: Orbits, Clocks and Earth Rotation Parameters.

AC: CDDIS	Address
EPH	ftp://cddis.gsfc.nasa.gov/gps/products/&gw/igs&gw&gpd.sp3.Z
EPH (GLO)	ftp://cddis.gsfc.nasa.gov/gps/products/&gw/igl&gw&gpd.sp3.Z
CLK	ftp://cddis.gsfc.nasa.gov/gps/products/&gw/igs&gw&gpd.clk.Z
CLK 30S	ftp://cddis.gsfc.nasa.gov/gps/products/&gw/igs&gw&gpd.clk_30s.Z
ERP	ftp://cddis.gsfc.nasa.gov/gps/products/&gw/igs&gw7.erp.Z
IGR EPH	ftp://cddis.gsfc.nasa.gov/gps/products/&gw/igr&gw&gpd.sp3.Z
IGR CLK	ftp://cddis.gsfc.nasa.gov/gps/products/&gw/igr&gw&gpd.clk.Z
IGR ERP	ftp://cddis.gsfc.nasa.gov/gps/products/&gw/igr&gw&gpd.erp.Z
IGU EPH	ftp://cddis.gsfc.nasa.gov/gps/products/&gw/igu&gw&gpd_&hr.sp3.Z
IGU ERP	ftp://cddis.gsfc.nasa.gov/gps/products/&gw/igu&gw&gpd_&hr.erp.Z
AC: CODE	Address
COD EPH	ftp://cddis.gsfc.nasa.gov/gps/products/&gw/cod&gw&gpd.ep
COD CLK	ftp://cddis.gsfc.nasa.gov/gps/products/&gw/cod&gw&gpd.cl
COD CLK 5S	ftp://ftp.unibe.ch/aiub/CODE/&YR/COD&gw&gpd.CLK_05S.Z
COD ERP	ftp://cddis.gsfc.nasa.gov/gps/products/&gw/cod&gw7.erp.Z
AC: ESA	Address
ESA EPH	ftp://cddis.gsfc.nasa.gov/gps/products/&gw/esa&gw&gpd.sp3.Z
ESA CLK	ftp://cddis.gsfc.nasa.gov/gps/products/&gw/esa&gw&gpd.clk.Z
ESA ERP	ftp://cddis.gsfc.nasa.gov/gps/products/&gw/esa&gw7.erp.Z
AC: GFZ	Address
GFZ EPH	ftp://cddis.gsfc.nasa.gov/gps/products/&gw/esa&gw&gpd.sp3.Z
GFZ CLK	ftp://cddis.gsfc.nasa.gov/gps/products/&gw/esa&gw&gpd.clk.Z
GFZ ERP	ftp://cddis.gsfc.nasa.gov/gps/products/&gw/esa&gw7.erp.Z
AC: JPL	Address
JPL EPH	ftp://cddis.gsfc.nasa.gov/gps/products/&gw/jpl&gw&gpd.sp3.Z
JPL CLK	ftp://cddis.gsfc.nasa.gov/gps/products/&gw/jpl&gw&gpd.clk.Z
JPL ERP	ftp://cddis.gsfc.nasa.gov/gps/products/&gw/jpl&gw7.erp.Z

Table B.2 (continued): WEB addresses of GNSS Precise Ephemeris Products: Orbits, Clocks and Earth Rotation Parameters.

AC: NGS	Address
NGS EPH	ftp://cddis.gsfc.nasa.gov/gps/products/&gw/ngs&gw&gpd.sp3.Z
NGS CLK	ftp://cddis.gsfc.nasa.gov/gps/products/&gw/ngs&gw&gpd.clk.Z
NGS ERP	ftp://cddis.gsfc.nasa.gov/gps/products/&gw/ngs&gw7.erp.Z
AC: EMR	Address
EMR EPH	ftp://cddis.gsfc.nasa.gov/gps/products/&gw/emr&gw&gpd.sp3.Z
EMR CLK	ftp://cddis.gsfc.nasa.gov/gps/products/&gw/emr&gw&gpd.clk.Z
EMR ERP	ftp://cddis.gsfc.nasa.gov/gps/products/&gw/emr&gw7.erp.Z
AC: MIT	Address
MIT EPH	ftp://cddis.gsfc.nasa.gov/gps/products/&gw/mit&gw&gpd.sp3.Z
MIT CLK	ftp://cddis.gsfc.nasa.gov/gps/products/&gw/mit&gw&gpd.clk.Z
MIT ERP	ftp://cddis.gsfc.nasa.gov/gps/products/&gw/mit&gw7.erp.Z
AC: CNES	Address
GRG EPH	ftp://cddis.gsfc.nasa.gov/gps/products/&gw/grg&gw&gpd.sp3.Z
GRG CLK	ftp://cddis.gsfc.nasa.gov/gps/products/&gw/grg&gw&gpd.clk.Z
GRG ERP	ftp://cddis.gsfc.nasa.gov/gps/products/&gw/grg&gw7.erp.Z
MGEX	Address
MGEX EPH COD	ftp://cddis.gsfc.nasa.gov/gps/products/mgex/&gw/com&gw&gpd.sp3.Z
MGEX EPH TUM	ftp://cddis.gsfc.nasa.gov/gps/products/mgex/&gw/tum&gw&gpd.sp3.Z
MGEX EPH GFZ	ftp://cddis.gsfc.nasa.gov/gps/products/mgex/&gw/gfm&gw&gpd.sp3.Z
MGEX EPH GRG	ftp://cddis.gsfc.nasa.gov/gps/products/mgex/&gw/grm&gw&gpd.sp3.Z
AC: IGN	Address
EPH	ftp://igs.ensg.ign.fr/pub/igs/products/&gw/igs&gw&gpd.sp3.Z
EPH (GLO)	ftp://igs.ensg.ign.fr/pub/igs/products/&gw/igl&gw&gpd.sp3.Z
CLK	ftp://igs.ensg.ign.fr/pub/igs/products/&gw/igs&gw&gpd.clk.Z
CLK 30S	ftp://igs.ensg.ign.fr/pub/igs/products/&gw/igs&gw&gpd.clk_30s.Z
ERP	ftp://igs.ensg.ign.fr/pub/igs/products/&gw/igs&gw7.erp.Z
IGR EPH	ftp://igs.ensg.ign.fr/pub/igs/products/&gw/igr&gw&gpd.sp3.Z
IGR CLK	ftp://igs.ensg.ign.fr/pub/igs/products/&gw/igr&gw&gpd.clk.Z
IGR ERP	ftp://igs.ensg.ign.fr/pub/igs/products/&gw/igr&gw&gpd.erp.Z
IGU EPH	ftp://igs.ensg.ign.fr/pub/igs/products/&gw/igu&gw&gpd_&hr.sp3.Z
IGU ERP	ftp://igs.ensg.ign.fr/pub/igs/products/&gw/igu&gw&gpd_&hr.erp.Z

Table B.3: Differential Code Biases.

DCB P1P2	ftp://ftp.unibe.ch/aiub/CODE/&YR/P1P2&yr&mn.DCB.Z
DCB P1C1	ftp://ftp.unibe.ch/aiub/CODE/&YR/P1C1&yr&mn.DCB.Z
DCB P2C2	ftp://ftp.unibe.ch/aiub/CODE/&YR/P2C2&yr&mn.DCB.Z

Table B.4: Troposphere and Ionosphere.

IGS ZPD	ftp://cddis.gsfc.nasa.gov/gps/products/troposphere/zpd/&YR/&doy/%s&doy0.&yrzpd.gz
CODE TRO	ftp://ftp.unibe.ch/aiub/CODE/&YR/COD&gw&gpd.TRO.Z
IGS TEC	ftp://cddis.gsfc.nasa.gov/gps/products/ionex/&YR/&doy/igsg&doy0.&yri.Z
IGR TEC	ftp://cddis.gsfc.nasa.gov/gps/products/ionex/&YR/&doy/igrg&doy0.&yri.Z
CODE ION	ftp://ftp.unibe.ch/aiub/CODE/&YR/COD&gw&gpd.ION.Z

Table B.5: ANTEX files.

IGS ZPD	ftp://cddis.gsfc.nasa.gov/gps/products/troposphere/zpd/&YR/&doy/%s&doy0.&yrzpd.gz
IGS TEC	ftp://cddis.gsfc.nasa.gov/gps/products/ionex/&YR/&doy/igsg&doy0.&yri.Z
IGR TEC	ftp://cddis.gsfc.nasa.gov/gps/products/ionex/&YR/&doy/igrg&doy0.&yri.Z

Table B.6: VMF1 GRID data.

VMF GRID	http://ggosatm.hg.tuwien.ac.at/DELAY/GRID/VMFG/&YR/VMFG_&YR&mn&doy.H&hr

Table B.7: ITRF Coordinates and velocities.

ITRF 2014 Coordinates	ftp://ftp.unibe.ch/aiub/BSWUSER52/STA/ITRF2014_R.CRD
ITRF 2014 Velocities	ftp://ftp.unibe.ch/aiub/BSWUSER52/STA/ITRF2014_R.VEL
CODE Daily ITRF Coordinates	ftp://ftp.unibe.ch/aiub/BSWUSER52/STA/&YR/COD&yr&doy.CRD.Z

Table B.8: IERS Ocean Loading File.

FES2004.BLQ	ftp://ftp.unibe.ch/aiub/BSWUSER52/STA/FES2004.BLQ

Table B.9: Phase Center Variations file.

PCV_COD.I14	ftp://ftp.unibe.ch/aiub/BSWUSER52/GEN/PCV_COD.I14

CURRICULUM VITAE

Name Surname **:** Engin TUNALI

Place and Date of Birth **:** Bulgaria / 30.01.1983

E-Mail **:** tun.engin@gmail.com

EDUCATION **:**

- **B.Sc.** **:** 2008, Istanbul Technical University, Civil Engineering Faculty, Geodesy and Photogrammetry Engineering Department.
- **M.Sc.** **:** 2010, Istanbul Technical University, Department of Geomatics Engineering, Geomatics Engineering Programme.

PROFESSIONAL EXPERIENCE AND REWARDS:

- 2009 - : Research Assistant at Geomatics Engineering Department at Hacettepe University.

PUBLICATIONS, PRESENTATIONS AND PATENTS ON THE THESIS:

- **Tunalı, E.** (2016). Hassas Konum Belirlemede (PPP) Farklı Atmosfer Modelleri Kullanarak Troposfer Kaynaklı Gecikmelerin Karşılaştırılması. *8. Ulusal Mühendislik Ölçmeleri Sempozyumu*, İstanbul, Turkey. October 19-21, 2016.
- **Tunalı, E.** (2017). Gerçek Zamanlı PPP Servisleri ve Sayısal Hava Tahmin Modelleri ile Atmosferdeki Su Buharı Değişimlerinin İzlenmesi. *16. Türkiye Harita Bilimsel ve Teknik Kurultayı*. Ankara, Turkey. May 3-6, 2017.
- **Tunalı, E., Özlüdemir., M. T.** (2017). Monitoring troposphere variations over afforested and deforested European regions by using GNSS PPP. *Journal of the Faculty of Forestry Istanbul University.* In Review.
- **Tunalı, E.** (2017). PPP ve IGS Gerçek Zaman Servisi ile Su Buharı Hareketlerinin İzlenmesi. *Afyon Kocatepe Üniversitesi Fen Bilimleri Dergisi.* Accepted 12.11.2017.